

**Resonant and High-Energy X-Ray Scattering
Studies on Strongly Correlated Electron Systems
in Transition Metal Oxides**

Von der Fakultät Mathematik und Physik der Universität Stuttgart
zur Erlangung der Würde eines Doktors der Naturwissenschaften (Dr. rer. nat.)
genehmigte Abhandlung

vorgelegt von

Ioannis Zegkinoglou
aus Athen (Griechenland)

Hauptberichter: Prof. Dr. Bernhard Keimer
Mitberichter: Prof. Dr. Helmut Dosch
Tag der mündlichen Prüfung: 10. Januar 2007

Max-Planck-Institut für Festkörperforschung
Stuttgart 2007

Contents

Introduction	5
1 Transition Metal Oxides	9
1.1 Introduction	9
1.2 Crystal Structure	10
1.3 Electronic Structure	11
1.3.1 Crystal Field Theory	12
1.4 Mott insulators	17
1.4.1 Hubbard Model	19
1.4.2 Orbital Degeneracy and Orbital Ordering	21
1.5 Superconductivity	23
1.5.1 The Phenomenon of Superconductivity	23
1.5.2 The BCS Theory	25
1.5.3 High-Temperature Superconductors	26
2 X-ray Diffraction	31
2.1 Introduction	31
2.2 Synchrotron Radiation	31
2.3 Non-resonant Scattering	34
2.3.1 Kinematical Theory. Charge, Spin and Orbital Scattering	34
2.3.2 High-energy Diffraction	36
2.4 Resonant Diffraction from Antiferromagnets	37
2.4.1 Basic Principles and Historical Background	37
2.4.2 Resonant Electric Dipole Scattering Length	39
2.5 Orientation Matrix	44
3 The system $\text{Ca}_{2-x}\text{Sr}_x\text{RuO}_4$ ($x = 0, 0.1$)	47
3.1 Crystal Structure	48
3.2 Electronic Structure and Orbital Order	52
3.3 Magnetic Properties	57
3.4 Transport Properties and the Metal-Insulator Transition	58

3.5	Experimental	61
3.5.1	Samples	61
3.5.2	Experimental Setup	64
3.6	Investigations at the (1 0 0) Reciprocal Space Position	74
3.6.1	Alignment	74
3.6.2	Energy Scans: Polarization and Temperature Dependence	75
3.6.3	Reciprocal Space Scans: Temperature Dependence	80
3.6.4	Reciprocal Space Scans: Azimuthal Angle Dependence	87
3.7	Investigations at the (0 1 1) Reciprocal Space Position	91
3.7.1	Alignment	91
3.7.2	Energy Scans: Temperature Dependence	92
3.7.3	Reciprocal Space Scans: Temperature Dependence	93
3.7.4	Reciprocal Space Scans: Azimuthal Angle Dependence	95
3.8	Investigations at the (1 1 0) Reciprocal Space Position	99
3.8.1	Alignment	99
3.8.2	Energy Scans: Temperature Dependence	99
3.8.3	Reciprocal Space Scans: Temperature Dependence	101
3.8.4	Reciprocal Space Scans: Azimuthal Angle Dependence	102
3.8.5	Tilt Order: Simulation	103
3.9	Investigations at Half-Integer Reciprocal Space Positions	105
3.10	Muon Spin Rotation Measurements	106
3.11	The $\text{Ca}_{1.9}\text{Sr}_{0.1}\text{RuO}_4$ System	108
3.12	Discussion	114
4	The system $\text{RuSr}_2\text{GdCu}_2\text{O}_8$	123
4.1	Crystal and Electronic Structure	123
4.2	Magnetism and Superconductivity	125
4.3	Experimental	127
4.3.1	Samples	128
4.3.2	Experimental Setup	129
4.4	Determination of the Magnetic Moment Direction	130
4.5	Magnetic Order Parameter	136
4.6	Discussion	138
5	The system $\text{YBa}_2\text{Cu}_3\text{O}_{6+x}$	141
5.1	Crystal Structure and Oxygen Order	142
5.2	Superconductivity and Stripes	146
5.3	Isotope substitution: ^{16}O - vs. ^{18}O -rich compounds	148
5.4	Experimental	149
5.4.1	Samples	149
5.4.2	Experimental Setup	150

5.5	X-ray Diffraction Investigations	154
5.5.1	Underdoped $\text{YBa}_2\text{Cu}_3\text{O}_{6+x}$ compounds	154
5.5.2	Optimally doped and overdoped $\text{Y}_{1-y}\text{Ca}_y\text{Ba}_2\text{Cu}_3\text{O}_{6+x}$ compounds	158
5.5.3	The stoichiometric $\text{YBa}_2\text{Cu}_4\text{O}_8$ compound	162
5.6	Discussion	163
6	Summary	169
A	Calculation of the absorption coefficient μ from fluorescence measurements	171
B	Trigonometric calculations for determining the magnetic moment direction in $\text{RuSr}_2\text{GdCu}_2\text{O}_8$	173
C	Maple code for calculating the azimuthal dependence due to tilt order in Ca_2RuO_4	177
	Bibliography	183
	Deutsche Zusammenfassung	191
	Acknowledgements	195
	Curriculum Vitae	199

Introduction

The physical properties of transition metal oxides have been in the focus of scientific interest for a number of years. The strongly correlated electron systems in these compounds are susceptible to instabilities, in which several degrees of freedom are often involved. The interplay between lattice, charge, spins and orbitals results in interesting phenomena, but at the same time makes the understanding of the underlying physics a difficult task. Ruthenium oxides of the type $\text{Ca}_{2-x}\text{Sr}_x\text{RuO}_4$ are a good example of such a case. Magnetism and orbital correlations are intimately coupled in this $4d$ electron system. What is more, the substantial distortions of the lattice contribute to the lifting of the degeneracy of the $4d$ electronic states, thus influencing the associated orbital occupations, which in turn influence the lattice deformations around the metal sites. The investigation of the interplay among all these degrees of freedom is necessary for obtaining an insight into the rich phase diagram of the system. Interestingly, the substitution of calcium for strontium leads to a remarkable variation of the material's properties, that extend from unconventional spin-triplet superconductivity, in one of the two end-members of the series (Sr_2RuO_4), to orbital ordering in a Mott insulating antiferromagnetic phase, at the other end of the strontium-content range (Ca_2RuO_4).

Different kinds of instabilities determine the properties of the $3d$ electron systems in layered copper oxides. The high-temperature superconductivity which is established in these systems when they are doped with charge carriers, and the unusual electronic properties which they exhibit in their normal state, above the superconducting transition temperature, like, for example, the opening of an electronic pseudogap, have motivated a large number of scientific studies in the last years, which could however achieve only small steps towards the establishment of a generic theory of high-temperature superconductivity. Several excitations have been suggested to play an important role in the pairing mechanism of the electrons. One-dimensional charge and spin 'stripes' of dynamic nature within the copper-oxygen planes of these materials belong to the most popular and, at the same time, most controversial of the proposed excitations. Many of the experimental investigations that dealt with this issue were carried out on the bilayered compound $\text{YBa}_2\text{Cu}_3\text{O}_{6+x}$. Several observations in neutron and x-ray scattering experiments on this material

were interpreted as possible signatures of one-dimensional spin and charge excitations. The interpretation of the data is however complicated, partly because of the existence of one-dimensional structural units (copper-oxygen chains) in the lattice, and partly because of the so-called twinning effect. The one-dimensional character of the observed excitations is thus questioned by other studies and the long-lasting discussion about the possible existence and role of fluctuating stripes in $\text{YBa}_2\text{Cu}_3\text{O}_{6+x}$ and other cuprates remains open.

Combining several of the properties of the above described $4d$ electron ruthenates and $3d$ electron cuprates, the hybrid ruthenocuprate compound $\text{RuSr}_2\text{GdCu}_2\text{O}_8$ is a very interesting system. Its most salient feature is the intriguing coexistence of long-range magnetic order and superconductivity within a fairly broad temperature range. The crystal structure of the material enables this unusual coexistence. This is characterized by alternating copper-oxygen and ruthenium-oxygen planes. Superconductivity is established in the copper-oxygen planes, exactly like in $\text{YBa}_2\text{Cu}_3\text{O}_{6+x}$, below a transition temperature which lies between 15 K and 46 K. The ruthenium-oxygen layers, on the other hand, are antiferromagnetically ordered below a significantly higher Néel temperature of around 136 K. The two phenomena, magnetism and superconductivity, being spatially separated within the unit cell, seem to be established independent from each other. The investigations that have been carried out so far have not indicated any interplay between the two order parameters. However, good quality single crystals of this compound were only recently made available and the need for a more careful re-examination of this issue under better experimental conditions arises.

X-rays are an appropriate probe for the study of the above described physical phenomena in transition metal oxides. The great advances achieved in synchrotron radiation facilities in the last two decades have enabled the use of x-ray scattering techniques for purposes that extend far beyond the 'traditional' methods of structure determination and material analysis. X-rays couple directly to the charge. The high brightness of the produced radiation at synchrotron facilities allows the observation of very weak diffuse features, and thus the investigation of short-range charge superstructures that are characterized by correlation lengths comparable to or even smaller than one unit cell dimension – as is the case in $\text{YBa}_2\text{Cu}_3\text{O}_{6+x}$. What is more, by tuning the photon energy of the x-rays close to an absorption edge of the transition metal, the probe becomes sensitive also to the magnetic structure and orbital arrangement of the material. The large resonant enhancement of the scattering intensity, obtained in particular at the L -edges of the transition metals, in combination with the sensitivity of the corresponding structure factor on the magnetic moment direction in the investigated sample, make the newly developed resonant x-ray diffraction technique ideal for the study of the $\text{Ca}_{2-x}\text{Sr}_x\text{RuO}_4$ and $\text{RuSr}_2\text{GdCu}_2\text{O}_8$ systems. Of particular importance is the fact that, thanks to the very good collimation that characterizes synchrotron x-ray beams, even very small

scattering volumes, down to the order of 10^{-3} mm³ or smaller, are sufficient for the investigations. This is a significant advantage of resonant x-ray diffraction over other complementary techniques, such as neutron scattering.

The work at hand is organized in six chapters:

- Chapter 1 gives a short overview of the basic properties of transition metal oxides. The main predictions of the crystal field theory for the electronic structure of d -electron systems are described. An introduction to the single-orbital Hubbard model, which can satisfactorily explain many of the magnetic properties of Mott insulators, as well as a brief reference to the principal features of conventional and high-temperature superconductors, are also included in the chapter.
- Chapter 2 deals with the principles of x-ray scattering. After a short presentation of the properties of synchrotron radiation, the kinematical theory of diffraction is introduced and the scattering amplitude for non-resonant scattering is given. The principles of resonant x-ray diffraction from antiferromagnets are discussed in the following in more detail and the resonant electric dipole scattering length is calculated as a function of the azimuthal angle ψ of the investigated sample.
- In Chapter 3 the experimental results of the resonant x-ray diffraction investigations of the $\text{Ca}_{2-x}\text{Sr}_x\text{RuO}_4$ system at the Ru L_{II} absorption edge are presented. The first four sections contain background information about the material. The technical details of the experimental procedure, including information about the experimental setup and the investigated samples, are given in Section 5. The results of the measurements carried out on Ca_2RuO_4 at reciprocal space positions (1 0 0), (0 1 1) and (1 1 0) are presented in the following. In Section 11 the measurements carried out on the Sr-doped $\text{Ca}_{1.9}\text{Sr}_{0.1}\text{RuO}_4$ compound are described. The chapter ends with a discussion of the obtained results, together with the main conclusions of the studies.
- Chapter 4 contains the experimental results of the resonant x-ray diffraction investigations of the hybrid $\text{RuSr}_2\text{GdCu}_2\text{O}_8$ system at the Ru L_{II} absorption edge. After a reference to all relevant background information concerning the material (Sections 1 and 2) and a description of the investigated samples (Section 3), the obtained experimental results are presented. First, the determination of the direction of the magnetic moment based on the azimuthal dependence of the magnetic scattering intensity is described in detail (Section 4). The possible coupling between magnetism and superconductivity is investigated in the following (Section 5). The chapter ends with a discussion of all results, where the main conclusions are summarized.

- Chapter 5 deals with the investigation of the high-temperature superconductor $\text{YBa}_2\text{Cu}_3\text{O}_{6+x}$ with high-energy x-ray diffraction. The material-related background information is given in the first three sections of the chapter, while the experimental details in the fourth. The experimental results of the studies on underdoped, optimally doped and overdoped $\text{YBa}_2\text{Cu}_3\text{O}_{6+x}$, as well as on stoichiometric $\text{YBa}_2\text{Cu}_4\text{O}_8$, are presented in Section 5. The chapter ends, as usual, with a combined evaluation of all results and a presentation of the main conclusions of the studies.
- The last chapter of the thesis summarizes the main results and conclusions of the work.

Chapter 1

Transition Metal Oxides

1.1 Introduction

Transition metals are the elements which occupy the central part of the periodic table, namely from Group IIIB (3) through Group IIB (12) inclusive. They are divided into three series, which consist of the elements from scandium to zinc (atomic numbers $Z=21$ to $Z=30$), from yttrium to cadmium ($Z=39$ to $Z=48$) and from hafnium to mercury ($Z=72$ to $Z=80$), respectively (Figure 1.1). To these a fourth series of artificial radioactive elements can be added, namely the elements from rutherfordium to ununbium ($Z=104$ to $Z=112$). The main common feature of all these elements is the progressive filling of shells of d orbitals across each series. In this way, they represent a gradual transition from Group 2 elements to Group 13 elements, which justifies their name. The exact definition of transition metals is, however, rather loose and the precise boundaries of the transition series vary according to the definition used. Group IIB, for instance, the elements of which have a fully occupied d orbital, is often not included in the transition series. Scandium is also often excepted because, together with zinc, it lacks a basic property of all other transition metals, responsible for a large number of their physical properties, that is, the ability to contribute valence electrons from s orbitals before d orbitals. In oxides the properties related to the d orbitals are most apparent with the transition elements between titanium and copper in the $3d$ series, between zirconium and silver in the $4d$ series and between hafnium and gold in the $5d$ series. These are the elements the present chapter is going to concentrate on.

Transition metal oxides (TMOs) exhibit some of the most fascinating physical properties among all inorganic solids. The high-temperature superconductivity discovered in layered copper oxides, commonly known as cuprates, and the colossal magnetoresistance (CMR) observed in many manganese oxides, commonly named manganites, are only two of the numerous examples that can be mentioned. These

1	IA	H	IIA											0	He									
2		Li	Be											IIIA	B	IVA	C	VA	N	VIA	O	VIIA	F	Ne
3		Na	Mg	IIIB	IVB	VB	VIB	VII B	VII	IB	IIB	Al	Si	P	S	Cl	Ar							
4		K	Ca	Sc	Ti	V	Cr	Mn	Fe	Co	Ni	Cu	Zn	Ga	Ge	As	Se	Br	Kr					
5		Rb	Sr	Y	Zr	Nb	Mo	Tc	Ru	Rh	Pd	Ag	Cd	In	Sn	Sb	Te	I	Xe					
6		Cs	Ba	*La	Hf	Ta	W	Re	Os	Ir	Pt	Au	Hg	Tl	Pb	Bi	Po	At	Rn					
7		Fr	Ra	+Ac	Rf	Ha	Sg	Ns	Hs	Mt	110	111	112	113										
				* Lanthanide Series																				
				58	59	60	61	62	63	64	65	66	67	68	69	70	71							
				Ce	Pr	Nd	Pm	Sm	Eu	Gd	Tb	Dy	Ho	Er	Tm	Yb	Lu							
				+ Actinide Series																				
				90	91	92	93	94	95	96	97	98	99	100	101	102	103							
				Th	Pa	U	Np	Pu	Am	Cm	Bk	Cf	Es	Fm	Md	No	Lr							

Figure 1.1: Periodic table of the elements. The transition metals occupy the central part of the table, between Groups IIIB and IIB.

properties are the result of a number of factors associated with the electronic and crystal structure of the systems, but a complete general theory that describes their exact origin does not exist. A key role is certainly played by the strong electron correlations induced by the narrow electronic bands, which are the result of the small overlap between the d orbitals of the transition metals and the p orbitals of the neighboring oxygen ions. The interactions between the charge, spin and orbital degrees of freedom of the d electrons and their coupling to the lattice lead to a large range of electronic and magnetic properties, which have attracted a great deal of scientific interest in the recent years. The low-dimensional features which arise from the crystal structure of many transition metal oxides and the distortions of the lattice further contribute to the richness of the observed properties.

1.2 Crystal Structure

Transition metal oxides exist in a large variety of crystal structures. Most of them are derived from variations and distortions of the ideal perovskite structure. The latter is very common among compounds of the formula AMO_3 , with M being a transition metal ion and A typically a pre-transition metal, such as K or Sr, with size larger than transition metals. Ideally the ionic radii r_A , r_M and r_O of the A, M and O ions, respectively, satisfy the condition:

$$r_A + r_O = \sqrt{2}(r_M + r_O) \quad (1.1)$$

In real perovskite oxides, however, the condition takes rather the form:

$$r_A + r_O = t\sqrt{2}(r_M + r_O) \quad (1.2)$$

with the prefactor t taking values between approximately 0.8 and 1.0 [1]. In such a three-dimensional structure every transition metal ion M is surrounded by six oxygen (O) ions that form an octahedron. An ideal AMO_3 perovskite built up of corner-sharing MO_6 octahedra is illustrated in Figure 1.2(a).

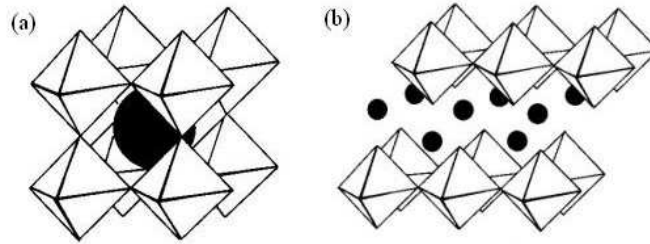


Figure 1.2: Schematic view of the ideal perovskite (AMO_3) (a) and the layered perovskite or K_2NiF_4 (b) structures. The transition metal ions M are located at the centres of the octahedra, surrounded by six oxygen ions, which occupy the sites at the corners of the octahedra. The dark-colored bullets represent the metal ions A [2].

Compounds with a chemical formula of the type $A_{n+1}M_nO_{3n+1}$ have usually a two-dimensional, layered structure known as the layered perovskite structure. For $n = 1$ this formula gives the so-called K_2NiF_4 -structure, which is composed of layers of octahedra that are corner-sharing only in two dimensions, with the ions of the larger in size metal A separating two successive octahedra layers. Such a structure, which is very common among many high-temperature superconductors, like $La_{2-x}Sr_xCuO_4$ for instance, is illustrated in Fig. 1.2(b).

1.3 Electronic Structure

Transition metal oxides exist in a large variety of structures reflected in the great richness of their physical properties. This makes it difficult to create a general theory that would satisfactorily describe all their different features. The models that have been developed in this direction can in general be divided into two main categories, depending on the degree of localization that each of them assumes for the interacting electrons in the investigated systems. On one hand, the so-called ionic models take a localized view of the electron systems, concentrating on the properties of the individual ions and considering them to have integral charges determined by the valence states of the elements involved. They usually ignore the overlaps of orbitals between different atoms. On the other hand, the band theory models provide a much more delocalized picture of the electron systems, calculating the wavefunctions of the transition metal d -electrons within the periodic lattice of the solid. The latter

theories are obviously better applicable in materials with mostly metallic character, while the former ones in non-metallic solids.

It is clear that both groups of theories give only an oversimplified picture of the real physics involved and that the truth lies usually somewhere in between. Thus in the last years several intermediate models have been suggested, that attempt to interpolate between the localized and non-localized theories and to provide a more realistic description of the electronic structure of transition metal oxides. Such are, for example, the cluster models, which are a variation of the ionic models that take more explicitly into consideration the electronic interactions within a small group of atoms; or models that use band theory as a starting point, but then take also into account interactions which cause the electronic states to be more localized than predicted by band theory – like the electron-electron interaction, for instance. Despite the inability of all the above models to give a good theoretical description of all features of all transition metal oxides, they can still provide a satisfactory general scheme, which can often be used as a basis for the understanding of many properties and for making predictions about many others.

1.3.1 Crystal Field Theory

One of the models of mostly ionic character which is often successfully used for the description of many transition metal oxides is the crystal field theory. The oxides investigated in the present work are all non-metallic and crystal field theory is usually an appropriate starting point for them.

Crystal Field Splitting

The electrons of the d shell of a transition metal ion M have orbital angular momentum quantum number $l = 2$ and magnetic quantum number m with $-2 \leq m \leq 2$. The resulting five quantum states of the d electrons are degenerate, that is, they have the same energy, when the ion M is in a spherical potential. This degeneracy is, however, partly or fully lifted when the ion M is within a crystal.

In a transition metal oxide, every transition metal ion M is surrounded by a number of oxygen ions. For example, every Ru^{+4} ion in Ca_2RuO_4 is surrounded by six O^{-2} ions which form a RuO_6 octahedron, while every in-plane Cu^{+2} ion in $\text{YBa}_2\text{Cu}_3\text{O}_{6+x}$ is surrounded by five O^{-2} ions that form a square pyramid. The valence d electrons of every ion M are thus under the influence of the Coulomb potential of the surrounding oxygen ions. In particular, the potential acting on a d electron situated at position \mathbf{r} is given by the equation:

$$V(\mathbf{r}) = \sum_i \frac{Z_i e^2}{|\mathbf{r} - \mathbf{R}_i|} \quad (1.3)$$

where \mathbf{R}_i , Z_i are the position vector and the charge of the i -th ion, respectively. This potential is called the crystal field potential. The quantity

$$V_0 = \sum_i \frac{Z_i e^2}{|\mathbf{R}_i|} \quad (1.4)$$

is called the Madelung potential and expresses the crystal field potential acting on a point charge at position $\mathbf{r} = 0$. The crystal field potential is obviously not spherical. In high-symmetry crystals with ideal perovskite structure it is cubic, but its symmetry can be tetragonal or even lower when there are lattice distortions present. In a cubic crystal field, the eigenfunctions of the d -shell electrons of ion M are given by the linear combinations of the spherical harmonics $Y_m^2(\theta, \phi)$ as follows [1]:

$$\begin{aligned} d(x^2 - y^2) &\propto \sqrt{\frac{2\pi}{5}}(Y_2^2 + Y_2^{-2}) = \frac{\sqrt{3}}{2} \frac{(x^2 - y^2)}{r^2} \\ d(3z^2 - r^2) &\propto \sqrt{\frac{4\pi}{5}}Y_2^0 = \frac{1}{2} \frac{(3z^2 - r^2)}{r^2} \\ d(xy) &\propto \frac{1}{i} \sqrt{\frac{2\pi}{5}}(Y_2^2 - Y_2^{-2}) = \sqrt{3} \frac{xy}{r^2} \\ d(yz) &\propto \sqrt{\frac{2\pi}{5}}(Y_2^{-1} + Y_2^1) = \sqrt{3} \frac{yz}{r^2} \\ d(zx) &\propto \frac{1}{i} \sqrt{\frac{2\pi}{5}}(Y_2^{-1} - Y_2^1) = \sqrt{3} \frac{zx}{r^2} \end{aligned} \quad (1.5)$$

The electronic charge distributions that correspond to the above eigenfunctions are schematically shown in Figure 1.3.

Under the influence of the cubic crystal field potential, the degeneracy of the d orbital states is, as already mentioned, partly lifted. The five states are energetically split into two groups. The one with the lower energy consists of the orbitals d_{xy} , d_{yz} and d_{zx} , which are called t_{2g} orbitals, while the one with the higher energy consists of the remaining two, so-called e_g orbitals, that is $d_{x^2-y^2}$ and $d_{3z^2-r^2}$. The names t_{2g} and e_g originate from group theory and denote the irreducible representations of the corresponding orbitals. The crystal field splitting Δ between the t_{2g} and the e_g orbitals has for typical oxides with perovskite structure a value of 2-4 eV. If this splitting is written as $10Dq$, then the e_g level is situated $6Dq$ above the energy all orbitals would have in a spherical potential, while the t_{2g} level is situated $4Dq$ below this. Thus the centre of gravity of the d orbitals remains unchanged after the crystal field splitting.

The reason of the splitting of the d energy states in a cubic field potential is the fact that the strength of the orbitals' interactions with their chemical environment

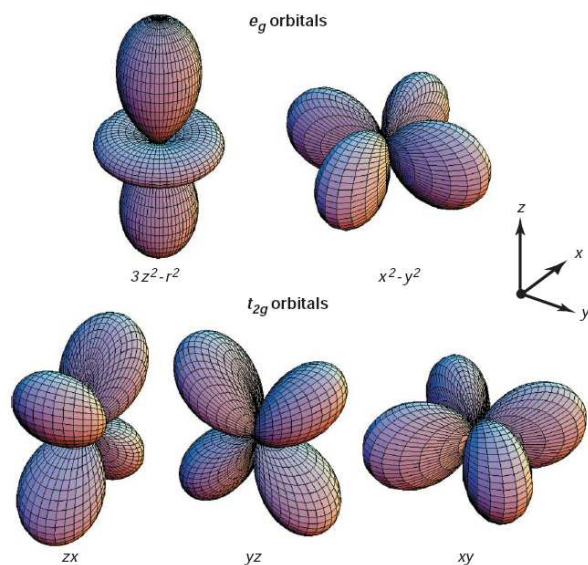


Figure 1.3: Schematic view of the electronic charge distribution given by the eigenfunctions of the d -shell electrons of an ion [3]. In a spherical potential all five d orbitals have the same energy. Within a cubic crystal field, this degeneracy is partly lifted and the d states are split into t_{2g} and e_g orbitals.

is not the same for all d orbitals. The e_g orbitals have lobes of maximum probability extending along the coordinate axes, towards the neighboring O^{2-} ions. The result is a strong Coulomb repulsive interaction, which raises the energy of the e_g levels correspondingly. On the other hand, the t_{2g} orbitals have nodal planes pointing towards the closest oxygen ions. The lobes of high electronic charge density extend away from these ions and thus the Coulomb repulsion from them is weaker in this case, resulting to a lower energy. Taking this into consideration, it can be understood why crystal field effects are so weak and unimportant in rare earth ions compared to transition metal ions. In rare earths the partially filled $4f$ shells lie deep inside the ion core, beneath the filled $5s$ and $5p$ shells, which provide an effective screening against the potential of the surrounding oxygen ions.

The assumption that the d orbital energy splitting is purely of ionic nature, arising from the electrostatic interaction of the transition metal d orbitals with the surrounding ions, is oversimplified and inadequate. Covalent interactions and orbital overlaps play an important role and have to be taken into consideration as well. However, the crystal field model is very useful in providing a first understanding of the electronic structure of transition metal oxides, which is often good enough for interpreting many of their main properties.

High- and Low-Spin States

The way the valence electrons are distributed in the five orbitals of the d -shell in a transition metal ion is determined by the relative magnitudes of the crystal field splitting on one hand, and the energy of the exchange interactions of the electrons on the other. Let us assume a transition metal ion in a cubic crystal field with d^4 electronic configuration, that is, with four electrons in its valence d orbitals. The first three of these electrons will occupy the triply degenerate t_{2g} states, which lie lower in energy. Thus, each one of the three degenerate t_{2g} orbitals will be half-filled with one electron. For the fourth electron there are two possibilities. It can either half-fill one of the doubly-degenerate e_g orbitals, that lie $10Dq$ higher in energy, with its spin parallel to the spins of the electrons in the t_{2g} states, or be situated as well in one of the t_{2g} orbitals, forming a pair with the electron already being there and leading to a complete filling of the corresponding orbital. Of course in the latter case the spin of the fourth electron must be antiparallel to the spin of the other electron in the same orbital, due to Pauli's exclusion principle. The first of these two possible arrangements of electrons leads to a high-spin state of the system (total spin: $S = 2$), while the second one to a low-spin state ($S = 1$).

The high-spin state corresponds to a lower total exchange energy of the electrons. This is expressed in a semi-empirical rule called Hund's first rule. According to this, in an ion with a partially filled shell, independent of whether the ion is in a spherical potential or in a crystalline environment, the electronic configuration which corresponds to the lowest total energy is the one that has the largest total spin S that is consistent with Pauli's exclusion principle. Thus, the total exchange energy of the electrons is minimized by placing them as far as possible, with parallel spins in different orbitals. Here comes in play the second determining factor of the electronic arrangement: the crystal field splitting Δ between the t_{2g} and e_g states. If the crystal field splitting is larger than the energy difference of the low- and high-spin configurations, then the energy cost for placing an electron in an e_g orbital is higher than the energy gain resulting from the lower exchange energy, according to Hund's rule. In this case, the low-spin state is energetically preferred and the e_g orbitals will remain completely empty. If, on the contrary, the crystal field splitting is smaller than the energy difference of the two spin configurations, the high-spin state will be preferred.

The energy difference of the low- and high-spin states is equal to Hund's coupling J_H . The latter expresses the exchange (spin-dependent) interaction between electrons that are in different orbitals in the same ion. Other energy terms that have to be considered are the energy U due to the Coulomb interaction between electrons that occupy the same orbital, also called Hubbard interaction, as well as the energy U' of the Coulomb interaction between electrons in different orbitals. Neglecting for simplicity the so-called pair hopping interaction and the terms which are the same in

the two possible spin configurations, the total energy of the electrons in the low-spin state is equal to U , with U referring in this case to the Coulomb repulsion between the two electrons within the same t_{2g} orbital. In the high-spin configuration, the total energy of the electrons is $U' + J_H$, with U' referring to the Coulomb repulsion between the e_g and the t_{2g} electrons and J_H to the corresponding Hund coupling. Thus the energy difference of the two spin configurations is: $D = U - U' - J_H$. But the relation: $U = U' + 2J_H$ holds [4]. So the energy difference is: $D = J_H$.

In conclusion, the above described conditions for the low- and high-spin configurations can be summarized in the following expressions:

If: $\Delta < J_H$, the system is in the high-spin state.

If: $\Delta > J_H$, the system is in the low-spin state.

Jahn-Teller Effect

As already mentioned above, the symmetry of the crystal field determines the extent, to which the degeneracy of the d electron states is lifted. In a tetragonal crystal field, besides the splitting of the t_{2g} and e_g states taking place in a cubic field, there is an additional splitting between the two e_g states, as well as a partial splitting of the t_{2g} states. A further lowering of the crystal field symmetry can totally lift the remaining degeneracy. The lowering of the symmetry is performed via distortions of the lattice, which usually involve elongations, contractions or rotations of the polyhedra formed by the oxygen ions that surround the transition metal ions. They strongly influence orbital ordering and the electronic charge distribution in the system in general.

One of the most common reasons for such distortions is the so-called Jahn-Teller effect. According to the Jahn-Teller theorem [5], if a magnetic ion is at a crystal site of such high symmetry that its ground state is degenerate, then it is energetically favorable for the crystal to distort (for example, by displacing the equilibrium position of the ion) in such a way, that its symmetry is lowered and the degeneracy is removed. Especially for magnetic ions possessing odd numbers of electrons, the Jahn-Teller distortion takes place if the ground-state degeneracy of the ion is higher than the minimum determined by Kramers' theorem. According to the latter, the ground state of an ion with an odd number of electrons and a time-reversal invariant Hamiltonian, is always at least doubly degenerate, independent of the crystal field symmetry and in absence of magnetic field. Thus, in such an ion the lattice is Jahn-Teller distorted if the ground state has a three-fold or higher degeneracy.

The Jahn-Teller distortions taking place in a polyhedron around a transition metal ion are of course not independent from the ones taking place in the neighboring polyhedra. The total energy of the crystal is minimized if all distortions follow a well-defined pattern. Depending on the particular crystal and electronic properties of every compound, the distortions can be either all in the same direction, leading

to a ferrodistortive state, or in different directions, leading to an antiferrodistortive state. The ordering of the distortions changes the global symmetry of the crystal and often sets in at a well-defined transition temperature. The effect is then associated to a structural phase transition and is called cooperative Jahn-Teller effect.

Quenching of the Orbital Angular Momentum

Besides the lift of the degeneracy of the d electron energy states, another effect of the crystal field is the quenching of the orbital angular momentum \mathbf{L} , which takes place when the crystal field splitting Δ is much larger than the spin-orbit coupling. The mean angular momentum then vanishes and the total magnetic moment is equal to the spin moment:

$$\langle \Psi | \mathbf{L} | \Psi \rangle = \int \Psi^*(\mathbf{r}) \mathbf{L} \Psi(\mathbf{r}) d^3r = 0 \quad (1.6)$$

where Ψ is the wavefunction of a d electron of the transition metal ion [1].

The reason for the quenching of \mathbf{L} is that, since the time-independent Schrödinger equation is a real equation, its non-degenerate eigenfunctions $|\Psi\rangle$ are within a phase factor real functions. So, given the fact that the orbital angular momentum operator $\mathbf{L} = -i\hbar \mathbf{r} \times \frac{\partial}{\partial \mathbf{r}}$ is an imaginary operator, the quantity $\langle \Psi | \mathbf{L} | \Psi \rangle$ is imaginary. As a measurable quantity, however, it must be real. The only possible value, for which both of the above statements are true, is zero: $\langle \Psi | \mathbf{L} | \Psi \rangle = 0$.

This is usually the case in $3d$ transition metal oxides, like manganites and cuprates. In $4d$ and $5d$ oxides, like ruthenates, where the transition metal has a larger atomic number Z , the spin-orbit coupling is stronger and cannot be completely ignored. If the symmetry of the crystal field is sufficiently high, then the ground state of the transition metal ion is degenerate and the wavefunctions can be complex. The orbital angular momentum is then not always quenched.

Independent of the spin-orbit coupling, if the symmetry of the crystal field is sufficiently low (e.g orthorhombic), then all irreducible representations become one-dimensional, the wavefunctions are essentially real, and the orbital angular momentum is always quenched.

1.4 Mott insulators

Insulators are materials with vanishing dc electrical conductivity in the limit of zero temperature:

$$\lim_{T \rightarrow 0} \sigma(T) = 0 \quad (1.7)$$

According to band theory, an electronic system is an insulator if the density of states at its Fermi level is equal to zero: $\rho(E_F) = 0$, and metallic otherwise: $\rho(E_F) \neq 0$. The Fermi level is determined by the highest occupied energy level in the ground

state. A band with n -fold orbital degeneracy can accommodate up to $2n$ electrons per unit cell. This number is obviously always even. Thus, if a system has an odd number of electrons per unit cell, then the orbital with the highest energy is half-filled with only one electron and the density of states at the Fermi level is non-zero, therefore the material is metallic. In order to have an insulating material, the number of electrons per unit cell must be even. This condition is necessary but not sufficient. The reason is that, even if the number of electrons is exactly equal to the number of one-electron states of the valence band, the zero-density of states at the Fermi level is not guaranteed, because the valence and conduction bands may overlap.

The above basic prediction of band theory fails in a number of cases. There are several materials which, according to band theory, should be metallic, but instead they are good insulators. One of the oldest-known examples is CoO. With an electronic configuration $3d^74s^2$ for Co and $2s^22p^4$ for O, this material has an odd number of electrons per unit cell, so according to band theory it should be metallic. Instead it is one of the best insulators known. Its insulating properties are maintained not only in the ground state, in the low-temperature antiferromagnetic phase, but also at high temperatures, in the paramagnetic phase. Other examples of insulators predicted by band theory to be metallic include NiO, LaTiO₃ and V₂O₃.

The reason for the failure of band theory in cases like the ones above is that band theory provides an independent-electron description of materials. There are cases, however, where strong electron-electron interactions, not taken into consideration by band theory, play a very important role and determine to a large extent the behavior of the material. In systems with interacting electrons moving in a narrow band, the energy U of the Coulomb interaction between electrons in the same ion, introduced in Section 1.3 as Hubbard interaction, is the most important energy term. If this energy is sufficiently high, that is, if the on-site Coulomb repulsion of the electrons is sufficiently strong, then the hopping of electrons from site to site, and thus the metallic conductivity, is suppressed and the material is insulating, although the highest occupied bands are not completely full. The materials where such an interaction-induced collective localization of the electrons takes place are called Mott insulators.

There are substantial differences between a conventional (band) insulator and a Mott insulator. In a conventional insulator conductivity is hindered by Pauli's exclusion principle. The highest occupied band is, namely, fully occupied with two electrons per unit cell (or $2n$ if there is n -fold orbital degeneracy) and the electrons cannot move, simply because there are no empty orbitals to move to. In a Mott insulator, on the contrary, the highest occupied band is only half-filled with one electron per unit cell. Although in principle it is possible for an electron to hop from a half-filled orbital of an ion to a half-filled orbital of another ion, creating a doubly-occupied site with the electron already being there, this requires a very large

amount of energy, due to the strong mutual Coulomb repulsion of the electrons that would form the doubly occupied site, and is thus energetically not preferred. The resulting insulating phase is highly correlated: the electrons minimize the energy of their Coulomb interaction by avoiding each other as much as possible. If the number of electrons is equal to the number of sites, they achieve this by staying localized at each lattice site.

1.4.1 Hubbard Model

Mott insulators are usually antiferromagnetic. The simplest model that can provide an understanding of their magnetic properties is the Hubbard model, which was introduced in 1963 [6] as an approach to a theory of correlation effects in the d -bands of transition metals. The model introduces a many-body Hamiltonian (Hubbard Hamiltonian) for the description of the d -electrons of a transition metal, taking into account the two main opposing properties of these electrons: on one hand, their desire to delocalize themselves via electron hopping into itinerant states, leading to metallic behavior. This desire for delocalization is expressed with the kinetic energy of the electrons. And on the other hand, their tendency to localize on particular sites, due to the electron-electron interactions between them, approximated usually by the on-site repulsive Coulomb interactions, which drive the system to be a Mott insulator. The Hubbard Hamiltonian can be expressed in the following way [1]:

$$H = -t \sum_{\langle i,j \rangle} \sum_{\sigma} (c_{i\sigma}^{\dagger} c_{j\sigma} + c_{j\sigma}^{\dagger} c_{i\sigma}) + U \sum_i \hat{n}_{i\uparrow} \hat{n}_{i\downarrow} \quad (1.8)$$

The first term of the Hamiltonian describes the kinetic energy (hopping) of the electrons, while the second one the on-site Coulomb interaction. Here, t is the hopping integral of electrons between nearest neighbor sites i, j ; $c_{i\sigma}^{\dagger}$ and $c_{i\sigma}$ are the creation and annihilation operators, respectively, for an electron in the Wannier state $\phi(\mathbf{r} - \mathbf{R}_i)$ at lattice site i with spin σ ; $\hat{n}_{i\sigma} = c_{i\sigma}^{\dagger} c_{i\sigma}$ is the corresponding occupation number operator; and U is the energy of the intraionic Coulomb interaction between electrons sharing the same orbital. It is assumed that there is only one Wannier state for each site (single-orbital Hubbard model).

The zero-temperature behavior of the Hubbard model is governed by two parameters: the relative interaction strength U/t , and the electron density $n = N/L$, where N is the total number of electrons and L the number of lattice sites (or unit cells, for non-Bravais lattices). Instead of U/t , the ratio U/W is often used as a measure of the strength of the electron-electron interactions in a material, with W being the bandwidth. For the single-orbital Hubbard model, the electron density takes values: $0 \leq n \leq 2$. For $n = 1$ one has the half-filling case, where the number of electrons is equal to the number of sites. It is in this case, that above a particular critical value of U the electrons are completely localized at the ion sites and the material

is a Mott insulator. Away from half-filling ($n \neq 1$), the electrons always maintain a propagating motion, even for infinitely strong Hubbard interactions ($U \rightarrow \infty$).

Despite the localization of the electrons in a Mott insulator, the kinetic energy term of the Hamiltonian, that describes the band motion of the electrons, is still present and plays a very important role. It is actually exactly this term which gives rise to the antiparallel nearest neighbor spin interactions that lead to the antiferromagnetic properties of the Mott insulators [7]. The physical basis of this is that electrons with antiparallel spins can gain some energy by occupying non-orthogonal overlapping orbitals, which electrons with parallel spins cannot do. Although in a Mott insulator the Coulomb repulsion U of electrons in the same ion prevents the permanent occupation of ionized states, the system can gain a certain amount of energy by virtually occupying to a small extent ionized states which are connected to the ground state via the transfer integrals t [8]. This energy gain is equal to: $\Delta E = -\frac{2t^2}{U}$. Due to Pauli's exclusion principle, and given the fact that the transfer integrals t carry the electrons without change of spin, the hopping of an electron to a neighboring site is possible only if its spin is antiparallel to the one of the electron being there. In other words, the energy is gained only in the presence of a nearest neighbor with antiparallel spin, thus only in the case of an antiferromagnetic alignment of the spins.

For a more quantitative understanding of the above process, one can start with the Mott insulating state and consider the virtual occupation of the ionized state as a second order process with energy:

$$H' = - \sum_{\langle i,j \rangle} \sum_{\sigma, \sigma'} \frac{2t^2}{U} c_{i\sigma'}^\dagger c_{j\sigma'} c_{j\sigma}^\dagger c_{i\sigma} \quad (1.9)$$

The process is schematically illustrated in Figure 1.4. The hopping of an electron to a neighboring site via the transfer integral t leads to an intermediate state (b), in which a site is doubly-occupied by two electrons with antiparallel spins, according to Pauli's exclusion principle [1]. The energy of the intermediate state is higher by U than the energy of the ground state. Two different final states are possible, depending on which electron goes to which ion. The energy of the process (1.9) can be written in terms of spin operators as follows:

$$H' = \sum_{\langle i,j \rangle} \frac{4t^2}{U} (\mathbf{S}_i \cdot \mathbf{S}_j - \frac{1}{4} n_i n_j) \quad (1.10)$$

The latter equation directly reflects the fact that the virtual occupation of ionized states is only possible if the spins at neighboring sites are antiparallel. Indeed, if the spins are instead parallel, then $\mathbf{S}_i \cdot \mathbf{S}_j = \frac{1}{4}$. But since in the half-filled case all sites are occupied with one electron, that is, $n_i = n_j = 1$, Equation (1.10) then gives: $H' = 0$.

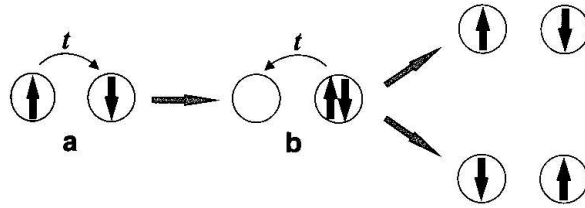


Figure 1.4: The process of the superexchange interaction [1]. The hopping of an electron to a neighboring site via the transfer integral t leads to an intermediate state (b). Depending on which electron then goes to which site, two different final states are possible.

In transition metal oxides, most of which are antiferromagnetic insulators, the above description based on the kinetic exchange interaction between d -electrons, which works quite well for the single-orbital Hubbard model, seems rather difficult to apply. The reason is that in transition metal oxides the cations that possess the d -electrons are separated by large oxygen anions, so the direct hopping of electrons from cation to cation is unlikely. However, Anderson [8] has shown that the concept of kinetic exchange interaction can be extended also to such situations and that the interaction is even enhanced by the covalent mixing between cation and anion orbitals.

In particular, the overlap between the d -orbitals of the transition metal ions and the p -orbitals of oxygen gives rise to a covalent mixing which allows the nominally p -electrons of oxygen to partially occupy d -orbitals of the cations. The degree of mixing depends on the relative orientation of the spins of the d -electrons. It can be shown that the parallel configuration of the d -electron spins leads to a smaller degree of orbital mixing and costs more energy than the antiferromagnetic configuration. The latter is thus energetically preferred. The exchange interaction between the d -orbital electrons which is mediated by the oxygen ions is known as superexchange interaction.

In the extreme case where: $t = 0$, there is absolutely no exchange interaction between neighboring sites and no magnetic order is established. In this case, the ground state is infinitely degenerate.

1.4.2 Orbital Degeneracy and Orbital Ordering

As described above, in the non-degenerate single-orbital Hubbard model the superexchange interaction of the d -electrons is always antiferromagnetic. However, in systems with an orbital degree of freedom, that is, with orbital degeneracy in the d -shells, the physics of transition metal oxides is much more complicated and a number of interesting phenomena arise. In such a system the sign of the superexchange

interaction (ferro- or antiferromagnetic), as well its strength, depend on the orbital occupation, which determines the degree of the overlap of the participating states.

Let us assume two electrons occupying two sites, each with a two-fold orbital degeneracy. If ϕ_a and ϕ_b are the two degenerate orbitals at every site, and assuming that the orbitals are not mixed with hopping, then the one-electron part of the Hamiltonian, which expresses the band motion (hopping) of the electrons, is:

$$H_{hop} = -t_a \sum_{\sigma} (c_{1a\sigma}^{\dagger} c_{2a\sigma} + c_{2a\sigma}^{\dagger} c_{1a\sigma}) - t_b \sum_{\sigma} (c_{1b\sigma}^{\dagger} c_{2b\sigma} + c_{2b\sigma}^{\dagger} c_{1b\sigma}) \quad (1.11)$$

where $c_{ja\sigma}^{\dagger}$ and $c_{jb\sigma}^{\dagger}$ are the Wannier operators which create electrons with spin σ in orbitals ϕ_a and ϕ_b , respectively, at site j ($j = 1, 2$) [7].

If the two electrons are at the same site, they interact with each other via Coulomb repulsion U_a , U_b or U_{ab} , depending on whether they are both in orbital ϕ_a , both in orbital ϕ_b or one in ϕ_a and one in ϕ_b , respectively. In the latter case, when the electrons are in different orbitals, they can have either antiparallel spins and form a low-spin (singlet) state, or parallel spins and form a high-spin (triplet) state. According to Hund's first rule (Section 1.3), the triplet state has a lower energy and is preferred. Thus the exchange interaction between two electrons on the same site is ferromagnetic. If $2J$ is the exchange constant of this ferromagnetic interaction, then the part of the Hamiltonian containing the diagonal interaction terms is:

$$H_{int} = U_a \sum_{j=1}^2 \hat{n}_{ja\uparrow} \hat{n}_{ja\downarrow} + U_b \sum_{j=1}^2 \hat{n}_{jb\uparrow} \hat{n}_{jb\downarrow} + U_{ab} \sum_{j=1}^2 \sum_{\sigma\sigma'} \hat{n}_{ja\sigma} \hat{n}_{jb\sigma'} - 2J \sum_{j=1}^2 (S_{ja}^z S_{jb}^z + \frac{1}{4}) \quad (1.12)$$

where $S_{ja}^z = \frac{\hat{n}_{ja\uparrow} - \hat{n}_{ja\downarrow}}{2}$ (similarly for the ϕ_b orbital) and $\hat{n}_{ja\sigma}$, $\hat{n}_{jb\sigma}$ are the occupancy operators (Equation 1.8).

The spin-flip terms of the exchange interaction are contained in the term:

$$H_{flip} = -J \sum_{j=1}^2 (c_{ja\uparrow}^{\dagger} c_{ja\downarrow} c_{jb\downarrow}^{\dagger} c_{jb\uparrow} + c_{ja\downarrow}^{\dagger} c_{ja\uparrow} c_{jb\uparrow}^{\dagger} c_{jb\downarrow}) \quad (1.13)$$

The full Hamiltonian of the system is the sum of the above terms:

$$H = H_{hop} + H_{int} + H_{flip} \quad (1.14)$$

Depending on the orbitals which are occupied by the two electrons and the relative orientation of their spins, four different triplet and four singlet states are possible. It is interesting to determine if the ground state of the system is a singlet or a triplet state. For this we need to know in which case the energy is lower.

If the electrons at the two sites are both in orbital ϕ_a or both in orbital ϕ_b and have antiparallel spins (singlet state), then it is possible for them to hop from one

site to the other. The resulting antiferromagnetic exchange interaction has a kinetic exchange energy of $E_{a,sing} \approx -\frac{4t_a^2}{U_a}$ or $E_{b,sing} \approx -\frac{4t_b^2}{U_b}$, respectively. If the electrons at the two sites are both in ϕ_a or both in ϕ_b but with parallel spins (triplet state), then the hopping from one site to the other is not possible due to Pauli's exclusion principle and the energy of the exchange interaction is zero: $E_{a,tripl} = E_{b,tripl} = 0$. Several triplet states are possible when the electron of one of the sites is in orbital ϕ_a and that of the other site in orbital ϕ_b with parallel spins. It can be shown that among the energies of all possible triplet states the lowest is:

$$E_{ab,tripl} \approx -\frac{(t_a + t_b)^2}{U_{ab} - J} \quad (1.15)$$

where U_{ab} is the Coulomb interaction between the two electrons when occupying different orbitals. This interaction is obviously less strong than the one between electrons occupying orbitals of the same type, i.e. $U_{ab} < U_a$ and $U_{ab} < U_b$. This results in: $E_{ab,tripl} < E_{a,sing}$ and $E_{ab,tripl} < E_{b,sing}$.

The state with the lowest energy is therefore a triplet state. This means that when orbital degeneracy is present, the intra-atomic interactions of the electrons lead to intersite ferromagnetic exchange, instead of antiferromagnetic like in the single-electron Hubbard model.

At the same time it becomes obvious that for the establishment of ferromagnetic exchange coupling it is necessary that the electrons at neighboring sites occupy different orbitals. This means that in general the ferromagnetism which results from the intra-atomic exchange interactions favors an 'antiferro-orbital' pattern of orbital order. The sign of the superexchange in a transition metal system depends however also on the angle of the chemical bond between the transition metal ions and the oxygen ions. The exact way the magnetic superexchange determines the orbital configuration and vice versa is summarized in the Goodenough-Kanamori-Andersen rules [9].

1.5 Superconductivity

1.5.1 The Phenomenon of Superconductivity

The phenomenon of superconductivity is characterized by two main properties: zero electrical resistance and perfect diamagnetism (e.g. [10, 11]). Superconducting materials exhibit these properties below a particular temperature, called superconducting transition temperature T_c . Above that temperature the materials are in their so-called normal state, that is, they are normal metals, without however usually being very good conductors.

Superconductivity was observed for the first time in 1911 by H. Kamerlingh Onnes in mercury (Hg). Three years after having success in liquifying helium and with that obtaining a refrigerating technique required to reach temperatures as low as a few degrees Kelvin, Onnes found that the dc resistance of mercury drops to zero below 4.15 K. One year later he discovered that application of a sufficiently strong magnetic field restores the resistance to its normal value. In 1913 a similar drop of resistance to zero was also observed in lead (Pb) below 7.2 K, while the discovery of superconductivity in niobium (Nb) in 1930 raised the highest- T_c record to 9.2 K. In the following decades the highest superconducting transition temperature followed only a slow increase with time, reaching in 1973 the value of approximately 23 K for Nb₃Ge, one of the so-called A15 compounds, which held the highest- T_c record till 1986. The discovery of superconductivity with T_c around 30 K in the La_{2-x}Ba_xCuO₄ system by J.G. Bednorz and K.A. Müller in 1986 [12] initiated the era of high-temperature superconductivity, that led to the discovery of materials which, not only have dramatically higher superconducting transition temperatures¹, but also belong to a completely new class of superconductors, the description of which most probably demands the introduction of new theories, beyond the ones used for the description of conventional superconductors.

The zero electrical resistance, i.e. the perfect conductivity, is the most easily observable property of superconductivity and the one which was historically first observed. Currents flowing through superconducting materials show no measurable decrease in their intensity for years and a minimum decay time of the order of 10⁵ years can be determined with the use of nuclear resonance. The second main property of superconductivity – the perfect diamagnetism – means that no externally applied magnetic field can penetrate in the interior of a superconducting material. The magnetization \mathbf{M} of the material is always exactly the opposite of the applied magnetic field \mathbf{H} : $\mathbf{M} = -\mathbf{H}$, so that the total magnetic field in the interior of the material is exactly equal to zero. This can be also expressed in terms of the magnetic susceptibility $\chi = -\frac{M}{H}$, which is obviously exactly equal to -1: $\chi = -1$.

The determination of the onset of superconductivity from susceptibility measurements is from the thermodynamic point of view a more typical way for doing so than the use of the zero electrical resistance property, since magnetization is a thermodynamic state variable. Generally, the T_c value determined from resistivity measurements is slightly higher than the one determined from susceptibility. The reason is that a single superconducting path between the measuring electrodes consisting of tiny parts of the material that already have zero resistance, is enough to give zero resistance for the whole material. On the other hand, for the drop of susceptibility, more extensive regions of superconductivity are required, since macro-

¹The record for the highest superconducting transition temperature at ambient pressure is being held since 1994 by the Tl-doped HgBa₂Ca₂Cu₃O_{8+δ} system with $T_c = 138$ K [13].

scopic current loops are needed in order to shield a large part of the material from the applied magnetic field. The sharpness of the drop of either the resistance or the susceptibility around the superconducting transition temperature is a measure of how good or pure the investigated material is. A broad temperature range, within which the transition from the normal to the superconducting range is completed, usually indicates a low-purity sample.

The phenomenon of perfect diamagnetism which characterizes superconducting materials can be expressed in two different aspects. The first is flux exclusion: if a material in the normal state is cooled below T_c without any magnetic field present (zero field cooling, ZFC) and then, once in the superconducting state, placed within an external magnetic field, then the magnetic field will be excluded from the material, i.e. no magnetic lines will enter it. The second is flux expulsion, also known as Meissner effect: if a material in the normal state is placed into a magnetic field, the field will penetrate the material and will have almost the same value inside and outside it. If the material is then cooled below T_c while being in the magnetic field (field cooling, FC), the field will be expelled from the material once this is superconducting. Although the two processes have in the end the same result as far as the superconducting material is concerned, that is, no magnetic flux in the superconductor, they are not equivalent. This becomes obvious, for example, in solids with open cavities, where ZFC and FC lead to different final states as far as the magnetic flux in the cavities is concerned.

1.5.2 The BCS Theory

The BCS theory is a microscopic theory of superconductivity proposed in 1957 by Bardeen, Cooper and Schrieffer [14], which predicts quantitatively many of the properties of elemental superconductors. It is consistent with the predictions of the previously suggested macroscopic theory of Landau and Ginzburg and until the discovery of high-temperature superconductivity by Bednorz and Müller in 1986 [12] it provided a sufficient understanding of the origin of superconductivity. Copper-oxide superconductors, however, changed the situation quite a lot. It is so far not clear whether the BCS theory can be applied appropriately modified also to this new class of superconductors or if, on the contrary, a completely new theory has to be developed for their description.

The BCS theory is based on the idea that even a very weak effective interaction between electrons is sufficient to bind them as pairs into a bound state. Already in 1956 Cooper showed that the Fermi sea of electrons is unstable against the formation of at least one bound pair, independent of how weak the interaction between the electrons is, as long as it is attractive. This result is a consequence of the Fermi statistics and for its existence the filled Fermi sea background is essential. It can be shown that the bound state formed of two electrons with energy higher than

the Fermi energy E_F ($k > k_F$), interacting via the attractive potential V , always has a negative energy with respect to the Fermi surface, no matter how small the interaction V is. The excess kinetic energy of the electrons with respect to the Fermi surface is thus outweighed by the contribution to the energy of the attractive potential. This is the reason why the normal state is unstable against the formation of so-called Cooper pairs.

The origin of the attractive force which leads to the formation of Cooper pairs is the interaction of the electrons with phonons, that is, with propagating vibrations of the lattice. The basic physical idea which lies behind this interaction is that an electron causes a small distortion of the lattice by attracting the neighboring positive ions, this excess of positive charge then attracts a second electron, and the result is an effective attraction between the two electrons mediated by the distortion of the lattice. If this attraction is strong enough to override the repulsive screened Coulomb interaction of the electrons, then the net interaction is attractive and Cooper pairs are formed. The resulting state is a highly correlated many-electron state characterized by superconductivity. A macroscopic number of Cooper pairs can undergo Bose condensation into a single orbital level and carry supercurrent without losses.

Superconductivity is characterized by an order parameter Ψ , which is an operator, the thermal average of which is zero in the high-temperature disordered state and non-zero in the low-temperature ordered phase. For conventional superconductors the order parameter is a pair function, the magnitude of which gives the superconducting energy gap Δ_{sc} . This energy gap is in conventional superconductors independent of the position on the Fermi surface, i.e. the pairs are in a rotationally symmetric 's-wave' state.

1.5.3 High-Temperature Superconductors

There are indications that the mechanism of superconductivity in the materials belonging to the class of high-temperature superconductors discovered by Bednorz and Müller in 1986 [12] is so different from the one in conventional superconductors, that a small modification of the BCS theory would not be sufficient for its description. Although the order parameter in high-temperature superconductors is also a pair function, its symmetry is not s-wave, like in conventional superconductors, but d-wave. This means that the order parameter changes sign under a 90-degree rotation, thus there are points on the Fermi surface where the superconducting energy gap vanishes completely. The question is whether such a d-wave gap can be included in a suitably modified BCS-based theory. Although the issue remains open, several ideas suggested in the last years point towards the direction of a non-BCS theory (for a review, see e.g. Refs. [15], [16]).

High- T_c copper oxide superconductors are all characterized by two main features

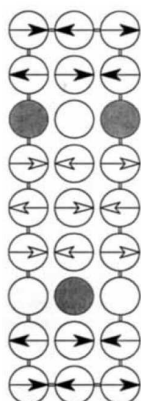


Figure 1.5: Idealized representation of the static charge- and spin-stripe pattern, suggested by Tranquada *et al.* for $\text{La}_{2-x-\delta}\text{Nd}_\delta\text{Sr}_x\text{CuO}_4$ [18]. Only the Cu atoms are shown in the picture. The arrows indicate the direction of the magnetic moment at the metal sites. The holes introduced by doping (filled circles) reside along antiphase domain boundaries, forming charge and spin stripes.

which strongly influence their behavior and are, to a large degree, responsible for their unique properties. The first is their extreme anisotropy, leading in many cases to a quasi-two-dimensional character, caused by the layered structure of the materials, which is always made up of CuO_2 planes that interact only weakly with each other. The second is their proximity to a Mott insulating phase. High- T_c superconductivity is created by adding charge carriers (doping) to Mott insulators. As explained in Section 1.4, Mott insulators are systems with one electron per unit cell in the highest occupied band. Electron motion and thus conductivity is hindered by the electron-electron Coulomb repulsion, that prevents the formation of doubly-occupied sites. By doping such a system with charge carriers, new sites are created, to which electrons can move without any cost in Coulomb energy, and electrical conductivity is restored. It has been suggested that the electrons in Mott insulators can be actually naturally paired in a spin liquid state, but are unable to move, due to the Coulomb repulsions [17]. Once the average occupancy is lowered from one by doping, the 'frozen' pairs become mobile and the material turns into a superconductor. The critical temperature T_c of the resulting superconducting phase depends sensitively on the charge carrier concentration (doping level) of the material.

A main issue that needs to be understood is, what the pairing mechanism of charge carriers is in high-temperature superconductors. One of the ideas that have been proposed is that fluctuations in electron spins may play a role similar to the role of lattice vibrations (phonons) in conventional BCS-type superconductors [19, 20]. Namely, the spin of a moving electron may distort nearby spins in such a way, that an

attractive force able to bind them into pairs evolves. Some researchers believe that more exotic excitations may be instead involved. One popular idea, for instance, is based on theoretical calculations, according to which charges and spins undergo in lightly doped Mott insulators a natural process of segregation. This may lead to the formation of charge and spin 'stripes' in the CuO_2 planes of cuprates, of either static or dynamic nature.

In this picture, the charge carriers (holes) that are introduced to the parent compound (Mott insulator) via doping are not distributed homogeneously in the material, but reside along well-defined antiphase boundaries forming charge stripes (Figure 1.5). The periodicity of the spin stripes is twice that of the charge stripes. Through the formation of stripes, the holes are expelled from regions with well-defined local moments. In addition, a certain gain of kinetic energy is obtained, due to the fact that the transverse wandering of stripes does not distort the spin alignment of its environment, in contrast to the hopping of isolated holes, which does. Which of the two factors might be the main driving force of stripe formation is not clear.

The exact role that stripes could play in the establishment of superconductivity is not clear either. One possibility is that the holes, being forced to reside together along the stripes, are bound into pairs already at relatively high temperatures, generating the so-called 'pseudogap' (see below) [21]. The condensation of these pairs into a single quantum state at lower temperatures would result in superconductivity, first only within the stripes, and eventually, below T_c , when the hopping of pairs between stripes is possible, in the whole material. For this theory to work, the stripes have to be fluctuating. Static stripes are suspected to be rather detrimental to superconductivity [22]. This is also supported experimentally. In Nd-doped $\text{La}_{2-x}\text{Sr}_x\text{CuO}_4$, for example, the first cuprate compound where static stripes were experimentally observed by neutron diffraction [18], the Nd-doping stabilizes a tetragonal phase which is *not* superconducting. In superconducting pure $\text{La}_{2-x}\text{Sr}_x\text{CuO}_4$, on the contrary, no static stripe order is observed. In this compound there is strong evidence that dynamic two-dimensional spin correlations are instead present [23, 24].

The discussion about whether stripes are a generic feature of all copper oxide superconductors and to what degree they are a prerequisite, helpful, detrimental or simply indifferent to superconductivity, is still open and no definite answer to these questions can be given at the moment (for a review article, see e.g. Ref. [25]). Meanwhile, other alternative approaches have been suggested. One of the most interesting of them is based on the idea of 'fractionalization' of electrons, namely the splitting of every electron into two free particles, one of which carries the spin (spinon) and the other the charge (chargon). This idea, which was first suggested already several years ago [17] and took new impulse with the work of Fisher and Senthil more recently [26], is particularly intriguing, since it predicts the establishment of superconductivity without any pairing of the charge carriers.

What relaxes in this case the charge carriers from the restrictions of Pauli's exclusion principle and allows them to condensate into one quantum state is the separation of charge and spin and not the formation of some kind of bosonic Cooper pairs.

Phase Diagram

Despite the numerous interesting features of high-temperature superconductivity, many of which are still by far not understood, it is actually the normal state of layered cuprates, above T_c , which has the most extraordinary and puzzling properties. An overview of the different electronic states of (hole-doped) cuprates can be obtained from their generic phase diagram, shown in Figure 1.6. At very low charge carrier concentrations h , close to the undoped insulating parent compound, all cuprates are antiferromagnetic. This region of the phase diagram is the best-understood. The magnetic order is suppressed rapidly with increasing hole concentration and vanishes already at a doping level of the order of 0.05 (material dependent).

With further increasing the hole concentration in the CuO_2 planes, the compound enters (at sufficiently low temperatures) the superconducting phase, indicated in the diagram with a half-elliptical region at intermediate doping levels. The critical temperature T_c , below which the system is superconducting, strongly depends, as already mentioned, on h , taking its maximum value at $h \approx 0.16$. A compound with such a hole concentration, the most favorable one for superconductivity, is characterized as 'optimally doped'. A compound with hole concentration higher or lower than the optimal one is called 'overdoped' or 'underdoped', respectively, and has a superconducting transition temperature which is lower than in the optimally doped system.

At relatively low doping levels (underdoped regime) and temperatures above T_c , cuprates are in the pseudogap phase. While the superconducting energy gap of conventional, BCS-type superconductors vanishes at temperatures above T_c , this is not the case in cuprates. An anomaly characterized by a very small electronic density of states at certain energies remains up to high temperatures, well above T_c . This anomaly is the pseudogap. It has been suggested, that the transition into this peculiar phase might indicate the formation of pairs among the charge carriers, which however still lack the phase coherence that is required for superconductivity to be established [27]. The onset of superconductivity at T_c would then signify not the formation of pairs, but the establishment of phase coherence among already existing pairs.

At temperatures above T_c and doping levels higher than what required for the pseudogap phase, cuprates behave as non-Fermi liquids. This region of the phase diagram is characterized by simple but unusual power laws in all transport properties, such as resistivity and optical and thermal conductivity, as a function of tempera-

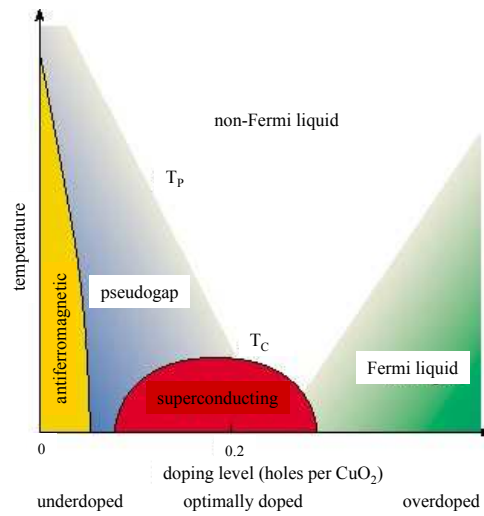


Figure 1.6: Generic phase diagram of cuprate high-temperature superconductors. Superconductivity is established within a half-elliptical region around hole concentration 0.16 (optimal doping), for which the superconducting transition temperature T_c is the highest.

ture. Interestingly, no well-defined quasi-particles have been observed (for example, with angle resolved photoemission spectroscopy - ARPES) in this phase.

Finally, in the highly overdoped area of the phase diagram the copper-oxide compounds appear to be 'normal' Fermi liquids, with their state well described by the Landau quasiparticle model and with a well-defined Fermi surface separating particles and holes in momentum space. This region of the phase diagram is also relatively well-understood.

It has to be mentioned that the borders of the above phases of high-temperature superconductors are, with the exception of the antiferromagnetic and superconducting states, not well-defined. It seems that the transition from one to the other does not take place through a sharp phase transition, but rather gradually, through a broad 'change-over' regime.

Chapter 2

X-ray Diffraction

2.1 Introduction

X-rays have been widely used as an excellent probe for the investigation of condensed matter down to the atomic level for almost a century. Since the first pioneering experiments by W.L. Bragg on crystalline sodium chloride (NaCl) in 1913, x-ray diffraction has been the main tool for structure determination and material analysis for virtually every kind of material. Meanwhile, the great possibilities opened by the advances in synchrotron radiation facilities in the last two decades have enabled the use of x-ray diffraction for applications far beyond lattice structure determination, such as the investigation of magnetic properties, the observation of orbital ordering and the study of short-range charge order producing weak superlattice diffuse scattering, to name only a few of them. This has contributed enormously in the research of strongly correlated systems and has helped in the understanding of many of their fascinating properties.

2.2 Synchrotron Radiation

Synchrotron radiation is the electromagnetic radiation produced by accelerating charged particles, usually electrons, moving with relativistic velocities along curved trajectories. It is characterized by a number of unique properties, that make it an extremely powerful tool for the investigation of condensed matter. The most important of them are: 1) very high brightness, up to 13 orders of magnitude higher than that of the radiation produced by the best conventional x-ray tube 2) tunability within a very broad spectral range 3) small angular divergence 4) temporal and spatial coherence, and 5) polarization.

Synchrotron radiation was theoretically studied by Schott already in 1912, but was experimentally first observed more than thirty years later, in 1947. It took

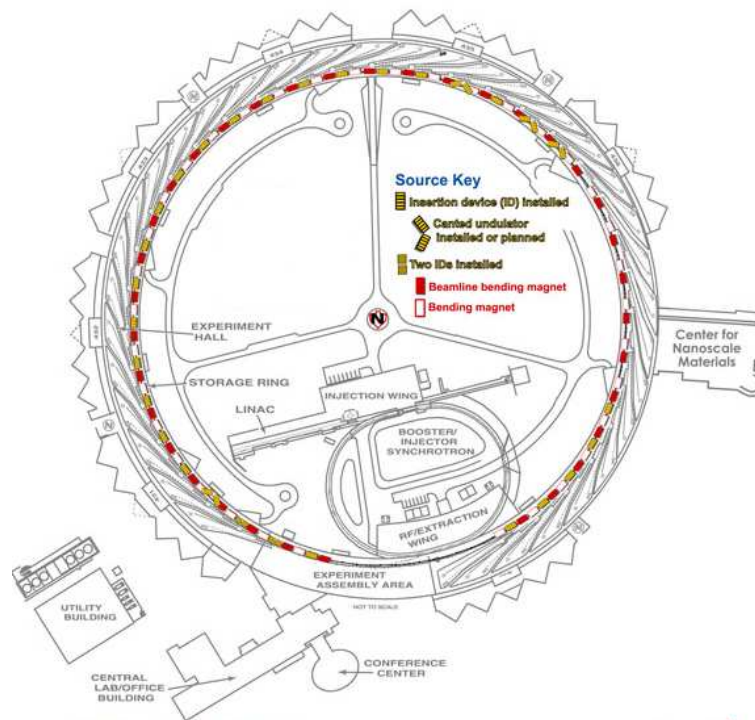


Figure 2.1: Plan view of a typical third-generation synchrotron source (here the Advanced Photon Source at APS). After being accelerated in the linear accelerator (Linac) and the booster ring to their final energy (7 GeV at APS), the electrons enter the storage ring, where they move with relativistic velocities along an almost circular trajectory. The change of the electrons' velocity direction at the bending magnets and the insertion devices causes the emission of electromagnetic radiation along the tangent of their trajectory.

twenty more years before some real research utilizing synchrotron radiation started being performed. Until the mid-1970s, this research was done parasitically, at accelerators designed and built for high-energy physics investigations. The unique properties of synchrotron radiation started then being realized and soon the first dedicated synchrotron facilities were built. The beginning was made with SRS (Synchrotron Radiation Source) at the Daresbury Laboratory in the UK, which operated at an electron energy of 2 GeV, to be followed soon by the NSLS (National Synchrotron Light Source) at Brookhaven, USA and the Photon Factory in Tsukuba, Japan. The largest synchrotron facilities currently operating in the world include the ESRF (European Synchrotron Radiation Facility) in Grenoble, France (electron energy 6 GeV), the APS (Advanced Photon Source) in Argonne, USA (7 GeV) and the SPring-8 (Super Photon Ring) in Nishi-Harima, Japan (8 GeV).

At a synchrotron facility electrons emitted from an electron gun are accelerated by electric fields, first in a linear accelerator, and then in a so-called booster ring,

at modern synchrotron facilities and used for the production of synchrotron radiation of higher brightness. There are two main types of insertion devices: multipole wigglers and undulators. A wiggler (Figure 2.2b) consists of a series of magnets with alternating polarity, which produces a magnetic field of alternating direction (up-down-up-down etc) along the axis of the device [28]. This forces the electrons to follow an almost sinusoidal path within the field, producing a continuum spectrum of radiation in the forward direction. The produced radiation is significantly enhanced in flux and brightness compared to that from a bending magnet. An undulator (Figure 2.2c) works according to the same principle, producing a magnetic field with alternating polarity, but instead of having only a small number of periods (only a few sets of dipole magnets) and a strong magnetic field, like a wiggler, it has a lot of periods and a weak field. The produced radiation is then concentrated within a significantly narrower spectral range, around a certain fundamental frequency and its harmonics. Due to the coherent enhancement of the radiation, its brightness can be several orders of magnitude higher than that of a wiggler.

2.3 Non-resonant Scattering

2.3.1 Kinematical Theory. Charge, Spin and Orbital Scattering

X-ray diffraction is the elastic, coherent scattering of x-rays by the bound electrons of a target material. In the classical picture, the electrons of the material's ions are accelerated by the electric and magnetic fields of the electromagnetic radiation and are set into oscillation. The oscillating electrons emit radiation, according to the classical electromagnetic theory, which has the same frequency as the primary x-ray beam. The emitted radiation is what we call scattered radiation.

For small crystals (so small relative to their distance from the x-ray source, that the primary x-ray beam can be treated by the plane-wave approximation), the kinematical theory of diffraction can be used for its description [29]. The theory is adequate if the diffracted beam is so weak, that the interaction of the incoming and the diffracted beams can be neglected. This means that multiple scattering effects, caused by the re-scattering of the diffracted beam back into the direction of the incident beam, are not taken into consideration. The reduction of the amplitude of the incident wave due to the scattering of a small fraction of it into the exit beam at every atomic plane in the crystal (extinction) is also ignored [30]. The fulfillment of this condition is guaranteed by the small size of the crystals, i.e. by the small number of atomic planes in the sample.

The cross-section of elastic scattering is determined by the diagonal matrix elements of the total scattering amplitude operator \mathbf{G} , averaged over the polarization

states of the primary x-ray beam. In kinematical theory, the cross-section for the elastically scattered signal observed in an element of solid angle $d\Omega$ is given by the trace operation:

$$\frac{d\sigma}{d\Omega} = r_e^2 \cdot \text{Tr}\{\boldsymbol{\mu} | \langle \mathbf{G} \rangle|^2\} \quad (2.1)$$

where r_e is the classical radius of the electron and $\boldsymbol{\mu}$ is a matrix describing the density of the photon polarization states [31]. The off-diagonal matrix elements of \mathbf{G} determine the cross-sections of inelastic scattering processes.

The average value of the scattering amplitude operator multiplied by the classical electron radius r_e is called scattering length g :

$$g = r_e \langle \mathbf{G} \rangle \quad (2.2)$$

The scattering length, which contains in general both charge and magnetic scattering contributions, can be expressed as a Fourier expansion in reciprocal space, in which the coefficients are unit cell structure factors:

$$g = r_e \langle \mathbf{G} \rangle = -r_e \sum_{\boldsymbol{\tau}} \delta(\mathbf{Q} - \boldsymbol{\tau}) [(\boldsymbol{\epsilon}' \cdot \boldsymbol{\epsilon}) F_c(\mathbf{Q}) - i\boldsymbol{\tau} \mathbf{F}_s(\mathbf{Q}) \cdot \mathbf{B}] \quad (2.3)$$

where $\boldsymbol{\epsilon}$, $\boldsymbol{\epsilon}'$ are the polarization vectors of the incoming and the scattered beams, respectively, $\boldsymbol{\tau}$ is a reciprocal lattice vector, and $F_c(\mathbf{Q})$, $\mathbf{F}_s(\mathbf{Q})$ are the Fourier transforms of the time-averaged electron charge and spin densities per unit cell, respectively, for the scattering vector \mathbf{Q} . The vector \mathbf{B} is given by:

$$\mathbf{B} = (\boldsymbol{\epsilon}' \times \boldsymbol{\epsilon}) - (\hat{\mathbf{k}}' \times \boldsymbol{\epsilon}') \times (\hat{\mathbf{k}} \times \boldsymbol{\epsilon}) + (\hat{\mathbf{k}}' \cdot \boldsymbol{\epsilon})(\hat{\mathbf{k}}' \times \boldsymbol{\epsilon}') - (\hat{\mathbf{k}} \cdot \boldsymbol{\epsilon}')(\hat{\mathbf{k}} \times \boldsymbol{\epsilon}) \quad (2.4)$$

where the unit vectors $\hat{\mathbf{k}}$ and $\hat{\mathbf{k}}'$ have directions along the incoming and scattered beams, respectively.

The first term of (2.3) is the contribution of the Thomson charge scattering to the total scattering length. The corresponding structure factor F_c is equal to:

$$F_c(\mathbf{Q}) = \sum_j f_c^j(\mathbf{Q}) e^{i\mathbf{Q} \cdot \mathbf{R}_j} \quad (2.5)$$

where the sum runs over all the ions j of the unit cell, and $f_c^j(\mathbf{Q})$ is the charge form factor of the ion at position \mathbf{R}_j [31]. The latter form factor is given by the Fourier transform of the electronic charge distribution $\rho_j(r)$ within the ion j [32]:

$$f_c^j(\mathbf{Q}) = -\frac{1}{e} \int \rho_j(\mathbf{r}) e^{i\mathbf{Q} \cdot \mathbf{r}} d\mathbf{r} \quad (2.6)$$

The second term of (2.3) is the contribution of magnetic scattering to the total scattering length. While the charge density structure factor (2.5) is a scalar quantity,

expressing (for $\mathbf{Q} = 0$) the total amount of charge in a unit cell, the spin density structure factor $\mathbf{F}_s(\mathbf{Q})$ is a vector quantity, expressing both the configuration and the orientation of the spin moments in the unit cell. In many materials it can be expressed as a sum of individual contributions from each ion of the unit cell:

$$\mathbf{F}_s(\mathbf{Q}) = \sum_j \langle \mathbf{S}_j \rangle f_s^j(\mathbf{Q}) e^{i\mathbf{Q} \cdot \mathbf{R}_j} \quad (2.7)$$

where $\langle \mathbf{S}_j \rangle$, $f_s^j(\mathbf{Q})$ are the spin moment and the spin form factor, respectively, of the ion located at position \mathbf{R}_j .

Away from resonance, the magnetic scattering amplitude is much smaller than the one of charge scattering. Non-resonant magnetic scattering intensity is typically at least six orders of magnitude weaker than the intensity of charge scattering. The two scattering processes are characterized by a phase shift of 90° and have a different influence on polarization: spin scattering causes a partial rotation of the polarization plane, while charge scattering causes no rotation, i.e. gives only $\sigma - \sigma'$ (or $\pi \rightarrow \pi'$) contribution. In the latter notation, σ is by definition the direction of the polarization component perpendicular to the diffraction plane and π the one parallel to it. These different properties can help distinguish between the charge and magnetic contributions in the scattered signal, in cases where charge and spin scattering occur at the same reciprocal lattice points (e.g. in ferromagnets). De Bergevin and Brunel investigated in detail the polarization dependence of the non-resonant magnetic scattering length and suggested for its expression the use of a basis with components perpendicular and parallel to the scattering plane [33]. This formalism is particularly useful for experimental applications and was later applied also in resonant x-ray diffraction investigations, as will be seen in Section 2.4.

In most electron systems, electrons form pairs of time-reversed orbits, thus the net orbital momentum is practically zero and no orbital scattering term needs to be considered for the calculation of the total elastic scattering length. However, in magnetically ordered systems this time-reversal symmetry is broken and the following term has to be added to the scattering length expression (2.3):

$$i\tau \langle \mathbf{Z} \rangle \cdot \boldsymbol{\epsilon}' \times \boldsymbol{\epsilon} = -\frac{\tau}{\hbar k^2} \langle \sum_j e^{i\mathbf{Q} \cdot \mathbf{R}_j} (\mathbf{Q} \times \mathbf{p}_j) \rangle \cdot (\boldsymbol{\epsilon}' \times \boldsymbol{\epsilon}) \quad (2.8)$$

where \mathbf{p}_j is the net momentum of ion j . The orbital scattering contribution to the scattering length is proportional to the vector product $\boldsymbol{\epsilon}' \times \boldsymbol{\epsilon}$, thus the $\sigma - \sigma'$ amplitude always vanishes.

2.3.2 High-energy Diffraction

Non-resonant diffraction performed at high photon energies, above 80 keV, offers significant advantages for the investigation of weak scattering produced by short-range

correlations in transition metal oxides. The absorption coefficient of electromagnetic radiation is reduced with increasing energy. Thus high-energy x-rays are only weakly absorbed by the investigated sample. This leads to an enhanced scattering volume that is probed by the x-rays and over which intensity is integrated, resulting in high total scattered intensities.

In addition, the short wavelengths allow the accessibility of a large volume of the reciprocal space. The radius of the Ewald sphere is inversely proportional to the radiation wavelength λ : $r = 2\pi/\lambda$. Thus for short-wavelength radiation the Ewald sphere is large and a correspondingly large fraction of the reciprocal space can be reached and investigated.

Further advantages of high-energy x-rays can be derived beyond the kinematical approximation. In large crystals, where extinction and multiple-scattering effects are significant, the dynamical theory of diffraction holds. It can be shown that short-wavelength x-rays provide large wave-vector resolution (due to the reduced Darwin width) and, in addition, result in large extinction depths for weak reflections, much larger than the corresponding absorption lengths. The latter ensures that at high energies the conditions for ideal kinematical diffraction are faster approached for weak reflections.

2.4 Resonant Diffraction from Antiferromagnets

2.4.1 Basic Principles and Historical Background

As already mentioned in Section (2.3), non-resonant magnetic scattering is generally several orders of magnitude weaker in intensity than charge scattering. This weakness makes magnetic investigations with x-ray scattering experiments a fairly difficult task. However, by tuning the energy of the incoming x-ray beam close to an absorption edge of the investigated material, a significant resonant enhancement of the magnetic scattering cross-section can be obtained. The resulting high scattering intensities enable the magnetic x-ray study of even weakly magnetically polarized materials. The technique that has been developed to exploit this effect is called x-ray resonance exchange scattering (XRES) and is a very powerful probe, complementary to neutron diffraction, providing, among others, element- and, in some cases, ionization-state-sensitivity.

The mechanism that gives rise to the resonant enhancement involves low-order (dipole (E1) or quadrupole (E2)) electric multipole transitions from a core level into an empty state above the Fermi level. Due to the exclusion principle, which allows electrons to move only into not fully occupied orbitals, the electric transitions lead to an exchange interaction. Through this exchange the magnetic resonance appears.

The phenomenon was first experimentally observed at the K -absorption edges

of ferromagnetic nickel (Ni) by Namikawa *et al.* in 1985 [34]. The resonant enhancement is much stronger at the L - and M - absorption edges of metals, which correspond to electric multipole transitions from initial states with magnetic quantum number $l > 0$, i.e. from initial states that are spin-orbit split. A large resonant enhancement of the x-ray magnetic scattering cross-section was first reported at the L_{III} -edge of holmium (Ho), which is a spiral antiferromagnet, by Gibbs *et al.* in 1988 [35]. The significant resonant enhancement of a factor of 50 reported in that case made clear the great potential of resonant x-ray diffraction and the new possibilities that it opened for the investigation of magnetic materials. Only one year later, Isaacs *et al.* reported a huge resonant enhancement of seven orders of magnitude at the M edges of the actinides, which resulted in a diffracted intensity of several thousand counts per second [36].

Since then, XRES has been established as a powerful probe of magnetic order in strongly correlated electron systems. Related resonant scattering techniques have been more recently developed for the investigation of other degrees of freedom, besides magnetism, such as orbital order for instance [37]. In all cases, a resonant enhancement of the scattering intensity is achieved through a second-order process, in which a core level electron is promoted to an intermediate excited state, which subsequently decays. In the following we refer to these techniques with the general term 'resonant x-ray diffraction' (RXD). Besides providing high scattering intensities, all resonant diffraction techniques have the additional advantage of being element-specific. Only phenomena related to the element with the absorption edge, to which the energy of the incoming x-ray beam is tuned, are observed. In cases where different valence states of the same element involve different electric transitions, the method is also ionization-state sensitive.

Resonant x-ray diffraction has been used with remarkable success for the investigation of numerous transition metal oxides. Resonant diffraction at the K - absorption edges of titanium (Ti) and manganese (Mn), for instance, has been employed for the study of $3d$ compounds, such as YTiO_3 [38], LaMnO_3 [37], $\text{Pr}_{0.6}\text{Ca}_{0.4}\text{MnO}_3$ [39] and RbMnF_3 [40]. At the K -absorption edges, the resonance is driven by electric dipole transitions from the $1s$ core level to the unoccupied $4p$ level, and gives an enhancement which is usually a factor of three to five of the scattering intensity off resonance.

Significantly larger resonance enhancements can be obtained at the L - absorption edges of transition metals, where the probed electric dipole transitions drive the electrons directly into the partly occupied d band, which is responsible for the magnetic phenomena in these materials. The probing of the d band enables the direct observation of orbital ordering. The technique has recently been used for the study of orbitally ordered states in $3d$ ($\text{La}_{2-2x}\text{Sr}_{1+2x}\text{Mn}_2\text{O}_7$ [41], $\text{La}_{0.5}\text{Sr}_{1.5}\text{MnO}_4$ [42], $\text{Pr}_{0.6}\text{Ca}_{0.4}\text{MnO}_3$ [43]) and $5d$ (K_2ReCl_6 [44]) electron compounds. The investigations presented in this work are the first L -edge resonant diffraction studies of

a $4d$ electron system [45]. Several technical difficulties are associated with working at x-ray energies close to the L -edges of $4d$ metals (around and below 3 keV). This energy regime is difficult to access both in hard x-ray and in soft x-ray synchrotron facilities, for reasons related to the operation of the insertion devices (e.g. undulators) and the monochromators (gratings), respectively. In addition, the advantages that were mentioned in Section 2.3.2 for high-energy diffraction, count now inverted as drawbacks: the low energy value results in severe absorption of the x-ray beam by the air, thus the experimental setup has to be especially optimized, so that there is as little air as possible in the beam flight-path; and the large wavelengths result in a small Ewald sphere radius, which means that only a small part of the reciprocal space is accessible for investigations. As will be seen in the experimental parts of Chapters 3 and 4, the present work has been successful in overcoming the above difficulties and fully exploiting the unique possibilities of XRES at the L -edges of transition metals, providing valuable information on the electronic properties of the investigated materials.

2.4.2 Resonant Electric Dipole Scattering Length

The total coherent elastic scattering length g for a magnetic ion, containing both non-resonant and resonant contributions, can be written as a sum of four terms:

$$g = g_0 + g' + ig'' + g_m \quad (2.9)$$

where $g_0 \propto -Zr_e$ is the Thomson charge scattering contribution, with Z being the atomic number of the ion and r_e the classical electron radius, g_m is the non-resonant spin-dependent magnetic scattering length, and $g' + ig''$ is the contribution (both resonant and non-resonant) from dispersive and absorptive processes [46].

For an electric 2^L -pole (EL) resonance in a magnetic ion, the resonant contribution to the coherent scattering length is [46]:

$$g_{EL}(\omega) = \frac{4\pi}{|k|} W_D \sum_{M=-L}^L [\hat{\epsilon}'^* \cdot \mathbf{Y}_{LM}(\hat{\mathbf{k}}') \mathbf{Y}_{LM}^*(\hat{\mathbf{k}}) \cdot \hat{\epsilon}] F_{LM}(\omega) \quad (2.10)$$

In (2.10) the functions $\mathbf{Y}_{LM}(\hat{\mathbf{k}})$ are vector spherical harmonics, W_D is the Debye-Waller factor (a factor which takes into consideration the reduction of the scattering intensity caused by the thermal vibrations of the ions around their equilibrium positions), \mathbf{k} , \mathbf{k}' are the wavevectors of the incoming and scattered beams, respectively, $\hat{\epsilon}$, $\hat{\epsilon}'$ are the corresponding polarization vectors, and $F_{LM}(\omega)$ is a factor that determines the strength of the resonance and which depends on atomic properties of the scattering ion:

$$F_{LM}(\omega) = \sum_{\alpha, n} \left[\frac{P_\alpha P_\alpha(\eta) \Gamma_x(\alpha M \eta; EL)}{\Gamma(\eta)} \right] / [x(\alpha, \eta) - i] \quad (2.11)$$

Here $|\alpha\rangle$ is the initial ground state of the ion; $|\eta\rangle$ is the final state, where an electron has been excited to a higher level leaving a hole in the core level; P_α is the probability of the ion being in the initial state α ; $P_\alpha(\eta)$ is the probability of a transition from the initial state $|\alpha\rangle$ to the final state $|\eta\rangle$, which is determined by the overlap integrals of the two states; Γ_x is the partial line width of the excited state for a pure 2^L -pole (EL) radiative decay from $|\eta\rangle$ to $|\alpha\rangle$; Γ is the total width of the excited state for all deexcitations of $|\eta\rangle$, radiative and non-radiative; and finally x is the deviation from the resonance condition in units of the total half-width: $x = \frac{E_\eta - E_\alpha - \hbar\omega}{\Gamma/2}$.

The above are valid for isotropic systems, in which the symmetry is broken by the magnetic moment. In systems where particular point group symmetries are applied, the allowed terms are altered.

In order to make clear the polarization dependence of resonant magnetic scattering and its sensitivity to individual components of the magnetic moment, it is useful to express the vector spherical harmonics in the scattering length (2.10) as a function of the polarization vectors $\boldsymbol{\epsilon}$, $\boldsymbol{\epsilon}'$ of the incoming and scattered beams. For electric dipole (E1) transitions ($L = 1$, $M = \pm 1$), which usually dominate the resonant scattering cross-section, the scattering length of resonant elastic scattering can be written as follows [47]:

$$g_{E1}(\omega) = [(\boldsymbol{\epsilon}' \cdot \boldsymbol{\hat{\epsilon}})F^{(0)} - i(\boldsymbol{\epsilon}' \times \boldsymbol{\hat{\epsilon}}) \cdot \boldsymbol{\hat{\mu}}F^{(1)} + (\boldsymbol{\epsilon}' \cdot \boldsymbol{\hat{\mu}})(\boldsymbol{\hat{\epsilon}} \cdot \boldsymbol{\hat{\mu}})F^{(2)}] \quad (2.12)$$

where

$$F^{(0)} = \frac{3}{4k}[F_{11} + F_{1-1}] \quad (2.13)$$

$$F^{(1)} = \frac{3}{4k}[F_{11} - F_{1-1}] \quad (2.14)$$

$$F^{(2)} = \frac{3}{4k}[2F_{10} - F_{11} - F_{1-1}] \quad (2.15)$$

and $\boldsymbol{\hat{\mu}}$ is a unit vector along the local magnetic moment direction.

The first term of (2.12) is the anomalous dispersion term. It is the contribution to the Bragg charge scattering and shows no dependence on the magnetic moment. The polarization dependence enters through the scalar product $\boldsymbol{\epsilon}' \cdot \boldsymbol{\epsilon}$ of the polarization vectors, just like in non-resonant charge scattering (2.3). The scalar product is non-zero for non-perpendicular incoming and outgoing polarization vectors. Thus no rotation of the polarization plane is caused by the anomalous dispersion term. The scattering is either $\sigma \rightarrow \sigma'$ or $\pi \rightarrow \pi'$.

The second term is the one responsible for magnetic circular dichroism in ferromagnets. It depends on the difference in magnetic resonance strength between states with magnetic quantum numbers $M = 1$ and $M = -1$. The polarization dependence enters through the vector product $\boldsymbol{\epsilon}' \times \boldsymbol{\epsilon}$. Thus, for a σ -polarized incoming beam, it causes a rotation of the polarization plane, i.e. leads to $\sigma \rightarrow \pi'$

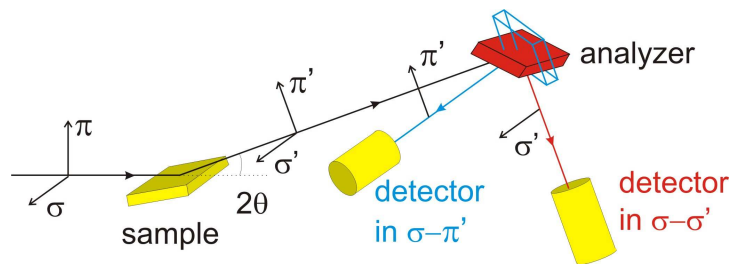


Figure 2.3: Schematic view of the experimental configuration in a resonant x-ray diffraction experiment. The incoming beam is linearly polarized along the σ direction. The diffracted beam has, in the general case, polarization components both along σ' (perpendicular to the diffraction plane) and along π' (parallel to the d.p.). The two polarization components can be separated with the use of a proper analyzer crystal.

scattering. For a π -polarized primary beam, both rotated ($\pi \rightarrow \sigma'$) and unrotated ($\pi \rightarrow \pi'$) scattering are allowed. As far as the dependence on the magnetic moment is concerned, this is linear, just like in non-resonant magnetic scattering. Both types of magnetic scattering produce first-order magnetic satellites, at the same reciprocal space points.

The third and last term of the total resonant scattering length is related to magnetic linear dichroism. It has a relatively complicated polarization dependence which generally leads to a partial rotation of the polarization plane. Its dependence on the magnetic moment is quadratic, producing second-harmonic magnetic satellites, which are not observed off-resonance. Magnetic x-ray linear dichroism is generally much weaker than circular dichroism, especially at hard x-ray absorption edges, thus the last term of (2.12) is also correspondingly weak compared to the other two.

Following the procedure used by de Bergevin and Brunel for the derivation of the cross-section of non-resonant elastic magnetic scattering [33], we can similarly express the resonant scattering length with the use of 2×2 matrices in a basis, the components of which are perpendicular (σ) and parallel (π) to the scattering plane, as suggested by Hill and McMorro [47]. Figure 2.3 shows a schematic view of a typical experimental setup for a resonant x-ray scattering experiment involving polarization analysis of the diffracted beam. If $\hat{\epsilon}_\sigma$, $\hat{\epsilon}_\pi$ are the components of the polarization vector ϵ of the incoming x-ray beam along the σ and π directions, and $\hat{\epsilon}'_\sigma$, $\hat{\epsilon}'_\pi$ the components of the polarization vector ϵ' of the diffracted beam along σ' and π' , respectively, then: $\hat{\epsilon}'_\sigma \cdot \hat{\epsilon}_\sigma = 1$, $\hat{\epsilon}'_\pi \cdot \hat{\epsilon}_\pi = \cos 2\theta = \hat{\mathbf{k}} \cdot \hat{\mathbf{k}'}$, $\hat{\epsilon}'_\sigma \cdot \hat{\epsilon}_\pi = \hat{\epsilon}'_\pi \cdot \hat{\epsilon}_\sigma = 0$. The scalar product in the first term of (2.12) can be thus written as a diagonal matrix, the diagonal elements of which correspond to the unrotated ($\sigma \rightarrow \sigma'$, $\pi \rightarrow \pi'$) scattering processes:

$$\hat{\epsilon}' \cdot \hat{\epsilon} = \begin{pmatrix} 1 & 0 \\ 0 & \hat{\mathbf{k}}' \cdot \hat{\mathbf{k}} \end{pmatrix} \quad (2.16)$$

As far as the second term of (2.12) is concerned, there we have: $\hat{\epsilon}'_{\sigma} \times \hat{\epsilon}_{\sigma} = 0$, $\hat{\epsilon}'_{\pi} \times \hat{\epsilon}_{\pi} = \hat{k}' \times \hat{k}$, $\hat{\epsilon}'_{\sigma} \times \hat{\epsilon}_{\pi} = \hat{k}$, and $\hat{\epsilon}'_{\pi} \times \hat{\epsilon}_{\sigma} = -\hat{k}'$. Thus the vector product in the circular magnetic dichroism term can be written as:

$$\hat{\epsilon}' \times \hat{\epsilon} = \begin{pmatrix} 0 & \hat{k} \\ -\hat{k}' & \hat{k}' \times \hat{k} \end{pmatrix} \quad (2.17)$$

The third term can be also expressed as a matrix containing products of \hat{k} , \hat{k}' and $\hat{\mu}$. These vectors can be analyzed along the main axes \hat{U}_1 , \hat{U}_2 and \hat{U}_3 of a coordinate system, in which the plane defined by \hat{U}_1 , \hat{U}_3 is parallel to the scattering plane, and \hat{U}_3 is antiparallel to the scattering vector (Figure 2.4). The following expression for the total resonant electric dipole scattering length can be then found:

$$g_{E1} = F^{(0)} \begin{pmatrix} 1 & 0 \\ 0 & \cos 2\theta \end{pmatrix} - iF^{(1)} \begin{pmatrix} 0 & \mu_1 \cos \theta + \mu_3 \sin \theta \\ \mu_3 \sin \theta - \mu_1 \cos \theta & -\mu_2 \sin 2\theta \end{pmatrix} \\ + F^{(2)} \begin{pmatrix} \mu_2^2 & -\mu_2(\mu_1 \sin \theta - \mu_3 \cos \theta) \\ \mu_2(\mu_1 \sin \theta + \mu_3 \cos \theta) & -\cos^2 \theta(\mu_1^2 \tan^2 \theta + \mu_3^2) \end{pmatrix} \quad (2.18)$$

where θ is the scattering angle and μ_1 , μ_2 , μ_3 the components of $\hat{\mu}$ along \hat{U}_1 , \hat{U}_2 , \hat{U}_3 , respectively.

Starting from Equation 2.18, one can express the resonant electric dipole scattering length as a function of the azimuthal angle ψ , namely the angle between the projection of the magnetic moment on the plane that is perpendicular to the scattering plane, and the scattering plane. By definition, $\psi = 0^\circ$ when the magnetic moment lies in the diffraction plane. Expressing the scattering length as a function of ψ is particularly useful for resonant scattering experiments.

We assume a magnetic basis consisting of N ions with two possible spin directions, for which the notations 'spin-up': \uparrow and 'spin-down': \downarrow are used. According to (2.18), in the $\sigma \rightarrow \pi'$ scattering geometry, the scattering length for a 'spin-up' ion is:

$$g_{E1,\uparrow}^{\sigma \rightarrow \pi'} = -iF^{(1)}(\mu_3 \sin \theta - \mu_1 \cos \theta) + F^{(2)}\mu_2(\mu_1 \sin \theta + \mu_3 \cos \theta) \quad (2.19)$$

With α being the angle between the magnetic moment $\hat{\mu}$ and the scattering vector (Figure 2.4), the magnetic moment components can be written as follows:

$$\begin{aligned} \mu_1 &= \sin \alpha \cos \psi \\ \mu_2 &= \sin \alpha \sin \psi \\ \mu_3 &= -\cos \alpha \end{aligned} \quad (2.20)$$

So 2.19 gives:

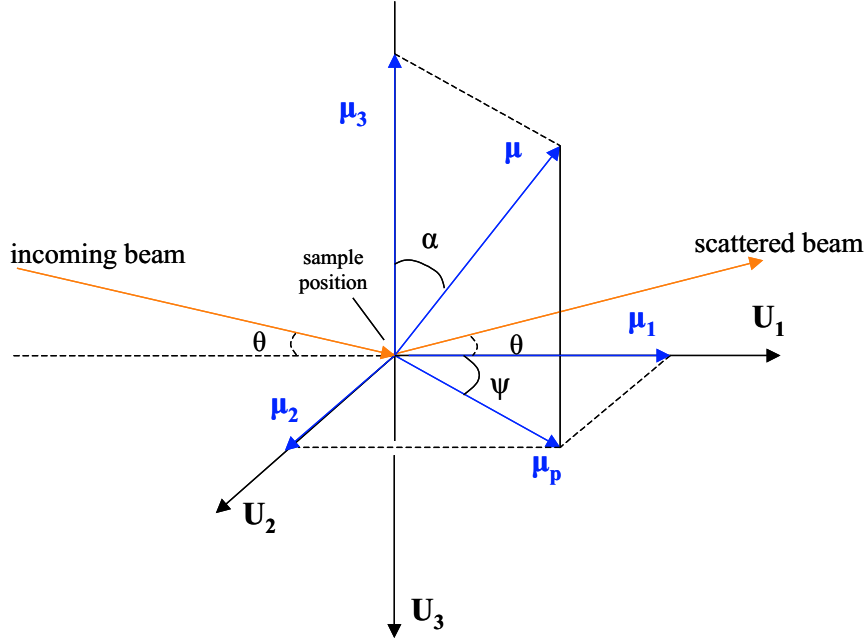


Figure 2.4: Configuration of the scattering process, used in the calculation of the resonant electric dipole scattering length. The axis \mathbf{U}_3 of the coordinate frame is antiparallel to the scattering vector. θ is the Bragg angle, α the angle between the magnetic moment $\boldsymbol{\mu}$ and the scattering vector, and ψ the angle between the diffraction plane (defined by the incoming and scattered beams) and the projection of $\boldsymbol{\mu}$ on a plane perpendicular to the diffraction plane. By definition, $\psi = 0^\circ$ when the magnetic moment lies in the diffraction plane.

$$\begin{aligned}
g_{E1,\uparrow}^{\sigma \rightarrow \pi'} &= -iF^{(1)}(-\cos \alpha \sin \theta - \sin \alpha \cos \psi \cos \theta) \\
&\quad + F^{(2)} \sin \alpha \sin \psi (\sin \alpha \cos \psi \sin \theta - \cos \alpha \cos \theta) \Rightarrow \\
g_{E1,\uparrow}^{\sigma \rightarrow \pi'} &= iF^{(1)} \cos \alpha \sin \theta + iF^{(1)} \sin \alpha \cos \theta \cos \psi \\
&\quad + F^{(2)} \sin^2 \alpha \sin \theta \sin \psi \cos \psi \\
&\quad - F^{(2)} \sin \alpha \cos \alpha \cos \theta \sin \psi
\end{aligned} \tag{2.21}$$

Similarly for the 'spin-down' ion (opposite direction of $\hat{\boldsymbol{\mu}}$) we have:

$$g_{E1,\downarrow}^{\sigma \rightarrow \pi'} = -iF^{(1)}(-\mu_3 \sin \theta + \mu_1 \cos \theta) + F^{(2)}(-\mu_2)(-\mu_1 \sin \theta - \mu_3 \cos \theta) \tag{2.22}$$

which gives:

$$\begin{aligned}
g_{E1,\downarrow}^{\sigma \rightarrow \pi'} &= -iF^{(1)} \cos \alpha \sin \theta - iF^{(1)} \sin \alpha \cos \theta \cos \psi \\
&\quad + F^{(2)} \sin^2 \alpha \sin \theta \sin \psi \cos \psi \\
&\quad - F^{(2)} \sin \alpha \cos \alpha \cos \theta \sin \psi
\end{aligned} \tag{2.23}$$

The total resonant electric dipole scattering length for the N ions of the basis in $\sigma \rightarrow \pi'$ geometry is then:

$$g_{E1}^{\sigma \rightarrow \pi'} = \sum_{j=1}^N g_{E1, S_j}^{\sigma \rightarrow \pi'} e^{i\mathbf{Q} \cdot \mathbf{R}_j} \quad (2.24)$$

with S_j being the spin of ion j (up or down) and $g_{E1, S_j}^{\sigma \rightarrow \pi'}$ being given by (2.21) or (2.23). The scattering intensity measured in the $\sigma \rightarrow \pi'$ polarization channel at a particular reciprocal space position (hkl) is proportional to the square of the amplitude of the corresponding total scattering length:

$$I_{(hkl)}^{\sigma \rightarrow \pi'} \propto |g_{E1}^{\sigma \rightarrow \pi'}|^2 \quad (2.25)$$

For the $\sigma \rightarrow \sigma'$ scattering geometry, Equation (2.18) gives for the scattering lengths of the ions of the basis:

$$g_{E1, \uparrow}^{\sigma \rightarrow \sigma'} = g_{E1, \downarrow}^{\sigma \rightarrow \sigma'} = F^{(0)} + F^{(2)} \mu_2^2 = F^{(0)} + F^{(2)} \sin^2 \alpha \sin^2 \psi \quad (2.26)$$

The total scattering length is in this case:

$$g_{E1}^{\sigma \rightarrow \sigma'} = \sum_{j=1}^N g_{E1, S_j}^{\sigma \rightarrow \sigma'} e^{i\mathbf{Q} \cdot \mathbf{R}_j} \quad (2.27)$$

and the scattering intensity in $\sigma \rightarrow \sigma'$:

$$I_{(hkl)}^{\sigma \rightarrow \sigma'} \propto |g_{E1}^{\sigma \rightarrow \sigma'}|^2 \quad (2.28)$$

Equations 2.25 and 2.28 give the relative resonant scattering intensity in the $\sigma \rightarrow \pi'$ and $\sigma \rightarrow \sigma'$ polarization geometries as a function of the azimuthal angle ψ . The expressions, in the specific form they assume when applied on the magnetic cell of a particular material, can be used for identifying the magnetic contribution in the total scattering signal and for determining the direction of the magnetic moment in the investigated system. The importance of these possibilities will become obvious in Chapters 3 and 4.

2.5 Orientation Matrix

The matrix which establishes the orientation of the sample with regard to the diffractometer in a scattering experiment is called the orientation matrix UB. It relates the coordinate system of the diffractometer to the reciprocal lattice system of the scattering crystal, allowing the calculation of the Miller indices of a particular reflection if the corresponding four diffractometer angles ($2\theta, \theta, \chi, \phi$; Figure 2.5) are known:

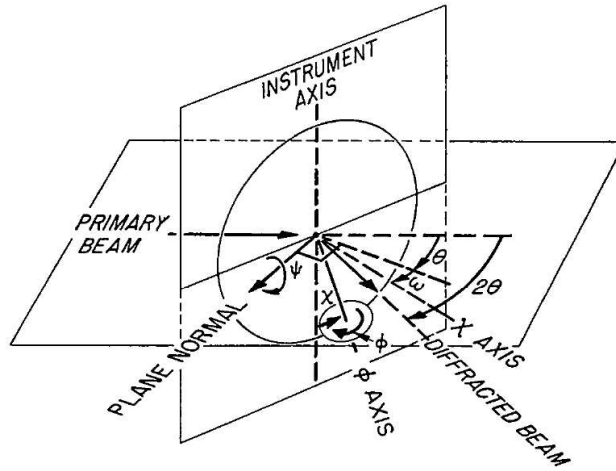


Figure 2.5: Schematic representation of the angle configuration in a 4-circle diffractometer, as used for the orientation matrix calculations by Busing and Levy [48].

$$\mathbf{q}_\phi = \mathbf{U} \mathbf{B} \mathbf{q} \quad (2.29)$$

where the column vectors \mathbf{q} and \mathbf{q}_ϕ have as elements the Miller indices h, k, l and the scattering vector coordinates in the ϕ -system, respectively, of a particular reflection.

As explained by Busing and Levy in 1967 [48], for the determination of the orientation matrix, one needs to know either the lattice parameters of the sample and the diffractometer angles for two reflections from non-parallel planes, or only the diffractometer angles for three non-coplanar reflections. A more precise determination of the UB matrix is achieved by collecting a large number of reflections and then applying the least-squares method to refine the cell parameters and the orientation parameters simultaneously.

Chapter 3

The system $\text{Ca}_{2-x}\text{Sr}_x\text{RuO}_4$ ($x = 0, 0.1$)

The two-dimensional ruthenate system $\text{Ca}_{2-x}\text{Sr}_x\text{RuO}_4$ is in many aspects an interesting material. Although the gradual substitution of calcium (Ca) by strontium (Sr) is isovalent, the electronic properties of the material vary significantly with the Sr content x , resulting in a rich phase diagram (Figure 3.1). The $x = 2$ end-member of the series has attracted particular attention. Sr_2RuO_4 is a metallic compound, turning below 1.5 K into an unconventional spin-triplet superconductor [49, 50], the only known layered perovskite without copper exhibiting superconducting properties. It is currently an issue of debate how strongly the $4d$ electrons are correlated in this system, how exactly the electron correlations determine the material's properties, and what the role of magnetic and orbital fluctuations is in the establishment of superconductivity. On the other side of the phase diagram, Ca_2RuO_4 ($x = 0$) is a Mott insulator, exhibiting antiferromagnetic ordering with a weak ferromagnetic component due to spin canting below 110–150 K [51]. The narrow electron bands induce strong electron correlations and the substantial spin-orbit coupling implies that the orbital degree of freedom is active and plays a crucial role in the magnetic properties of the material. Several, partly controversial theoretical predictions have been made for the orbital ordering pattern of the $4d$ orbitals in Ca_2RuO_4 [52, 53, 54, 55]. Investigating the interplay between the magnetic and orbital degrees of freedom in Ca_2RuO_4 can help understand the origin of many of the electronic properties of the $\text{Ca}_{2-x}\text{Sr}_x\text{RuO}_4$ system, including the establishment of superconductivity in Sr_2RuO_4 . This may give insight into the properties of transition metal oxides in general, and in particular of high-temperature superconducting cuprates, which are isostructural to $\text{Ca}_{2-x}\text{Sr}_x\text{RuO}_4$.

The present chapter concentrates on the main features of the undoped compound Ca_2RuO_4 and gives a detailed presentation of the experimental results obtained from its investigation with resonant x-ray diffraction. The case of the lightly Sr-doped

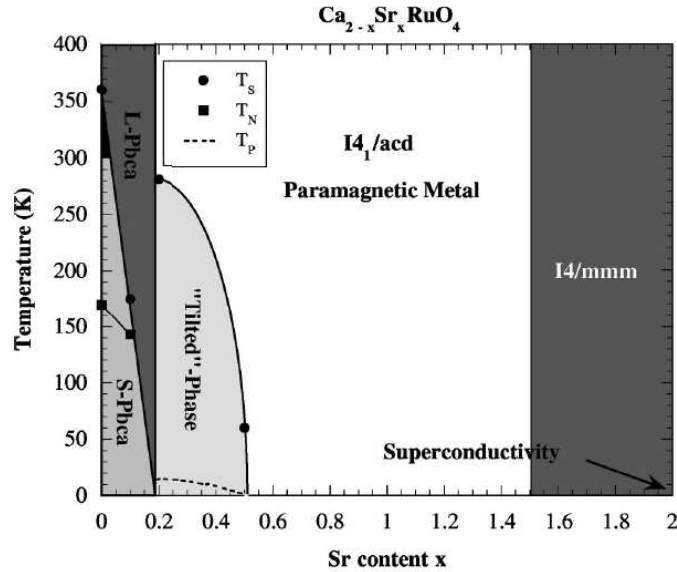


Figure 3.1: Phase diagram of the $\text{Ca}_{2-x}\text{Sr}_x\text{RuO}_4$ system [56]. The $x = 0$ end member is an antiferromagnetic Mott insulator, turning metallic at 356 K, in a first-order phase transition, which is accompanied by substantial structural distortions. The $x = 2$ end member, on the other hand, is metallic, turning below 1.5 K into a spin-triplet superconductor.

compound $\text{Ca}_{1.9}\text{Sr}_{0.1}\text{RuO}_4$ is discussed in Section 3.11. The general conclusions drawn for the $x < 0.2$ region of the phase diagram from the combined evaluation of the two compounds are presented in Section 3.12.

3.1 Crystal Structure

The crystal structure of Ca_2RuO_4 is orthorhombic (space-group $Pbca$), with lattice parameters $a=5.4097(3)$ Å, $b=5.4924(4)$ Å and $c=11.9613(6)$ Å at room temperature [51]. It is a layered perovskite, consisting of RuO_2 layers which are made up of corner-sharing RuO_6 octahedra (Figure 3.2). Its structure is, however, strongly distorted and significant deviations from the ideal K_2NiF_4 -structure (space-group $I4/mmm$) are observed. The orthorhombic distortion, already present at room temperature, is further increased upon cooling. The lattice parameters and the unit cell volume follow an unusual temperature dependence, which even leads to an increase of the volume with decreasing temperature. Figure 3.3 shows the variation with temperature of the lattice parameters, of the orthorhombic strain, defined as the ratio $(b - a)/(b + a)$, and of the lattice volume, as determined with powder neutron diffraction measurements [56].

In addition, a strong distortion related to the RuO_6 octahedra is observed. This

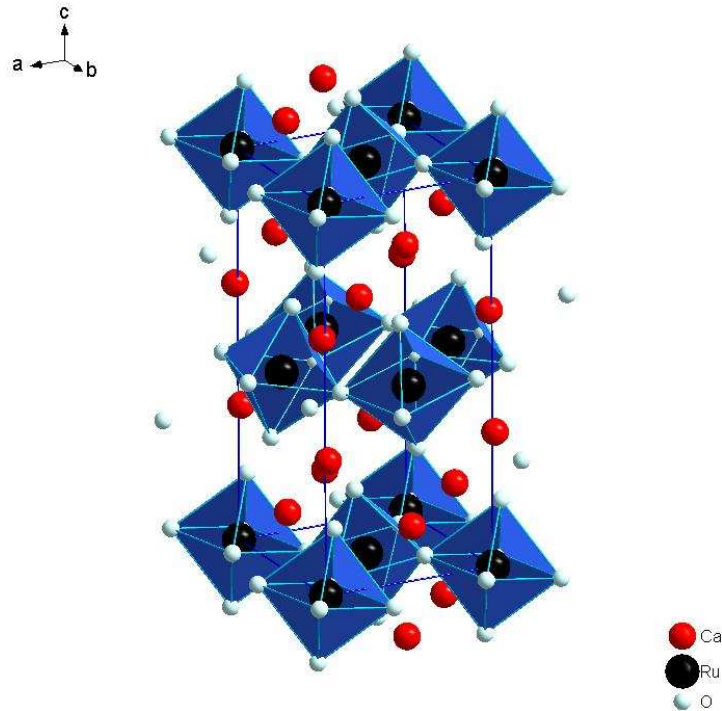


Figure 3.2: Crystal structure of Ca_2RuO_4 (space-group $Pbca$). The Ru ions occupy the centers of corner-sharing RuO_6 octahedra, forming RuO_2 layers that extend parallel to the ab plane. The octahedra are significantly tilted around an axis lying in the RuO_2 planes and rotated around the long crystallographic axis c . The structural distortions are strongly dependent on temperature and stoichiometry.

latter distortion can be described as the result of a combined 'tilt plus rotation' movement, namely, a tilt of the octahedra around an axis which lies in the RuO_2 plane plus a rotation of them around the long crystallographic axis c [51]. Such distortions are relatively common in perovskite-type materials and have been studied already by Goldschmidt in 1926 [57] and Goodenough in 1955 [58]. The underlying idea is that the octahedral tilts lower the total energy of the AMO_3 (or $\text{A}_{n+1}\text{M}_n\text{O}_{3n+1}$) system, by reducing the length of the A - O bonds, while keeping the length of the M - O bonds constant. In Ca_2RuO_4 the angle ϕ describing the rotation of the octahedra around c is temperature independent and has a value of approximately 11.8° . On the other hand, the tilt of the octahedra with regard to the ab -plane is strongly temperature dependent. It can be described either using the basal plane oxygen sites O(1), or the apical oxygen sites O(2). The angle θ_1 between the Ru-O(1) bond and the ab -plane has a value of 11.2° at room temperature and of 12.7° at 11 K. The angle θ_2 between the Ru-O(2) bond and the long axis c is slightly smaller than θ_1 , but shows the same variation with temperature. The temperature dependence

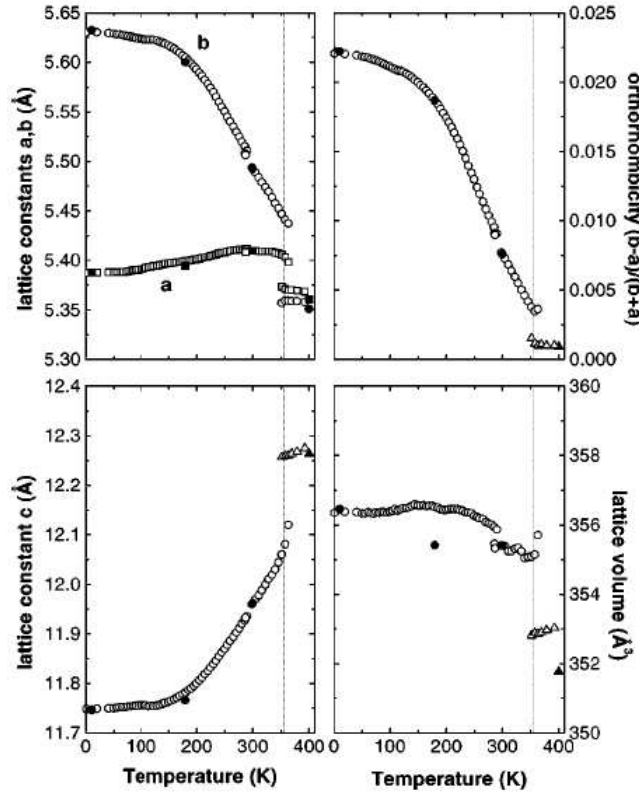


Figure 3.3: Variation with temperature of the lattice parameters a , b (upper left panel) and c (lower left), of the orthorhombic strain (orthorhombicity) $(b - a)/(b + a)$ (upper right), and of the unit cell volume (lower right) of Ca_2RuO_4 , as determined with neutron diffraction [56]. The discontinuous changes observed in all parameters at $T_{\text{MI}} = 356$ K denote the large structural distortions that accompany the first-order metal-insulator transition.

of both tilting angles θ_1, θ_2 is shown in Figure 3.4 [51].

The shape of the octahedra also changes slightly with temperature. The increase by about 2% of the b lattice parameter with decreasing temperature leads to an elongation of the Ru-O(1) in-plane bond. This in-plane elongation almost parallel to b is accompanied by a decrease by a similar amount of the length of the out-of-plane Ru-O(2) bonds, that extend almost parallel to the c direction (tilted by the angle θ_2). The result is a small but noticeable flattening of the octahedra upon cooling.

In the opposite direction, increasing temperature leads to a significant elongation of the RuO_6 octahedra along the long axis. Up to approximately 300 K, the in-plane Ru-O bond still remains longer than the out-of-plane one, though the difference

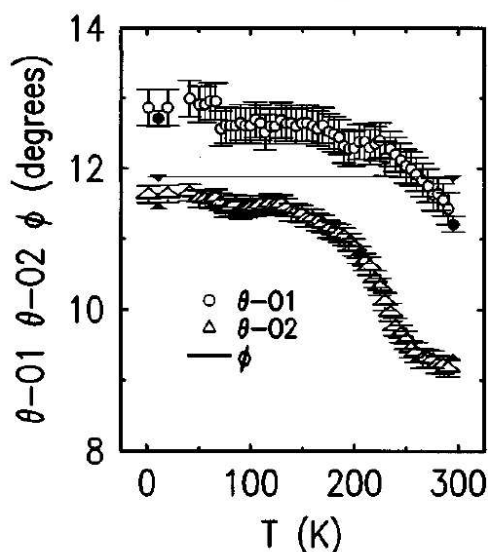


Figure 3.4: Variation with temperature of the tilt angles θ_1 (bullets), θ_2 (triangles), and of the rotation angle ϕ of the RuO_6 octahedra in Ca_2RuO_4 , as determined with neutron diffraction [51]. The definition of the angles is given in the text.

between them is reduced fast (Figure 3.5). At 300 K the lengths of the two bonds become equal to each other. The elongation of the octahedra continues also above that temperature, so that the out-of-plane bond now becomes the longest one.

The most dramatic effect in the Ru-O bond lengths is, however, observed a little higher in temperature. As will be discussed in Section 3.4, a first-order metal-insulator transition takes place in the Ca_2RuO_4 system at the temperature of $T_{\text{MI}} = 356$ K. This phase transition is accompanied by substantial structural distortions, which result in significant, discontinuous changes in the tilting angles of the RuO_6 octahedra, the Ru-O bonds, and subsequently the lattice parameters of the material, as neutron diffraction investigations have shown [56]. These changes can be seen as abrupt, sharp steps in the temperature dependence of the lattice parameters (Figure 3.3) and of the Ru-O bond lengths (Figure 3.5). The structural phase of Ca_2RuO_4 above the metal-insulator transition is usually named the *L-Pbca* phase, due to the longer *c*-lattice parameter that characterizes it, while the low-temperature phase below T_{MI} , characterized by a shorter *c*-parameter, is called the *S-Pbca* phase. The large deformations of the crystal when passing through the metal-insulator phase transition result in its macroscopic cracking and shattering into very small pieces, which makes the measurement of any property of the material around that temperature on single crystals an extremely difficult task.

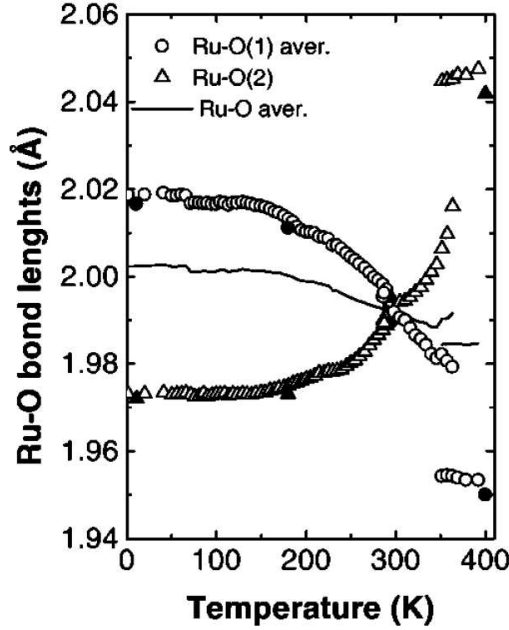


Figure 3.5: Variation with temperature of the Ru-O bond lengths in Ca_2RuO_4 , as determined with neutron diffraction [56]. The distance of the Ru^{+4} sites from both the basal (bullets) and the apical (triangles) O^{2-} sites, as well as their average value at every temperature (solid line), are shown. The discontinuous changes observed in all bond lengths at $T_{\text{MI}} = 356$ K denote the large structural distortions that accompany the first-order metal-insulator transition.

3.2 Electronic Structure and Orbital Order

The formal oxidation state of ruthenium in Ca_2RuO_4 is +4. Every Ru^{+4} ion has four electrons in the $4d$ orbitals. The degeneracy of the electronic states of the $4d$ band is partly lifted, as described in Section 1.3.1, due to the (tetragonal) crystal field effect. This is significantly stronger in Ca_2RuO_4 than in $3d$ oxides, because the larger radial extent of the $4d$ shell leads to a stronger interaction of Ru^{+4} with the surrounding ions in the lattice. The energy difference $\Delta = 10D_q$ between the three lower-lying t_{2g} (d_{xy}, d_{yz}, d_{zx}) orbitals and the two higher-lying e_g ($d_{x^2-y^2}, d_{3z^2-r^2}$) orbitals is estimated with band structure calculations approximately equal to 4 eV [59]. The crystal field splitting Δ is in this case larger than the Hund coupling J_H . Thus, as described in Section 1.3.1, the Ru^{+4} ions are in the low-spin configuration: all four $4d$ electrons are in the t_{2g} states, leaving the e_g states completely empty. The Jahn-Teller-like distortion of the RuO_6 octahedra leads in addition to a partial splitting of the t_{2g} orbitals, with the d_{yz}/d_{zx} states now having slightly higher energy than d_{xy} . The tilting distortion of the octahedra further contributes to the lifting of

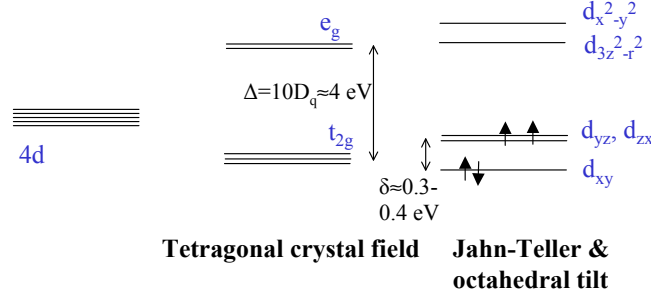


Figure 3.6: Schematic view of the $4d$ electronic states of Ca_2RuO_4 . The initially degenerate states are split, under the influence of the crystal field, into t_{2g} and e_g orbitals. The remaining t_{2g} degeneracy is further lifted due to distortions of the RuO_6 octahedra.

the degeneracy of the t_{2g} orbitals (Figure 3.6).

Based on the above simple picture, the d_{xy} orbital, which has the lowest energy among all t_{2g} orbitals, should be always fully occupied, as seen in Figure 3.6, i.e. the hole population in d_{xy} should be zero. The first theoretical calculations of the electronic density of the t_{2g} states, performed by Anisimov *et al.*, indeed predicted a 'ferro-orbital' (FO) ordering pattern in Ca_2RuO_4 , with the d_{xy} orbitals occupied at all Ru^{+4} sites [52]. For the calculations, the LDA+ U method was used, that is, the usual local density approximation with the inclusion of an effective Coulomb repulsion parameter U that expresses the on-site correlations.

New experimental data, however, surprisingly put under question the homogeneous occupancy of the d_{xy} orbitals. Based on x-ray absorption spectroscopy investigations, Mizokawa *et al.* claimed that the hole population ratio of the d_{xy} and d_{yz}/d_{zx} orbitals is roughly equal to 1 : 1 at room temperature, dropping to 0.5 : 1.5 at 90 K, due to the compression of the octahedra [60]. Such a hole population would be inconsistent with the one expected from the crystal field effects and indicates that the orbital degree of freedom has to be taken into consideration as well in the determination of the electronic structure of Ca_2RuO_4 . In an attempt to explain the spectroscopic data, Mizokawa *et al.* argued that the ground state may favor the occupation of complex orbitals, as a result of the strong spin-orbit coupling. In particular, it was suggested that, while at 300 K the two t_{2g} holes are located at the d_{xy} and $\frac{d_{zx}+id_{yz}}{\sqrt{2}}$ orbitals, with the spin (S) and orbital (L) angular momenta aligned along the z axis, at 90 K, where the out-of-plane Ru-O bond is shorter, the antiferromagnetic state with the two holes in the d_{yz} and $\frac{d_{xy}+id_{zx}}{\sqrt{2}}$ is stabilized instead, and the L, S momenta are aligned along the x (or y) axis.

Hotta and Dagotto took into consideration the new experimental information and

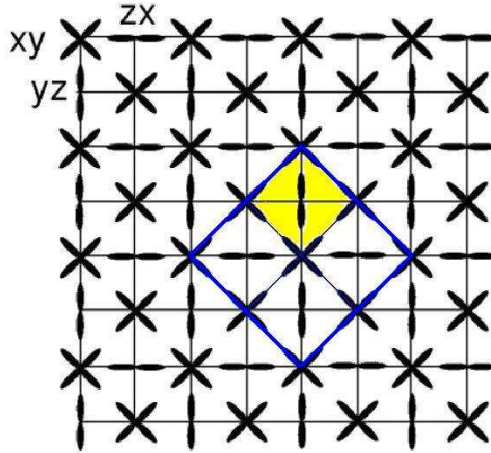


Figure 3.7: Schematic view of the antiferro-orbital-ordered state suggested for Ca_2RuO_4 by Hotta and Dagotto [53]. According to this model, different t_{2g} orbitals are occupied at nearest-neighbor Ru^{+4} sites, resulting in a doubling of the crystal periodicity in all three crystallographic directions. The initial lattice unit cell, corresponding to the lattice parameters a , b , c given in Section 3.1 (color shaded; compare with magnetic cell in Fig. 3.8), is replaced in the orbitally ordered state by a much larger cell (thick lines).

proposed a theoretical model for the orbital order in Ca_2RuO_4 that was consistent with the hole populations suggested by Mizokawa *et al.* [53]. Using a three-orbital Hubbard model tightly coupled to lattice distortions and by means of numerical and mean-field techniques, they suggested an 'antiferro-orbital-ordering' (AFO) pattern, that is, a pattern where *different* t_{2g} orbitals are occupied at nearest-neighbor sites [53]. This means that, for every Ru^{+4} ion with occupied d_{xy} orbital, its nearest neighbors along the x and y axes have instead their d_{zx} or d_{yz} orbitals, respectively, occupied. Thus, instead of having a uniform population of the d_{xy} orbitals, only half of the Ru^{+4} sites have these orbitals occupied. A schematic view of such a configuration is shown in Figure 3.7. It can be seen that the proposed orbital order leads to a doubling of the crystal periodicity in the ab -plane. If the same antiferro-orbital order is assumed along c , then the doubling of the periodicity occurs along that direction, too. Whether this doubling indeed takes place can be experimentally checked with x-ray diffraction and be used as a test of the validity of the model, as will be seen in Section 3.12.

The above conclusions by Hotta and Dagotto were extracted mainly from numerical calculations applied to a small-size (2×2) plaquette cluster. Extending the study to larger lattices was not possible due to technical, computer-related limitations. For this purpose, a mean-field approximation analysis had to be employed as well. The latter can provide qualitatively correct results for the insulating ground

state with static lattice distortions. In this way, up to 8×8 -large clusters could be investigated. Besides the information about the orbital order, the theoretical study resulted in two more significant conclusions: firstly, that both Coulomb and phononic (electron-lattice) interactions are necessary for the stabilization of the antiferromagnetic phase of Ca_2RuO_4 (Section 3.3); and secondly, that the possibility of large magnetoresistance phenomena, reminiscent of the colossal magnetoresistance (CMR) of manganites, may exist for ruthenates, too.

A different orbitally ordered state, that actually combines the above mentioned ferro-orbital- and antiferro-orbital-ordering patterns, was proposed by Lee *et al.* [54]. Based on optical spectroscopy investigations and using for their calculations the multi-orbital Hubbard model, they suggested that the FO and AFO ordering states may coexist in the ground state of Ca_2RuO_4 , making it an interesting system composed of two kinds of Mott insulators. The AFO state was found to be the prevalent phase, consistent with the hole populations suggested by Mizokawa *et al.*, but the FO correlations increase and become important with decreasing temperature. The phase coexistence of these two ordered states was interpreted as the result of two competing tendencies: in the two-dimensional square network at room temperature, the AFO order is preferred, because of the gain in the kinetic energy that it provides via allowing the electron hopping between nearest neighbors, as described by Hotta *et al.*. However, at lower temperatures the distortion of the lattice favors the FO ordering state, consistent with what Anisimov *et al.* claimed. If the energy difference between these two competing phases is small, then it is possible that they coexist in the ground insulating state of the system.

The situation changed again when Jung *et al.* put into question the orbital hole populations suggested by Mizokawa *et al.*, on which the theories of Hotta *et al.* and Lee *et al.* were based [55]. Using, as well, optical spectroscopy measurements and theoretical, first-principles LDA+ U calculations, they showed that the reproduction of the x-ray absorption spectroscopy data of Mizokawa *et al.* can be achieved without necessarily assuming a low-temperature hole population ratio of 0.5 : 1.5 for the d_{xy} and d_{yz}/d_{zx} orbitals. Their study clearly indicated a predominant occupation of d_{xy} at all Ru^{+4} sites, in other words a d_{xy} ferro-orbital (FO) ordering. For the calculation of the projected density of states, a strong mutual mixture of the t_{2g} orbitals due to the rotation and tilting of the RuO_6 octahedra (Section 3.1), as well as due to the extended nature of the $4d$ states, was taken into consideration. The results show among others a substantial suppression of the d_{xy} hole population at low temperatures compared to room temperature, as well as a corresponding enhancement of the d_{yz}, d_{zx} populations, in accordance with the experimentally observed significant changes of the electronic configuration of Ca_2RuO_4 with decreasing temperature.

In the same direction, Fang *et al.* concluded, based as well on LDA+ U calculations, a ferro-orbital ordering of the t_{2g} orbitals with dominant d_{xy} occupation [59]. The stabilization of the d_{xy} orbital state was attributed mainly to three factors:

first and most important, the energy level splitting caused by the two-dimensional crystal field in the layered structures, which had not been taken into consideration in the analysis by Hotta *et al.*; second, the splitting caused by the Jahn-Teller compression of the RuO_6 octahedra upon cooling; and third, the hybridization of the occupied and unoccupied orbitals, which is the origin of the superexchange. The combination of the above factors leads to an estimated total energy splitting of the d_{xy} and d_{yz}/d_{zx} orbitals of approximately 0.3 - 0.4 eV, which is about one tenth of the crystal field splitting Δ between the t_{2g} and e_g states. The suggested orbital configuration is claimed to be in good agreement both with the x-ray absorption spectroscopy (XAS) data by Mizokawa *et al.* [60], and with optical conductivity measurements. Concerning the latter, it is argued that the spectral features which were used by Lee *et al.* to argue against the ferro-orbital order [54], are actually not inconsistent with it, as long as one takes into consideration the orthorhombic distortion and the admixture of the d_{xy} and d_{yz}/d_{zx} states.

The latest information regarding the orbital states in Ca_2RuO_4 was provided by Kubota *et al.* with the use of the newly developed resonant x-ray interference technique at the Ru K absorption edge [61]. The technique is based on the calculation of the interference term obtained by subtracting the fluorescence intensity spectra that correspond to two different polarization angles. In this way it is possible to observe ferro-type orbital ordering, which conventional resonant x-ray scattering (RXS) cannot achieve, since the scattering signal originating from the orbital order cannot be in this case separated from the strong coexisting charge scattering contribution. The main conclusions of the study, based mainly on the azimuthal angle dependence of the interference term, are that a ferro-type order of the Ru^{+4} t_{2g} orbitals occurs in Ca_2RuO_4 and that this order is maintained up to the metal-insulator transition temperature $T_{MI} = 357$ K (Section 3.3). It is further argued that, since the orbital order is present even at room temperature, where the Jahn-Teller distortion is very small [51], this distortion cannot be considered as the main origin of the orbital order.

Despite the numerous studies, both experimental and theoretical, which have concentrated on the determination of the electronic structure of Ca_2RuO_4 , the occupancy of the t_{2g} Ru^{+4} orbitals and the resulting ordering pattern remain open issues. The experimental data that have been available till now have not allowed the definite exclusion of one of the possible orbital configurations, and the proposed theoretical models are to a large degree contradictory to each other. It is noteworthy that not even the propagation vector of the orbital order could be determined. The resonant x-ray diffraction investigation presented in this work provided significant information concerning this question. Based on the resulting data, specific conclusions about the general features of the orbital order pattern could be drawn. The results will be discussed in Section 3.12.

3.3 Magnetic Properties

The material Ca_2RuO_4 is at low temperatures an antiferromagnetic insulator. Its magnetic structure is characterized by two coexisting magnetic modes with different propagation vectors, as powder neutron diffraction investigations have shown [51]. A schematic view of the two magnetic modes in space-group $Pbca$ is shown in Figure 3.8.

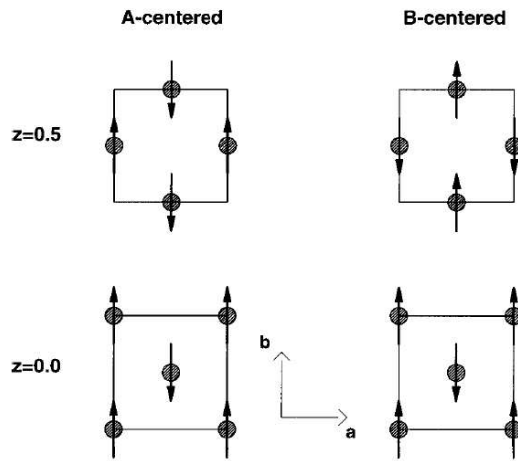


Figure 3.8: Schematic view of the spin arrangement in the Ru^{+4} sublattice in the magnetically ordered phase of Ca_2RuO_4 , as determined with neutron diffraction [51]. Two different antiferromagnetic modes coexist. The so-called A-centered mode (left) is the dominant one in stoichiometric compounds.

In the so-called *A-centered* magnetic mode, the spin of the Ru^{+4} ion located at position $(0\ 0\ 0)$ is aligned parallel to the one at position $(0\ \frac{1}{2}\ \frac{1}{2})$. This magnetic arrangement has propagation vector $(1\ 0\ 0)$ (La_2CuO_4 -type) and sets in below the ordering (Néel) temperature of $T_N = 110$ K. On the contrary, in the *B-centered* magnetic mode, the Ru^{+4} spin at position $(0\ 0\ 0)$ is antiparallel to the one at $(0\ \frac{1}{2}\ \frac{1}{2})$ and parallel, instead, to the spin at site $(\frac{1}{2}\ 0\ \frac{1}{2})$. This magnetic arrangement has propagation vector $(0\ 1\ 0)$ (La_2NiO_4 -type) and ordering temperature $T_N^B = 150$ K. The temperature dependence of the magnetic moment per Ru ion for the two magnetic modes, as determined by refinement based on the neutron diffraction data [51], is shown in Figure 3.9. The ordered moment of the B-centered phase saturates at the temperature where the A-centered mode sets in. In the stoichiometric version of Ca_2RuO_4 , on which the present work concentrates, the A-centered mode is predominant and can be considered as the main contribution to the antiferromagnetic ordering. In high-quality single crystals the dominance of the A-centered mode is even more distinct than in powder samples and no traces of the B-centered mode

can be usually detected, even with the particularly sensitive μSR technique (Section 3.10).

The value of the antiferromagnetic ordering temperature is confirmed by dc magnetization measurements [62, 63]. The temperature dependence of the magnetic susceptibility $\chi = M/H$ for applied magnetic field $H = 10$ kG is shown in Figure 3.10. The main feature of the susceptibility data is the sharp increase of χ observed at 113 K when the applied magnetic field is aligned along the a or b crystallographic directions (in $Pbca$ notation), denoting the occurrence of the magnetic transition. The Néel temperature determined in this way is very close to the value found with neutrons.

Of particular interest for our investigations is the broad peak observed in the temperature dependence of the magnetic susceptibility around 260 K when the applied field \mathbf{H} is aligned along \mathbf{c} . This feature indicates the existence of paramagnetic fluctuations occurring below that temperature, the exact origin of which has not been satisfactorily explained to date. Fukazawa *et al.* suggested that the anomaly expresses the influence on the magnetic anisotropy of the changes in the orbital and spin angular momenta induced by the distortion of the RuO_6 octahedra [63]. The x-ray study presented in this work provided significant new information concerning this issue, which will be discussed in Section 3.12.

For both magnetic modes, the magnetic moment $\boldsymbol{\mu}$ of the Ru^{+4} ions is aligned along the crystallographic b -direction. This is concluded both by the neutron diffraction investigations, via the comparison of the intensities of different magnetic reflections, and by the magnetic susceptibility measurements, via the comparison of the temperature dependences obtained for different directions of the applied magnetic field. The magnetization measurements indicate in addition a canting of the antiferromagnetic order as a result of the tilting and rotation of the RuO_6 octahedra. Such a canting could give rise to a non-zero ferromagnetic moment along $[1\ 0\ 0]$ or $[0\ 0\ 1]$ [62]. The estimated magnitude of the magnetic moment is $\mu = 1.3\ \mu_B$ [51].

The magnetic transition is accompanied by small anomalies observed in the temperature dependence of the lattice parameters near T_N (Figure 3.3). The distortion of the RuO_6 octahedra affects the antiferromagnetic ordering, because the lengths and angles of the Ru-O-Ru bonds that connect neighboring Ru sites influence the in-plane superexchange constant which dominates the magnetic order.

3.4 Transport Properties and the Metal-Insulator Transition

The insulating properties of Ca_2RuO_4 around and below room temperature were asserted already in the first report on the synthesis of the compound [64] and confirmed

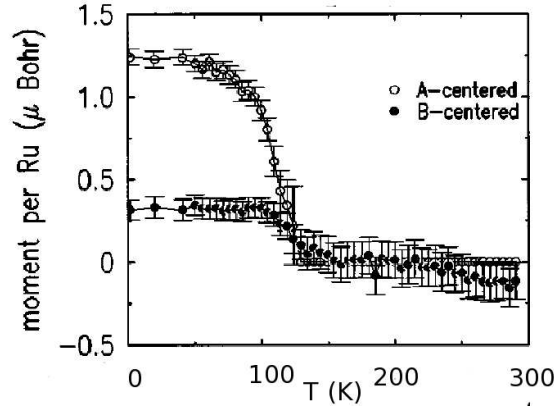


Figure 3.9: Variation with temperature of the magnetic moment per Ru^{+4} ion for the two different magnetic modes shown in Fig. 3.8, as determined by refinement based on neutron diffraction measurements [51]. The ordered moment of the B-centered phase saturates at the temperature where the A-centered phase sets in.

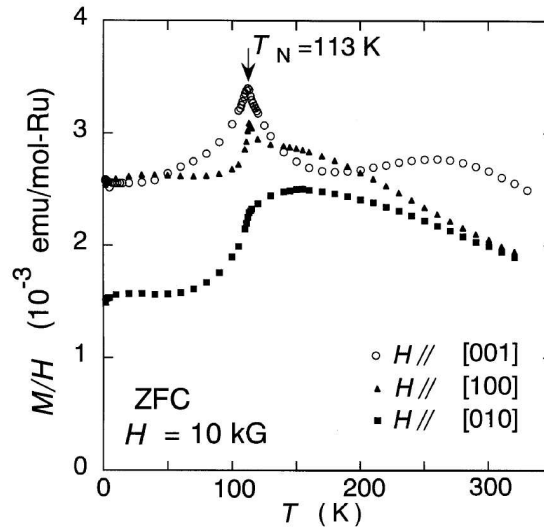


Figure 3.10: Temperature dependence of the magnetic susceptibility $\chi = M/H$ of Ca_2RuO_4 for magnetic field 10 kG applied along the three crystallographic directions, as shown in the plot [62]. Besides the sharp peak denoting the magnetic transition at $T_N = 110$ K, an additional broad feature is observed around 260 K when $\mathbf{H} // c$.

later by further transport studies [65]. The electric resistivity ρ in the ab -plane shows a non-metallic behavior ($\frac{d\rho}{dT} < 0$) in the whole temperature range below 300 K. The temperature dependence of ρ is shown in Figure 3.11. The resistivity increases by eight orders of magnitude with decreasing temperature from 300 K down to approx-

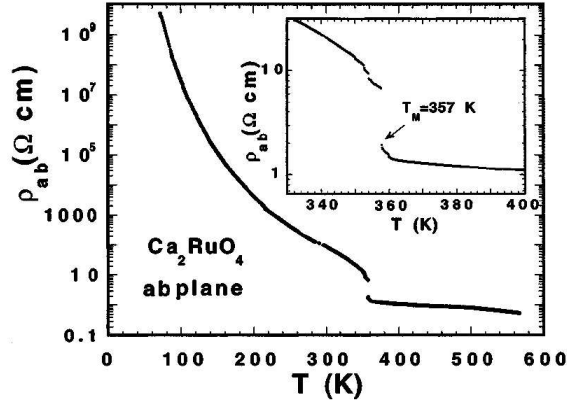


Figure 3.11: Variation with temperature of the electrical resistivity in the ab -plane of Ca_2RuO_4 [66]. The inset shows a detail of the temperature dependence near the metal-insulator transition.

imately 70 K, where it becomes too high to be measured with most electrometers due to saturation effects. No anomaly is observed either in resistivity or its temperature derivative at the Néel temperature $T_N = 110$ K. This indicates that the superexchange or other mechanism which couples the Ru magnetic moments does not involve conduction electrons.

The material undergoes a first-order phase transition at ambient pressure from the low-temperature orthorhombic Mott insulating phase to a high-temperature tetragonal metallic phase at $T_{MI} = 357$ K [66]. The abrupt drop of the resistivity by a factor of 3.5, denoting the occurrence of the metal-insulator transition, can be seen in the diagram of Figure 3.11. Magnetization measurements have shown that Ca_2RuO_4 remains paramagnetic both below and above this phase transition. Despite a small yet well defined anomaly observed in the temperature dependence of the magnetic susceptibility at T_{MI} , neither the hysteresis nor the negative curvature of the isothermal magnetization that would be expected for a ferromagnet below T_{MI} are observed. The phase transition is accompanied by substantial structural distortions, which result in significant, discontinuous changes in all structural parameters of the material, as already discussed in Section 3.1.

The first-order nature of the metal-insulator transition is confirmed among others by the large hysteresis of about 20 K observed in measurements of the lattice volume with neutron diffraction [56]. As far as the origin of the transition is concerned, this has been attributed to the reduction of the elastic energy of the system with increasing temperature and the change of the balance between it and the electronic coherence energy [66]. At temperatures below T_{MI} the gain in elastic energy due to the tilting and rotation of the octahedra is larger than the loss in the electronic

coherence energy for having the system in the insulating phase. However, as temperature increases, the thermal vibrations reduce the distortion of the RuO_6 octahedra, the tilting angle θ becomes smaller, and the electronic bandwidth $W \propto \cos(\theta/2)$ increases. Above T_{MI} the gain in elastic energy becomes smaller than the loss in electronic energy, and the stabilization of a metallic state becomes energetically favorable.

3.5 Experimental

The magnetic properties and orbital order in Ca_2RuO_4 were investigated with resonant x-ray diffraction at the L_{II} and L_{III} absorption edges of ruthenium (Ru), i.e. at x-ray energies of 2.968 keV and 2.838 keV, respectively. The measurements were carried out on single crystals of the compound. The work was the first reported investigation of a $4d$ electron material with resonant x-ray diffraction [45]. The results are significant for two reasons:

First, they provide new information on the electronic properties of Ca_2RuO_4 , far beyond what powder neutron diffraction and magnetization or transport measurements had revealed to date. Of particular importance is the observation of a novel orbital ordering phase transition at the wave-vector which characterizes the low-temperature antiferromagnetic phase. The data contribute to the long-lasting discussion about the orbitally ordered state in the system, by showing which of the so-far suggested theoretical models are in the right direction and which, on the contrary, are most probably not adequate for its description. The precise determination of the wave-vector that characterizes the t_{2g} orbital order in the Ru^{+4} subsystem certainly belongs to the most important findings of the investigation.

Secondly, our results demonstrate the great potential of resonant x-ray diffraction at the L -absorption edges of transition metals also for $4d$ electron compounds. It was shown that, despite the difficulties related to the inconvenient energy range, the technique is an excellent probe for magnetic and orbital ordering investigations in these materials, providing resonant enhancements of a factor of five hundred at least. Especially in cases where only very small single crystals are available as samples, the technique offers unique advantages over neutron scattering and other methods that require large sample volumes.

3.5.1 Samples

The investigated Ca_2RuO_4 samples were single crystals grown by the floating-zone method, employing an infrared image furnace, by H. Fukazawa *et al.* at the Department of Physics at Kyoto University [62, 63]. The feed rod used in the growing procedure was synthesized by mixing CaCO_3 and RuO_2 powders with a molar ratio

of 2 : 1.3 at a temperature of 1000°C in air atmosphere. Four samples were used, in total, for the investigations presented in this work: two aligned along the (1 0 0) reciprocal space direction, one along (0 1 1), and one along (1 1 0).

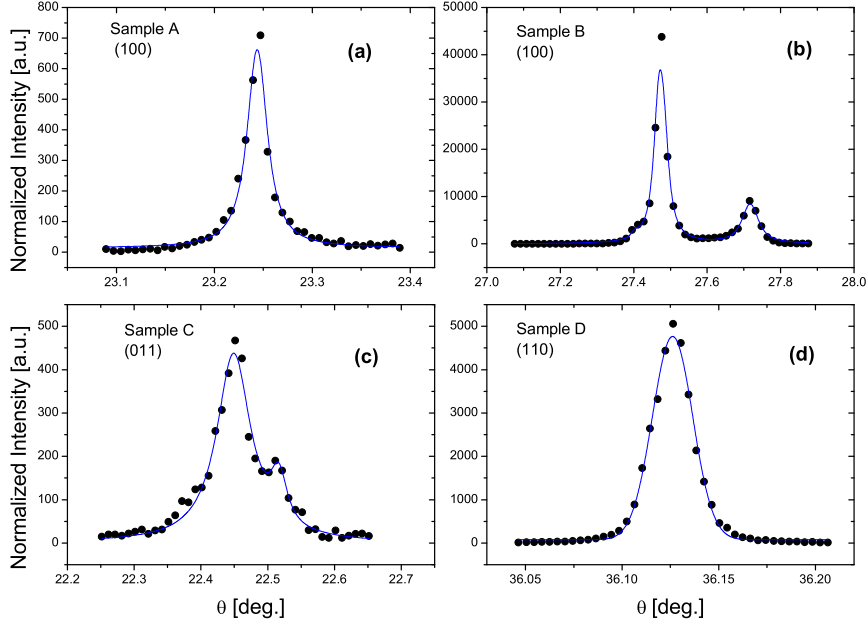


Figure 3.12: Rocking curves of the four Ca_2RuO_4 single crystals used in our x-ray diffraction investigations. The presented θ -scans were carried out at the Ru L_{II} absorption edge, at low temperatures, around the reciprocal space positions indicated on the plots. The lineshape, width and height of the peaks provide information about the quality of the investigated samples. The solid lines are the results of fitting of the measured intensities with Lorentzian (a - c) or Gaussian (d) profiles.

The (1 0 0)-aligned samples, named in the following A and B, had sizes of approximately $500 \times 500 \times 50 \mu\text{m}^3$ and $900 \times 600 \times 100 \mu\text{m}^3$, respectively. Sample A provided at the (1 0 0) magnetic reflection a maximum intensity of approximately 800 counts per second (cps) at the L_{II} edge at low temperatures. The same intensity was obtained in two different, subsequent experiments. The full width at half maximum (FWHM) of the corresponding rocking-curve (θ -scan) is of the order of 0.022° , as seen in Figure 3.12(a). The sharp, single peak in the θ -scan indicates that the crystal is of good quality, with a narrow mosaic width and an apparently single-domain structure.

Sample B provided a much stronger scattering signal. At the first experiment carried out on this sample, a huge magnetic intensity of up to 52000 cps at the L_{II} edge was measured. This corresponds to more than one quarter of the intensity obtained at the main Bragg (2 0 0) peak with the third harmonic component of the

diffracted beam (~ 200000 cps). The full width at half maximum of the rocking curve was of the order of 0.031° , slightly larger than that of sample A (Figure 3.12(b)). The main characteristic of sample B is the fact that it consists of several grains, of different sizes and orientations, each of which gives a scattering signal of different intensity. The double-peak structure in the rocking curve of Figure 3.12(b) is due to the contribution of two such grains. As long as the x-ray beam keeps being scattered by a particular crystallite of the sample, good quality scans can be carried out, thanks to the large scattering intensity and the small mosaic distribution of every grain. However, even the slightest movement of either the x-ray beam or the sample results in large changes in the scattered intensity due to 'hopping' of the beam to neighboring grains. The scattering intensity is, thus, strongly dependent on the region of the sample which scatters the beam. This feature affected the investigations in the following way: first, the azimuthal dependence of the scattered intensity was difficult to determine, as will be discussed in Section 3.6.4, since the intensity fluctuations due to the grain hopping were often larger than the intrinsic variation with azimuth of the resonant scattering amplitude. And second, the huge magnetic intensity achieved in the first experiment, as mentioned above, could not be recovered in a later experiment carried out on the same sample, probably because the scattering area was then different. In the latter experiment, the scattered intensity obtained was of the order of 10000 cps, which is still a very large signal, but a factor of 5 smaller than the intensity in the first experiment. The full width at half maximum of the rocking curve remained practically the same (0.027°).

The sample aligned along the (0 1 1) direction, named in the following sample C, was a little smaller in size, with approximate dimensions $800 \times 500 \times 50 \mu\text{m}^3$. The θ -scan performed around the (0 1 1) magnetic reflection (Figure 3.12(c)) reveals the existence of more than one domain in this crystal, too. However, the larger width (FWHM) of the rocking curve (of the order of 0.060°) makes the measurements less sensitive to slight angular movements of the sample. The maximum scattering intensity obtained on the magnetic peak at the L_{II} edge and at low temperatures was a little lower than 500 cps.

Finally, sample D, which was aligned along (1 1 0), had almost the same size as sample B, and was characterized by a good mosaicity, with a full width at half maximum of only 0.021° , and an apparently single-domain structure (Figure 3.12(d)). The maximum scattering intensity on the (1 1 0) peak was of the order of 5100 cps.

Selected photographs of one of the investigated samples, taken with the use of microscope, are shown in Figure 3.13.

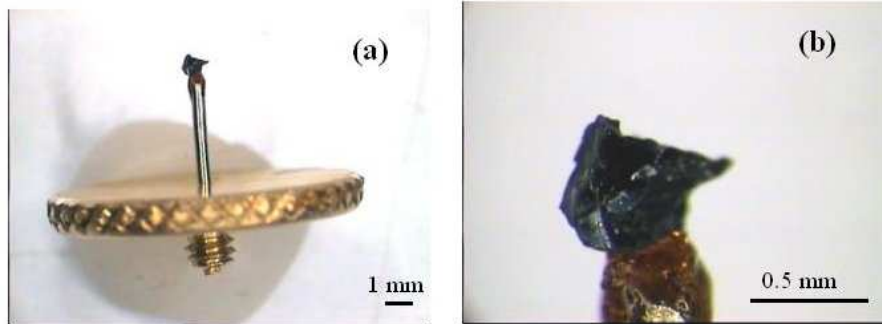


Figure 3.13: Views of Sample A under the microscope. In (a), the crystal is shown glued on the tip of the sample holder used in the diffraction experiments. In (b), a closer view of the crystal reveals details of the physical appearance of the sample.

3.5.2 Experimental Setup

Synchrotron Beamline

The resonant x-ray diffraction investigations described in Chapters 3 and 4 of the present thesis were carried out at beamline 4ID-D of the Advanced Photon Source (APS) at Argonne National Laboratory (USA). The insertion device utilized as source by the beamline is a 72-pole undulator (APS standard undulator A) with a nominal minimum gap of 11 mm. The beamline was originally designed for hard x-ray operations in the energy range between 3 keV and 50 keV. Special modifications had to be applied on the vacuum chamber of the undulator to allow the further closing of the gap below 11 mm. In this way, energies as low as 2.8 keV could be reached, as needed for performing resonant experiments at the Ru L-absorption edges.

A schematic view of the configuration inside the 4ID-D experimental station (experimental hutch) is shown in Figure 3.14. Parts of the setup can be seen in the photographs of Figures 3.15, 3.16. Although the setup was to some degree optimized over the period of 2.5 years covered by the investigations, the described configuration is very close to what was used for the large majority of the measurements. The beamline is run by Sun workstations (UNIX/Solaris) and VME-based electronics. The VME-based equipment is controlled by EPICS via the software client SPEC.

The x-ray beam produced at the undulator is monochromatized in a separate station (station B) before entering the experimental hutch. A KOHZU system consisting of two Si(1 1 1) crystals is used as monochromator. The monochromatic beam is focussed at a toroidal SiO_2 mirror (vertically bent horizontal cylinder) mounted immediately after the monochromator. A flat Pd-coated SiO_2 mirror is also used for suppressing the high-order harmonics of the beam (with energies above approx-

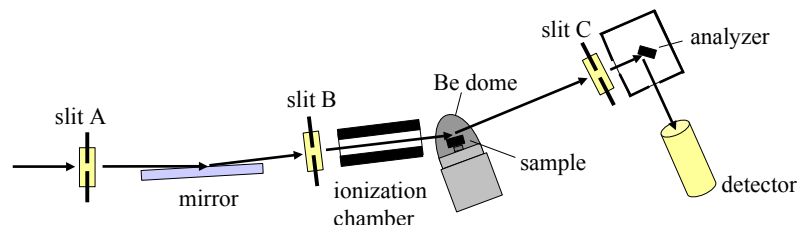


Figure 3.14: Schematic view of the experimental setup inside the experimental station. The flight-path of the incoming beam, which starts at the entrance slit A and ends just after the ionization chamber, is kept under slight He overpressure. The sample environment (below the Be dome) and the flight-path of the scattered beam, including the analyzer chamber, are under vacuum. The detector is illustrated in $\sigma \rightarrow \sigma'$ polarization geometry. In $\sigma \rightarrow \pi'$ it would be pointing out of the page (see Figures 2.3, 3.17).

imately 12 keV). Through a 160 μm -thick beryllium (Be) window the beam enters the experimental station. The size of the beam at the entrance of the station (slit A), as determined by the focussing mirror, was in all our experiments of the order of $200 \mu\text{m} \times 100 \mu\text{m}$. An 8-circle HUBER diffractometer used in vertical scattering geometry is available in the experimental station. Besides the flat SiO_2 mirror used in the monochromator hutch for suppressing the high-energy harmonics, a second, smaller mirror of the same type is also used in the experimental hutch for further suppressing the harmonics of relatively low energies (below approximately 12 keV). Passing through an ionization chamber, used to monitor the incoming x-ray intensity, the beam reaches the sample position at the center of the diffractometer. A slit set just before the ionization chamber (slit B) cuts out background contributions and ensures that a well-defined beam is diffracted by the sample.

The whole flight-path of the incoming beam is kept under He atmosphere in slight overpressure conditions, with continuous helium gas flow from one end of the path to the other. The use of helium is necessary, because low-energy x-rays are strongly absorbed by air (attenuation length at 3 keV: $l \approx 5.3 \text{ cm}$), thus the incoming intensity would drop to zero over the length of the flight-path if this were kept instead under air atmosphere. Some kind of gas does have to be present for the operation of the ionization chamber. A 50 μm -thick Be window closes the flight-path very close to the sample position. Splitting of the flight-path into more than one part with different filling atmospheres (e.g. He in the ionization chamber and vacuum in the rest) would require the use of more Be windows, which could not be afforded for absorption reasons.

The beam which is diffracted by the sample enters through another 50 μm -thick Be window into a second flight-path, at the end of which the detector is mounted.

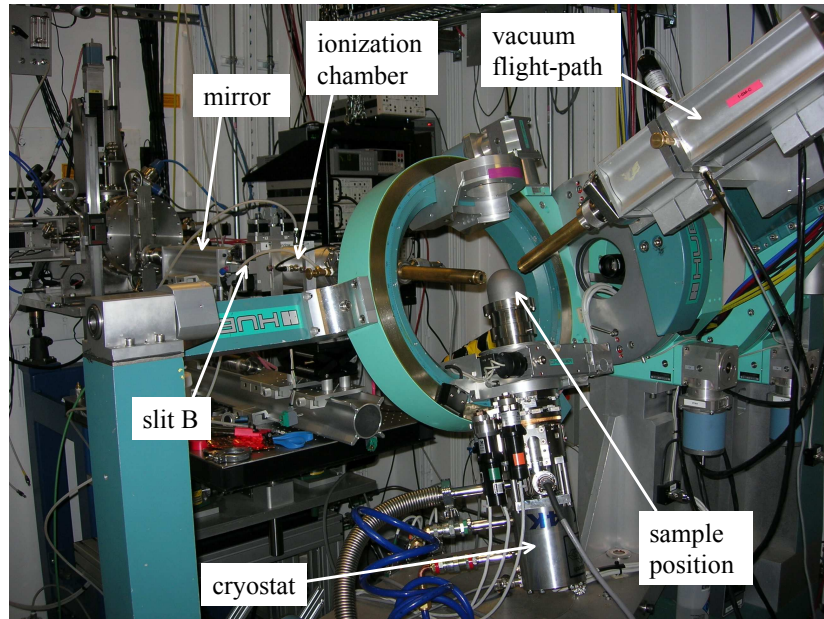


Figure 3.15: Photograph of the diffractometer inside the 4ID-D experimental hutch at APS, at diffracting position. The x-ray beam enters the hutch on the left side of the photograph. Through a He-filled flight-path, it reaches the sample, located beneath a Be-cap, under vacuum and low-temperature conditions, at the end of the cryostat's cold finger. The intensity of the diffracted beam is measured with a scintillation detector (not seen) mounted at the end of a vacuum flight-path, on the right-hand side of the picture.

This second flight-path is kept constantly under vacuum. A slit system (slit C) is mounted immediately before the detector, mainly for suppressing the background. An OXFORD *Cyberstar* NaI scintillation detector was used. The detector was mounted directly onto the end of the vacuum flight-path, so that no Be window was needed at the end of the path, in addition to the one of the detector itself. The detector window has a thickness of $200\ \mu\text{m}$.

For performing polarization analysis of the diffracted beam, an in-vacuum polarization analyzer can be mounted between the last slit (slit C) and the detector. A perfect Si(1 1 1) crystal ($\text{FWHM} < 0.01^\circ$) was used as analyzer in our measurements, providing a scattering angle of 41.8° at the Ru L_{II} absorption edge. The chamber that houses the analyzer has two openings at 90° from each other, through which the beam passes, before and after the scattering by the analyzer. The whole chamber can be rotated around an axis parallel to the beam incident on the analyzer. Depending on whether the detector is parallel or perpendicular to the diffraction plane of the sample, only the polarization component of the beam which is perpendicular (σ') or parallel (π'), respectively, to the diffraction plane is detected (Figure 3.17).

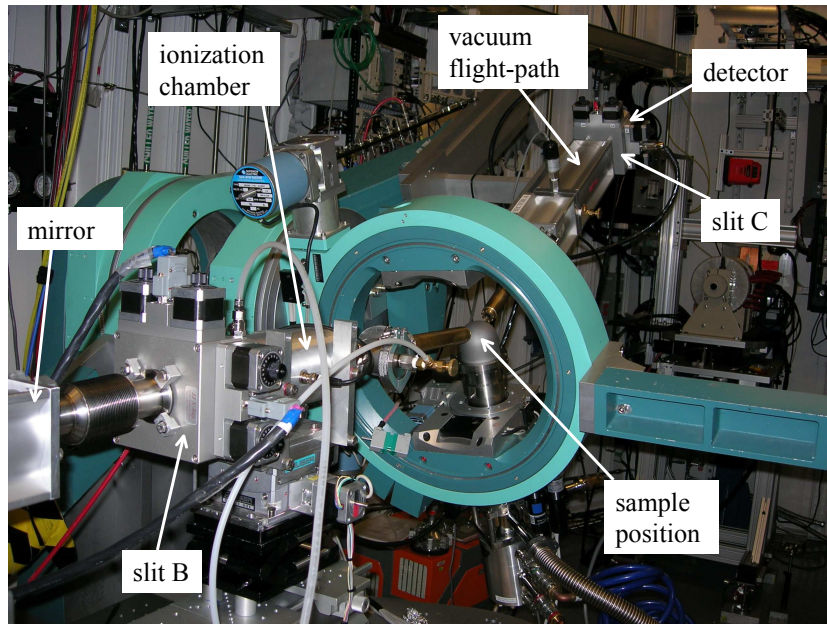


Figure 3.16: Opposite view of the setup seen in Figure 3.15. Parts of the He-filled flight-path of the incoming beam can be seen in more detail. The detector is mounted at the end of the vacuum flight-path, on the right-hand side of the picture, behind slit system C.

The deviation of the analyzer's scattering angle from the ideal value of 45° results in a 'contamination' of every polarization channel with a small contribution from the complementary one. This, however, causes no problems and the separation of the two components is good enough, as will be seen, for example, in Section 3.6.3.

Sample Environment

The holder bearing the investigated sample is screwed onto a small STOE goniometer head, which is mounted on the end of the cold finger of a closed-cycle (Displex) cryostat capable of reaching temperatures between 6 K and 340 K. In one experiment, a high-temperature cryostat capable of reaching temperatures up to 800 K was used instead. The cryostat is mounted on a motorized x-y-z translation system on the ϕ -circle of the diffractometer.

The sample position is covered by a dome-shaped beryllium cap (thickness: $500 \mu\text{m}$), inside which high vacuum is achieved with the use of a turbo pump (Figure 3.18). Normally, besides the vacuum shield, an additional inner beryllium shield (thickness: $250 \mu\text{m}$) is mounted around the sample, for reducing the thermal losses from the sample environment and enabling the access of temperatures as low as the nominal base temperature of the cryostat ($\approx 6 \text{ K}$). In our experiments, however,

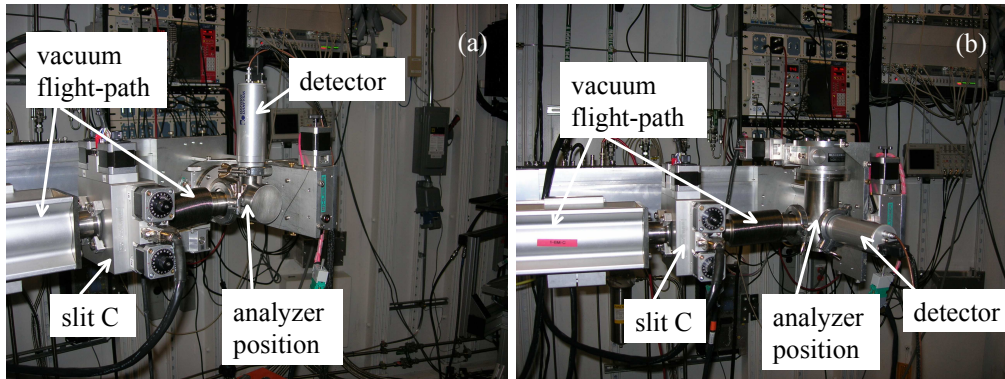


Figure 3.17: Detail of the experimental setup, with the polarization analyzer mounted before the detector. The analyzer crystal is housed in a vacuum chamber, which can be rotated around an axis, so that the detector is either in the diffraction plane (a) or perpendicular to it (b). In this way, only the beam component with polarization perpendicular (σ') or parallel (π'), respectively, to the diffraction plane can be detected.

the x-rays are, due to their low energy, strongly absorbed even by beryllium. The inner shield would cause an attenuation of the beam by a factor of 3. Since the reflections we want to investigate are very weak, such an intensity loss could not be afforded. For this reason, no inner thermal shield was used in the setup. The price that had to be paid for minimizing the absorption was the inability to reach very low temperatures. In order to reduce the thermal losses in the sample environment, a thin copper- or aluminum- foil was mounted as thermal shield around the goniometer head (Figure 3.19). Its height extended up to just below the sample position, so that the x-ray beam was not blocked. Furthermore, for improving the thermal conduction between the cold finger and the sample, long-shaped pieces of copper foil were glued (with silver paste) between the copper base at the bottom of the goniometer head, close to the sensor, and the sample holder, a few millimeters away from the crystal. Despite these measures, temperatures below approximately 30 K (at the sample sensor) were never reached in the experiments.

The holders on which the investigated samples were mounted were 'home-made' components designed by H. Klann and manufactured at the machine-shop of the Max-Planck-Institute in Stuttgart. They consist of a metal plate on which a vertical rod is attached. Initially the plate was made of brass and the rod of steel, but both were replaced on later-made holders by copper pieces, for having better thermal conduction to the sample. The sample was glued on the tip of the holder's rod using GE-varnish, an adhesive which is appropriate for use at low temperatures and in vacuum, providing good thermal contact.

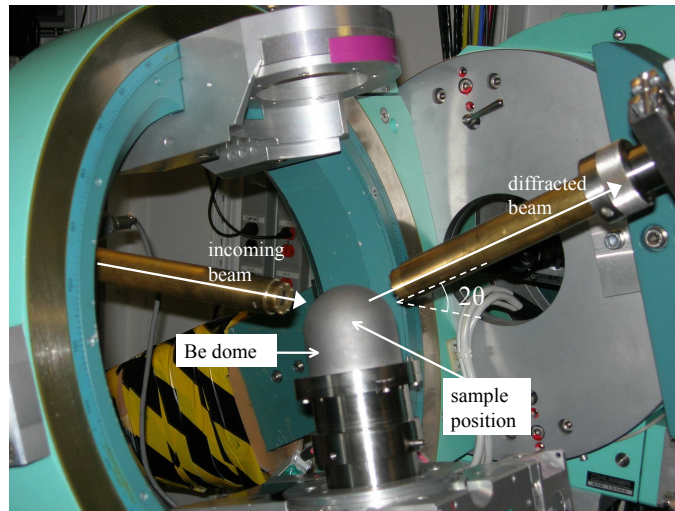


Figure 3.18: Detail of the experimental setup around the sample position. The sample is glued on the tip of a holder, which is screwed on the end of the cryostat's cold finger, and is surrounded by a beryllium dome, beneath which high vacuum is achieved. A second shield, normally used for suppressing thermal losses, is omitted, for minimizing the absorption of the x-rays.

Temperature Reading

A significant amount of information about the electronic properties of Ca_2RuO_4 is obtained in the following via the investigation of the temperature dependence of the scattered intensity. It is therefore quite important to know how reliably and accurately the temperature of the diffracting sample can be determined in every case, so that the scientific significance of possible anomalies or other features in the obtained data can be judged. For this reason, it is essential at this point to make a few comments concerning the type of temperature sensors which were used in our experiments and the reliability of their readings.

In most of the experiments where Ca_2RuO_4 crystals were investigated, two Si diodes were used as temperature sensors, one mounted on the cryostat's cold finger close to the heater (control sensor) and one as close as possible to the sample position (sample sensor). The sample sensor provides the temperature of the sample. It is this value that appears as temperature in all the relevant plots in the following. The control sensor measures the temperature in the heater's direct environment. Based on this, the temperature controller determines the applied heating power via a PID algorithm: for every desired input value R (set point) and actual output Y (temperature measured by the control sensor), the error signal $e = R - Y$, as well as its derivative and integral, are calculated by the controller. The signal u sent then

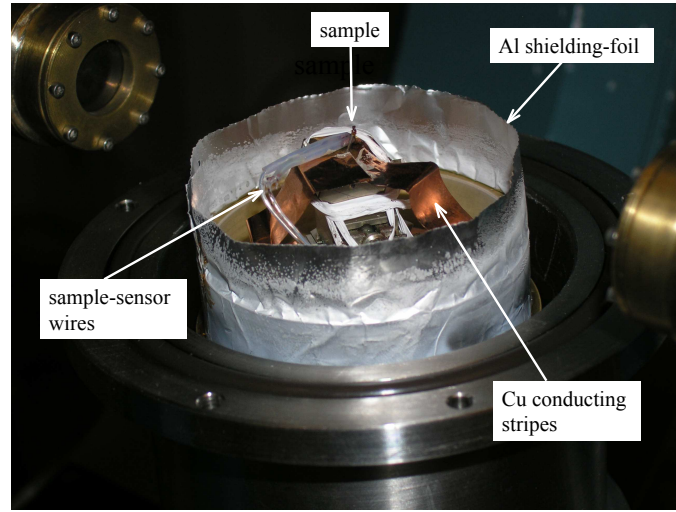


Figure 3.19: Detail of the experimental setup around the sample position, without the beryllium dome. An aluminum foil is mounted around the goniometer head as thermal shield. Copper stripes improve the thermal conduction between the sample holder and the plate on which the goniometer head is screwed.

by the controller is equal to:

$$u = K_P e + K_I \int e dt + K_D \frac{de}{dt} \quad (3.1)$$

where K_P , K_I , K_D are the proportional, integral and derivative gains (P, I, D values), respectively. The new output Y is sent back to the controller, which calculates the new error e , and a new signal u is sent. The process goes on until the desired value R is reached.

Due to the the low thermal conductivity of the goniometer head, on which the sample was mounted, a certain amount of time was needed, after the control sensor had reached the set-point, for the sample temperature to equilibrate at this value, too. For this reason, when carrying out temperature dependence investigations, a long enough waiting time had always to be considered after every change of the temperature set-point. This was typically of the order of 10 minutes for a temperature change of 10 K. For positive temperature changes (warming-up) the needed time was shorter at low temperatures and longer at higher temperatures. Of course the exact time for equilibration depended in every case on the particular experimental conditions.

In the experiment where the high-temperature Displex cryostat was used, an additional source of uncertainty in the temperature reading has to be considered. The high-temperature cryostat has four instead of two temperature sensors available

in total for covering the whole temperature range from 10 K to 800 K where it can be operated. The available sensors are: 1) a Si diode mounted near the base of the cold finger, close to the heater, which operated satisfactorily only at temperatures below 100 K, 2) a platinum (Pt) sensor mounted relatively (but not quite) close to the sample, at the bottom of the goniometer head, which operated well at temperatures above approximately 100 K, and 3) two thermocouples mounted close to the base of the cold finger. One of them provided reliable temperature readings in the largest part of the temperature range investigated, though the errors became larger at very low temperatures. This is the sensor that was used as control sensor in our experiment for the temperature range between 10 K and 320 K. The poor accuracy at low temperatures of the Pt sensor, which was the only one close to the sample, forced us to use two different sensors for determining the sample temperature. Above 100 K, the reading of the Pt sensor was used. Below 100 K, the temperature given by the control sensor (thermocouple) was used instead, after normalizing it to the reading of the Pt sensor (unfortunately no perfect agreement of the readings of the two sensors was achieved in the changeover regime). The unavoidable switch from one sensor to the other around 100 K and the lack of real overlap between the readings of the two sensors, obviously results in a decreased accuracy of the sample temperature determination in this regime. This should be taken into consideration when evaluating the experimental data (see, for example, Section 3.6.3). In all other experiments, where usual Displex cryostats were used and a single sensor always provided the sample temperature, such problems did not occur.

Another important issue is how close the temperature given by the sample sensor is to the actual temperature of the diffracting crystal. This depends mainly on how close to the crystal the sample sensor can be actually mounted. As explained previously, in order to minimize the absorption of the x-ray beam and obtain the strongest possible scattering signal, no inner beryllium dome was used as thermal shield around the sample position in any of the experiments. Because of the resulting thermal losses, the actual temperature at the sample position can be significantly higher than the nominal minimum temperature reached by the cryostat and a substantial temperature gradient may develop along the cold finger near the sample position, especially at very low temperatures. Thus if the sample sensor is mounted relatively far away from the crystal, the measured temperature may be different from the actual one of the sample. During the first experiments, the sample sensor was mounted on the copper base on which the whole goniometer head is mounted. Due to the rather poor thermal conductivity of the goniometer head, temperature deviations between sample and sensor were present. These deviations could be almost eliminated (at least above approximately 30 K) by using the conducting copper bands between the copper base and the sample holder, as well as the shielding foil around the sample position, as described above. In the later experiments the setup was further optimized, by mounting the sample sensor directly onto the sample

holder, just a couple of millimeters away from the crystal.

The above difficulties give an idea of how non-trivial an experiment can be, which is carried out at low temperatures at an energy where x-rays are strongly absorbed. Independent of that, it has to be clearly stated, that these difficulties have influenced absolutely none of the major conclusions drawn in this work. Only for the evaluation of minor details of the plots it is necessary in some cases to know the limits of our technique. The correctness and accuracy of the sample temperature determination in the whole temperature range above 40 K is proved, among others, by the observation of the magnetic transition exactly at the temperature where this was expected based on older neutron diffraction investigations (110 K) (Section 3.6.3).

Laboratory Setup

For the crystallographic characterization, the quality verification and the pre-alignment of the samples investigated in the present work, the experimental setup of the x-ray diffraction laboratory of Prof. Keimer's department at the Max-Planck-Institute for Solid State Research was used. The availability of this setup was of great significance for the success of the investigations carried out at the synchrotron source. Every synchrotron experiment was preceded by a preparation phase, during which the best available crystals were chosen as samples and eventually aligned along the exact crystallographic direction that was of interest for the experiment. In this way, a large amount of valuable beam-time could be saved at the synchrotron. In some cases, where the selection of good quality crystals of the right growing phase demanded a lot of attempts (e.g. in $\text{RuSr}_2\text{GdCu}_2\text{O}_8$, Section 4.3.1), or where the determination of the crystallographic directions and the alignment of one of them along the scattering vector was not trivial (e.g. due to the co-existence of more than one domains and/or the very small size of the crystal), the synchrotron experiments would have been practically impossible without the infrastructure of the x-ray laboratory.

The main available x-ray source in the laboratory is a RIGAKU molybdenum (Mo) rotating anode. The maximum power of the source is 4.5 kW. The source generates x-rays at the Mo $K\alpha_1$, $K\alpha_2$ and $K\beta$ emission lines, which correspond to energies of 17.479 keV, 17.374 keV and 19.608 keV, i.e. to wavelengths of 0.7093 Å, 0.7136 Å and 0.6323 Å, respectively. For the production of x-rays, electrons emitted thermionically by a cathode filament are accelerated by a high-voltage electric field (≈ 54 kV). The electron beam impinges onto the anode, a cylinder with a Mo-covered surface, which rotates around its axis. By excitation and subsequent decay of the anode's Mo ions, x-rays with the above characteristic energies are generated, exactly like in conventional x-ray tubes. By the rotation of the anode around its axis, the heat produced due to the conversion of a part of the accelerated electrons'

kinetic energy to thermal energy, is not concentrated only in the area covered by the cross-section of the electron beam, but can be spread over the whole surface of the anode. In this way, the overheating of the anode and the resulting damage is avoided and higher x-ray beam intensities can be achieved.

The produced x-ray beam is monochromatized and focussed with the use of two multilayer monochromators. The first of them focusses the beam vertically and the second horizontally. Through the scattering on the multilayers, the K_β component of the beam is spatially separated from $K\alpha_1$, $K\alpha_2$ (due to the different scattering angles) and eventually filtered by a slit system at the entrance of the experimental hut. Thus the beam reaching the sample has only K_α energy components. A 4-circle HUBER diffractometer, similar to the one used at the synchrotron source, is available in the experimental hut. It is used in horizontal scattering geometry. For low-temperature measurements, a closed cycle (Displex) cryostat can be mounted on the diffractometer, capable of reaching temperatures down to 6 K. The temperature is stabilized using a LAKESHORE 330 temperature controller.

Two different kinds of detectors are available for measuring the scattered intensity. Besides a scintillation counter, similar to the ones used in the synchrotron investigations, a BRUKER SMART-1000 charged-coupled device (CCD) is also used. The CCD camera allows, thanks to its large detection area, the detection of a reflection even if the Bragg scattering condition for the 2θ angle is not exactly satisfied. Furthermore, it allows the simultaneous detection of more than one reflection which are relatively close to each other in the reciprocal space. In this way, it makes it easier to determine the crystallographic directions of a completely unknown crystal and to align it along a particular direction, by performing a refinement (Section 2.5). A large number of reflections are collected by rotating the sample in the beam while keeping the detector at a fixed position. The least squares fitting that is required is performed with the help of an appropriate software program (SMART). From the relative distances of the observed reflections and the comparison of them with the ones expected for a particular space-group, the vectors \mathbf{a} , \mathbf{b} , \mathbf{c} defining the primitive unit cell of the crystal are determined. Once the lattice parameters and crystallographic directions are roughly known, the scintillation detector can be used for obtaining more accurate results (rocking curve widths, precise values for the lattice constants etc).

The movements of the diffractometer motors are controlled by two different software environments. When the CCD camera is used, the system is operated via the data acquisition program SMART, which runs under Windows. When the scintillation detector is instead mounted, the Linux program SPEC is utilized.

3.6 Investigations at the (1 0 0) Reciprocal Space Position

As mentioned in Section 3.3, the A-centered magnetic arrangement of the Ru^{+4} spins, which is the dominant one in stoichiometric Ca_2RuO_4 , has a characteristic propagation vector (1 0 0). In a diffraction experiment, this spin arrangement gives rise to a magnetic reflection at position (1 0 0) of the reciprocal space at temperatures below the Néel temperature $T_N = 110$ K. The magnetic signal is strongly enhanced when the energy of the x-ray beam lies close to an absorption edge of the magnetic ion. The (1 0 0) position is structurally forbidden, i.e. the structure factor of charge Bragg scattering is equal to zero there. Resonant scattering of magnetic origin can be thus easily investigated at this position, without any disturbing charge Bragg contribution. For this reason the position was selected as a starting point for our investigations.

3.6.1 Alignment

As already explained, for the determination of the full orientation matrix of a sample, the lattice parameters of which are already known, at least two main Bragg reflections with non-parallel wave-vectors are needed (Section 2.5). Nevertheless, if for the needs of the experiment only scans along the scattering vector have to be carried out, then the observation of a single reflection along the direction of this vector is sufficient for the establishment of the orientation.

This is the case in the investigation of the (1 0 0) magnetic reflection. For performing h -scans around (1 0 0), the (h 0 0) direction needs to be determined, for which the observation of one main Bragg reflection along this direction is necessary. Due to the low energy of the x-ray beam, only a small fraction of the reciprocal space is accessible. The scattering angles at the fundamental x-ray energy, even for reflections with small Miller indices, are so large, that they cannot be reached by the diffractometer. For instance, the scattering angle θ_{200} for the (2 0 0) reflection, the very first Bragg reflection with non-zero structure factor, is equal to 50.54° at the Ru L_{II} absorption edge (energy: $E = 2.968$ keV, wavelength: $\lambda = 4.177$ Å):

$$2d_{200} \sin \theta_{200} = \lambda \Rightarrow \sin \theta_{200} = \frac{\lambda}{2d_{200}} = \frac{\lambda}{2 \frac{1}{\sqrt{(2/a)^2}}} = \frac{\lambda}{a} = \frac{4.177}{5.4097} = 0.772$$

$$\Rightarrow \theta_{200} = 50.54^\circ \quad (3.2)$$

This angle is due to geometrical restrictions too large to be reached by the diffractometer. Of course, since Bragg charge scattering is non-resonant, an energy value higher than the Ru L_{II} edge could be in principle chosen for the observation of the

(2 0 0) reflection, so that the corresponding scattering angle is small enough to be within the geometrically allowed range. However, it is preferred to determine the orientation of the crystal at the exact energy position where the magnetic investigations are subsequently going to be carried out, namely with the fundamental energy of the beam tuned at the absorption edge, because the orientation matrix is then better optimized. Furthermore, the highest energy that can be reached at the instrument with no significant changes in the experimental setup is only 3.5 keV. The reduction of the scattering angle achieved via such a small increase of the energy would anyway not be sufficient for the (2 0 0) reflection to be accessible at the fundamental energy.

For these reasons, for the observation of the (2 0 0) main Bragg reflection a higher-order harmonic of the incident beam was used. By setting the fundamental energy at the Ru L_{II} edge, and adjusting the energy window of the single channel analyzer (SCA) that filters the detector signal around an energy value equal to three times the energy of the edge, the third harmonic with wavelength $\lambda/3$ is selected. Its intensity is, despite its suppression by the mirrors, large enough for providing a strong scattering signal. For $\lambda = 4.177 \text{ \AA}$ (Ru L_{II} edge), the third harmonic has a wavelength of $\lambda/3 = 1.392 \text{ \AA}$ and gives at (2 0 0) a scattering angle of 14.91° , which can be accessed with no problem by the diffractometer. Since the orientation matrix is going to be used at the L_{II} edge, where the magnetic measurements are carried out, it is convenient to index the observed reflection as $(\frac{2}{3} 0 0)$. One has then to set the SCA window back to the L_{II} energy position and simply move, by using the UB matrix, along the scattering vector to the desired (1 0 0) position, in order to start the magnetic investigations.

3.6.2 Energy Scans: Polarization and Temperature Dependence

Once the scattering vector is aligned along the (1 0 0) direction, the sample is cooled to a temperature below $T_N = 110 \text{ K}$, and the x-ray energy is tuned to an absorption edge of Ru, the magnetic reflection can be observed. Non-resonant magnetic intensity is expected to be present at this position, too, but this is too weak to be observed. Figure 3.20 shows the energy dependence of the scattered intensity of the (1 0 0) magnetic reflection around the L_{II} and L_{III} absorption edges of Ru at a sample temperature of 20 K. The measurements were taken with the magnetic moment μ of the material, and thus the b direction, lying in the diffraction plane. The azimuthal angle ψ is at this position by definition equal to zero: $\psi = 0^\circ$. No polarization analyzer was used in the setup in this case, thus the scattering intensity shown is the total intensity. The data have been normalized to the intensity at the ionization chamber used as monitor before the sample position, to account for

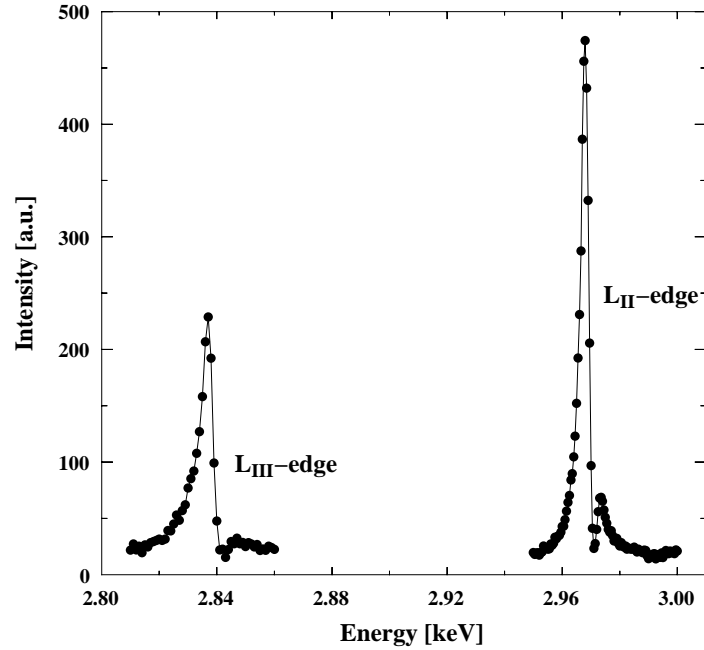


Figure 3.20: Energy dependence of the scattered intensity at the (1 0 0) reciprocal space position around the Ru L_{II} and L_{III} absorption edges, at sample temperature $T = 20$ K and azimuth $\psi = 0^\circ$. The energy profiles are not corrected for absorption.

variations of the incoming beam intensity due to factors not related to the diffraction procedure. Such are the variation of the intensity of the first harmonic of the undulator with energy, random motions of the beam, as well as fluctuations of the current intensity in the synchrotron ring. No correction of the energy profiles, to account for effects caused by the energy-dependent absorption of the x-ray beam by the sample, has been applied on the data shown in Figure 3.20.

The resonant character of the (1 0 0) magnetic reflection becomes immediately obvious. When the energy of the incoming beam is tuned to the L_{II} or L_{III} absorption edges of Ru, significant scattering intensity is obtained. Away from resonance no scattering intensity above the background is observed. The scattered intensity at the L_{II} edge is up to 500 times larger than the off-resonance background, thus the resonant enhancement at L_{II} is at least a factor of 500. The enhancement at L_{III} is about half of that.

Figure 3.21 shows the energy dependence of the scattered intensity around the L_{II} edge in more detail (closed bullets). The spectrum is dominated by the large resonant enhancement of the scattering signal directly at the energy of the edge (2.968 keV). The peak is not symmetric, but has a steeper profile on its higher-energy side. A second, weaker peak is observed in addition approximately 4 eV higher in

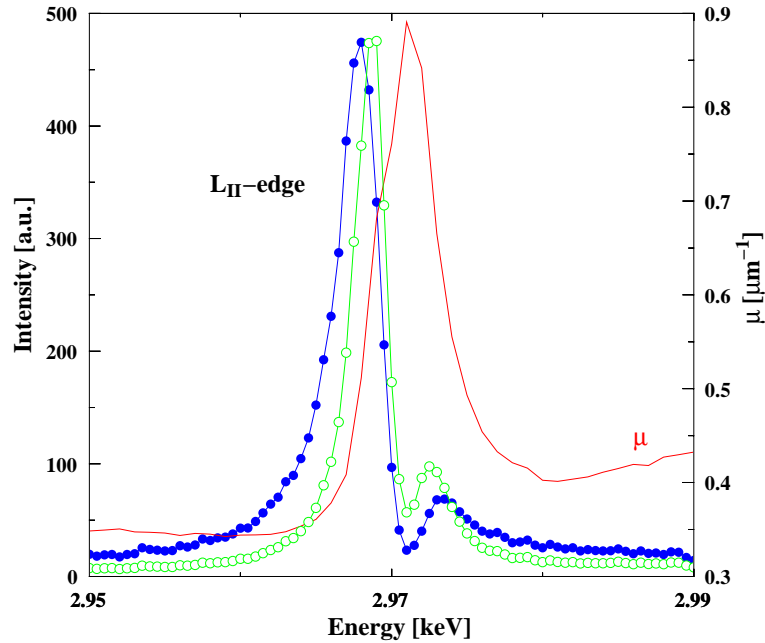


Figure 3.21: Energy dependence of the scattered intensity of the (1 0 0) reflection around the Ru L_{II} absorption edge. Besides the resonant peak at the edge, a second, weaker peak is present 4 eV higher in energy. The energy lineshape is shown both as-measured (closed bullets) and corrected for absorption (empty bullets; normalized to the uncorrected data). For the absorption correction the raw data are multiplied by the square of the absorption coefficient μ . The energy dependence of μ , as calculated from fluorescence measurements, is also included in the plot (right scale).

energy (2.972 keV). The origin of this higher-energy peak will be addressed below. In the following, the lower-energy peak, at 2.968 keV, will be referred to as the ' L_{II} peak', while the one at 2.972 keV as the ' L_{II}' peak'. The energy dependence of the absorption coefficient μ is also shown in the same plot. The absorption coefficient is calculated from the fluorescence yield of the investigated sample, following Reference [67]. More information about the calculations can be found in Appendix A. The two peaks of the energy scan coincide with the inflection points of the absorption coefficient curve, that is, with the points where the second derivative of the function $\mu(E)$ changes sign.

The lineshape of the energy scan needs to be corrected for the absorption of the x-ray beam by the sample. In non-resonant diffraction experiments, the absorption over one beam coherence length is usually weak, although the total sample absorption can be important. In such cases the calculation of the absorption correction proceeds by summing the scattering intensities from all coherence volumes inside the beam path, without having to integrate within every coherence length. The total

scattered intensity in the detector has to be multiplied by the absorption coefficient μ to give the scattered signal we would have without the absorption effects. The above lie on the basic assumption, that both the effective coherence volume of the x-ray beam and its penetration depth in the diffracting material are much larger than the elemental diffracting volume of the sample. However, these basic assumptions are not any more valid when a partially coherent beam enters a highly absorbing medium, as is, for instance, the case in a resonant diffraction experiment, where the photon energy is tuned close to an absorption edge of the diffracting material. Then the absorption depth becomes similar to or smaller than the diffracting volume, and both the coherence length of the probing beam and absorption effects on the scattering amplitude need to be taken into account [68]. The changes in the scattering amplitude due to absorption within one longitudinal probe coherence length cannot be neglected in this case. As shown by Bernhoeft [69], the absorption effects lead under these circumstances to a significant broadening and possible splitting of the energy profiles of the scattered intensity. For the absorption correction of the energy profiles, the scattered intensity in the detector has to be multiplied by the *square* μ^2 of the absorption coefficient.

After the absorption correction the resonant peaks in the energy scans become more symmetric (empty bullets in Figure 3.21, and Figure 3.22). However, the splitting of the two peaks is still clearly present, showing that it is an intrinsic feature of the material and not an artifact caused by the influence of the beam absorption. This is further strongly supported by the temperature dependence of the scattered intensity at the two energy positions, as will be discussed below. The branching ratio, defined as the ratio of the scattering intensities at the L_{II} and L_{III} absorption edges, is calculated approximately equal to 2.1. For this calculation the maximum intensities of the low-temperature energy scans around the two edges at the (1 0 0) position were used. The obtained value should be considered only as an approximation, because the intensities could not be corrected for absorption in this case, due to insufficient fluorescence data at the L_{III} edge. Normalization of the resonant intensities to a main Bragg peak was also not possible due to the geometrical restrictions mentioned before (Section 3.6.1). The result is in good agreement with the branching ratio (2.3) obtained previously with the same technique in a $5d$ electron system [44]. In $3d$ systems, on the contrary, the intensity at the L_{II} edge is smaller than at L_{III} and the branching ratio is smaller than 1 (of the order of 0.5 in manganites [43]).

Figure 3.22(a) shows the development of the lineshape of the energy scans around the L_{II} edge with increasing sample temperature. Three of these scans, corresponding to three characteristic sample temperatures (base temperature, just above the magnetic transition temperature T_N and room temperature) are selected and displayed separately in Figure 3.22(b), with the vertical (intensity) axis being now on a logarithmic scale.

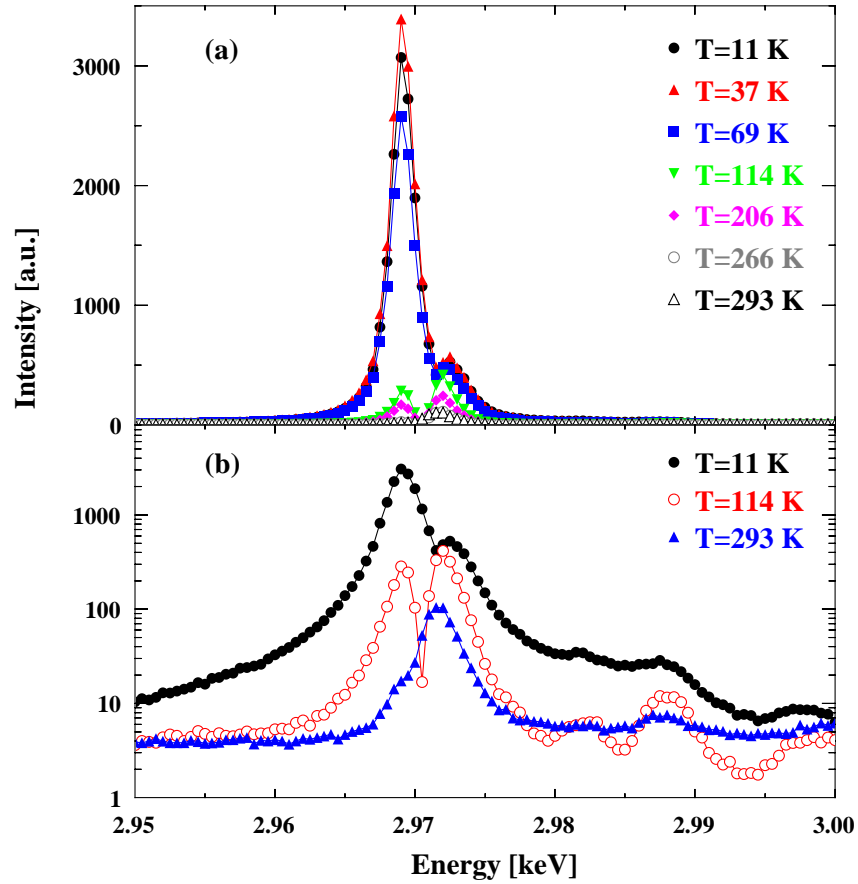


Figure 3.22: Energy dependence of the scattered intensity of the (1 0 0) reflection around the Ru L_{II} absorption edge at azimuth $\psi = 0^\circ$ for selected sample temperatures, on linear (a) and on logarithmic (b) intensity scale. All energy scans are corrected for absorption.

It immediately becomes obvious that the two peaks observed in the energy scans follow quite different temperature dependences. The intensity of both is decreasing, as expected, with increasing temperature. However, while the intensity of the lower-energy (L_{II}) peak undergoes two rapid decreases, first at the magnetic ordering temperature T_N and then around 260 K, the intensity of the higher-energy (L_{II}') peak decreases smoothly and slowly with temperature without showing any anomalies. As a result, the ratio of the scattered intensity at the two energy positions changes significantly with temperature. While at $T = 11$ K the intensity at L_{II} is a factor of 6 larger than the intensity at 2.972 keV, at $T = 114$ K, i.e. just above the magnetic transition temperature, the two intensities become practically equal to each other. Further increase of the sample temperature up to $T = 293$ K results in an almost (but not complete) vanishing of the L_{II} peak, while the L_{II}' resonance is

still present with a significant intensity. So the intensity ratio changes from 6 : 1 at base temperature to 1 : 1 above T_N to approximately 1 : 8 at room temperature. The different temperature dependences of the two resonant features clearly indicate that they are of different origin. We will come back to this issue later.

The most interesting and significant piece of information provided by the variation with temperature of the scattered intensity around the L_{II} edge is the fact that the scattered intensity at (1 0 0) does not drop to zero at the magnetic transition temperature T_N , as expected based on the powder neutron diffraction investigations, but is still present, though very weak, even up to room temperature. This clearly shows that an additional ordering mechanism, besides the magnetic ordering, which is characterized by the same propagation vector, but sets in at a higher temperature than magnetism, is present in Ca_2RuO_4 . Such an additional ordering has not been reported by any other experimental studies so far.

3.6.3 Reciprocal Space Scans: Temperature Dependence

Measurements at the L_{II} edge

In order to obtain a clear view of the temperature dependence of the order parameters in Ca_2RuO_4 , scans along the scattering vector (a^* direction) around the (1 0 0) reciprocal space position were carried out, and the corresponding integrated intensities were calculated, for various sample temperatures. Figure 3.23 shows two such (h 0 0)- scans, performed at a sample temperature of $T = 20$ K at the azimuthal position $\psi = 0^\circ$ (i.e. with the b -direction in the diffraction plane), with the energy of the incoming x-ray beam fixed at the L_{II} edge. The two scans correspond to the two different polarization geometries, $\sigma \rightarrow \pi'$ and $\sigma \rightarrow \sigma'$, seen in Figure 2.3.

The full bullets represent the data collected with the polarization analyzer at the position, for which only the part of the scattered beam with polarization parallel to the diffraction plane is detected; the empty bullets, on the other hand, represent the contribution to the total intensity of the part of the scattered beam which has a polarization parallel to the diffraction plane. It is obvious that practically the whole scattered intensity measured comes from the $\sigma \rightarrow \pi'$ polarization channel, while the $\sigma \rightarrow \sigma'$ contribution is almost equal to zero. The very weak intensity measured in the $\sigma \rightarrow \sigma'$ channel amounts to approximately 1% of the intensity in $\sigma \rightarrow \pi'$. This is no real $\sigma \rightarrow \sigma'$ contribution, but comes from the 'leakage' from the $\sigma \rightarrow \pi'$ channel, resulting from the fact that the scattering angle of the polarization analyzer at this energy is not exactly equal to 45° , and thus the separation of the two polarization components of the scattered beam is not perfect. Indeed, the scattering angle provided by the Si(111) analyzer crystal at the L_{II} edge is $\theta_{Si} = 41.8^\circ$. Thus, the scattering intensity in $\sigma \rightarrow \pi'$ is: $I_{\sigma\pi'} \propto I_0 \sin^2(2\theta_{Si}) = 0.988 I_0$, while the intensity in $\sigma \rightarrow \sigma'$ is: $I_{\sigma\sigma'} \propto I_0 \cos^2(2\theta_{Si}) = 0.012 I_0$. The latter result means

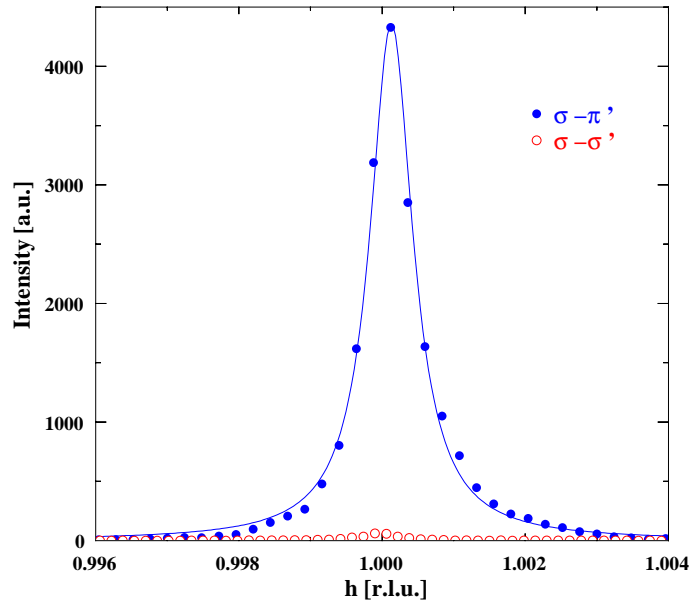


Figure 3.23: Variation of the scattering intensity around the (1 0 0) reciprocal space position in $\sigma \rightarrow \pi'$ (full bullets) and $\sigma \rightarrow \sigma'$ (empty bullets) polarization geometries, measured at the Ru L_{II} edge, at azimuth $\psi = 0^\circ$ and low temperatures ($T=20$ K). The solid line is the result of a fit of a Lorentzian profile to the $\sigma \rightarrow \pi'$ data. The scattering intensity in the $\sigma \rightarrow \sigma'$ polarization channel is practically equal to zero.

that there is in the $\sigma \rightarrow \sigma'$ channel a weak intensity equal to 1.2% of the incoming intensity I_0 . This coincides exactly with the intensity of the weak signal detected in this polarization geometry in the reciprocal space scan shown in Figure 3.23.

The h -scan in $\sigma \rightarrow \pi'$ geometry shown in Figure 3.23 can be fitted by a Lorentzian profile (solid line in graph). The fitting provides the integrated scattering intensity at $T = 20$ K. The procedure is repeated for various sample temperatures, in 5 to 10 K intervals, up to room temperature. Two series of such measurements were performed in the experiment, one with the analyzer in $\sigma \rightarrow \pi'$ geometry, as in Figure 3.23, and one without the use of an analyzer. The two series of measurements were carried out on different samples. By comparing the two temperature dependences, it could be concluded whether the scattered intensity is at every temperature of purely π' polarization, as suggested by the h -scans at 20 K, or if, on the contrary, some $\sigma \rightarrow \sigma'$ contribution also comes up within a particular temperature range.

Figure 3.24 shows the temperature dependence of the integrated intensity of the reciprocal space scans determined as described above, on a linear (panel a) and on a logarithmic (panel b) scale. The intensities obtained with the analyzer in $\sigma \rightarrow \pi'$ geometry are, due to losses at the analyzer crystal, a factor of 15 weaker than the ones obtained without analyzer. The corresponding plots have been normalized to

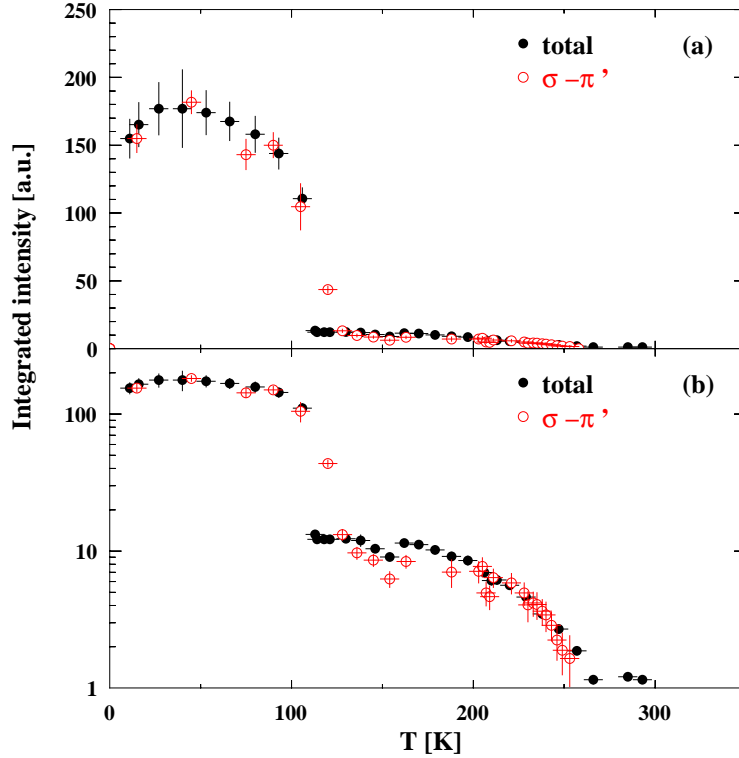


Figure 3.24: Temperature dependence of the integrated scattering intensity at the (1 0 0) reciprocal space position at the Ru L_{II} edge, as determined from h -scans at $\psi = 0^\circ$, both without polarization analyzer (full bullets) and in $\sigma \rightarrow \pi'$ geometry (empty bullets), presented on linear (a) and on logarithmic (b) intensity scales. The two plots have been scaled to their base temperature intensities. The dependences without analyzer and in $\sigma \rightarrow \pi'$ are virtually identical to each other. Non-zero scattering intensity is observed above the Néel temperature, revealing a new phase transition at 260 K.

the base-temperature intensity values. We notice that the temperature dependences in $\sigma \rightarrow \pi'$ geometry and without analyzer are practically identical. Some minor differences will be discussed later. The conclusion from this is that, within the whole temperature range investigated, the total scattering intensity (measured without analyzer) at the L_{II} edge originates exclusively from the $\sigma \rightarrow \pi'$ polarization channel, i.e. has polarization which is purely parallel to the diffraction plane, just like at 20 K (Figure 3.23). Any $\sigma \rightarrow \sigma'$ contribution would result in deviations between the total signal and the $\sigma \rightarrow \pi'$ intensity, which are not observed. Thus, the use of analyzer is not necessary for the investigation of the resonant scattering at the (1 0 0) position, since it does not provide any additional information. Working without analyzer is much easier, because the obtained intensity is then higher and the rocking curves broader. The latter is particularly important when carrying out azimuthal angle

dependences. Indeed, a small rocking-curve width as a result of a perfect analyzer can lead to intensity losses when rotating the sample around the scattering vector (due to moving off the maximum of the peak) and make the azimuthal investigations difficult.

Let us now concentrate on how exactly the scattering intensity changes with increasing temperature. At low temperatures the magnetic scattering dominates. In the temperature range between approximately 40 K and 100 K, the integrated intensity follows a slow decrease with increasing temperature. The experimental data indicate a small but noticeable inversion of this tendency at lower temperatures, below 40 K, where the order parameter seems to be increasing, instead of decreasing, with increasing temperature. With only two data points available below 40 K, and due to the relatively large size of the corresponding vertical error bars with regard to the observed small suppression of the scattering intensity, it cannot be fully excluded that the anomaly is due to statistical fluctuations. However, the independent observation of the anomaly on two different samples investigated in two different polarization geometries suggests that the effect originates from intrinsic properties of the material. What the cause for such a suppression of the magnetic moment at very low temperatures could be, is not clear.

A large reduction of the integrated scattering intensity is observed at the anti-ferromagnetic transition temperature $T_N = 110$ K. Our resonant x-ray diffraction investigations are thus consistent with older neutron diffraction and magnetization measurements (e.g. [51, 65]), which reported a phase transition of Ca_2RuO_4 from an antiferromagnetic to a paramagnetic state at 110 K, as mentioned in Section 3.3.

The scattered intensity above the Néel temperature T_N does not drop to zero. Instead, there is some significant intensity remaining, which is a factor of 20 weaker than the one at low temperatures, around the 40 K maximum. This intensity follows a smooth, slow decrease with increasing temperature and eventually almost vanishes at the temperature of $T_{OO} = 260$ K in an order-parameter-like fashion. Our results thus clearly indicate the existence of a second phase transition occurring in Ca_2RuO_4 at 260 K, far above the Néel temperature, but well below the metal-insulator transition. This phase transition has not been reported so far and can be considered as the most significant finding of our Ca_2RuO_4 investigations.

There are two more features of the temperature dependence at the (1 0 0) position that should be mentioned. Firstly, some extremely weak scattering intensity, of the order of 0.5 % of the strong magnetic signal below T_N , is still present even above the 260 K phase transition, persisting at least up to room temperature. Secondly, the data indicate the possible existence of a minor anomaly at the temperature of 150 K, depicted by a small dip in the intensity at this temperature, both when no polarization analysis is used and when only the $\sigma \rightarrow \pi'$ contribution is measured. Although this observation is based only on one or two experimental data points and although the intensity drop is comparable in size with the error bar (at least in

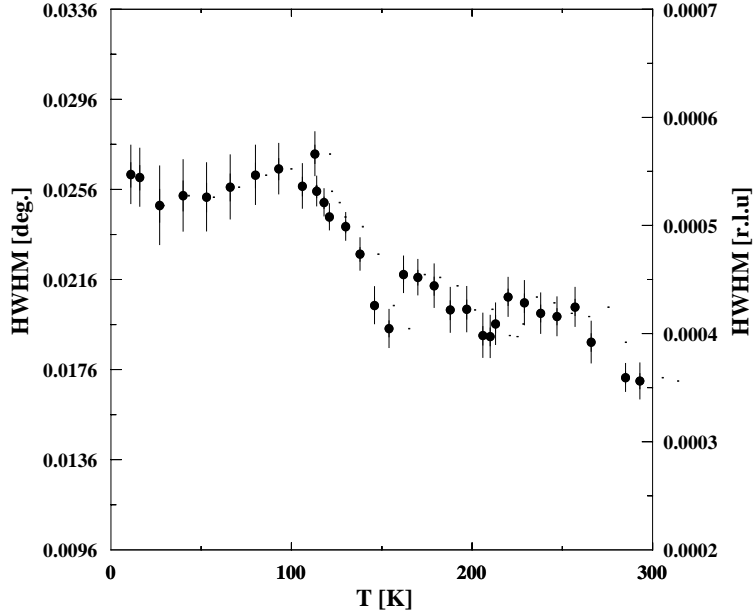


Figure 3.25: Variation with temperature of the half width at half maximum of the (1 0 0) peak in h -scans carried out at the Ru L_{II} edge at $\psi = 0^\circ$, without polarization analyzer. A small decrease of the peak's width is observed above the Néel temperature.

the case of the $\sigma \rightarrow \pi'$ measurement), the fact that the anomaly was observed at exactly the same temperature on two different samples, makes the possibility of pure coincidence rather unlikely. The possible origin of these features will be discussed in Section 3.12.

Finally, we return to the issue of the minor differences observed between the total and the $\sigma \rightarrow \pi'$ intensity in the temperature dependence presented in Figure 3.24. A quick look at the graphs may create the impression that the magnetic transition observed when the polarization analyzer is used, is broader than the one indicated by the total intensity, leading to a slightly higher Néel temperature. At first sight, this impression is confusing: the total intensity *includes* the π' polarized signal and cannot be smaller than it. If the magnetic transition is still not completed in either of the polarization channels, it cannot be already completed in the total signal. This discrepancy is nevertheless not related to the use or no-use of polarization analysis. One should take into consideration the following facts: first, the measurements with and without analyzer were carried out on different crystals. It cannot be excluded that the crystals had slightly different Néel temperatures, for example, due to small differences in their stoichiometry. In addition, the coupling of the samples to the sample holder and, consequently, to the cold finger of the cryostat might have been

different in the two cases (for example, due to different gluing of the crystals). A worse coupling of the sample to the sample holder would result in a slightly higher actual temperature of the sample compared to what measured by the sensor which is attached to the holder, and would lead to an apparent increase of the magnetic transition temperature. Finally, in the experiment where the presented data were collected, two different sensors were used for the measurement of the sample temperature, one for the low-temperature regime and one for the higher-temperature (above 100 K) regime (Section 3.5.2). The observed discrepancy occurs close to the temperature at which the changeover from one sensor to the other takes place and where, as previously explained, the horizontal error bars may for this reason be locally larger. It is not possible to say which of the above factors played the most important role in the discussed discrepancy of the temperature dependences, which is, after all, actually caused by a single data point of the $\sigma \rightarrow \pi'$ graph. In any case, the issue is not significant, is not related to the use of polarization analysis and does not influence the main conclusion that is drawn from the comparison of the two graphs, namely, that no $\sigma \rightarrow \sigma'$ contribution to the total scattering intensity is observed at (1 0 0) in the whole temperature range investigated.

Figure 3.25 shows the variation with temperature of the half width at half maximum of the (1 0 0) reflection. The determination of the width is done using the same reciprocal space scans, from which the integrated intensity was also obtained, by fitting the data with Lorentzian profiles. A significant decrease of the peak's width by approximately 30% is observed above the antiferromagnetic transition temperature (110 K). This indicates that the ordered phase observed above T_N is characterized by a correspondingly larger correlation length than the magnetically ordered low-temperature phase. The correlation length ξ_a along a^* can be estimated through the expression:

$$\xi_a = \frac{a}{2\pi \cdot \text{HWHM}} \quad (3.3)$$

where the correlation length and the lattice parameter a are in \AA , and HWHM is the half width at half maximum of the corresponding h -scan. The expression gives: $\xi_a \approx 1560 \text{ \AA}$ below T_N and $\xi_a \approx 2150 \text{ \AA}$ above T_N .

Measurements at L_{II}'

It is particularly interesting that the temperature dependence of the (1 0 0) scattering intensity at the L_{II}' energy (2.972 keV) is quite different from the one at the L_{II} edge (2.968 keV). This difference, which became obvious already from the energy scans, can be better seen, in a more quantitative way, by using the integrated intensities of reciprocal space scans. Figure 3.26 shows the variation with temperature of the integrated intensities of the reciprocal space scans around (1 0 0) at the L_{II}' energy position, determined by fitting, as described for the L_{II} edge. The

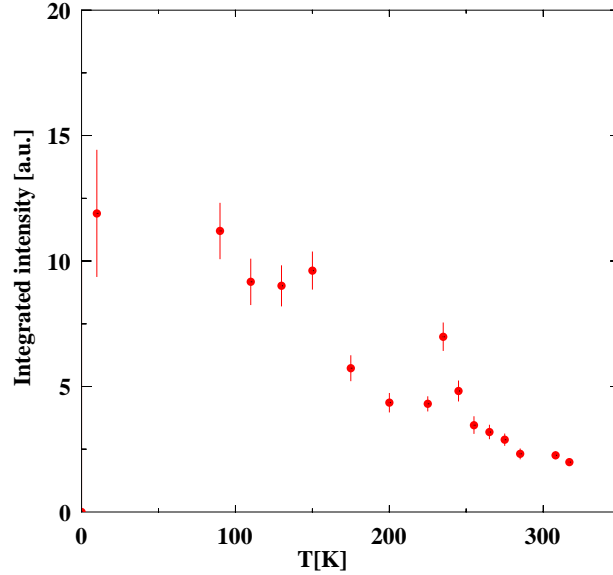


Figure 3.26: Temperature dependence of the integrated scattering intensity at the $(1\ 0\ 0)$ reciprocal space position at the L_{II}' energy position (2.972 keV), as determined from h -scans at $\psi = 0^\circ$ without polarization analyzer. The intensity at 11 K was estimated from the corresponding energy scan, as explained in the text. No anomalies are observed in the temperature dependence at least up to room temperature.

measurements were taken without polarization analyzer and with the magnetic moment lying in the diffraction plane ($\psi = 0^\circ$). The integrated intensity of the h -scans at L_{II}' can be reliably determined only for temperatures above approximately 90 K. Below that temperature, the intensity at L_{II}' is overwhelmed by a strong contribution from the L_{II} resonance. For this reason, for determining the L_{II}' scattering intensity at low temperatures, we are forced to use energy scans instead. The latter cannot provide integrated intensities, but have the advantage that they allow the separation of the two resonant contributions by fitting the data with two Lorentzian peaks. Accordingly, the L_{II}' maximum scattering intensity of the 90 K energy scan was first determined by fitting. By dividing this by the integrated intensity obtained from the corresponding h -scan, a normalizing factor was calculated. By dividing in the following the L_{II}' maximum of the 11 K energy scan by this normalizing factor, the integrated scattering intensity at base temperature was estimated. It is this intensity which is displayed by the low-temperature data-point in Figure 3.26.

The temperature dependence at L_{II}' shows, in contrast to the one at the L_{II} absorption edge, no anomalies in the whole temperature range investigated. No phase transitions are observed, neither at the magnetic transition temperature ($T_N = 110$ K), nor at $T_{OO} = 260$ K, nor at any other temperature. The integrated scattering intensity decreases smoothly with increasing temperature, with no change of the data curve slope within our experimental sensitivity. Furthermore, non-zero scattering intensity is still observed up to 310 K, the highest temperature investigated.

The different temperature dependence at the L_{II}' energy position compared to that at the L_{II} absorption edge indicates that the two resonances have different origins and reflect different aspects of the electronic structure of the material. The issue will be discussed in detail in Section 3.12.

3.6.4 Reciprocal Space Scans: Azimuthal Angle Dependence

$T < T_N$:

The azimuthal angle dependence of the magnetic scattering intensity from Ca_2RuO_4 at the (1 0 0) reciprocal space position is given by the general equations 2.25 and 2.28 for the $\sigma \rightarrow \pi'$ and $\sigma \rightarrow \sigma'$ polarization geometries, respectively, applied on the particular magnetic unit cell of the material. The magnetic basis of stoichiometric Ca_2RuO_4 consists of four Ru^{+4} ions with 'up' and 'down' spins, as illustrated in Figure 3.27.

The position vectors of the basis ions are:

$$\begin{aligned} \mathbf{R}_1 &= 0 \\ \mathbf{R}_2 &= \frac{a}{2}\hat{\mathbf{x}} + \frac{c}{2}\hat{\mathbf{z}} \\ \mathbf{R}_3 &= \frac{b}{2}\hat{\mathbf{y}} + \frac{c}{2}\hat{\mathbf{z}} \\ \mathbf{R}_4 &= \frac{a}{2}\hat{\mathbf{x}} + \frac{b}{2}\hat{\mathbf{y}} \end{aligned} \quad (3.4)$$

where $\hat{\mathbf{x}}$, $\hat{\mathbf{y}}$, $\hat{\mathbf{z}}$ are unit vectors along the crystallographic directions a , b , c , respectively.

In $\sigma \rightarrow \pi'$ geometry, the total resonant electric dipole scattering length in the antiferromagnetic phase ($T_N < 110$ K) for $\mathbf{Q} = (1\ 0\ 0)$ is, according to Equation 2.24, equal to:

$$\begin{aligned} g_{E1}^{\sigma \rightarrow \pi'} &= \sum_{j=1}^4 g_{E1,S_j}^{\sigma \rightarrow \pi'} e^{i\mathbf{Q} \cdot \mathbf{R}_j} = g_{E1,\uparrow}^{\sigma \rightarrow \pi'} e^0 + g_{E1,\downarrow}^{\sigma \rightarrow \pi'} e^{i\pi} + g_{E1,\uparrow}^{\sigma \rightarrow \pi'} e^0 + g_{E1,\downarrow}^{\sigma \rightarrow \pi'} e^{i\pi} \Rightarrow \\ g_{E1}^{\sigma \rightarrow \pi'} &= 2(g_{E1,\uparrow}^{\sigma \rightarrow \pi'} - g_{E1,\downarrow}^{\sigma \rightarrow \pi'}) \end{aligned} \quad (3.5)$$

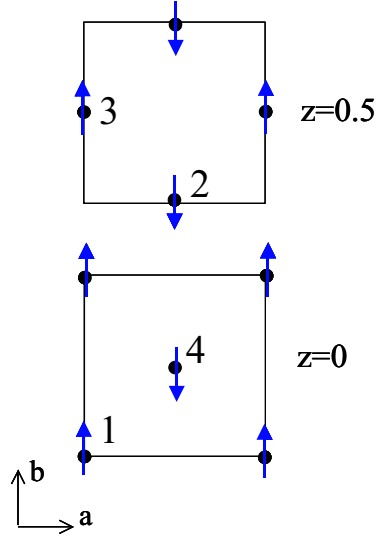


Figure 3.27: Schematic view of the magnetic unit cell of Ca_2RuO_4 , as determined by neutron diffraction [51]. The full dots represent Ru^{+4} lattice sites and the arrows show the direction of the spin ('up' or 'down') at every site. The numbered ions make up the magnetic basis.

The scattering lengths for the spin-up and spin-down ions are given by Equations 2.21 and 2.23. The total scattering length is therefore:

$$\begin{aligned} g_{E1}^{\sigma \rightarrow \pi'} &= 2 [2iF^{(1)} \cos \alpha \sin \theta + 2iF^{(1)} \sin \alpha \cos \theta \cos \psi] \\ &= 4iF^{(1)}(\sin \alpha \cos \theta \cos \psi + \cos \alpha \sin \theta) \end{aligned} \quad (3.6)$$

where for the $(1\ 0\ 0)$ reflection the scattering angle is: $\theta = 22.71^\circ$ (at the Ru L_{II} edge), and the angle α between the magnetic moment $\boldsymbol{\mu}$ and the scattering vector is: $\alpha = \text{angle}((010), \hat{(100)}) = 90^\circ$.

The magnetic scattering intensity in $\sigma \rightarrow \pi'$ at $(1\ 0\ 0)$ is proportional to the square absolute of the total scattering length:

$$I_{(100)}^{\sigma \rightarrow \pi'} \propto |g_{E1}^{\sigma \rightarrow \pi'}|^2 \propto (F^{(1)})^2 \cos^2 \theta \cos^2 \psi \quad (3.7)$$

Similarly, in $\sigma \rightarrow \sigma'$ geometry the total scattering length is given by:

$$g_{E1}^{\sigma \rightarrow \sigma'} = \sum_{j=1}^4 g_{E1,S_j}^{\sigma \rightarrow \sigma'} e^{i\mathbf{Q} \cdot \mathbf{R}_j} = 2(g_{E1,\uparrow}^{\sigma \rightarrow \sigma'} - g_{E1,\downarrow}^{\sigma \rightarrow \sigma'}) \quad (3.8)$$

The scattering lengths for the spin-up and spin-down ions are, according to Equation 2.26, equal to each other:

$$g_{E1,\uparrow}^{\sigma \rightarrow \sigma'} = g_{E1,\downarrow}^{\sigma \rightarrow \sigma'} = F^{(0)} + F^{(2)} \mu_2^2 = F^{(0)} + F^{(2)} \sin^2 \alpha \sin^2 \psi \quad (3.9)$$

Thus:

$$g_{E1}^{\sigma \rightarrow \sigma'} = 0 \quad (3.10)$$

and the magnetic scattering intensity in $\sigma \rightarrow \sigma'$ at (1 0 0) is zero:

$$I_{(100)}^{\sigma \rightarrow \sigma'} = 0 \quad (3.11)$$

The latter is consistent with the experimentally verified absence of scattering intensity in the $\sigma \rightarrow \sigma'$ polarization channel at low temperatures, mentioned in Section 3.6.2 (Figure 3.23).

Equations 3.7 and 3.11 show that the total magnetic scattering intensity at (1 0 0) is proportional to $\cos^2 \psi$, thus it is expected to take its maximum value for $\psi = 0^\circ$ and its minimum value (zero) for $\psi = 90^\circ$. This was indeed confirmed experimentally: at low temperatures, well within the antiferromagnetically ordered phase, the maximum scattering signal at the (1 0 0) position was obtained when the magnetic moment (i.e. the b -direction) was lying in the diffraction plane. A rotation of the sample around the scattering vector by 90° ($\psi = 90^\circ$) resulted in a complete vanishing of the scattering intensity.

A complete investigation of the azimuthal dependence of the (1 0 0) scattering intensity below the Néel temperature was not carried out. The magnetic properties of Ca_2RuO_4 are known from neutron diffraction and magnetization measurements, and the confirmation of the already established azimuthal dependence of the scattering intensity that originates from magnetic ordering was not among the high priorities of the present work. The clear observation of the magnetic transition at T_N and the confirmation of the 180° -periodicity in ψ were enough to demonstrate that the experimental technique can be successfully used for the investigation of the magnetic structure of single-crystal Ca_2RuO_4 .

$T > T_N$:

It is of great interest to determine the azimuthal dependence of the scattering intensity of the novel phase discovered above the Néel temperature. This could provide information about the origin and the properties of the new phase. To do so, scans along the (h 0 0) direction in reciprocal space were carried out around the (1 0 0) position, for different azimuthal positions ψ of the sample around the scattering vector. The measurements were performed at a sample temperature of 175 K, namely, well above the magnetic phase transition temperature $T_N = 110$ K, but well below the second phase transition at $T_{OO} = 260$ K. The h -scan conducted at every azimuthal position was fitted with a Lorentzian profile and the integrated intensity determined by the fitting was eventually plotted as a function of ψ . The resulting experimentally determined azimuthal dependence is shown in Figure 3.28. The solid line in the graph represents a fit to the data of a simple \cos^2 -function: $I(\psi) = C \cos^2 \psi$ (C : constant).

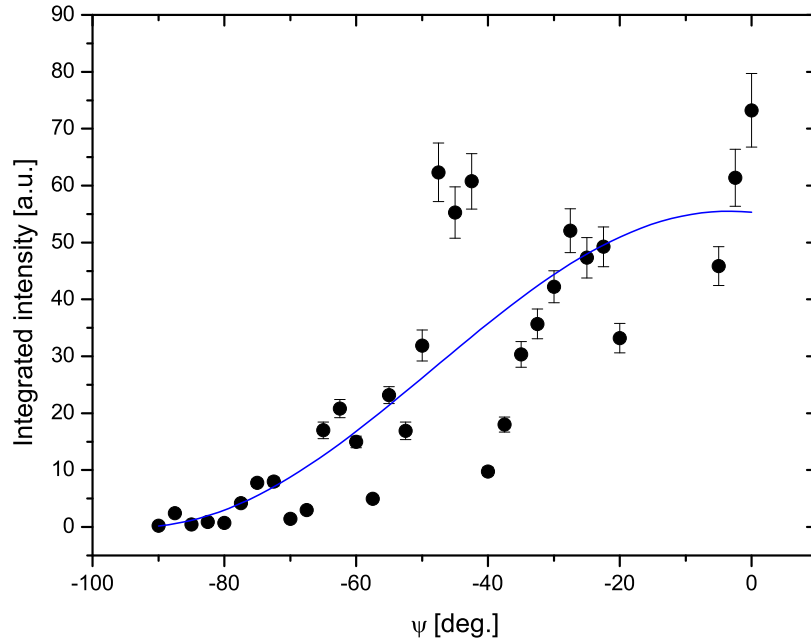


Figure 3.28: Azimuthal dependence of the integrated scattering intensity at the (1 0 0) reciprocal space position at the Ru L_{II} edge, as determined from h -scans at $T = 175$ K, without polarization analyzer. The solid line is a fit of a \cos^2 -function to the data.

The large intensity fluctuations depicted in the graph are due to the grain-related features of the investigated sample. The crystal that was used for azimuthal investigations at the (1 0 0) reciprocal space position (sample B, Section 3.5.1) was, as already mentioned, characterized by a mesoscopically inhomogeneous structure, consisting of several small domains (grains), aligned almost, but not perfectly, parallel to each other. The size of these grains was comparable to the dimensions of the incoming x-ray beam, and thus to the diameter of the scattering area on the sample surface (of the order of $100 \mu\text{m}$). Every time the sample was rotated around the scattering vector, in order to move to a different azimuthal position, slight horizontal translations of the sample in the x-ray beam occurred. Such small movements are practically unavoidable, because there is always a small deviation of the centre of the sample from the centre of rotation of the diffractometer. As a result of the slight movement of the sample, the x-ray beam was not scattered always by the same grain. The 'hopping' to different grains caused significant fluctuations of the measured intensity, not related to the intrinsic azimuthal dependence of the scattering amplitude, because the grains were of different sizes and had slightly different orientations. Of course, after every change of the azimuthal angle, alignment scans were performed for the optimization of both the scattering angle and the transla-

tional position of the sample. However, due to the very small width of the rocking curves (HWHM less than 0.02°), the iteration procedure, which is normally followed in an alignment process, did not optimize the intensity in this case. The result was an azimuthal dependence graph of suboptimal quality. These intensity fluctuations would have been avoided by normalizing to a main Bragg reflection (e.g. (1 0 0)), but none could be reached at this energy.

Despite the above difficulties, the data still allow to draw a clear conclusion about the periodicity of the azimuthal dependence which characterizes the phase observed in Ca_2RuO_4 above T_N . The scattering intensity follows a 180° periodicity, taking its maximum value at $\psi = 0^\circ$ and dropping to zero at $\psi = \pm 90^\circ$, and can be described by a \cos^2 -law. Thus, the azimuthal dependence of the intensity above the magnetic transition temperature is the same with the one theoretically predicted and experimentally confirmed for the low-temperature antiferromagnetic phase.

3.7 Investigations at the (0 1 1) Reciprocal Space Position

The *A-centered* magnetic arrangement of the Ru^{+4} spins in Ca_2RuO_4 (Section 3.3), which gives rise to the (1 0 0) magnetic reflection, results in a non-zero magnetic structure factor also for the (0 1 1) reciprocal space position. The latter is, alike (1 0 0), structurally forbidden, that is, free from charge Bragg scattering contributions. Detailed temperature- and azimuthal dependence investigations were carried out at this position at the Ru L_{II} absorption edge. The main motivation was to examine whether the features observed at (1 0 0) are present also at the magnetically equivalent (0 1 1) site. Of particular interest was to verify if the novel phase discovered at (1 0 0) below $T_{OO} = 260$ K gives rise to resonant scattering at (0 1 1), as well, and, if so, with what kind of azimuthal dependence. This information could be useful in our attempt to determine the origin and the properties of this new phase, and to obtain a complete picture of the electronic properties of Ca_2RuO_4 in general.

3.7.1 Alignment

The initial alignment of the sample in the x-ray beam was carried out using the third harmonic component $\lambda/3$ of the beam, as described in Section 3.6.1, with the fundamental tuned at the Ru L_{II} absorption edge ($\lambda = 4.177 \text{ \AA}$). The (0 2 2) Bragg peak was used for this purpose, a relatively weak reflection, giving a scattering intensity of the order of 400 counts per second at the scattering angle of $\theta = 16.2^\circ$.

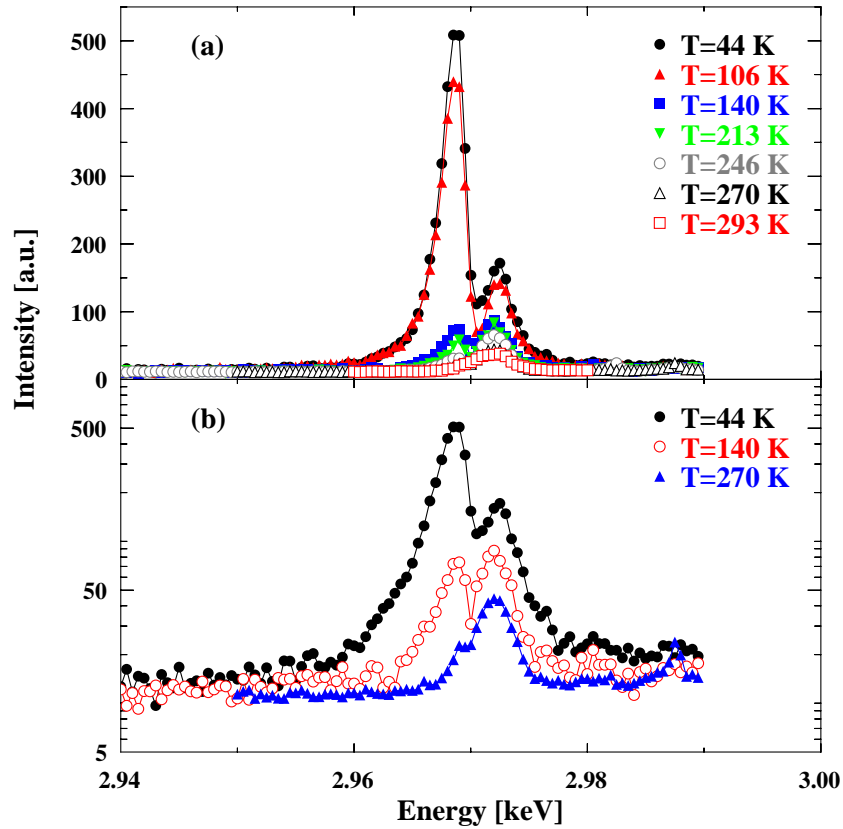


Figure 3.29: Energy dependence of the scattered intensity of the (0 1 1) reflection around the Ru L_{II} absorption edge at azimuth $\psi = 0^\circ$ for selected sample temperatures, in linear (a) and in logarithmic (b) intensity scale. All energy scans are corrected for absorption.

3.7.2 Energy Scans: Temperature Dependence

The variation of the scattering intensity with the photon energy of the incoming x-ray beam at the (0 1 1) reciprocal space position was investigated within a wide range of sample temperatures. The energy scans were carried out with the magnetic moment μ of the material (parallel to the b -direction) lying in the diffraction plane (azimuthal position $\psi = 0^\circ$). No polarization analyzer was used for the analysis of the scattered beam.

The energy scans are displayed in panel (a) of Figure 3.29. Three of them, corresponding to three characteristic temperatures, are selected and presented separately on a logarithmic intensity scale in panel (b) of the same figure. The intensities have been normalized to the ionization chamber used as monitor before the sample position, and have been corrected for the strong absorption of the x-ray beam by the sample. For the absorption correction, the normalized intensities were multiplied

by the square of the energy dependent absorption coefficient (Appendix A), following the same procedure as in Section 3.6.2. The measurements that correspond to temperatures above 240 K were taken independently from those at low temperatures, but on the same sample and during the same experiment. However, they gave significantly higher (factor of 2.4) scattering intensities, probably because of the already discussed grain-hopping effect. The intensities of the high-temperature measurements had, thus, to be normalized, using as reference the intensity at 240 K, which was available from both series of measurements.

The variation of the scattering intensity at position (0 1 1) of the reciprocal space with energy and temperature is practically identical to the one observed at (1 0 0). The resonant enhancement at the L_{II} edge results in a double-peak structure, with the higher energy peak (L_{II}') being approximately 4 eV above the edge. The intensity at both energy positions decreases with increasing temperature, but following quite different dependences. While the intensity at L_{II} undergoes two strong, relatively sharp decreases first at the magnetic ordering temperature T_N and then around 260 K, the intensity at L_{II}' decreases only slowly and smoothly with temperature without showing any anomalies. This results in an inversion of the intensity ratio of the two peaks around the magnetic transition temperature, exactly like at the (1 0 0) position. Close to room temperature the scattering intensity at L_{II} is close to zero, while a significant intensity remains at L_{II}' .

The fact that significant scattering intensity remains above the magnetic transition temperature ($T_N = 110$ K), shows that the novel phase discovered at (1 0 0) is observed also at the magnetically equivalent (0 1 1) position.

3.7.3 Reciprocal Space Scans: Temperature Dependence

For determining the integrated scattering intensity at the (0 1 1) reciprocal space position, scans along the scattering vector Q in form of $\theta - 2\theta$ scans were carried out at various temperatures. In a $\theta - 2\theta$ scan the scattered intensity is measured during a simultaneous rotation of the sample around the scattering angle that satisfies the Bragg condition, and of the detector by twice the amount of change of the scattering angle. Such a scan is equivalent to a Q -scan (i.e. a kl -scan in this case).

Figure 3.31 shows a $\theta - 2\theta$ scan around the (0 1 1) position at low temperatures (45 K). The integrated intensity is determined by fitting of a Gaussian profile to the data. The procedure is repeated for several temperatures up to 294 K. All scans were carried out without polarization analyzer and with the magnetic moment lying in the diffraction plane ($\psi = 0^\circ$). The variation of the integrated intensities with temperature is shown in Figure 3.30. For comparison, the temperature dependence of the (1 0 0) reflection (from Figure 3.24) is shown in the same plot, normalized to the intensity at 130 K. The low- and high-temperature ($T > 130$ K) (0 1 1) data are from two different series of measurements (taken on the same sample, during the

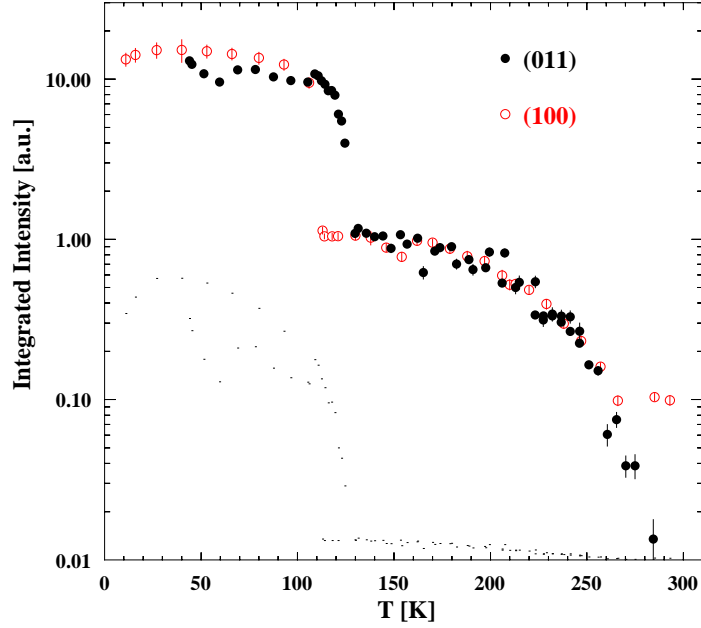


Figure 3.30: Temperature dependence of the integrated scattering intensity at the $(0\ 1\ 1)$ reciprocal space position at the Ru L_{II} edge, as determined from $\theta - 2\theta$ -scans at $\psi = 0^\circ$, without polarization analyzer (full bullets). For comparison, the corresponding temperature dependence for the $(1\ 0\ 0)$ position (Fig. 3.24) is shown in the same plot (empty bullets), normalized to the intensity at 130 K. The temperature dependences at the two positions are virtually identical to each other. A second phase transition, besides the antiferromagnetic at T_N , is in both cases observed around 260 K.

same experiment), normalized also at 130 K.

The main features of the temperature dependence at $(0\ 1\ 1)$ are almost identical to the ones at $(1\ 0\ 0)$. The magnetic transition is clearly observed through a sharp drop of the intensity, equal to one order of magnitude, at T_N . The magnetic transition seems to be slightly less sharp than at $(1\ 0\ 0)$ and is completed at a relatively higher temperature (around 130 K). Concerning this issue, the reader is referred to the comments made in Section 3.6.3 about the differences observed there between the total and the $\sigma \rightarrow \pi'$ intensity at $(1\ 0\ 0)$. The novel phase observed at $(1\ 0\ 0)$ above T_N is also present at $(0\ 1\ 1)$. It follows exactly the same smooth power-law decrease in intensity with increasing temperature and vanishes a little above 270 K. In contrast to the $(1\ 0\ 0)$ position, there is no indication for additional non-zero scattering intensity above the T_{OO} phase transition. The intensity at 300 K is zero within our experimental sensitivity. The small dip in intensity observed at $(1\ 0\ 0)$ at 150 K (independently in the total signal and in the $\sigma \rightarrow \pi'$ polarization channel) is not present at $(0\ 1\ 1)$.

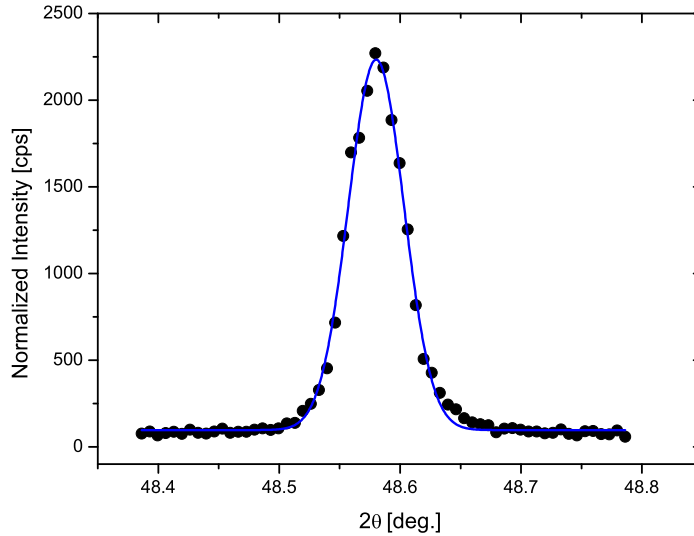


Figure 3.31: $\theta - 2\theta$ -scan around the (0 1 1) position at the Ru L_{II} edge, carried out at sample temperature $T = 45$ K and azimuth $\psi = 0^\circ$. The solid line is a fit of a Gaussian profile to the data. From the fitting, the integrated intensity and the half width at half maximum of the reflection are determined.

Figure 3.32 shows the variation with temperature of the the half width at half maximum of the (0 1 1) reflection, as determined from the $\theta - 2\theta$ -scans. As was the case at (1 0 0), the resonant peak at (0 1 1) also shows a significant decrease by approximately 35% of its width at the antiferromagnetic transition temperature. This again indicates that the ordered phase above T_N is characterized by a correspondingly larger correlation length than the magnetically ordered low-temperature phase. The width of the peak appears in general larger than at (1 0 0), but direct comparisons are difficult to make because of the different fitting function which had to be used at (0 1 1) (Gaussian instead of Lorentzian) due to angular resolution effects. The 'noisy' appearance of the data and the relatively large error bars above approximately 170 K are due to the weakness of the resonant signal at high temperatures, which makes the fitting less precise.

3.7.4 Reciprocal Space Scans: Azimuthal Angle Dependence

The azimuthal angle dependence of the resonant electric dipole scattering length in the low-temperature antiferromagnetic phase ($T < 110$ K) of Ca_2RuO_4 at the (0 1 1) reciprocal space position is calculated, alike for the (1 0 0) position (Section 3.6.4), from Equations 2.25 and 2.28 applied on the magnetic unit cell of the material (Figure 3.27), with the position vectors \mathbf{R}_j given by Equations 3.4 and the \mathbf{Q} vector

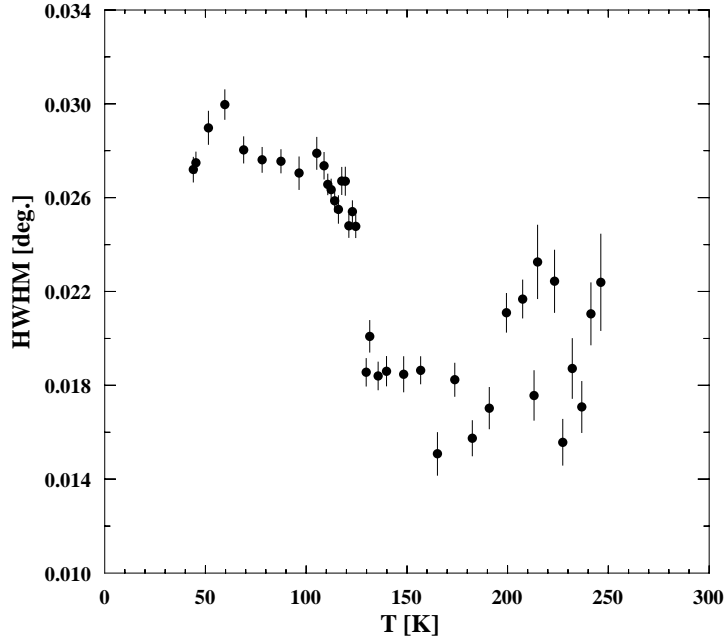


Figure 3.32: Variation with temperature of the half width at half maximum of the (0 1 1) reflection, as determined with $\theta - 2\theta$ -scans carried out at the Ru L_{II} edge at $\psi = 0^\circ$ without polarization analyzer. The peak's width is clearly reduced above the Néel temperature, exactly like at the (1 0 0) position (Fig. 3.25). The increased errors at high temperatures are due to the small scattering intensity there.

being in this case: $\mathbf{Q} = (0 \ 1 \ 1) = \frac{2\pi}{b}\hat{\mathbf{y}} + \frac{2\pi}{c}\hat{\mathbf{z}}$.

In the $\sigma \rightarrow \pi'$ polarization geometry the total scattering length $g_{E1}^{\sigma \rightarrow \pi'}$ is thus:

$$g_{E1}^{\sigma \rightarrow \pi'} = \sum_{j=1}^4 g_{E1,S_j}^{\sigma \rightarrow \pi'} e^{i\mathbf{Q} \cdot \mathbf{R}_j} = g_{E1,\uparrow}^{\sigma \rightarrow \pi'} e^0 + g_{E1,\downarrow}^{\sigma \rightarrow \pi'} e^{i\pi} + g_{E1,\uparrow}^{\sigma \rightarrow \pi'} e^{i2\pi} + g_{E1,\downarrow}^{\sigma \rightarrow \pi'} e^{i\pi} \quad (3.12)$$

which gives:

$$g_{E1}^{\sigma \rightarrow \pi'} = 2(g_{E1,\uparrow}^{\sigma \rightarrow \pi'} - g_{E1,\downarrow}^{\sigma \rightarrow \pi'}) \quad (3.13)$$

The scattering lengths for the spin-up and spin-down ions of the basis are given by Equations 2.21 and 2.23. The total scattering length is therefore:

$$\begin{aligned} g_{E1}^{\sigma \rightarrow \pi'} &= 2 [2iF^{(1)} \cos \alpha \sin \theta + 2iF^{(1)} \sin \alpha \cos \theta \cos \psi] \\ &= 4iF^{(1)} (\sin \alpha \cos \theta \cos \psi + \cos \alpha \sin \theta) \end{aligned} \quad (3.14)$$

where for the (0 1 1) reflection the scattering angle is: $\theta = 24.73^\circ$ (at the Ru L_{II} edge) and the angle α between the magnetic moment $\boldsymbol{\mu}$ (which is parallel to (0 1 0)) and the scattering vector (0 1 1) is equal to: $\alpha = 24.66^\circ$.

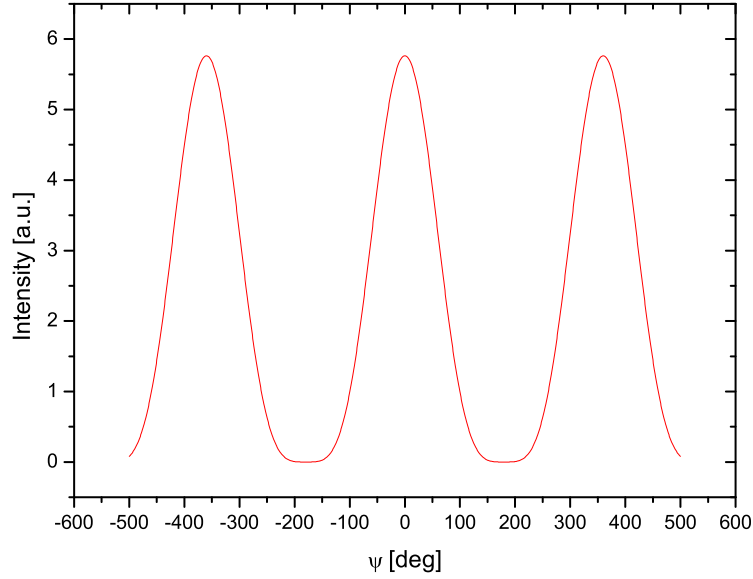


Figure 3.33: Simulation of the azimuthal dependence of the magnetic scattering intensity at the (0 1 1) reciprocal space position in $\sigma \rightarrow \pi'$ polarization geometry, as determined from the general expression for the resonant electric dipole scattering length (Eq. 2.24) applied on the magnetic unit cell of Ca_2RuO_4 (Fig. 3.27).

The magnetic scattering intensity in $\sigma \rightarrow \pi'$ at (0 1 1) is proportional to the square absolute of the total scattering length:

$$I_{(011)}^{\sigma \rightarrow \pi'} \propto (F^{(1)})^2 [\sin \alpha \cos \theta \cos \psi + \cos \alpha \sin \theta]^2 \quad (3.15)$$

A simulation of the azimuthal dependence of the magnetic scattering intensity in $\sigma \rightarrow \pi'$ is illustrated in Figure 3.33. Although the simulation was not confirmed experimentally, due to time restrictions at the experiment, the azimuthal dependence of the electric dipole scattering length is well-established and leaves no doubts about the validity of the resulting intensity variation.

Similarly, in the $\sigma \rightarrow \sigma'$ polarization geometry, the total resonant electric dipole scattering length is:

$$g_{E1}^{\sigma \rightarrow \sigma'} = 2(g_{E1,\uparrow}^{\sigma \rightarrow \sigma'} - g_{E1,\downarrow}^{\sigma \rightarrow \sigma'}) \quad (3.16)$$

with the spin-up and spin-down scattering lengths given by Equation 2.26:

$$g_{E1,\uparrow}^{\sigma \rightarrow \sigma'} = g_{E1,\downarrow}^{\sigma \rightarrow \sigma'} = F^{(0)} + F^{(2)} \sin^2 \alpha \sin^2 \psi \quad (3.17)$$

Thus:

$$g_{E1}^{\sigma \rightarrow \sigma'} = 0 \quad (3.18)$$

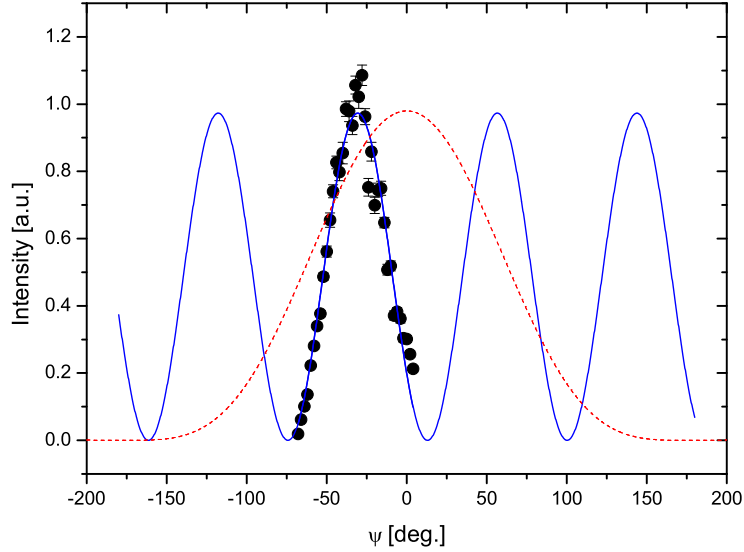


Figure 3.34: Azimuthal dependence of the integrated scattering intensity at the (0 1 1) reciprocal space position at the Ru L_{II} edge, as determined from $\theta - 2\theta$ -scans at $T = 144$ K, without polarization analyzer. The solid line is a fit of a $\cos^2(2\psi - \psi_o)$ -function to the data. For comparison, the simulation of the azimuthal dependence of the magnetic scattering intensity (Fig. 3.33) below T_N is also shown (dashed line). The two dependences are clearly different.

and the scattering intensity in $\sigma \rightarrow \sigma'$ is zero:

$$I_{(011)}^{\sigma \rightarrow \sigma'} = 0 \quad (3.19)$$

While the azimuthal dependence of the scattering intensity in the antiferromagnetic phase of Ca_2RuO_4 is known, as described above, this is not the case for the resonant scattering observed at (0 1 1) above the Néel temperature. This was determined experimentally, by carrying out $\theta - 2\theta$ scans around the (0 1 1) position for different azimuthal angles at sample temperature $T = 144$ K, and then calculating for every azimuthal angle the corresponding integrated intensity via fitting of a Gaussian profile to the data. The resulting azimuthal dependence is shown in Figure 3.34. It can be described by an equation of the type: $I \propto \cos^2(2\psi - \psi_o)$ (solid line in plot). The simulation of the magnetic scattering is clearly not consistent with the high-temperature data.

The azimuthal dependence of the scattered intensity in the novel phase between T_N and T_{OO} at (0 1 1) is thus quite different from the one expected for the magnetic phase below T_N at this position. It also differs from the dependence found for the high-temperature phase at (1 0 0). It is interesting that the scattering intensity shown in Figure 3.34 takes neither its maximum nor its minimum value when the

magnetic moment lies in the diffraction plane ($\psi = 0^\circ$). The maximum is reached instead when the moment is 30° off the plane. The characteristic period of the dependence is half the period found for the high-temperature phase at the (1 0 0) position (Figure 3.28) (90° instead of 180°).

3.8 Investigations at the (1 1 0) Reciprocal Space Position

The (1 1 0) reciprocal space position is not allowed for Bragg charge scattering by the *Pbca* space group. In addition, the magnetic structure factor is at this position equal to zero. Indeed, using for the magnetic basis ions the position vectors \mathbf{R}_j given by Equations 3.4, the total magnetic structure factor in $\sigma \rightarrow \pi'$ geometry is calculated for $\mathbf{Q} = (1\ 1\ 0) = \frac{2\pi}{a}\hat{\mathbf{x}} + \frac{2\pi}{b}\hat{\mathbf{y}}$ as follows:

$$\begin{aligned} g_{E1}^{\sigma \rightarrow \pi'} &= \sum_{j=1}^4 g_{E1, S_j}^{\sigma \rightarrow \pi'} e^{i\mathbf{Q} \cdot \mathbf{R}_j} = g_{E1, \uparrow}^{\sigma \rightarrow \pi'} e^0 + g_{E1, \downarrow}^{\sigma \rightarrow \pi'} e^{i\pi} + g_{E1, \uparrow}^{\sigma \rightarrow \pi'} e^{i\pi} + g_{E1, \downarrow}^{\sigma \rightarrow \pi'} e^{i2\pi} \\ &= g_{E1, \uparrow}^{\sigma \rightarrow \pi'} - g_{E1, \downarrow}^{\sigma \rightarrow \pi'} + g_{E1, \downarrow}^{\sigma \rightarrow \pi'} - g_{E1, \uparrow}^{\sigma \rightarrow \pi'} = 0 \end{aligned} \quad (3.20)$$

The same is the case in the $\sigma \rightarrow \sigma'$ polarization geometry. Thus, no magnetic scattering occurs at (1 1 0).

Nevertheless, resonant scattering intensity was still observed at (1 1 0). It is characterized by a polarization which has components both parallel and perpendicular to the scattering plane. Thus, in contrast to the scattering at the previously discussed positions, it gives contributions in both polarization channels, $\sigma \rightarrow \pi'$ and $\sigma \rightarrow \sigma'$. Its temperature- and azimuthal angle dependence in the two different polarization geometries provide information about the origin of the scattering.

3.8.1 Alignment

The initial alignment of the sample in the x-ray beam was carried out using the third harmonic component $\lambda/3$ of the x-rays, as described in Section 3.6.1, with the fundamental energy tuned at the Ru L_{II} absorption edge ($\lambda = 4.177 \text{ \AA}$). The (2 2 0) Bragg reflection was used for this purpose, which has at this energy a scattering angle of $\theta = 21.17^\circ$.

3.8.2 Energy Scans: Temperature Dependence

Energy scans around the Ru L_{II} absorption edge were carried out at the (1 1 0) position at various sample temperatures. They were performed with the magnetic

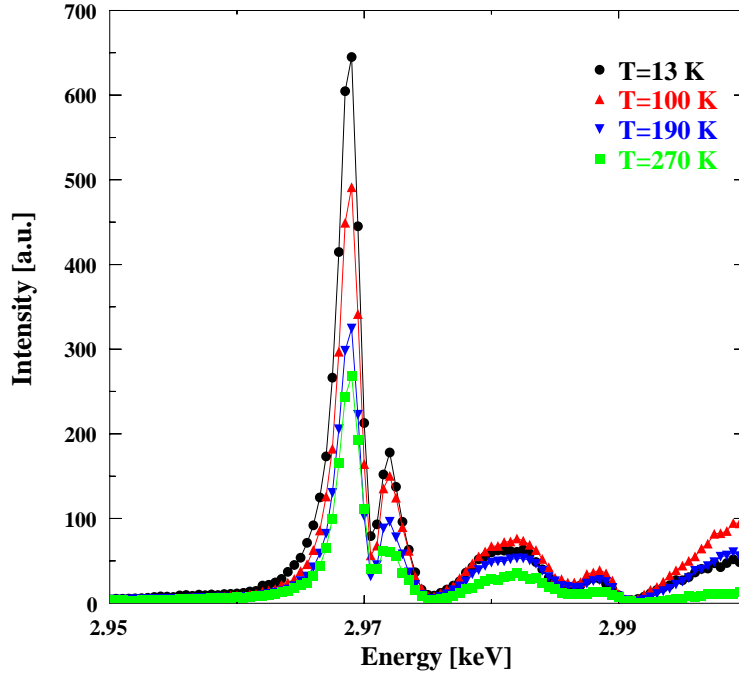


Figure 3.35: Energy dependence of the scattered intensity of the (1 1 0) reflection around the Ru L_{II} absorption edge at azimuth $\psi = 0^\circ$ for selected sample temperatures. All energy scans are corrected for absorption.

moment lying in the diffraction plane ($\psi = 0^\circ$) and without the use of polarization analyzer. A selection of these scans, corresponding to four characteristic temperatures, is presented in Figure 3.35. The scattering intensities have been normalized, as always, to the monitor before the sample position, and corrected for absorption by multiplying by the square of the absorption coefficient.

The lineshape of the energy scans at (1 1 0) is very similar to the one observed at the magnetic positions (1 0 0) and (0 1 1) at low temperatures. It is characterized by a double-peak structure, with the lower energy resonant peak exactly at the L_{II} edge and the higher energy (L_{II}') peak 4 eV above that. In contrast to what was the case at the magnetic positions, the two peaks follow at (1 1 0) practically the same temperature dependence up to room temperature. The ratio of their intensities stays therefore practically the same (factor of 4) within the whole temperature range investigated. Close to room temperature significant scattering intensity is still present at both energy positions. The broad spectral features observed at high energies, above the L_{II}' peak, at all reciprocal space positions investigated, are at (1 1 0) more pronounced than at (1 0 0) and (0 1 1).

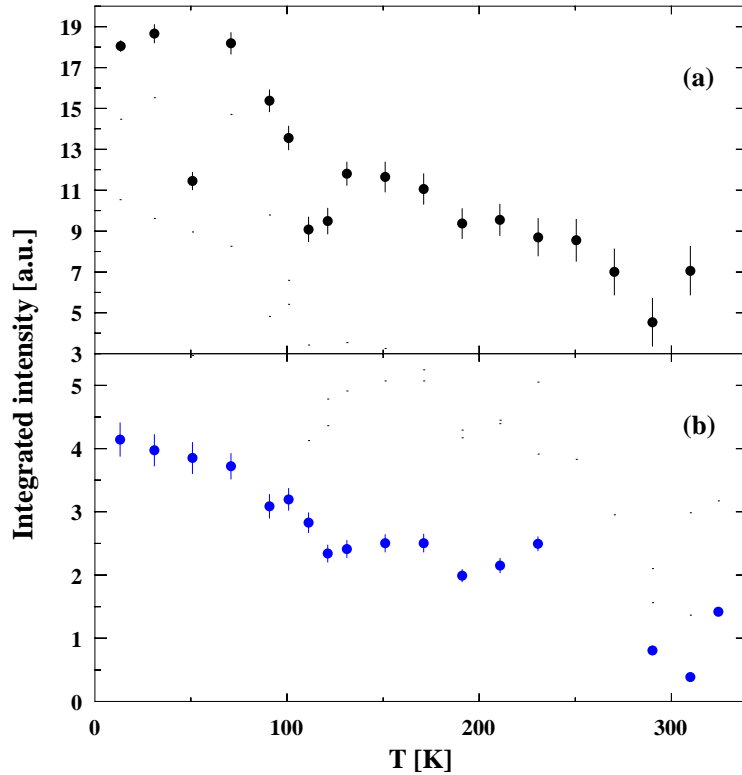


Figure 3.36: Temperature dependence of the integrated scattering intensity at the (1 1 0) reciprocal space position at the Ru L_{II} edge, as determined from $\theta - 2\theta$ -scans at $\psi = 0^\circ$, both without polarization analyzer (a) and in $\sigma \rightarrow \pi'$ geometry (b). The two dependences are practically identical to each other. No anomalies are observed up to 325 K, the highest temperature investigated.

3.8.3 Reciprocal Space Scans: Temperature Dependence

For determining the integrated scattering intensity at (1 1 0), $\theta - 2\theta$ scans were carried out around this position at various temperatures, both without the use of polarization analyzer, and in $\sigma \rightarrow \pi'$ geometry. The scans were performed with the magnetic moment lying in the scattering plane ($\psi = 0^\circ$). The resulting plots were fitted with Lorentzian profiles. The integrated intensities obtained from the fittings are plotted as a function of temperature in Figure 3.36. The upper panel shows the temperature dependence of the total scattering intensity (i.e. when no polarization analyzer is used), while the lower one the dependence in $\sigma \rightarrow \pi'$ polarization geometry.

In both cases, the integrated intensity decreases smoothly with increasing temperature, with no anomalies observed up to 325 K, the highest temperature investi-

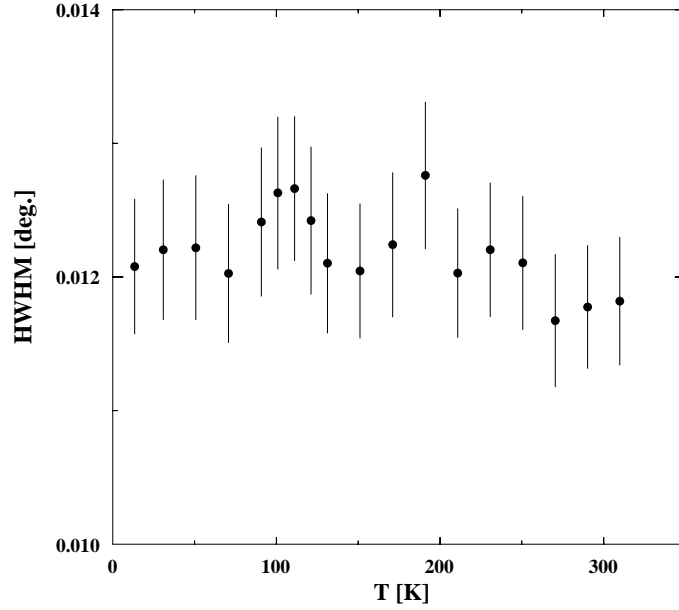


Figure 3.37: Variation with temperature of the half width at half maximum of the (1 1 0) peak in $\theta - 2\theta$ -scans carried out at the Ru L_{II} edge at $\psi = 0^\circ$, without polarization analyzer.

gated. This temperature dependence reminds strongly of the one observed at (1 0 0) at the L_{II}' energy position (2.972 keV) (Figure 3.26).

The variation with temperature of the half width at half maximum of the resonant peak at (1 1 0) is shown in Figure 3.37. For the determination of the width, the same $\theta - 2\theta$ -scans, fitted with Lorentzian profiles for the calculation of the integrated intensities, were again used. The resulting plot shows a constant peak width within the experimental error, with no anomalies observed in the whole temperature range investigated. The obtained width value ($\sim 0.012^\circ$) might be enhanced due to instrumental angular resolution limitations.

3.8.4 Reciprocal Space Scans: Azimuthal Angle Dependence

The azimuthal angle dependence of the resonant scattering intensity at (1 1 0) was also determined via $\theta - 2\theta$ scans, carried out at low temperatures ($T \approx 13$ K) separately in $\sigma \rightarrow \pi'$ and $\sigma \rightarrow \sigma'$ polarization geometries. The resonant peak obtained in every scan was fitted as previously with a Lorentzian profile, which provided the integrated intensity at the corresponding ψ -position. Figure 3.38 shows the experimentally determined azimuthal dependences at the (1 1 0) position in the two polarization channels. The solid lines are simulations based on a model

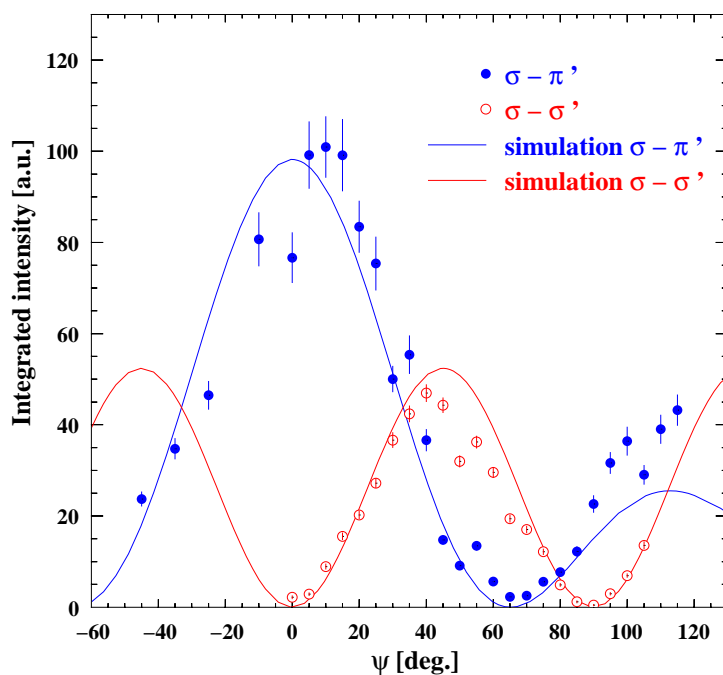


Figure 3.38: Azimuthal dependence of the integrated scattering intensity at the (1 1 0) reciprocal space position at the Ru L_{II} edge, as determined from $\theta - 2\theta$ -scans at $T = 13$ K, both in $\sigma \rightarrow \pi'$ (full bullets) and in $\sigma \rightarrow \sigma'$ (empty bullets) polarization geometries. The solid lines are simulations of the scattering intensity that originates from the breaking of the space-group symmetry caused by the tilt distortions of the RuO_6 octahedra.

explained below. At $\psi = 0^\circ$ the $\sigma \rightarrow \pi'$ component of the scattering intensity takes its maximum value, while the $\sigma \rightarrow \sigma'$ component is zero. With changing ψ , the $\sigma \rightarrow \sigma'$ intensity follows a $\sin^2 2\psi$ -dependence with a 90° periodicity, while the dependence of the $\sigma \rightarrow \pi'$ intensity is more complicated, probably of the type: $I \propto (\sin \psi \cos \theta - \cos 2\psi \sin \theta)^2$, with θ being the scattering angle. The maximum-intensity ratio $I_{\max}^{\sigma \rightarrow \pi'} / I_{\max}^{\sigma \rightarrow \sigma'}$ of the two components is approximately equal to 2 : 1.

3.8.5 Tilt Order: Simulation

As already mentioned in Section 3.1, Ca_2RuO_4 exhibits, like many other materials with perovskite-type structure, a distortion of its lattice characterized by a tilt order of the RuO_6 octahedra. Conventional, non-resonant x-ray scattering is insensitive to this tilting. Anomalous resonant x-ray scattering, on the contrary, is not. The reason is, that close to an absorption edge of the scattering material the atomic scattering factor for every ion site transforms from a scalar to a tensor with respect

to the polarization of the x-rays and thus becomes sensitive to the local electronic structure and the charge anisotropies of the ions. The tilting of the octahedra in Ca_2RuO_4 results in having Ru sites which, despite being crystallographically equivalent, have different oxygen environments. The atomic scattering factors for two such ions are in resonant diffraction different tensors. The result is non-zero scattering intensity at reciprocal space positions which are not allowed by the space group. In terms of electronic transitions, the tilting of the octahedra contributes to the splitting of the Ru $4d$ t_{2g} states, to which the core electrons are promoted in the resonant process. This splitting is necessary for the resonant cross-section to give non-zero scattering intensity.

Based on the above, resonant x-ray diffraction at the Ru absorption edges can be used as a probe of the tilt order in Ca_2RuO_4 . The reciprocal space positions where resonant scattering occurs provide information about the periodicity of the tilt order, while the width of the corresponding intensity peaks is proportional to the inverse correlation length that characterizes it. Such octahedral tilt order investigations have been previously reported for $3d$ compounds, such as LaMnO_3 , $\text{Pr}_{1-x}\text{Ca}_x\text{MnO}_3$ [70] and YTiO_3 [38].

The azimuthal dependence of the tilt order scattering intensity from Ca_2RuO_4 at a particular reciprocal space position can be calculated with the help of a simple model, for which the occupancies of the relevant (t_{2g}) orbitals, the tilting angles of the octahedra and the space group symmetry of the compound need to be known. We assume for the ion located at site 1 (Figure 3.27) a diagonal form factor of the type:

$$f_1 = \begin{pmatrix} f_\alpha & 0 & 0 \\ 0 & f_\alpha + \Delta f_\alpha & 0 \\ 0 & 0 & f_\alpha \end{pmatrix} \quad (3.21)$$

where f_α is the isotropic term and Δf_α the anisotropic strength of the form factor [38]. Based on the currently dominant theories about the orbital occupancies in Ca_2RuO_4 (Section 3.2), we assume a fully occupied (0 holes/site) d_{xy} orbital and half-occupied (1 hole/site) d_{yz}/d_{zx} orbitals to start with, thus a wavefunction of the form:

$$\Psi = c_1|zx\rangle + c_2|xy\rangle \quad (3.22)$$

with: $c_2 = 2c_1$ and $c_1^2 + c_2^2 = 1$. The occupancy factors c_1 , c_2 determine the rotation angles for expressing the form factor in the coordinate frame of the crystal. Further rotation matrices are introduced for taking into account the tilt angles α , β and γ of the octahedra around the axes c , b and a of the coordinate frame of the crystal, respectively. For Ca_2RuO_4 we have: $\alpha = 11.8^\circ$ and $\beta = 12.7^\circ$ (Section 3.1, the low temperature values are used). After multiplying the original form factor by these rotation matrices, the symmetry operations of the space group have to be applied, in order to obtain the form factors for the rest of the sites. Then the structure factor

for a particular reciprocal space position can be calculated. For (1 1 0) it reads:

$$F_{(110)} = \sum_{j=1}^4 f_j e^{i\mathbf{Q}\cdot\mathbf{R}_j} = f_1 - f_2 - f_3 + f_4 \quad (3.23)$$

The scattering geometry enters the calculations via the rotation matrices which transform the structure factors into the coordinate frame of the laboratory. For (1 1 0), a rotation around y by 134.57° , as well as one around x by 90° are needed. As far as the polarization of the x-rays is concerned, this can be expressed in the laboratory frame for the linearly polarized incoming beam with the vector $[0 \ 1 \ 0]$, and for the $\sigma \rightarrow \pi'$ and $\sigma \rightarrow \sigma'$ components of the scattered beam with the vectors $[-\sin \theta \ 0 \ \cos \theta]$ and $[0 \ 1 \ 0]$, respectively, where θ is the scattering angle ($\theta = 22.85^\circ$ for (1 1 0) at the Ru L_{II} edge).

The above calculations were carried out in the computer algebra programme MapleTM, with the help of a code previously developed by J.P. Hill for YTiO₃, appropriately modified for application on Ca₂RuO₄. The code can be found (with the output compressed) in Appendix C. The azimuthal dependence of the scattering intensity calculated in this way for the $\sigma \rightarrow \pi'$ and $\sigma \rightarrow \sigma'$ scattering geometries is displayed in Figure 3.38 (solid curves). The agreement of the simulated intensities with the experimental data is quite good.

3.9 Investigations at Half-Integer Reciprocal Space Positions

The theory suggested by Hotta and Dagotto for the orbitally ordered state in Ca₂RuO₄ [53] was the first to propose an 'antiferro-orbital' periodic pattern, with different Ru t_{2g} orbitals occupied at neighboring sites in the lattice. One of the main consequences of the proposed orbital arrangement is the doubling of the size of the system's unit cell in all three crystallographic directions (Figure 3.7). Such a doubling of the unit cell would result in reflections with non-zero intensity at reciprocal space positions with half-integer Miller indices. Motivated by these predictions, we searched for resonant scattering at positions $(\frac{1}{2} \ \frac{1}{2} \ \frac{1}{2})$ and $(\frac{1}{2} \ \frac{1}{2} \ 0)$ of the reciprocal space. No scattering above background was observed at these positions. Our experimental results therefore do not confirm the orbital order suggested by Hotta and Dagotto, or any other model proposing for Ca₂RuO₄ a unit cell larger than the atomic unit cell. An explicit exclusion of the models cannot be made though, because the possibility that weak non-zero scattering intensity is present at the above positions and remains unobservable in our experiments due to the very small structure factors, still exists.

3.10 Muon Spin Rotation Measurements

Motivated by the broad feature observed in susceptibility measurements around 260 K in Ca_2RuO_4 powder samples (Figure 3.10), we investigated the possibility that the new phase discovered above T_N in the single crystal diffraction experiments is of magnetic origin. For this, an experimental technique which is sensitive to small magnetic moments is needed. Muon spin rotation (μSR) is appropriate for investigating the magnetic structure and dynamics of matter on atomic scale and provides the required sensitivity. The technique involves implanting spin-polarized positive muons into a sample and observing the effect of the sample's local environment on the muons' behavior.

Muons are spin 1/2 unstable fundamental particles (leptons) with mass $m_\mu = 207m_e$ (m_e : electron mass), which decay after an average lifetime of 2.2 μs to produce a positron and two neutrinos. When implanted within a solid, a muon acts like a microscopic magnetometer. Its spin precesses under the influence of the local magnetic field and the direction that the spin eventually has at the moment of the muon's decay gives information about the local magnetic field with which the spin previously interacted. The final direction of the muon's spin can be determined with the help of the emitted positron. The emission of the positron takes place preferentially along the direction of the polarization of the muon at the moment of the decay. Thus, in conclusion, by detecting the eventually produced positrons, we can obtain information about the properties of the local magnetic field in the investigated solid. The power of the technique lies in the fact that it is a very local and sensitive probe of magnetic fields and their fluctuations. Its detection limit can be of the order of down to 0.01 μ_B .

Muon spin rotation measurements were carried out both on powder Ca_2RuO_4 samples and on single crystals of the same origin as the ones used in the diffraction experiments. The measurements were performed by C. Bernhard and J. Chakhalian at the General Purpose Spectrometer beamline at the Paul Scherrer Institute (PSI) in Switzerland. Figure 3.39 shows the non-magnetic fraction of a powder Ca_2RuO_4 sample as a function of temperature, as determined with μSR at transverse applied magnetic field 100 Oe. The data clearly show a magnetic transition taking place above approximately 110 K and being completed close to 170 K. The non-magnetic fraction of the sample above 170 K and all the way up to room temperature is, within the experimental sensitivity (of the order of 0.01 μ_B), equal to 100%. Indications for a magnetic phase transition close to 260 K are completely absent. A similar behavior is also observed in the single-crystal samples, but the magnetic transition is sharper there and the non-magnetic fraction of the sample reaches the value of 100% below 150 K. The difference is due to inclusions in the powder sample of the so-called B-centered magnetic phase, which is characterized by a higher Néel temperature ($T_N^B = 150$ K). This phase is apparently absent in the

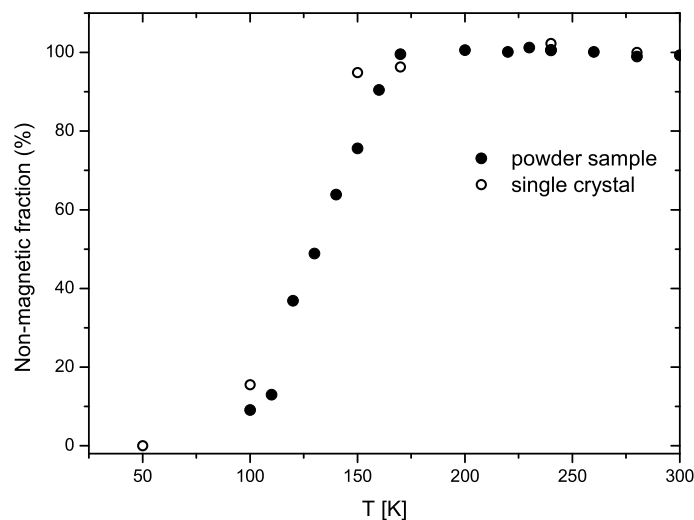


Figure 3.39: Non-magnetic fraction (in %) of the powder (closed bullets) and of the single-crystal (open bullets) Ca_2RuO_4 samples, as determined with muon spin rotation at transverse magnetic field 100 Oe. No ordered magnetic moment is measured above the Néel temperature. No anomaly is observed around 260 K.

single crystals, which have a higher degree of purity.

The important piece of information obtained by the above μSR data is that there is no ordered magnetic moment in Ca_2RuO_4 above the phase transition from the low-temperature antiferromagnetic to the high-temperature paramagnetic phase. The detection limit of the technique is one order of magnitude lower than the amplitude of the magnetic moment that would be expected in the new phase if it were magnetic, based on the ratio of the integrated scattered intensities below and above the magnetic phase transition (Figure 3.30). Indeed, given the fact that the amplitude of the magnetic moment in the low-temperature antiferromagnetic phase, as determined by neutron diffraction, is equal to $1.3 \mu_B$ [51], and that the scattering intensity above T_N is a factor of 20 weaker than at low temperatures (Figure 3.30), if the phase above T_N were magnetic, the ordered moment that would be needed to produce the observed scattering intensity would be a factor of $\sqrt{20}$ smaller than $1.3 \mu_B$, i.e. of the order of $0.3 \mu_B$. Such a magnetic moment is at least one order of magnitude larger than the detection limit of the μSR technique and would be easily detected if it existed. The fact that no such ordered moment is observed shows that the scattering intensity above T_N is not of magnetic origin. The newly discovered phase transition at 260 K is thus a transition between two paramagnetic phases.

3.11 The $\text{Ca}_{1.9}\text{Sr}_{0.1}\text{RuO}_4$ System

Doping Ca_2RuO_4 with Sr leads to a rapid decrease of the metal-insulator transition temperature T_{MI} , as seen in the phase diagram of Figure 3.1. For doping level $x = 0.1$ the transition from the high-temperature, metallic $L\text{-}Pbca$ phase to the low-temperature, insulating $S\text{-}Pbca$, takes place already around 175 K. Neutron and x-ray diffraction investigations show a large thermal hysteresis of about 50 K around the transition. Except for the lower phase transition temperature, the transition itself is quite similar to the one occurring at 356 K in the pure compound.

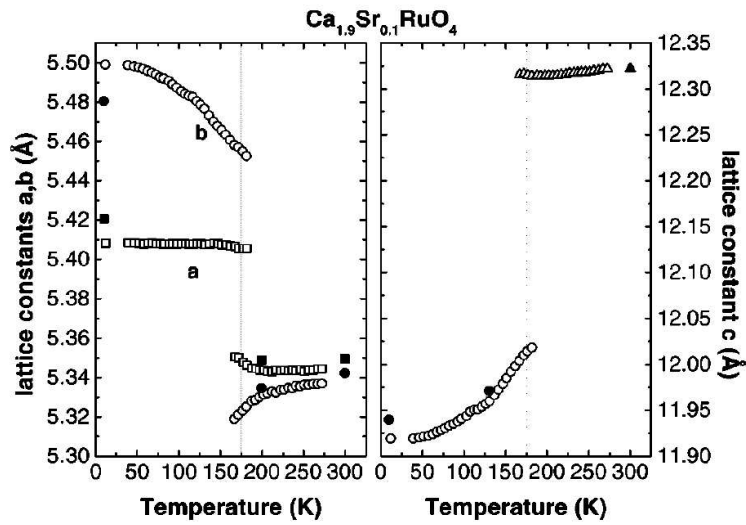


Figure 3.40: Variation with temperature of the lattice parameters a , b (left) and c (right) of $\text{Ca}_{1.9}\text{Sr}_{0.1}\text{RuO}_4$, as determined with neutron diffraction [56]. Large, discontinuous changes in all parameters accompany the first-order transition at $T_{MI} = 175$ K. The changes occurring within the low-temperature phase, below T_{MI} , are smaller than in Ca_2RuO_4 .

The lattice parameters, the Ru-O bond lengths and the octahedral tilt angles undergo in $\text{Ca}_{1.9}\text{Sr}_{0.1}\text{RuO}_4$ significant discontinuous changes at T_{MI} , similar to what was observed in Ca_2RuO_4 (Figures 3.40, 3.41). But the temperature dependence of all structural parameters below T_{MI} , within the $S\text{-}Pbca$ phase, is in $\text{Ca}_{1.9}\text{Sr}_{0.1}\text{RuO}_4$ much weaker than in the pure compound. The most important effect of this is that the out-of-plane Ru-O bonds (Ru-O(2)) never become shorter than the in-plane ones (Ru-O(1)), even at very low temperatures. In other words, the RuO_6 octahedra are never flattened perpendicular to c within the whole $S\text{-}Pbca$ phase. The octahedral shape observed in the pure compound within a small temperature range below the metal-insulator transition (between approximately 300 K and 360 K) is thus in the $x = 0.1$ doped material stable down to the lowest temperatures.

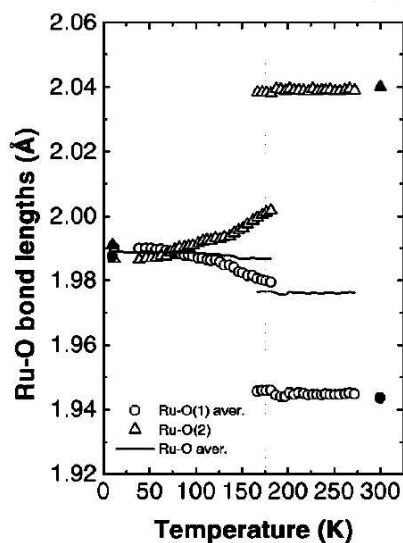


Figure 3.41: Variation with temperature of the Ru-O bond lengths in $\text{Ca}_{1.9}\text{Sr}_{0.1}\text{RuO}_4$, as determined with neutron diffraction [56]. The out-of-plane (Ru-O(2)) bonds are always longer than the ones in the ab -plane (Ru-O(1)) or at least equal to them, i.e. the RuO_6 octahedra remain, unlike in Ca_2RuO_4 , slightly elongated along c even at low temperatures.

As far as the magnetic properties are concerned, $\text{Ca}_{1.9}\text{Sr}_{0.1}\text{RuO}_4$ exhibits antiferromagnetic order below $T_N = 143$ K [56]. The Ru ions order according to the B-centered arrangement shown in Figure 3.8, different from Ca_2RuO_4 . However, the ordered magnetic moment is still aligned along the b direction, showing that it is mainly the tilt direction, and not the stretching of the octahedra, that determines the spin direction.

It is interesting to investigate how and to what degree the resonant x-ray diffraction features observed in Ca_2RuO_4 change upon Sr-doping. Determining their dependence on the Ru^{+4} spin arrangement on one hand, and the octahedral distortions on the other, can provide information about their origin.

The fact that the metal-insulator transition temperature lies in the $x = 0.1$ doped material below room temperature, but above the Néel temperature, makes its investigation technically difficult. For the material to reach the low-temperature magnetically ordered phase, it is necessary to pass through the metal-insulator transition. But this first-order transition has destructive results on the sample. The large, discontinuous structural distortions suffered by the crystal at T_{MI} result in its cracking and breaking. Most crystals are destroyed to such a degree at this temperature, that it is not possible to obtain any data thereafter. The experiments showed that, concerning this issue, it is preferred to use non-perfect crystals of relatively broad mosaic width for the measurements. Such crystals have more chances

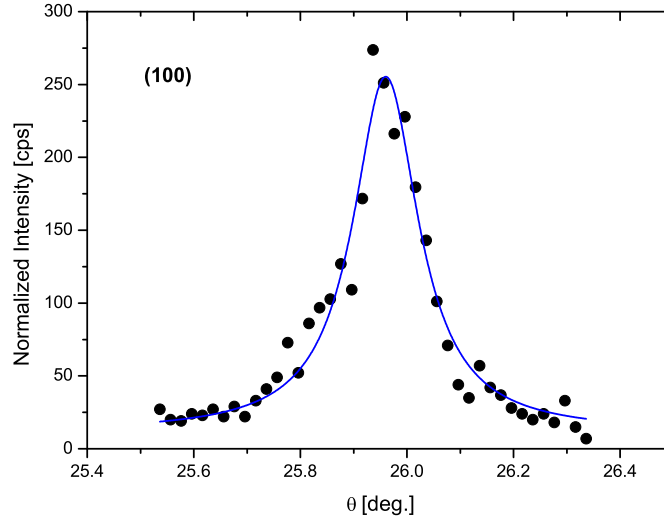


Figure 3.42: Rocking curve of the $\text{Ca}_{1.9}\text{Sr}_{0.1}\text{RuO}_4$ sample used in the x-ray diffraction investigations. The presented θ -scan was carried out at the Ru L_{II} absorption edge, at low temperatures ($\approx 20\text{ K}$), around the $(1\ 0\ 0)$ reciprocal space position. The solid line is a fit of a Lorentzian profile to the experimental data. The width of the reflection is significantly larger than of the Ca_2RuO_4 samples. The worse crystal quality increases the probability that the sample undergoes the metal-insulator transition without being totally destroyed.

to survive the phase transition, probably because the coexistence of several mosaic domains provides more space for the relaxation of the lattice.

The sample used in the investigations described in this section was grown by the floating-zone method by R. Jin and D. Mandrus at Oak Ridge National Laboratory (Oak Ridge, USA). The full width at half maximum of its rocking curve (θ -scan) at the $(1\ 0\ 0)$ position is around 0.15° (Figure 3.42), i.e. two to four times larger than most $\text{Ca}_{2-x}\text{Sr}_x\text{RuO}_4$ crystals (either pure (Section 3.5.1) or Sr-doped) grown by Maeno's group. The sample was able to undergo the first-order metal-insulator transition around 175 K without being totally destroyed. Despite cracking and moving, the largest part of it remained fixed on the sample holder in a condition which allowed the performance of measurements. The main problem that arises due to the large mosaic width of the sample is that no polarization analysis of the scattered signal can be performed. The imperfect sample satisfies the Bragg scattering condition within a relatively broad range of angles, over which the scattering intensity is distributed. Because of the fact that the Si(1 1 1) polarization analyzer is a much more perfect crystal, only a small fraction of the x-rays scattered by the sample are selected (through the scattering condition) by the analyzer and further diffracted into the detector.

Investigations at (1 0 0)

The B-centered magnetic arrangement, which is established in $\text{Ca}_{1.9}\text{Sr}_{0.1}\text{RuO}_4$ at low temperatures, is expected to give rise to magnetic reflections at reciprocal space positions (0 1 0) and (1 0 1). The positions (1 0 0) and (0 1 1), on the contrary, which were magnetically allowed in Ca_2RuO_4 , have zero magnetic structure factor in the doped system. It is interesting to examine whether the new phase discovered in Ca_2RuO_4 below 260 K at (1 0 0) and (0 1 1) is influenced by the change of the magnetic order from A-centered to B-centered.

Figure 3.43(a) shows the temperature dependence of the integrated scattering intensity, as determined from h -scans carried out around the (1 0 0) reciprocal space position, at the Ru L_{II} absorption edge, at azimuth $\psi = 0^\circ$ (with the b -direction in the diffraction plane). Lorentzian profiles have been used for the fitting of the data. The measurements were carried out without polarization analyzer, for the reasons explained above. The strong magnetic scattering intensity observed in Ca_2RuO_4 at (1 0 0) below 110 K (Figure 3.24) is absent in the Sr-doped compound. Some weak resonant intensity is still measured at this position, but this cannot be of magnetic origin, for reasons explained in Section 3.12. It decreases smoothly with increasing temperature, without showing any anomalies, and vanishes around 130 K. The variation of the peak's half-width at half-maximum with temperature is shown in panel (b) of Figure 3.43. It remains constant up to approximately 80 K, where it starts increasing significantly. Its final value is about 50% higher than at low temperatures. The observed widths in $\text{Ca}_{1.9}\text{Sr}_{0.1}\text{RuO}_4$ are in general larger than at the same reciprocal space position in Ca_2RuO_4 at temperatures above the magnetic transition (Figure 3.25), showing that Sr-doping reduces the correlation length of the ordering mechanism that gives rise to the (1 0 0) reflection.

Investigations at (1 1 0)

The (1 1 0) reciprocal space position is magnetically forbidden, not only for the A-centered magnetic phase established in Ca_2RuO_4 , but also for the B-centered arrangement of $\text{Ca}_{1.9}\text{Sr}_{0.1}\text{RuO}_4$. Nevertheless, as in Ca_2RuO_4 , resonant scattering intensity is present in the Sr-doped system at this position. Its variation with temperature is shown in Figure 3.44(a). The integrated intensities were calculated from $\theta - 2\theta$ -scans carried out around (1 1 0) at the Ru L_{II} edge at azimuth $\psi = 0^\circ$, without polarization analysis. Lorentzian profiles were used for the fitting of the experimental peaks at all temperatures. The intensity follows a smooth decrease with increasing temperature up to the metal-insulator transition, around 190 K, similar to the one observed at the same position in Ca_2RuO_4 . Just before the transition, it has a value of approximately 50% the scattering intensity at base temperature. Above the transition it drops to about 13% of the low-temperature value and remains

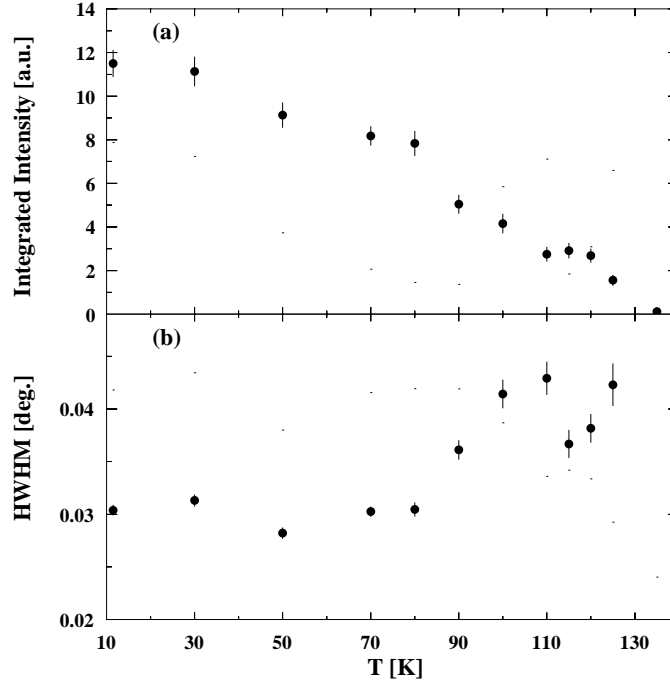


Figure 3.43: Temperature dependence of the integrated scattering intensity (a) and of the half-width at half-maximum (b) of the (1 0 0) reflection at the Ru L_{II} edge in $\text{Ca}_{1.9}\text{Sr}_{0.1}\text{RuO}_4$, as determined from h -scans carried out at $\psi = 0^\circ$ without polarization analyzer and fitted with Lorentzian profiles. The given temperatures are control sensor values.

practically constant thereafter, up to 300 K, the highest temperature investigated. The variation with temperature of the peak's half-width at half-maximum is shown in panel (b) of the same figure. A broadening of the peak is observed towards the metal-insulator transition. Above 200 K the width is reduced again, almost back to its low-temperature value.

The azimuthal dependence of the scattering intensity at (1 1 0), as determined from h -scans carried out at low temperatures ($T \approx 26$ K) at the Ru L_{II} edge, is shown in Figure 3.45. Again no separate measurement of the σ' and π' components of the polarization was possible. The model used in Ca_2RuO_4 for the simulation of the resonant intensity arising from the octahedral tilt order (Section 3.8.5) can be applied also in $\text{Ca}_{1.9}\text{Sr}_{0.1}\text{RuO}_4$, but in this case, since only the total scattering intensity is available, the sum of the $\sigma \rightarrow \sigma'$ and $\sigma \rightarrow \pi'$ contributions given by the model is calculated and compared to the experimental data. The solid line in Figure 3.45 represents the simulated total intensity. Although the periodicity of the simulated curve is consistent with what is experimentally observed, the ratio of the maximum intensities of the two polarization components is in the simulation a factor

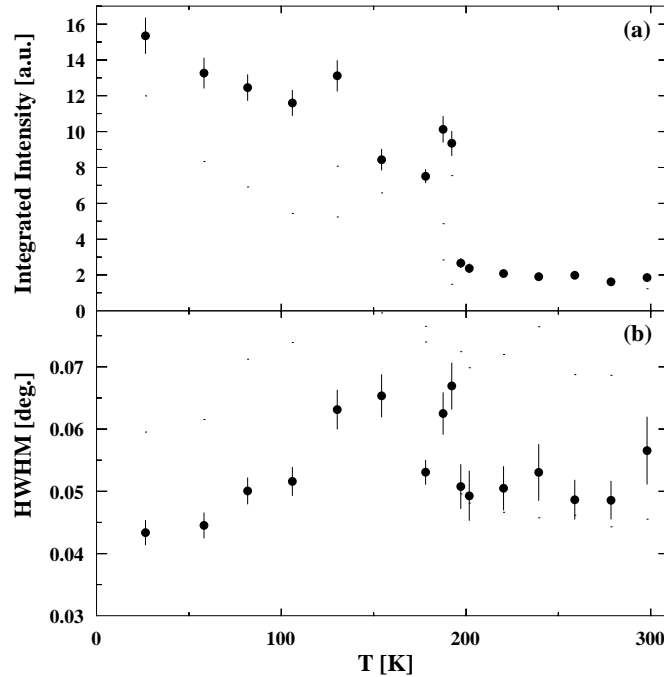


Figure 3.44: Temperature dependence of the integrated scattering intensity (a) and of the half-width at half-maximum (b) of the (1 1 0) reflection at the Ru L_{II} edge in $\text{Ca}_{1.9}\text{Sr}_{0.1}\text{RuO}_4$, as determined from $\theta - 2\theta$ -scans, carried out at $\psi = 0^\circ$ without polarization analyzer, and fitted with Lorentzian profiles.

of 3.5 larger than in the experimental results, resulting in a poor agreement between the curve and the data points in the plot. A best fit of the simulation to the data is achieved if the contribution from the $\sigma \rightarrow \sigma'$ polarization channel is suppressed by a factor of 3.5 with regard to the $\sigma \rightarrow \pi'$ component (inset of the figure).

The reason for the poor reproduction of the intensity ratio by the used tilt-order model is not quite clear. An important effect that has to be taken into consideration is the variation of the absorption of the x-ray beam by the sample as a function of the azimuthal position ψ . As the sample is rotated around the scattering vector, the orientation of the scattering surface with regard to the incoming beam changes. The geometrical factor s which is used in the calculation of the absorption coefficient μ from the fluorescence yield of the sample (Appendix A) is thus different at every azimuthal position. This effect has not been taken into consideration in the absorption correction of the scattered intensities, since the small size and the non-symmetric shape of the sample make the determination of the surface orientation at a certain ψ -value practically impossible. Depending on the shape of the sample and the degree of variation of the geometrical parameters with ψ , the imperfect absorption correction can lead to smaller or larger errors in the calculated intensities and the

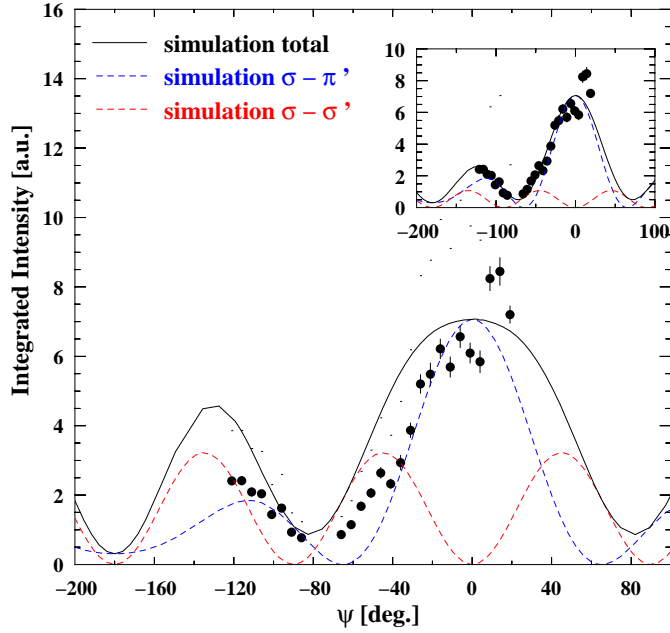


Figure 3.45: Azimuthal dependence of the integrated scattering intensity from $\text{Ca}_{1.9}\text{Sr}_{0.1}\text{RuO}_4$ at the $(1\ 1\ 0)$ reciprocal space position, as determined from h -scans carried out at the Ru L_{II} edge at $T \approx 26$ K without polarization analyzer. The solid line is the simulation of the total scattering intensity from the tilt order of the RuO_6 octahedra, calculated by summation of the $\sigma \rightarrow \sigma'$, $\sigma \rightarrow \pi'$ contributions given by the model (Section 3.8.5). The inset shows the same simulation, but with the $\sigma \rightarrow \sigma'$ contribution suppressed by a factor of 3.5, chosen to make the simulation agree with the data.

resulting azimuthal dependence. The problem could be eliminated by normalizing the resonant intensities to a main Bragg peak, but, as already explained, no charge Bragg reflection was accessible at the L_{II} absorption edge in the experiment.

3.12 Discussion

One of the most significant results of our investigations on Ca_2RuO_4 single crystals at the Ru L -absorption edges is the discovery of a new phase transition around 260 K at wave-vector positions, which are also magnetically allowed ($(1\ 0\ 0)$, $(0\ 1\ 1)$). Based on the above described experimental results, it is possible to draw conclusions on the origin of this phase transition and the properties of the ordered phase below its characteristic temperature.

Polarization analysis of the scattered radiation with use of a suitable analyzer crystal at the wave-vectors where the new phase is observed showed that the diffracted

beam has within the whole temperature range investigated only a π' component, i.e. its polarization is purely parallel to the diffraction plane (Section 3.6.3). This means that resonant scattering from the ordered phase observed above the Néel temperature results in a full rotation of the polarization of the x-ray beam from σ to π' . As mentioned in Section 2.4.2 (Equation 2.12), charge scattering (anomalous dispersion term of the resonant elastic scattering length) does not rotate the polarization plane of the incoming beam. Thus, for σ -polarized incoming x-rays, charge scattering would give σ' -polarized diffracted radiation. The fact that such an unrotated component of the polarization vector is not experimentally observed in the diffracted beam, shows that charge scattering does not contribute to the resonant intensity in the new phase.

The possibility that the phase transition at 260 K is of magnetic origin, in addition to the already known antiferromagnetic phase transition at $T_N = 110 - 150$ K, was investigated in the following. The complementary muon spin rotation (μ SR) measurements that were carried out on powder and single-crystal Ca_2RuO_4 samples (Section 3.10) showed no ordered magnetic moment above T_N . Based on this, and given the fact that the detection limit of the technique lies well below the amplitude of the ordered moment that should be expected if the scattering intensity in the new phase were due to magnetic order, it can be concluded that the observed signal is not of magnetic origin. The phase transition at 260 K is thus a transition between two paramagnetic phases.

Another possibility for the origin of the new phase is the tilting order of the RuO_6 octahedra. As already explained in Section 3.8.5, the tilt of the octahedra, in conjunction with the aspherical charge density of the Ru t_{2g} electrons, can give rise to resonant scattering at positions not allowed by the space group. The structure factor due to tilt order is, according to the simulation results (Section 3.8.5), small but non-zero at positions (1 0 0) and (0 1 1). However, the temperature dependence of the octahedral tilt angles in the insulating phase of Ca_2RuO_4 , as determined by powder neutron diffraction (Figure 3.4), does not support the tilt-related scenario for the origin of the new phase. Indeed, the tilt angles decrease smoothly with increasing temperature and show no anomalies at 260 K, where the phase transition is observed in the x-ray investigations. If the phase transition were due to cooperative tilt order phenomena, then a corresponding structural phase transition should be also observed in the temperature dependence of the tilt angles, which is not the case. What is more, the azimuthal angle dependences of the simulated intensities at positions (1 0 0) and (0 1 1) are different from the ones experimentally observed. The origin of the L_{II} resonant signal above T_N at these positions must be thus different from the octahedral tilt order.

Having excluded charge scattering, magnetic order and octahedral tilt order as possible origins of the resonant diffraction intensity above the Néel temperature, it is reasonable to assume that the observed intensity originates from the ordering of

the Ru $4d$ orbitals. An orbitally ordered phase in Ca_2RuO_4 has been theoretically predicted by several studies, as already stated in Section 3.2, and our experimental technique is expected to be sensitive to such an order, because it directly probes the relevant $4d$ electronic states. Since only the t_{2g} orbitals are partly occupied in the $4d$ band (Section 3.2), it is these orbitals which participate in the orbital order. From the fact that the orbital order reflections are observed at the same wave-vectors at which magnetic scattering occurs below T_N , we conclude that the propagation vector of the orbital order is in Ca_2RuO_4 identical to the propagation vector characterizing the low-temperature antiferromagnetic phase. The azimuthal dependence of the integrated intensity due to orbital order is at $(1\ 0\ 0)$ the same as the one expected for the magnetic intensity at this position, i.e. following a $\cos^2\psi$ -law. This is not the case at $(0\ 1\ 1)$, where the orbital-order intensity rather follows a $\cos^2(2\psi - \psi_o)$ -law instead of the dependence corresponding to the resonant electric dipole scattering length. The precise determination of the occupancy of the t_{2g} orbitals at every site of the unit cell based on this information would demand the performance of numerical calculations, which are so far not available. However, our experimental results can be already used for examining the viability of some of the theoretically suggested orbital order patterns.

In particular, a purely ferro-orbital arrangement, with the d_{xy} orbital completely full, would not be consistent with the observation of superstructures at positions forbidden for Bragg charge scattering. Indeed, a fully occupied d_{xy} orbital would result in having only one possible spin arrangement for the remaining two t_{2g} orbitals, which have the same energy. The doubly degenerate d_{yz}/d_{zx} -state would be half-occupied with two parallel spins at all Ru^{+4} sites and the orbital arrangement would have the periodicity of the lattice, thus no additional superstructure reflections would be observed. For the d_{yz}/d_{zx} degeneracy to produce an order with different periodicity from the lattice, electronic transitions from the core level into the d_{xy} orbital must be also possible. In other words, all three t_{2g} orbitals must be active and the energy difference between d_{xy} and d_{yz}/d_{zx} should be not larger than a couple of hundred meV. An antiferro-orbital order resulting in a doubling of the crystal periodicity in all three crystallographic directions would be also not consistent with our investigations, and in particular with the absence of resonant reflections at reciprocal space positions with half-integer Miller indices. Such a doubling would invoke non-zero structure factors at reciprocal space positions such as $(\frac{1}{2}\ \frac{1}{2}\ 0)$ and $(\frac{1}{2}\ \frac{1}{2}\ \frac{1}{2})$. No scattering intensity was observed at these positions, showing that such a scenario is not viable in this case. Other possibilities, like for instance a predominantly ferro-orbital arrangement with the occupied orbitals differently canted at neighboring sites, might have to be considered instead, for the interpretation of our results.

The orbital ordering phase transition discovered in Ca_2RuO_4 at 260 K is present also in the Sr-doped compound $\text{Ca}_{1.9}\text{Sr}_{0.1}\text{RuO}_4$, but at a lower critical temperature.

Indeed, as seen in Section 3.11, despite the change of the magnetic arrangement from A-centered to B-centered, which is caused by the Sr-doping and which results in having zero magnetic structure factor at $(1\ 0\ 0)$, a significant resonant scattering intensity is measured at this position below approximately 130 K (Figure 3.43). This scattering intensity apparently arises from an orbitally ordered phase similar to the one in Ca_2RuO_4 . The possibility that the resonant intensity at $(1\ 0\ 0)$ is not due to orbital ordering but of magnetic origin instead, arising from an inclusion of some A-centered phase in the compound, is negligible. Indeed, while in stoichiometric, undoped Ca_2RuO_4 a mixture of the two magnetic phases seems to be relatively common and very high quality single crystals are needed to ensure that the magnetic structure is purely A-centered, in oxygen-excess or Sr-doped compounds the B-centered magnetic phase is always the only one observed and the A-centered mode is reduced to only a few short-range-ordered domains that give negligible contribution [51, 56, 71]. It is thus quite unlikely that the A-centered phase in our $\text{Ca}_{1.9}\text{Sr}_{0.1}\text{RuO}_4$ sample is responsible for the strong resonance at $(1\ 0\ 0)$. In addition, the temperature dependence of the intensity measured at this position is quite different from what normally expected for a magnetic order parameter, namely following a power law (see, for example, the magnetic transition in Ca_2RuO_4 at 110 K in Figure 3.24). Instead, the $(1\ 0\ 0)$ intensity in $\text{Ca}_{1.9}\text{Sr}_{0.1}\text{RuO}_4$ follows a smooth, almost linear decrease with increasing temperature, which starts already at the base temperature and reminds strongly of the temperature dependence around the 260 K orbital ordering phase transition of Ca_2RuO_4 .

These results strongly indicate that orbital ordering at low temperatures is a generic feature of all $\text{Ca}_{2-x}\text{Sr}_x\text{RuO}_4$ compounds with low Sr-doping levels. A whole new phase can thus be added in the low-doping region of the $\text{Ca}_{2-x}\text{Sr}_x\text{RuO}_4$ phase diagram (Figure 3.1), extending in temperature up to 260 K at $x = 0$ and up to 130 K at $x = 0.1$. The propagation vector of the orbital order remains unaffected by the Sr-doping and the subsequent change of the Ru spin arrangement. This is concluded from the fact that the wave-vectors at which the scattering from the orbitally ordered phase occurs, remain unchanged in the doped compound, despite the shift of the magnetically allowed positions. The insensitivity of the propagation vector of the orbital order to Sr-doping is explained if one takes into consideration the layered structure of the material. The two magnetic modes, A- and B-centered, differ only in the way of stacking of antiferromagnetically ordered RuO_2 layers one above the other, i.e. in the sign of the effective interlayer exchange interaction. This interaction is expected to be weak, due to the quasi-two-dimensional structure of $\text{Ca}_{2-x}\text{Sr}_x\text{RuO}_4$. Because of the strong frustration which is present in the system, even small distortions of the lattice can strongly influence the interlayer exchange interaction. Such small lattice distortions, caused by the Sr substitution, are apparently responsible for the change of the magnetic structure upon doping. These are not sufficient though for influencing the orbital order. Given the fact that the

in-plane magnetic structure is identical in both cases, and that the interplane interaction is weak, it is not surprising that identical orbital ordering patterns are also found, independent of Sr doping.

The energy scans that were carried out in Ca_2RuO_4 around the Ru $L_{\text{II}}/L_{\text{III}}$ absorption edges showed a characteristic double-peak structure at all the investigated reciprocal space positions (Figures 3.22, 3.29, 3.35). Besides the resonance observed at the energy of the absorption edge, a second resonant enhancement of the scattering intensity is in all cases present approximately 4 eV above the edge. The double-peak character of the resonance remains also after the correction of the measured intensities for absorption effects. At the magnetically allowed reciprocal space positions (1 0 0) and (0 1 1), the scattering intensity follows quite different temperature dependences at the two energy positions (e.g. Figures 3.24, 3.26). Only the low-energy resonance, occurring at the absorption edge, is sensitive to the orbital ordering phase transition at 260 K. The higher-energy peak shows, on the contrary, no anomaly at least up to 310 K, the highest temperature investigated. At (1 1 0) no phase transitions are present neither at the low- nor at the high-energy position. Both resonant features in the energy scan follow there the same smooth decrease in intensity with increasing temperature (Figure 3.36). These results can be understood on the basis of electric dipole transitions in the Ru^{+4} ions at the L-absorption edges. Electrons from the $2p$ core level are promoted directly into the partly filled $4d$ band. The electronic transitions into the partly occupied t_{2g} states give rise to the low-energy resonant peak at 2.968 keV, while the transitions into the empty e_g states result in the higher-energy peak at 2.972 keV. The energy difference of 4 eV between the two peaks is consistent with the estimated splitting of the t_{2g} and e_g states, as determined with band-structure calculations [59](Section 3.2). Since only the t_{2g} orbitals are partly occupied, only they participate in the orbital order that is established below 260 K. Thus, the 260 K phase transition is observable only at the low-energy position (2.968 keV) and only at the wave-vectors at which the orbital order gives non-zero structure factors. At the higher-energy position (2.972 keV), as well as at both resonant positions at the wave-vectors where the structure factor for orbital scattering is zero, the scattering intensity is not sensitive to the orbital phase transition. Its temperature dependence is then determined by the underlying resonant contribution arising from the distortion of the lattice (tilting of the octahedra).

The tilt of the RuO_6 octahedra mentioned before was also probed in our investigations. The scattering intensity observed at (1 1 0), both in Ca_2RuO_4 and in $\text{Ca}_{1.9}\text{Sr}_{0.1}\text{RuO}_4$, was attributed to it. Three pieces of evidence support this conclusion. First, the (1 1 0) position is magnetically forbidden, both for the A-centered and for the B-centered magnetic arrangements (Eq. 3.20), which immediately excludes the possibility of a magnetic origin for the scattering there. Second, the temperature dependence of the intensity at (1 1 0) (Fig. 3.36, 3.44(a)) is quite different

from the one at positions (1 0 0) and (0 1 1). The orbital ordering phase transition observed at the latter positions, both in the undoped and in the doped compounds, are absent at (1 1 0). Instead, the scattering intensity decreases smoothly, without showing any anomalies up to the metal-insulator transition¹. The different temperature dependence of the scattering intensity at (1 1 0) strongly indicates that its origin is not the above described orbital order. In addition, the lack of anomalies in the (1 1 0) temperature dependence is consistent with the smooth variation with temperature of the tilting angles of the octahedra (Fig. 3.4). Finally, the azimuthal dependence of the scattering intensity at (1 1 0) in the two polarization geometries, $\sigma \rightarrow \sigma'$ and $\sigma \rightarrow \pi'$, can be well reproduced by a model which calculates the structure factors as a result of the octahedral tilts (Section 3.8.5). In Ca_2RuO_4 the agreement between the simulations and the experimental results is quite good (Fig. 3.38), in $\text{Ca}_{1.9}\text{Sr}_{0.1}\text{RuO}_4$ the periodicities are well reproduced, but the model overestimates the intensity ratio of the $\sigma \rightarrow \pi'$ to $\sigma \rightarrow \sigma'$ intensities (Fig. 3.45). In any case, based on the above information there can be hardly any doubt about the fact that the resonant scattering at (1 1 0) arises from the lift of the space-group symmetry caused by the tilting of the octahedra, in conjunction with the aspherical charge density of the Ru t_{2g} electrons.

In contrast to the significance of the tilting of the octahedra, the distortion which determines the length of the Ru-O bonds and thus the shape (elongated or flattened) of the RuO_6 octahedra, does not seem to play an important role in the scattering at (1 1 0). As seen in Figure 3.5, the in-plane and out-of-plane Ru-O bond lengths in Ca_2RuO_4 follow upon heating opposite dependences, resulting in their having the same value within a narrow temperature range around 300 K. At this temperature the octahedra are almost perfectly symmetric, namely the shape distortion is negligible. A further increase of temperature leads to an increase of the distortion again, in the opposite direction. The scattering intensity at (1 1 0) remains unaffected by the above changes (Fig. 3.36). At 300 K significant scattering is observed, despite the absence of the shape distortion. The intensity continues following its smooth decrease with temperature up to above room temperature, without showing any anomalies at all. The insignificant role which the shape of the octahedra plays in the scattering at (1 1 0) is made even more clear in $\text{Ca}_{1.9}\text{Sr}_{0.1}\text{RuO}_4$. There the in-plane and out-of-plane bonds have almost the same length in the whole low-temperature regime below approximately 100 K (Fig. 3.41). In the whole *S-Pbca* phase, below the metal-insulator transition (≈ 180 K), the shape distortion is in general quite small. Above the metal-insulator transition the distortion becomes much larger, while the tilting angles are reduced by more than 40% [56]. Inconsistent with that, the $\text{Ca}_{1.9}\text{Sr}_{0.1}\text{RuO}_4$ scattering intensity at (1 1 0) is significantly

¹In Ca_2RuO_4 , the highest temperature investigated was 320 K, approximately 40 K below the MI transition.

stronger *below* the metal-insulator transition, in the S-*Pbca* phase (Fig. 3.44(a)). This clearly shows that it is the tilting and not the elongation or flattening of the octahedra which determines the distortion-related scattering intensity.

An important feature of the orbitally ordered phase discovered in the investigated $\text{Ca}_{2-x}\text{Sr}_x\text{RuO}_4$ compounds is that the ordering of the orbitals is only weakly coupled to the crystal lattice. None of the structural parameters that characterize the materials, as determined by neutron diffraction, show any anomalies at the temperature where the orbital ordering phase transition occurs. Despite the significant rearrangement of the electronic occupancy of the t_{2g} orbitals at the Ru sites, neither the lattice parameters, nor the Ru-O distances, nor the tilts of the RuO_6 octahedra are influenced by the transition. The direct observation of the orbital ordering in our investigations demonstrates the power of resonant x-ray diffraction in studying electronically driven phenomena which are not or only weakly coupled to the crystal lattice.

Another interesting feature of the coexisting ordering phenomena in $\text{Ca}_{2-x}\text{Sr}_x\text{RuO}_4$ is that the magnetic order, the orbital order and the tilt order are characterized by different correlation lengths. The correlation lengths are calculated using the widths of the resonant peaks in the scans carried out along the scattering vector, as seen in Section 3.6.3. In Ca_2RuO_4 , for example, the magnetic order established below $T_N = 110$ K is characterized, both at (1 0 0) (Fig. 3.25) and at (0 1 1) (Fig. 3.32) by a correlation length of $\xi_m \approx 1560$ Å or approximately 300 unit cells. The orbital order observed at the same positions between T_N and $T_{OO} = 260$ K is characterized by a correlation length of $\xi_o \approx 2150$ Å or approximately 400 unit cells. Finally, the tilt order of the RuO_6 octahedra, investigated at position (1 1 0) (Fig. 3.37), is characterized by a correlation length of the order of $\xi_t \approx 3700$ Å or 700 unit cells². The fact that the tilt order is of longer-range periodicity than the orbital order, and both of them of longer-range than magnetic correlations, could be an additional indication of the weak coupling between the different types of order. It could, however, also indicate the different nature of defects which influence different types of order, causing finite correlation lengths.

The latter explanation is more probable to be correct, because there is evidence that the magnetic and orbital order parameters are actually to some degree dependent on each other. Such a piece of evidence are the anomalies that have been observed in magnetic susceptibility measurements around the orbital ordering transition temperature on single crystal Ca_2RuO_4 . As already described in Section 3.3, the magnetic susceptibility data show a broad peak around 260 K, the origin of which has not been satisfactorily explained to date [63]. This feature may seem at a first glance not consistent with the absence of ordered magnetic moment above the Néel temperature indicated by the μSR investigations (Section 3.10). However,

²The calculated correlation length for the tilt order might be angular-resolution limited.

it should not be overlooked that the 260 K peak in susceptibility is characterized by an unusually large broadness, extending in a temperature range of up to 100 K. This strongly indicates that the feature does not actually reflect any real magnetic phase transition, like the one depicted in the same measurements at 110 K, but merely paramagnetic fluctuations within a phase with otherwise no total magnetic moment. The redistribution of electron charge density at the Ru⁺⁴ sites apparently modifies the spin Hamiltonian and consequently influences the paramagnetic fluctuations above the Néel temperature. In this sense, the susceptibility data actually provide an additional, indirect 'signature' of the orbital ordering phase transition, probed directly in our resonant x-ray diffraction experiments, and are by no means in contradiction with the μ SR investigations.

Chapter 4

The system $\text{RuSr}_2\text{GdCu}_2\text{O}_8$

The hybrid ruthenocuprate system $\text{RuSr}_2\text{GdCu}_2\text{O}_8$ (Ru1212) has attracted significant scientific interest in recent years, mainly due to the intriguing coexistence of long-range magnetic order and superconductivity that it exhibits. The compound was synthesized for the first time by Bauernfeind in 1995 [72]. It is a layered system, with a crystal unit cell consisting of alternating Ru-O and Cu-O planes. The Ru spins in the Ru-O planes order antiferromagnetically below the Néel temperature of $T_N = 136(2)$ K [73], while the Cu-O planes become superconducting below a transition temperature of $T_c \approx 15 - 46$ K [74, 75, 76]. Due to the relatively high value of T_c , magnetism and superconductivity coexist within a fairly broad temperature range. This makes $\text{RuSr}_2\text{GdCu}_2\text{O}_8$ an ideal compound for investigating the interplay between the two cooperative phenomena and determining how and to what extent the corresponding order parameters interact with each other.

4.1 Crystal and Electronic Structure

The crystal unit cell of $\text{RuSr}_2\text{GdCu}_2\text{O}_8$ is illustrated in Figure 4.1. The Ru ions are located at the centers of corner-sharing RuO_6 octahedra, the equatorial planes of which form Ru-O layers that extend parallel to the ab crystallographic plane at the top and the bottom of the unit cell. The copper ions are located at the centers of the bases of corner-sharing CuO_5 square pyramids, forming Cu-O layers that are parallel to the Ru-O planes and are separated by the central gadolinium ion of the cell. The system is isostructural to the high-temperature superconductor $\text{YBa}_2\text{Cu}_3\text{O}_{6+x}$ with the yttrium, barium and chain copper ions being replaced by gadolinium, strontium and ruthenium, respectively. The crystal structure is tetragonal (space-group $P4/mmm$) with room-temperature lattice parameters $a = b = 3.836$ Å and $c = 11.563$ Å [77]. The c/a axis ratio of 3.014 at 300 K is very close to the ideal value for a triple perovskite structure. Due to the mismatch between the lengths

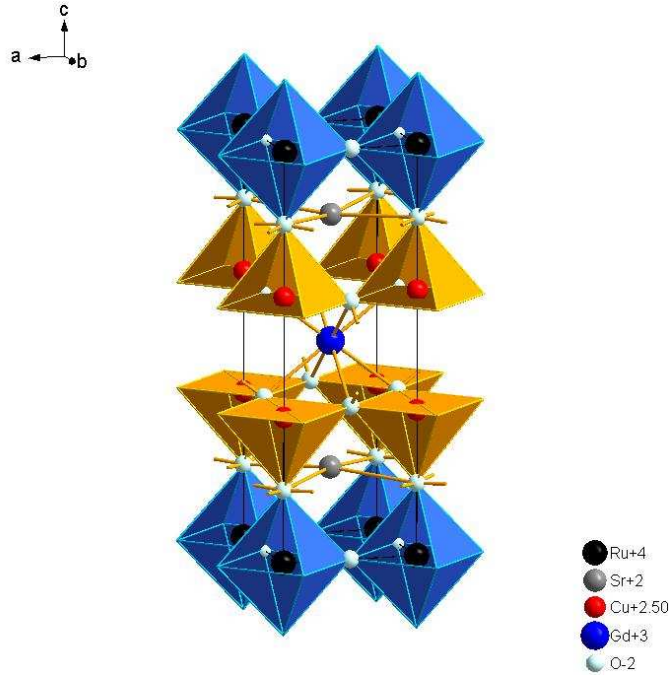


Figure 4.1: Crystal structure of $\text{RuSr}_2\text{GdCu}_2\text{O}_8$ (space-group $P4/mmm$). The Ru ions are located at the centers of corner-sharing RuO_6 octahedra, the equatorial planes of which form Ru-O layers, that extend parallel to the ab crystallographic plane at the top and the bottom of the unit cell. The Cu ions are located at the centers of the bases of corner-sharing CuO_5 square pyramids, forming Cu-O layers, which are parallel to the Ru-O planes and are separated by the central Gd ion of the cell.

of the in-plane Ru-O and Cu-O bonds, the RuO_6 octahedra are rotated around the crystallographic c -axis by about 13.8° [77], leading to a lifting of the inversion symmetry of the four equatorial oxygen ions. A slight tilting of the octahedra that reduces the Cu-O-Ru angle to 173° is also observed [78]. These structural distortions are not significantly different at low temperatures.

The formal oxidation states of ruthenium and copper in $\text{RuSr}_2\text{GdCu}_2\text{O}_8$ are close to +5 and +2, respectively. However, the exact values are determined by the charge transfer between the Ru-O and Cu-O planes. If p is the amount of charge transferred between the planes, the oxidation states are $5 - 2p$ and $2 + p$, respectively. For $p = 0$ the oxidation state of Ru is exactly +5, and there are three electrons in the Ru $4d$ band. Under the influence of the crystal field, which has an O_h symmetry, the electronic states of the $4d$ band are split into t_{2g} and e_g levels separated by an energy difference of $\Delta = 10D_q$, as described in Section 1.3. The three $4d$ electrons then occupy the three lower-lying t_{2g} states, leading to a $t_{2g}^3 e_g^0$ configuration. Nevertheless, x-ray absorption near-edge studies clearly

indicate a non-zero charge transfer between the Ru-O and Cu-O planes, with a p value around 0.2 [79], resulting in an average Ru oxidation state of +4.6. Other studies have suggested even higher values for p [78]. The latter would be, however, not consistent with the superconducting properties exhibited by $\text{RuSr}_2\text{GdCu}_2\text{O}_8$.

4.2 Magnetism and Superconductivity

Long-range magnetic order is established in the Ru-O layers of $\text{RuSr}_2\text{GdCu}_2\text{O}_8$ below a critical temperature of approximately 136 K. The magnetic structure of the system remains controversial. While dc-magnetization and muon spin rotation (μ -SR) studies initially suggested a ferromagnetic type of order [74], later neutron powder diffraction investigations showed that the order of the Ru spins is predominantly antiferromagnetic in all three crystallographic directions (G-type antiferromagnetism), with only a small ferromagnetic component of up to $0.1 \mu_B$, which is enhanced in the presence of applied magnetic field [73]. The predominantly antiferromagnetic character of the spin order was supported by subsequent magnetization studies, carried out on a Eu-substituted compound [80]. Other magnetization studies concluded instead that, while the coupling between neighboring RuO_2 planes is antiferromagnetic, the interactions within every plane are rather ferromagnetic, i.e. a 'type-I' antiferromagnetic order is established [81]. Recent nuclear magnetic resonance (NMR) measurements also support the type-I-antiferromagnetism scenario [82], but the inconsistency of such an order with the doubling of the crystal unit cell observed in the neutron diffraction experiments has not been satisfactorily explained so far.

The temperature dependence of the magnetic order parameter of the Ru spin system as determined by neutron powder diffraction is shown in Figure 4.2. The magnetic phase transition is observed via the vanishing of the integrated scattering intensity of the $(\frac{1}{2} \frac{1}{2} \frac{1}{2})$ magnetic Bragg peak at $T_N = 136$ K. Below T_N , the magnetic intensity increases smoothly with decreasing temperature and reaches its saturation value around 60 K. The intensity remains constant thereafter, with no anomalies observed down to the lowest temperatures investigated.

The direction of the Ru magnetic moment in $\text{RuSr}_2\text{GdCu}_2\text{O}_8$ remains also an issue of debate. The neutron diffraction data suggest a magnetic moment which is aligned along the crystallographic c -axis and has a magnitude of approximately $1.18 \mu_B$. As will be discussed in Section 4.4, this conclusion was drawn based on the intensity ratio of two magnetic reflections and is not definite. On the contrary, the above mentioned magnetization and NMR studies [81, 82] strongly suggest a moment direction within the ab plane, as also indicated by the early μ -SR results [74]. Recent magnetization measurements performed for the first time on *single-crystal* $\text{RuSr}_2\text{GdCu}_2\text{O}_8$ samples could also not confirm the moment direction suggested by

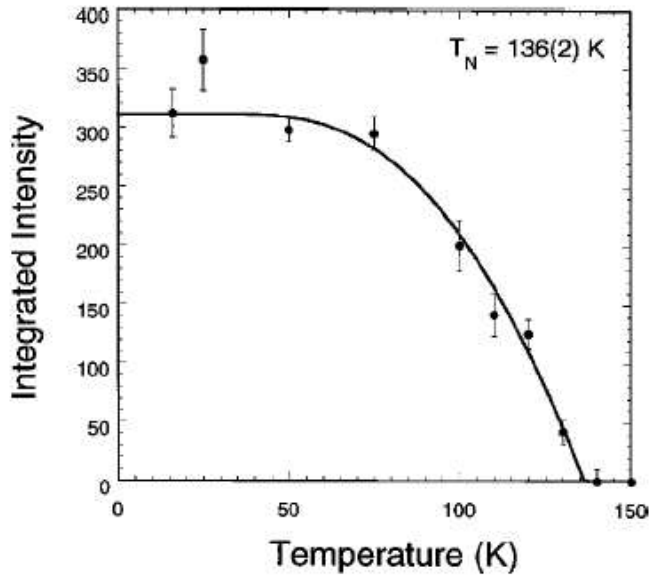


Figure 4.2: Temperature dependence of the magnetic scattering intensity from the Ru spin system in $\text{RuSr}_2\text{GdCu}_2\text{O}_8$, as determined with powder neutron diffraction [73]. The magnetic phase transition is clearly observed at $T_N = 136$ K.

the neutron experiments [83, 84]. The variation with temperature of the magnetization for applied magnetic field parallel and perpendicular, respectively, to the c direction is shown in Figure 4.3(a). A comparison of the data with the theoretically expected temperature dependence of the magnetic susceptibility χ of an antiferromagnet, for applied magnetic field perpendicular (\perp) and parallel (\parallel) to the magnetic moment direction (Figure 4.3(b)), reveals that the Ru spins in $\text{RuSr}_2\text{GdCu}_2\text{O}_8$ are not aligned along c , but have a significant component in the ab -plane. How large exactly this component is, cannot be determined by the magnetization data.

Our resonant x-ray diffraction investigations further support the conclusion that the magnetic moment is not aligned along c . As will be seen in Section 4.4, the moment direction is found to lie in-between the ab -plane and the c -axis. The exact angle between the magnetic moment and the c -axis could be for the first time precisely determined.

Independent from the Ru ions, the Gd ions also order antiferromagnetically along all three crystallographic directions. The ordering in the Gd spin system is established at the much lower temperature of $T_{N,\text{Gd}} = 2.50$ K. The magnetic moment is aligned along the c -axis, and has a magnitude of $7 \mu_B$. The fact that the Ru and Gd magnetic structures interact only very weakly with each other, although they correspond to identical spin configurations, is due to the position in the crystal of

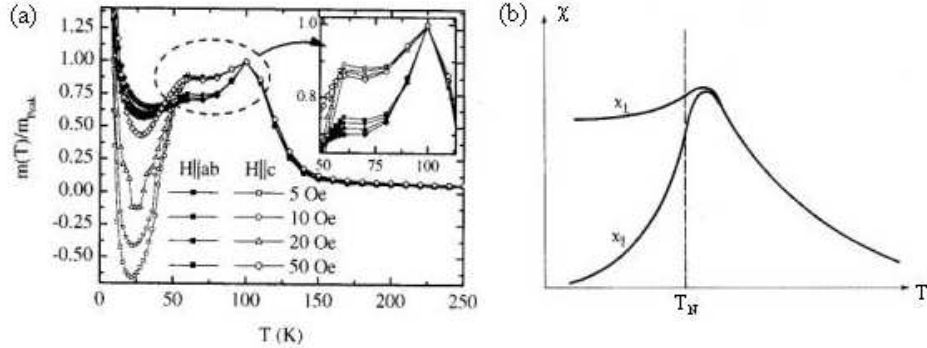


Figure 4.3: (a) Magnetization measurements on $\text{RuSr}_2\text{GdCu}_2\text{O}_8$ single crystals of the same origin as the ones used in our x-ray diffraction investigations [83]. The theoretically expected temperature dependence of the magnetic susceptibility χ of an antiferromagnet, for applied magnetic field perpendicular (\perp) and parallel (\parallel) to the magnetic moment direction, is shown in (b). The comparison with the experimental results reveals that the magnetic moment is not along c , but has instead a significant ab -component.

the Gd ions. The latter are located at the body-center of the simple tetragonal Ru lattice, symmetrically positioned with regard to the Ru ions of the nearest Ru-O planes. The antiferromagnetic alignment of the Ru spins results in an average cancellation of the magnetic interaction between the Ru and Gd ions.

While the Cu-O planes play no role in the above described magnetic ordering, they are of crucial importance when it comes to the second cooperative phenomenon that characterizes the low-temperature properties of $\text{RuSr}_2\text{GdCu}_2\text{O}_8$: superconductivity. The occurrence of bulk superconductivity in the system has been confirmed with resistivity, thermopower and heat-capacity measurements, which determined a Meissner fraction of up to approximately 100% at 4.2 K [75]. The superconducting transition temperature T_c is strongly dependent on the preparation conditions of the crystal. Depending on the synthesis and annealing procedures used, T_c can have values between approximately 15 K and 46 K. The superconducting and magnetic order parameters interact only very weakly with each other.

4.3 Experimental

Resonant x-ray diffraction at the L_{II} and L_{III} absorption edges of ruthenium (Ru), i.e. at x-ray energies of 2.968 keV and 2.838 keV, respectively, was used to investigate the magnetic properties of $\text{RuSr}_2\text{GdCu}_2\text{O}_8$ on single crystals of the compound. Neutron diffraction, which is in general an appropriate technique for studying mag-

netic phenomena, can only be applied on powder $\text{RuSr}_2\text{GdCu}_2\text{O}_8$ samples, because no single crystals of sufficiently large mass can currently be grown for neutron investigations. In addition, the element gadolinium (Gd) contained in the compound strongly absorbs neutron radiation and significantly reduces the observed diffracted intensity. Because of the above restrictions, neutron diffraction can in this case provide information of only limited precision as far as the determination of the magnetic order parameter and of the direction of the magnetic moment in the system are concerned. Resonant x-ray diffraction at the L-edges of Ru is in this aspect a very useful complementary technique. Thanks to the large resonant enhancement of the magnetic scattering intensity that it provides, it allows the investigation of magnetic order and gives valuable information about the electronic properties of the ruthenocuprate system, even when only very tiny single-crystal samples are available.

For the investigations discussed in the following, the magnetic reflection at the $(\frac{1}{2} \frac{1}{2} \frac{1}{2})$ reciprocal space position was used. At the Ru L_{II} absorption edge, the reflection is observed at a scattering angle of $\theta = 23.37^\circ$. For the determination of the orientation matrix of the sample at room temperature, the third harmonic ($\lambda/3$) of the incident beam was used at the (1 1 1) reciprocal space position, which corresponds to $(\frac{1}{3} \frac{1}{3} \frac{1}{3})$ for the fundamental wavelength. A very weak main Bragg reflection is observed there. The access of the (1 1 1) position at the fundamental energy (L_{II} edge) is not possible due to geometrical restrictions of the diffractometer (Section 3.6.1).

4.3.1 Samples

The investigated $\text{RuSr}_2\text{GdCu}_2\text{O}_8$ samples were single crystals grown with the self-flux method by H. Luo, C.T. Lin *et al.* at the Max-Planck-Institute for Solid State Research in Stuttgart [85]. They were obtained via proper treatment of an initial mixture of RuO_2 , SrCO_3 , Gd_2O_3 and CuO with a solvent composition of Ru : Gd : Cu = 0.8 : 0.4 : 1.7. The treatment involved an initial heating of the mixture in aluminum crucibles in air atmosphere at 880°C , as well as a subsequent calcination of the intermediate pellets in Pt crucibles under flowing oxygen at a temperature of 920°C .

The final growth product contains small single crystals of $\text{RuSr}_2\text{GdCu}_2\text{O}_8$ of sizes smaller than $100 \times 100 \times 50 \mu\text{m}^3$. These single crystals are mixed with other phases, the most important of which are Gd_2CuO_4 , Sr_2RuO_4 , as well as the recently identified $\text{RuSr}_{10}\text{Pt}_2\text{Cu}_3\text{O}_{14}$ phase. The latter is a result of the specific growing procedure used, and in particular of its last stage, performed, as already mentioned, in Pt crucibles. Further information about the phases co-existing with the $\text{RuSr}_2\text{GdCu}_2\text{O}_8$ phase can be found in Ref. [76].

The tiny $\text{RuSr}_2\text{GdCu}_2\text{O}_8$ single crystals, which are of interest for our investi-

gations, needed to be identified and separated from the rest of the phases, out of a large polycrystalline piece, named 'LuoRu-12' by its growers, consisting of many thousands of single crystals. Of all the non-Ru1212 phases, only Gd_2CuO_4 can be relatively easily identified by eye under the microscope, due to the smooth, shiny appearance of its crystallites. The rest of the phases are not easy to distinguish from $\text{RuSr}_2\text{GdCu}_2\text{O}_8$ just by their appearance. The separation was performed by crystallographic characterization of the candidate crystals with the use of x-ray diffraction. Via determination of the space-group of the investigated crystals, it becomes clear which of them correspond to the desired $\text{RuSr}_2\text{GdCu}_2\text{O}_8$ composition with the expected tetragonal structure (Section 4.1) and which to one of the other phases, that are irrelevant for the current work. Empirically, one or two out of ten investigated crystals came out to have the right Ru1212 phase.

It has to be mentioned that, due to the extremely small size of the available single crystals, the above described experimental procedure was a non-trivial task. The crystallites that were selected from the large polycrystalline piece were in some cases barely visible with naked eye. After careful observation under the microscope, a few of them were chosen as candidate samples. In general, the crystallites that had a symmetric shape with well-defined, but not too shiny surfaces were preferred, since the experience showed that the probability of finding good quality samples of the right phase was higher among such crystals. The handling of the samples and the right positioning and gluing of them on the sample holder was carried out with the help of very fine tweezers. In most cases it was not possible to lift the samples just by placing them between the tweezers' arms, therefore other techniques had to be employed. For example, touching with one of the tweezers' tips the surface of a sticky tape made also the tip sticky enough for the crystallite to be attached for a short while to it, without any remnants of the adhesive substance staying on the crystal in the end. In order to avoid the direct contact to the sample as much as possible during the above described selection procedure, a small glass surface was often used as 'carrying tray'.

Due to the very small mass of the crystals used in the x-ray diffraction investigations (significantly less than 1 mg), the superconducting transition temperature T_c could not be determined directly with SQUID measurements. Based on previous investigations on polycrystalline samples and larger single-crystals of the same origin as ours [76, 83, 84], it could be estimated that T_c lies close to the upper limit of the usually achieved range, i.e. around 45 K (midpoint). The onset of superconductivity takes place presumably already above 50 K.

4.3.2 Experimental Setup

The investigations on $\text{RuSr}_2\text{GdCu}_2\text{O}_8$ reported in this chapter were carried out at beamline 4ID-D of the Advanced Photon Source (APS) at Argonne National Labo-

ratory (USA), at the same experimental setup used also for the Ca_2RuO_4 studies. The setup was described in detail in Chapter 3 (Section 3.5). For cooling the sample, the standard closed-cycle (Displex) cryostat of the beamline was used. Like in the Ca_2RuO_4 experiments, in order to minimize the x-ray absorption, no inner thermal shield was mounted around the sample. The sample environment was optimized to compensate for the resulting thermal losses, with a copper /aluminum foil extending around the goniometer head up to just below the sample position, and with copper stripes improving the thermal conductivity between the sample holder and the cold finger. The sample temperature sensor was attached (with copper grease and teflon tape) onto the flat part of the sample holder, a few millimeters away from the crystal. The temperature given by this sensor was thus very close to the actual temperature of the sample. Despite the optimized sample environment, the omission of the beryllium thermal shield resulted in not being able to reach sample temperatures lower than 40 K.

4.4 Determination of the Magnetic Moment Direction

Previous Results: Neutron Diffraction

Due to the difficulties in growing large $\text{RuSr}_2\text{GdCu}_2\text{O}_8$ single crystals, the determination of the exact direction of the Ru magnetic moment below $T_N = 136$ K in a definitive and precise way, for example with magnetization measurements, has not been possible so far. Based on neutron diffraction investigations performed on powder $\text{RuSr}_2\text{GdCu}_2\text{O}_8$ samples, and in particular on the intensity ratio of the magnetic peaks observed at the $(\frac{1}{2} \frac{1}{2} \frac{1}{2})$ and $(\frac{1}{2} \frac{1}{2} \frac{3}{2})$ reciprocal space positions, Lynn *et al.* suggested that the direction of the moment is along the tetragonal c axis [73]. The determination was done as follows:

The integrated magnetic scattering intensity for a collinear structure is given by the expression [73, 86]:

$$I_M(\boldsymbol{\tau}) = C |F_M(\boldsymbol{\tau})|^2 \frac{m_{hkl} A_{hkl}}{\sin \theta \sin(2\theta)} \langle 1 - (\hat{\boldsymbol{\tau}} \cdot \hat{\boldsymbol{\mu}})^2 \rangle \quad (4.1)$$

where C is an instrumental constant, m_{hkl} is the multiplicity of the powder peak with Miller indices h, k, l for the reciprocal lattice vector $\boldsymbol{\tau}$, A_{hkl} is the absorption factor, θ is the scattering (Bragg) angle, $\hat{\boldsymbol{\mu}}$ is a unit vector in the direction of the magnetic moment, and the brackets indicate an average over a whole domain of the powder sample. The magnetic structure factor F_M is given by:

$$F_M(\boldsymbol{\tau}) = \sum_{j=1}^N \langle \boldsymbol{\mu}_j^z \rangle f_j(\boldsymbol{\tau}) e^{i\boldsymbol{\tau} \cdot \mathbf{R}_j} e^{-W_D} \quad (4.2)$$

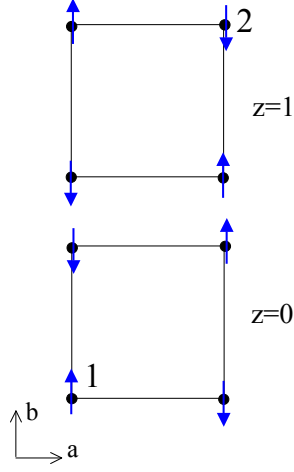


Figure 4.4: The magnetic unit cell of $\text{RuSr}_2\text{GdCu}_2\text{O}_8$, as determined by powder neutron diffraction [73]. The Ru spins order antiferromagnetically in all three crystallographic directions. The numbered ions make up the magnetic basis.

where $\boldsymbol{\mu}_j^z$ is the magnetic moment of the j^{th} ion of the unit cell, located at position \mathbf{R}_j , $f_j(\boldsymbol{\tau}) \equiv f_j(hkl)$ is the corresponding magnetic form factor, W_D is the Debye-Waller factor, and the summation is over all ions of the unit cell.

The basis of the magnetic unit cell of $\text{RuSr}_2\text{GdCu}_2\text{O}_8$ consists of two Ru ions with antiparallel spins located at positions: $\mathbf{R}_1 = 0$ and $\mathbf{R}_2 = a\hat{x} + b\hat{y} + c\hat{z}$ (Figure 4.4). Their magnetic form factors are equal in absolute values but with opposite sign due to the antiparallel spins: $f_1(hkl) = -f_2(hkl) \equiv f(hkl)$. The magnetic structure factor (4.2) is thus:

$$F_M(hkl) = f(hkl)(1 - e^{i2\pi(h+k+l)}) \langle \boldsymbol{\mu}_j^z \rangle e^{-W_D} \quad (4.3)$$

Within the dipole approximation (spherical symmetry), the magnetic form factor $f(hkl)$ is given by:

$$f(hkl) = \langle j_0(hkl) \rangle + \left(1 - \frac{2}{g_L}\right) \langle j_2(hkl) \rangle \quad (4.4)$$

Assuming a Landé splitting factor of $g_L = 2$, we have: $f(hkl) = \langle j_0(hkl) \rangle$. The form factor $\langle j_0(hkl) \rangle$ is given as an analytical approximation by:

$$\langle j_0(s) \rangle = Ae^{-a_0s^2} + Be^{-b_0s^2} + Ce^{-c_0s^2} + D \quad (4.5)$$

where $s = \frac{\sin\theta}{\lambda}$ in \AA^{-1} . The values of the coefficients in the last expression are given for Ru^+ in the International Tables for Crystallography [87]. No coefficients are available for Ru^{+5} , the valence state which is relevant for $\text{RuSr}_2\text{GdCu}_2\text{O}_8$, but we

assume that as a first approximation the values for Ru⁺ can be used instead with no large error, especially since in the end we are only interested in the ratio of the intensities of the magnetic peaks and not in the absolute values.

For a neutron wavelength of $\lambda = 2.359 \text{ \AA}$, the scattering angles θ_1 and θ_2 for the magnetic reflections $(\frac{1}{2} \frac{1}{2} \frac{1}{2})$ and $(\frac{1}{2} \frac{1}{2} \frac{3}{2})$, respectively, are calculated from Bragg's equation:

$$2d_{hkl} \sin \theta = \lambda \quad (4.6)$$

with:

$$d_{hkl} = \frac{1}{\sqrt{(\frac{h}{a})^2 + (\frac{k}{b})^2 + (\frac{l}{c})^2}} \quad (4.7)$$

as follows: $\theta_1 = 12.9044^\circ$ and $\theta_2 = 15.4185^\circ$. The corresponding s values are thus: $s_1 = 0.094669 \text{ \AA}^{-1}$ and $s_2 = 0.112703 \text{ \AA}^{-1}$. From Equations 4.3, 4.4 and 4.5, the magnetic structure factor can now be calculated for the two reflections $(\frac{1}{2} \frac{1}{2} \frac{1}{2})$ and $(\frac{1}{2} \frac{1}{2} \frac{3}{2})$. The squared structure factor ratio is:

$$\frac{|F_M(\frac{1}{2} \frac{1}{2} \frac{1}{2})|^2}{|F_M(\frac{1}{2} \frac{1}{2} \frac{3}{2})|^2} = 1.176678 \quad (4.8)$$

Based on Equation 4.1, and given the fact that for the two magnetic peaks the constant C and the multiplicity m_{hkl} are the same and the absorption factor A_{hkl} is also practically the same, the ratio of their intensities is:

$$R = \frac{I_{\frac{1}{2} \frac{1}{2} \frac{1}{2}}}{I_{\frac{1}{2} \frac{1}{2} \frac{3}{2}}} = \frac{|F_M(\frac{1}{2} \frac{1}{2} \frac{1}{2})|^2 \frac{\langle 1 - (\hat{\tau}_1 \cdot \hat{\mu})^2 \rangle}{\sin \theta_1 \sin 2\theta_1}}{|F_M(\frac{1}{2} \frac{1}{2} \frac{3}{2})|^2 \frac{\langle 1 - (\hat{\tau}_2 \cdot \hat{\mu})^2 \rangle}{\sin \theta_2 \sin 2\theta_2}} = 1.649316 \frac{\langle 1 - (\hat{\tau}_1 \cdot \hat{\mu})^2 \rangle}{\langle 1 - (\hat{\tau}_2 \cdot \hat{\mu})^2 \rangle} \quad (4.9)$$

If we assume that the magnetic moment is aligned along the c direction, then the scalar products in the last expression take the values: $\hat{\tau}_1 \cdot \hat{\mu} = 0.2284$ and $\hat{\tau}_2 \cdot \hat{\mu} = 0.5755$, resulting in an intensity ratio of: $R = \frac{I_{\frac{1}{2} \frac{1}{2} \frac{1}{2}}}{I_{\frac{1}{2} \frac{1}{2} \frac{3}{2}}} = 2.34$. This value is very close to the experimentally determined value of 2.49 [73]. Based on this, Lynn *et al.* suggested that the magnetic moment is aligned along c , pointing out, however, that this assignment was rather tentative, since with only two observable magnetic reflections, no definitive conclusion can be drawn.

Resonant X-ray Diffraction

Since the scattering intensity in resonant x-ray diffraction is dependent on the azimuthal position ψ of the investigated sample (Figure 2.4), the technique is highly sensitive to the magnetic moment direction. In antiferromagnets the scattering intensity is maximum when the magnetic moment lies in the diffraction plane ($\psi = 0^\circ$). Thus, if the magnetic moment in RuSr₂GdCu₂O₈ were along c , as suggested by Lynn

et al., the scattering intensity would take its maximum value at the azimuthal position where c is in the diffraction plane. Our investigations showed, however, that the scattering intensity is instead maximum when the c -direction is 53° off the scattering plane. This means that the magnetic moment is not along c , but has a significant ab component. The exact angle between the magnetic moment and the c -direction can be deduced from the azimuthal dependence as follows:

For the two Ru ions of the $\text{RuSr}_2\text{GdCu}_2\text{O}_8$ basis (Figure 4.4) we use the notation 'spin-up': \uparrow and 'spin-down': \downarrow to refer to their spin directions. The magnetic moment is analyzed along the axes of the coordinate system introduced in Section 2.4 (Figure 2.4), with the \hat{U}_3 axis being antiparallel to the scattering vector $(1\ 1\ 1)$ of the magnetic reflection. The total resonant electric dipole scattering length in $\sigma \rightarrow \pi'$ polarization geometry is given by Equation 2.24. For the ions of the $\text{RuSr}_2\text{GdCu}_2\text{O}_8$ basis ($\mathbf{R}_1 = 0$, $\mathbf{R}_2 = a\hat{x} + b\hat{y} + c\hat{z}$) the equation takes the form:

$$g_{E1}^{\sigma \rightarrow \pi'} = \sum_{j=1}^2 g_{E1,S_j}^{\sigma \rightarrow \pi'} e^{i\mathbf{Q} \cdot \mathbf{R}_j} = g_{E1,\uparrow}^{\sigma \rightarrow \pi'} + g_{E1,\downarrow}^{\sigma \rightarrow \pi'} e^{i3\pi} = g_{E1,\uparrow}^{\sigma \rightarrow \pi'} - g_{E1,\downarrow}^{\sigma \rightarrow \pi'} \quad (4.10)$$

and, due to (2.21), (2.23):

$$g_{E1}^{\sigma \rightarrow \pi'} = -2iF^{(1)} \cos \alpha \sin \theta + 2iF^{(1)} \sin \alpha \cos \theta \cos \psi \quad (4.11)$$

The scattering intensity measured at the $(\frac{1}{2}\ \frac{1}{2}\ \frac{1}{2})$ reciprocal space position in the $\sigma \rightarrow \pi'$ polarization channel is proportional to the square of the corresponding total scattering length:

$$\begin{aligned} I_{(\frac{1}{2}\ \frac{1}{2}\ \frac{1}{2})}^{\sigma \rightarrow \pi'} &\propto |g_{E1}^{\sigma \rightarrow \pi'}|^2 = |2iF^{(1)}(\sin \alpha \cos \theta \cos \psi - \cos \alpha \sin \theta)|^2 \implies \\ I_{(\frac{1}{2}\ \frac{1}{2}\ \frac{1}{2})}^{\sigma \rightarrow \pi'} &\propto (F^{(1)})^2(\sin^2 \alpha \cos^2 \theta \cos^2 \psi - 2 \sin \alpha \cos \alpha \sin \theta \cos \theta \cos \psi \\ &\quad + \cos^2 \alpha \sin^2 \theta) \end{aligned} \quad (4.12)$$

In the $\sigma \rightarrow \sigma'$ scattering geometry, Equation 2.27 gives:

$$g_{E1}^{\sigma \rightarrow \sigma'} = \sum_{j=1}^2 g_{E1,S_j}^{\sigma \rightarrow \sigma'} e^{i\mathbf{Q} \cdot \mathbf{R}_j} = g_{E1,\uparrow}^{\sigma \rightarrow \sigma'} + g_{E1,\downarrow}^{\sigma \rightarrow \sigma'} e^{i3\pi} = g_{E1,\uparrow}^{\sigma \rightarrow \sigma'} - g_{E1,\downarrow}^{\sigma \rightarrow \sigma'} \quad (4.13)$$

and finally, due to (2.26):

$$g_{E1}^{\sigma \rightarrow \sigma'} = g_{E1,\uparrow}^{\sigma \rightarrow \sigma'} - g_{E1,\downarrow}^{\sigma \rightarrow \sigma'} = 0 \quad (4.14)$$

Therefore, the scattering intensity in $\sigma \rightarrow \sigma'$ is zero:

$$I_{(\frac{1}{2}\ \frac{1}{2}\ \frac{1}{2})}^{\sigma \rightarrow \sigma'} = 0 \quad (4.15)$$

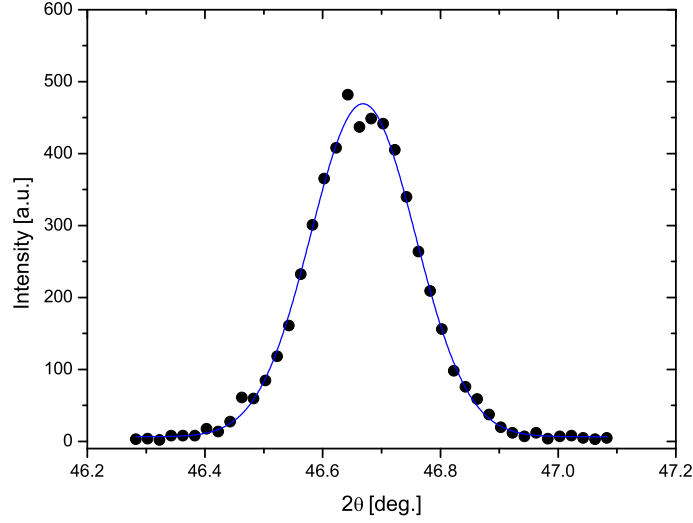


Figure 4.5: Example of a $\theta - 2\theta$ -scan, carried out around $(\frac{1}{2} \frac{1}{2} \frac{1}{2})$, at azimuth $\psi = 0^\circ$ and sample temperature 45 K, at the Ru L_{II} absorption edge. The scattering intensity is measured during a simultaneous rotation of the sample around the Bragg scattering angle and of the detector by twice the amount of change of the scattering angle. The data were fitted with a Gaussian profile to give the integrated intensity at this azimuthal position.

Since the $\sigma \rightarrow \sigma'$ polarization channel gives no contribution to the total scattered intensity, no polarization analysis of the diffracted signal is needed in the experiment – the measured intensity is of purely $\sigma \rightarrow \pi'$ origin and can be described by Equation 4.12, with a scattering angle θ of 23.37° .

At every azimuthal position ψ , the integrated intensity of the $(\frac{1}{2} \frac{1}{2} \frac{1}{2})$ magnetic reflection is determined from the area below the data-points in the corresponding $\theta - 2\theta$ -scan. A representative $\theta - 2\theta$ -scan (for $\psi = 0^\circ$) can be seen in Figure 4.5. For the determination of the integrated intensity a Gaussian profile is fitted to the data. The resulting azimuthal dependence of the integrated intensity is then fitted using the theoretical expression 4.12 (Figure 4.6). From the fit the values of the parameters α and $F^{(1)}$ are extracted. For $F^{(1)}$ we find: $F^{(1)} = 2.47 \pm 0.10$, while for the angle α we obtain the value: $\alpha = (0.856 \pm 0.020)$ rad = $49.0^\circ \pm 1.1^\circ$.

As previously mentioned, based on the fact that the maximum of the scattered intensity occurs at the azimuthal position at which the c -direction is 53° off the scattering plane, we draw the conclusion that the angle $(\widehat{\mu_p, c_p})$ (Figure 4.7) between the projections of the magnetic moment μ and of the c -axis direction, respectively, on the plane which is perpendicular to the scattering vector (111) is equal to 53° . Thus: $\widehat{BAE} = (\widehat{\mu_p, c_p}) = 53^\circ$. From this, we calculate the angle $\widehat{CAD} = (\widehat{\mu, c})$ between μ and c . We find: $\widehat{CAD} = 53.8^\circ$. The calculations can be found in

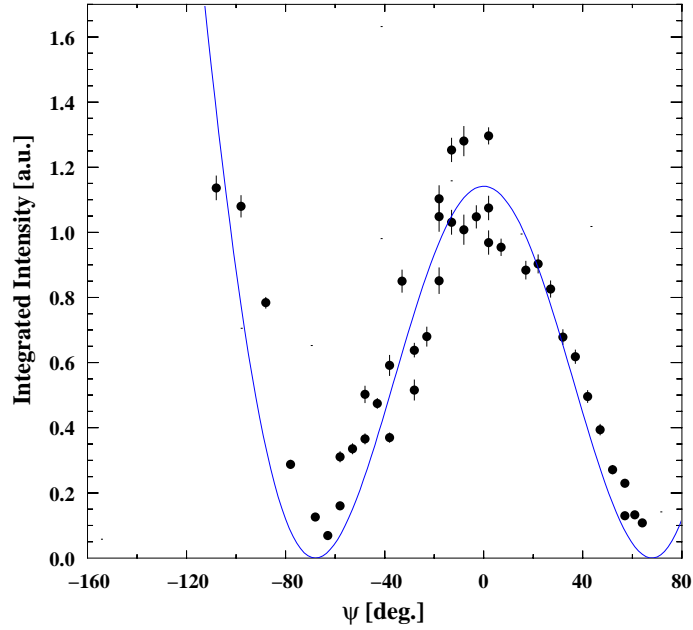


Figure 4.6: Azimuthal dependence of the integrated scattering intensity at the $(\frac{1}{2} \frac{1}{2} \frac{1}{2})$ reciprocal space position at the Ru L_{II} edge, as determined from $\theta - 2\theta$ -scans at $T = 45$ K. The solid line is a fit of the data to the theoretical expression (4.12), calculated from the corresponding resonant electric dipole scattering length. From the fitting, the angle α between the magnetic moment and the scattering vector is among others determined.

Appendix B.

To summarize, the direction of the magnetic moment $\boldsymbol{\mu}$ is along a reciprocal space vector $(h k l)$ which forms an angle of $\alpha = 49^\circ$ with $(1 1 1)$ and of 53.8° with $(0 0 1)$. This corresponds approximately to the $(1 0 2)$ reciprocal space direction: $((102), \widehat{(111)}) = 45.6^\circ$ and $((102), \widehat{(001)}) = 56^\circ$. Thus $(1 0 2)$ can be considered as the approximate direction of the magnetic moment.

It has to be emphasized that this result is still consistent with the previously mentioned neutron data. Indeed, the intensity ratio calculated when the magnetic moment is assumed along $(1 0 2)$ is exactly the same with the one obtained with the moment along c , and very close to the experimentally found value of 2.49. In other words, having the magnetic moment along c is not the only possibility for the magnetic moment direction that satisfies the condition of giving an intensity ratio of approximately 2.49 for the $(\frac{1}{2} \frac{1}{2} \frac{1}{2})$, $(\frac{1}{2} \frac{1}{2} \frac{3}{2})$ peaks. Lynn *et al.* considered one of the possibilities – the simplest one – but our x-ray diffraction data showed that another one is true.

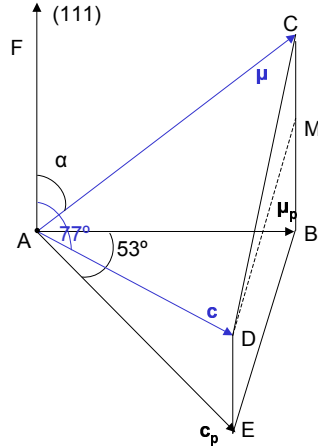


Figure 4.7: Vector representation used for the calculation of the angle between the Ru magnetic moment μ and the c crystallographic direction. From the position of c with regard to the scattering plane at the azimuth where the scattering intensity is maximum, the angle between the projections of μ and c on the plane which is perpendicular to the scattering plane can be determined. From the fitting of the azimuthal dependence (Fig. 4.6) the angle α between μ and the scattering vector is calculated. Based on these two angles, the direction of the magnetic moment can be estimated.

4.5 Magnetic Order Parameter

The investigations of $\text{RuSr}_2\text{GdCu}_2\text{O}_8$ carried out so far on powder samples have not indicated any kind of coupling between the magnetic order of the Ru spins in the Ru-O planes and the superconductivity in the Cu-O planes. The two phenomena seem to be established independently from each other. The neutron diffraction studies, in particular, have shown no influence of the onset of superconductivity at $T_c \approx 35$ K on the magnetic order parameter [73]. As seen in Section 4.2, the neutron results indicate that the integrated scattering intensity of the $(\frac{1}{2} \frac{1}{2} \frac{1}{2})$ magnetic reflection stays constant with increasing temperature up to approximately 60 K (Figure 4.8), without showing any anomalies at T_c . However, the small amount of the available experimental data at low temperatures (only two data points below 50 K) and the relatively large size of the corresponding error bars in intensity do not actually allow a definite exclusion of a weak interaction between magnetism and superconductivity.

Resonant x-ray diffraction provides the possibility to investigate the interplay of magnetism and superconductivity in $\text{RuSr}_2\text{GdCu}_2\text{O}_8$ using single-crystal samples.

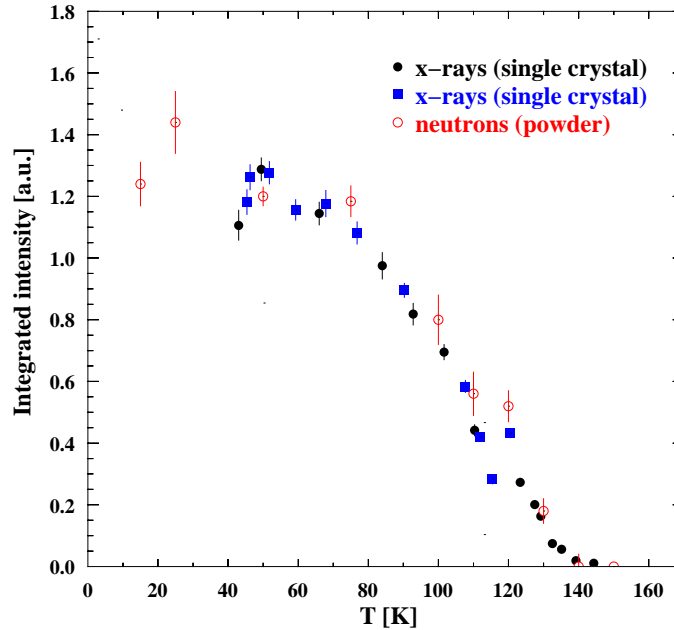


Figure 4.8: Variation with temperature of the integrated scattering intensity of the $(\frac{1}{2} \frac{1}{2} \frac{1}{2})$ magnetic reflection, as determined from $\theta - 2\theta$ -scans at azimuth $\psi = 0^\circ$ at the Ru L_{II} edge (filled symbols). The magnetic phase transition is clearly observed around 140 K. An anomaly in the magnetic order parameter is indicated below 50 K, where superconductivity sets in. The two kinds of filled symbols (circles, squares) correspond to different measurement cycles. For comparison, the powder neutron diffraction results from Ref. [73] are also shown (normalized) in the same plot (empty circles).

The high scattering intensities achieved at the Ru L_{II} resonance allow the collection of high precision data despite the small crystal size. The variation with temperature of the integrated scattering intensity at $(\frac{1}{2} \frac{1}{2} \frac{1}{2})$ is shown in Figure 4.8. The intensities were determined from $\theta - 2\theta$ -scans carried out at the Ru L_{II} edge at azimuth $\psi = 0^\circ$, by fitting the data with Gaussian profiles. The magnetic phase transition is clearly observed, as expected, around 140 K, in perfect agreement with the previously described neutron diffraction results. Below 140 K the magnetic intensity increases smoothly with decreasing temperature and reaches its highest value around 50 K. Below that temperature our results differ significantly from the neutron data. The magnetic intensity does not remain constant down to the lowest temperatures, but decreases instead again with cooling. Thus, the magnetic order parameter determined by resonant x-ray diffraction shows an anomaly just below 50 K, which was not observed in the neutron diffraction investigations, and which may be related to the onset of superconductivity around this temperature.

There are two problems which prevent us from definitely stating that the mag-

netic order in $\text{RuSr}_2\text{GdCu}_2\text{O}_8$ is really influenced by the onset of superconductivity, as indicated by the above results. First, the exact value of the superconducting transition temperature T_c for the investigated sample is not known precisely. The mass of the crystal lies below the minimum required by most SQUID magnetometers for performing magnetic susceptibility or resistivity measurements and the only available T_c values are the ones found in the literature. However, magnetization and resistivity measurements carried out on polycrystalline and single-crystal samples of larger mass grown by the same crystal-growers and under the same conditions as the sample investigated with x-ray diffraction, indicate a T_c around 45 K (mid-point) and an onset of superconductivity already above 50 K [76, 83, 84]. There is therefore a good chance that this is also true for the sample investigated with x-rays. Second, the anomaly is actually indicated by only two experimental points in the plot. As explained in Section 4.3, in order to minimize the absorption of the x-ray beam, no inner thermal beryllium dome was used in the setup. As a result, no temperatures below 40 K could be reached at the sample position and no further measurements could be taken at lower temperatures to confirm the indicated intensity drop below 50 K. Nevertheless, the presented data were collected during two different measurement cycles, performed independently at different times during the same experiment, as indicated by the different symbols in Figure 4.8. The data from the two cycles coincide perfectly with each other and the decrease of the order parameter below 50 K is well reproduced. This strengthens our confidence that the reported anomaly is related to a real change of the order parameter in the material and is no artifact.

4.6 Discussion

The coexistence of long-range magnetic order and superconductivity in strongly correlated electron systems has attracted considerable scientific interest since the early work by Ginzburg in 1953 [88]. Ferromagnetism has been always considered detrimental to superconductivity and the prevailing belief up to date is that the two order parameters cannot coexist in a microscopic scale, since the electromagnetic interaction and the exchange coupling between the electrons lift the degeneracy of the Cooper pair partners and cause strong pair breaking. For this reason, the report of both bulk superconductivity [75] and ferromagnetism [74] in $\text{RuSr}_2\text{GdCu}_2\text{O}_8$ below a critical temperature $T_c \approx 15 - 45$ K came rather surprisingly and attracted a lot of attention. Later neutron diffraction studies showed that the magnetic order established in $\text{RuSr}_2\text{GdCu}_2\text{O}_8$ is actually not ferromagnetic, as initially thought, but instead predominantly antiferromagnetic, with only a small ferromagnetic component, which becomes strong in the presence of applied magnetic field. The existence of a few antiferromagnetic superconductors was already previously known (Chevrel

phases, borocarbides, cuprates), but the rare-earth ordering in all these compounds is established at low temperatures, below 10 K. With a Néel temperature of 136 K and a superconducting transition temperature of up to 45 K, $\text{RuSr}_2\text{GdCu}_2\text{O}_8$ exhibits not only the, by far, highest magnetic transition among all antiferromagnetic superconductors, but also the broadest coexistence-region for magnetic order and superconductivity.

Although the intriguing properties of $\text{RuSr}_2\text{GdCu}_2\text{O}_8$ have motivated numerous investigations, the difficulty to grow single crystals of the compound, on one hand, and the presence of the highly neutron-absorbing element Gd, on the other, restricted the amount of information that could be obtained. Dc-magnetization and neutron diffraction techniques, usually employed for investigating magnetic materials, could not determine the magnetic moment direction in a definite and precise way, and could not unambiguously answer the question about the possible influence of superconductivity on the magnetic order parameter. Even after the first single crystals were finally grown [85], the situation did not improve significantly, because the mass of the grown crystals is up to date far too small for neutron diffraction to be applicable. Magnetization measurements are also very difficult to carry out on such small crystals and cannot provide a precise angle between the magnetic moment and the crystallographic axes.

In this context the significance of a complementary experimental technique, which is sensitive to magnetism, but, unlike neutron diffraction, is not dependent on large sample masses, becomes obvious. Resonant x-ray diffraction at the L -absorption edges of a transition metal probes directly the partly occupied d electron orbitals, which are responsible for the magnetic properties of the material, and can give important information about the magnetic order in the system. The strong resonant enhancement of the magnetic scattering intensity at the L -edges ensures that large scattering signals can be obtained even from sub-millimeter sized samples. For this, a well-collimated x-ray beam, a high-brilliance synchrotron source and an experimental setup optimized for minimizing absorption are necessary.

It is particularly interesting that, thanks to the sensitivity of the technique to the azimuthal position of the magnetic moment with regard to the scattering plane, it was possible in our investigations to determine the exact magnetic moment direction in $\text{RuSr}_2\text{GdCu}_2\text{O}_8$ based on the observation of a single magnetic reflection – the only one accessible at this energy. The magnetic moment was found to lie neither along the crystallographic c -axis, nor parallel to the ab -plane, but instead at an angle of approximately 54 degrees away from c . These results can reconcile at least some of the apparently contradictory, previously reported data concerning the magnetic moment direction mentioned above. The success of our investigations underlines that resonant x-ray diffraction can be a valuable tool, complementary to neutron scattering, for determining magnetic structures. In general, while in neutron diffraction the scattering factors of at least two magnetic reflections have

to be known for determining the magnetic moment direction, in resonant x-ray diffraction it is sufficient to know how the intensity of *one* particular reflection varies with the azimuthal position of the sample. This advantage can compensate for the restricted access of the reciprocal space as a result of the low x-ray energies.

The determination of the magnetic moment direction is not the only case where resonant x-ray diffraction can be useful. Also for the determination of the temperature dependence of the magnetic order parameter and the investigation of possible anomalies in it, the strong resonant x-ray scattering signals can be a good alternative to neutrons. Powder samples are in principle sufficient for this purpose, but the larger scattering intensities provided by single crystals in a resonant x-ray scattering experiment can reveal details that are not observed by neutrons. The results presented in Section 4.5 strongly indicate that the better statistics achieved in the x-ray experiment enable the investigation of the influence of superconductivity on the magnetic ordering in $\text{RuSr}_2\text{GdCu}_2\text{O}_8$ better than neutron diffraction techniques.

Chapter 5

The system $\text{YBa}_2\text{Cu}_3\text{O}_{6+x}$

The compound $\text{YBa}_2\text{Cu}_3\text{O}_{6+x}$ is one of the most extensively investigated high-temperature superconducting cuprates. The discovery of superconductivity with a transition temperature T_c of up to 93 K in this system in 1987, one year after the first observation of high-temperature superconductivity by Bednorz and Müller in $\text{La}_{2-x}\text{Ba}_x\text{CuO}_4$ (Section 1.5), signified the first case where a T_c higher than the boiling point of liquid nitrogen was reported [89]. Since then, numerous studies have helped understand many of the properties of this interesting material. However, several issues still remain unclear and are currently issues of debate. One of the most controversial of them is related to the generic question about the existence of charge- and spin-strips in cuprates and their role with regard to the establishment of superconductivity (Section 1.5.3).

Incommensurate low-frequency spin excitations observed with neutron scattering in underdoped $\text{YBa}_2\text{Cu}_3\text{O}_{6.6}$ were interpreted as an indication that fluctuating stripes exist in this bilayered cuprate [90]. Later phonon measurements supported the existence of a dynamic stripe phase, by revealing the presence of charge fluctuations with the periodicity of the domain walls separating the spin stripes seen with neutrons [91]. Stripes of static nature, however, similar to the ones clearly observed with neutron and hard-x-ray diffraction in single-layered $\text{La}_{1.48}\text{Nd}_{0.4}\text{Sr}_{0.12}\text{CuO}_4$ [18, 92], have not been found so far in the $\text{YBa}_2\text{Cu}_3\text{O}_{6+x}$ system, despite the numerous studies that have been carried out in this direction. In addition, recent inelastic neutron scattering studies questioned the one-dimensionality of the spin excitations in $\text{YBa}_2\text{Cu}_3\text{O}_{6+x}$ and suggested alternative two-dimensional models, returning the stripe-discussion to its starting point [93]. Independent of this, a recent x-ray diffraction investigation of underdoped $\text{YBa}_2\text{Cu}_3\text{O}_{6+x}$ ($x \approx 0.63$) interestingly reported the existence of an anomaly in the diffuse scattering intensity around the pseudogap temperature [94]. It was claimed that this could be a manifestation of charge stripes in the CuO_2 planes. However, the problem is complicated by the fact that superstructures due to short-range oxygen ordering and related lattice distortions, with

wave-vectors depending sensitively on the oxygen content, are also observed in this system. Both phenomena – electronic stripes and oxygen order – are associated with lattice distortions and are expected to be intimately coupled. It is therefore difficult to establish which features of the x-ray data are related to which phenomenon.

It is the goal of the high-energy x-ray diffraction investigations presented in this chapter to clarify the origin of the observed diffuse features and conclude on whether they can be indeed considered as a signature of electronic stripe formation or if, on the contrary, they merely arise from oxygen ion order in the interleaved chain layers and associated lattice distortions. Our results show that the latter is the case.

5.1 Crystal Structure and Oxygen Order

The compound $\text{YBa}_2\text{Cu}_3\text{O}_{6+x}$ is an oxygen-deficient layered perovskite. Close to optimal oxygen doping ($x=0.92$), it has an orthorhombic crystal structure (space-group $Pmmm$), with lattice parameters $a=3.8227(1)$ Å, $b=3.8872(2)$ Å and $c=11.6802(2)$ Å at room temperature [95]. At oxygen content $x = 0.75$ the lattice parameters take the values $a=3.8420(1)$ Å, $b=3.9139(1)$ Å and $c=11.8065(4)$ Å, while at oxygen content $x = 0.62$ the values $a=3.8579(1)$ Å, $b=3.9128(1)$ Å and $c=11.8434(4)$ Å [96]. The stoichiometric compound $\text{YBa}_2\text{Cu}_4\text{O}_8$ is also orthorhombic (space-group $Ammm$), with room temperature lattice parameters $a=3.8430(5)$ Å, $b=3.8730(5)$ Å and $c=27.252(4)$ Å [97].

The $\text{YBa}_2\text{Cu}_3\text{O}_{6+x}$ unit cell consists of a set of two CuO_2 planes, which extend parallel to the crystallographic a and b axes and are separated by the central Y^{+3} ion of the cell (Figure 5.1). Every Cu ion of the CuO_2 planes is surrounded by five O ions, with which it forms a CuO_5 square pyramid. The O ions occupy the corners of the pyramid and the Cu ion the center of its base. The pyramids are corner-sharing along the ab plane. The CuO_2 double-layers of two successive unit cells along c are separated by interleaved layers, which also contain Cu ions. These Cu ions are connected via O ions along the b direction, forming, at low temperatures and sufficiently high oxygen contents, one-dimensional CuO chains that run parallel to the CuO_2 planes.

The oxygen content of the CuO chains can be sensitively controlled by appropriate heat treatment. In this way, the concentration of charge carriers in the CuO_2 layers is also modified, i.e. the material is doped. In the parent compound $\text{YBa}_2\text{Cu}_3\text{O}_6$ all oxygen sites in the chains are empty and the crystal structure is tetragonal. Upon doping the material, oxygen ions partly occupy the vacant sites between the Cu ions in the interleaved layers. As long as the oxygen content is low ($x < 0.3$) the oxygen sites are occupied randomly, and no long-range order is established. Above a critical doping level, however, CuO chains begin to form, as described above, and the system undergoes a structural phase transition from a tetragonal disordered to an

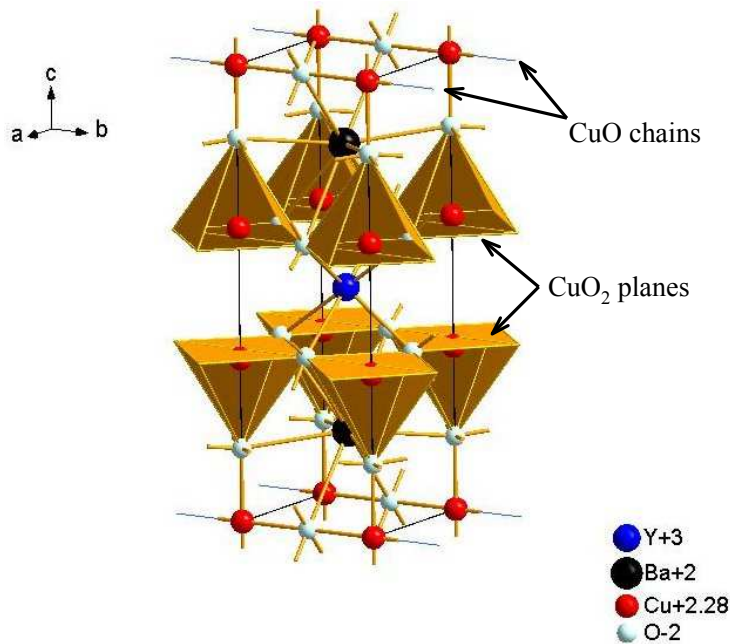


Figure 5.1: Crystal structure of $\text{YBa}_2\text{Cu}_3\text{O}_{6+x}$ (space-group $Pmmm$). The unit cell is made up of two CuO_2 planes, that extend parallel to the ab crystallographic plane at equal distances from the central Y^{+3} ion, and of CuO chains, which are parallel to the b direction. Every Cu ion in the CuO_2 planes is located at the basal center of a square CuO_5 pyramid. The CuO chains are the charge reservoirs of the CuO_2 planes. Their O content x is controlled by doping.

orthorhombic ordered phase. Sequences of 'full' (Cu-O) and 'empty' (Cu-vacancy) chains then appear, the periodicity of which along a depends sensitively on the oxygen stoichiometry.

Five different orthorhombic oxygen ordered structures have thus far been identified, commonly known as the ortho-I, ortho-II, ortho-III, ortho-V and ortho-VIII structures, respectively (Figure 5.2). Their formation was initially theoretically discussed by de Fontaine and coworkers, based on an Ising model consisting of three interpenetrating square lattices, one of which is occupied by copper ions and the other two by oxygen ions [99]. Extensive experimental investigations, both with neutron and with high-energy x-ray diffraction, have provided detailed information about the ordering pattern as a function of oxygen content for the whole doping range [100, 101, 98]. The superstructures can be well simulated with an extension of the asymmetric next nearest neighbour interaction (ASYNNI) model. For oxygen content $x = 0.5$, half of the available O sites are occupied and a chain sequence

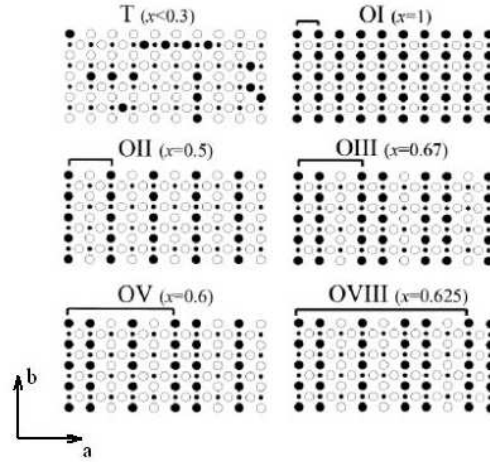


Figure 5.2: Idealized structural phases in $\text{YBa}_2\text{Cu}_3\text{O}_{6+x}$ [98]. The small bullets represent copper ions and the full (empty) large circles occupied (empty) oxygen sites. Depending on the O content x , a disordered tetragonal (T) or an orthorhombic ordered (O) phase with characteristic periodicity along a of the CuO chain sequence is established.

of the type 'full -empty -full -empty -etc' is established. The periodicity of the superstructure along a is then equal to two unit cells (ortho-II). For $x = 0.6$, a more complicated sequence of the type 'full -full -empty -full -empty -etc' is established, with a periodicity of five unit cells along a (ortho-V). For $x = 0.625$, the sequence is of the type 'full -full -empty -full -empty- full -full - empty -etc' and has a periodicity of eight unit cells along a (ortho-VIII). For $x = 0.67$, two out of the three oxygen sites are occupied and a three-unit-cell periodicity with two full chains followed by one empty is observed (ortho-III). Finally, in the stoichiometric compound $\text{YBa}_2\text{Cu}_3\text{O}_7$ ($x = 1$) all oxygen sites in the interleaved layers are occupied and the periodicity of the chain-superstructure is equal to one unit cell (ortho-I). A fully stoichiometric $\text{YBa}_2\text{Cu}_3\text{O}_7$ compound is quite difficult to prepare.

The structural phase diagram related to the oxygen order in $\text{YBa}_2\text{Cu}_3\text{O}_{6+x}$, as determined so far by neutron and high-energy x-ray diffraction, is shown in Figure 5.3 [98]. According to this, compounds with oxygen content higher than $x = 0.87$ have the ortho-I structure, with no sign of superstructure formation down to the lowest temperatures. The discovery in our investigations of a new ortho-IV ordered phase in optimally doped $\text{YBa}_2\text{Cu}_3\text{O}_{6+x}$ ($x = 0.92$) [102] revised this belief, as will be discussed in Section 5.5. The observation of the ortho-IV phase was independently reported also in Ref. [103].

Different from $\text{YBa}_2\text{Cu}_3\text{O}_{6+x}$, in $\text{YBa}_2\text{Cu}_4\text{O}_8$ there are *two* interleaved chain layers, instead of one, between two successive sets of CuO_2 planes. This double chain structure is very stable and prevents oxygen losses from the system. As a result, all

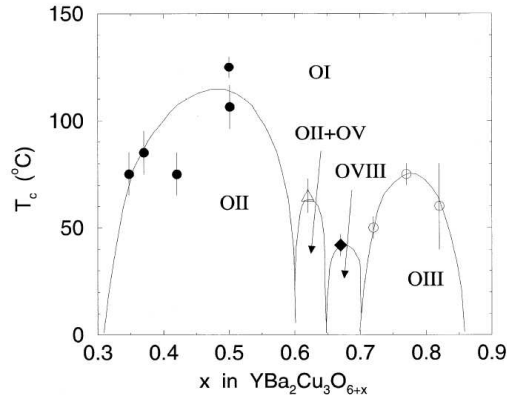


Figure 5.3: Structural phase diagram of $\text{YBa}_2\text{Cu}_3\text{O}_{6+x}$, showing the oxygen-ordered phases established at different oxygen contents, as determined by neutron and high-energy x-ray diffraction [98]. Our x-ray investigations revealed the existence of an additional new ortho-IV phase at optimal oxygen doping (Section 5.5), which is not shown here.

oxygen sites in the CuO chains are occupied and no change of the superconducting transition temperature can be achieved by changing the oxygen content via heat treatment. $\text{YBa}_2\text{Cu}_4\text{O}_8$ is fully stoichiometric, i.e. contains no oxygen vacancies, and therefore exhibits no superstructures like the ones described above.

Twining

The orthorhombicity of $\text{YBa}_2\text{Cu}_3\text{O}_{6+x}$ compounds with oxygen contents higher than $x \sim 0.3$ is small, i.e. the values of lattice parameters a and b , though different, are very close to each other. As a result, the a and b crystallographic directions can be mutually exchanged during the growing procedure in small regions of the crystal, depending on how the local thermal strains develop in every region. The structure of as-grown $\text{YBa}_2\text{Cu}_3\text{O}_{6+x}$ crystals is hence not homogeneous mesoscopically, but rather consists of twin domains, which are rotated by 90° one relative to the other in the ab plane, with the a and b axes mutually switched in neighboring domains. The domain walls are parallel to the $\{1\ 1\ 0\}$ crystallographic planes [104]. The size of the domains can vary significantly, from tens or hundreds of Ångströms up to fractions of a millimeter, depending on the growth conditions and the perfection of the crystals, but lies typically in the micrometer-range.

The presence of twins can be a problem in scattering experiments, when the direction and the periodicity of a superstructure needs to be determined. The scattering pattern from a fully twinned sample consists of equal contributions from both twin domains and has therefore a two-dimensional symmetry, even if the superstructure that generates it is microscopically one-dimensional. In order to resolve the real

symmetry of the superstructure, it is necessary to establish a single-domain structure in the ab -plane, i.e. to 'detwin' the crystal. For the detwinning, a thermomechanical method is usually employed, in which a uniaxial mechanical stress is applied along one of the tetragonal $\langle 1\ 0\ 0 \rangle$ axes of the polydomain crystal at elevated temperatures [105]. This leads to a reorientation of the ferroelastic domains and thus to an elimination of the twinning. The process is carried out in a gas atmosphere adjusted to the oxygen stoichiometry of the compound to prevent a change of the oxygen content. The method does not need to be applied in $\text{YBa}_2\text{Cu}_4\text{O}_8$, because this compound is naturally untwinned.

5.2 Superconductivity and Stripes

Bulk superconductivity is established in the two-dimensional CuO_2 planes of $\text{YBa}_2\text{Cu}_3\text{O}_{6+x}$ below a critical temperature T_c , which is sensitively dependent on the charge carrier concentration (hole doping) of the material. The hole concentration in the CuO_2 planes can be controlled either by changing the oxygen content x of the CuO chains (via annealing), or by chemically substituting part of the trivalent Y^{+3} ions with a divalent ion, such as Ca^{+2} .

Figure 5.4 shows the variation with oxygen content x of the superconducting transition temperature T_c of non-substituted $\text{YBa}_2\text{Cu}_3\text{O}_{6+x}$, as determined from Meissner effect measurements [95]. The material is superconducting for oxygen contents higher than $x \approx 0.4$. Above this value, T_c increases rapidly with increasing x and reaches a plateau at $x \approx 0.6$, which corresponds to a hole doping of around 0.125. The critical temperature at the plateau is approximately equal to 60 K. Via additional oxygen doping, T_c increases further and reaches its highest value $T_c(\text{opt}) = 93$ K at oxygen content $x = 0.92$, which provides a hole concentration around 0.16. At this oxygen content the compound is optimally doped. For $x > 0.92$ the material is overdoped and for $x < 0.92$ underdoped, with correspondingly lower T_c (Section 1.5.3).

For $x = 1$ ($\text{YBa}_2\text{Cu}_3\text{O}_7$) all oxygen sites in the CuO chains are occupied and the compound is stoichiometric. Higher oxygen contents are not possible. Due to the fact that the optimum doping is achieved for x very close to this maximum value, only slightly overdoped materials can be obtained via oxygen annealing. For more strongly overdoped systems, chemical substitution of Y^{+3} for a divalent cation, e.g. Ca^{+2} , is necessary. The generic phase diagram of copper-oxide superconductors, seen in Figure 1.6, is viable, as a general scheme, also for $\text{YBa}_2\text{Cu}_3\text{O}_{6+x}$.

The possible existence of charge- and spin- stripes in superconducting $\text{YBa}_2\text{Cu}_3\text{O}_{6+x}$ has been investigated in numerous studies. Inelastic neutron scattering experiments revealed the existence of low-frequency magnetic fluctuations in underdoped $\text{YBa}_2\text{Cu}_3\text{O}_{6.6}$, which change from commensurate to incommensurate

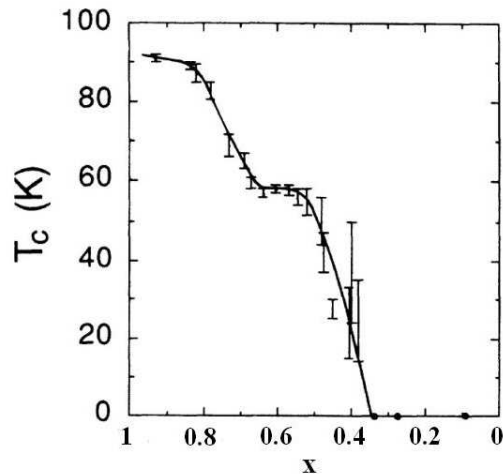


Figure 5.4: Variation of the superconducting transition temperature T_c with the oxygen content x in $\text{YBa}_2\text{Cu}_3\text{O}_{6+x}$ [95]. The optimal doping is achieved for $x = 0.92$ ($T_c = 92$ K).

upon cooling [106]. With the use of a newly developed two-dimensional position-sensitive neutron scattering imaging technique, it was later made possible to better resolve several quantitative issues and conclude that the excitations in $\text{YBa}_2\text{Cu}_3\text{O}_{6.6}$ are characterized by the same wavevectors, coherence lengths and spectral weights as the ones previously found in single-layered $\text{La}_{2-x}\text{Sr}_x\text{CuO}_4$ compounds with the same hole doping [23, 24]. This was claimed to be a first indication that stripes of dynamic nature are a rather generic feature of copper oxide superconductors, and not an exclusive property of single-layered cuprates of the $\text{La}_{2-x}\text{Sr}_x\text{CuO}_4$ family [90]. This evidence was supported by phonon measurements, which revealed the presence of charge fluctuations in underdoped $\text{YBa}_2\text{Cu}_3\text{O}_{6+x}$ [91]. The periodicity of the charge stripes was found to be consistent with the location of charge along the domain walls separating the spin stripes observed with neutrons.

Recent inelastic neutron studies, however, carried out on high-quality fully detwinned crystals, questioned the one-dimensional character of the low-energy spin excitations in nearly optimally doped and underdoped $\text{YBa}_2\text{Cu}_3\text{O}_{6+x}$ and reopened the stripe-debate [93]. Thanks to the almost twin-free structure of the samples, the scattering contribution from the minority domain was negligible in these experiments, and the geometry of the spin excitation spectrum could be clearly resolved. This was found to be two-dimensional, but with a strong anisotropy between the a^* and b^* crystallographic directions. The data were interpreted as excluding the existence of rigid arrays of one-dimensional stripes in superconducting $\text{YBa}_2\text{Cu}_3\text{O}_{6+x}$ and suggesting alternative two-dimensional models. A nematic liquid crystal striped phase, for instance, or a two-dimensional arrangement of charged domain walls could

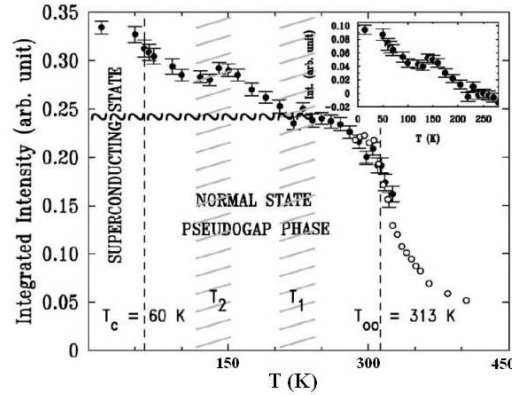


Figure 5.5: Temperature dependence of the integrated diffuse scattering intensity at $(4.4\ 0\ 0)$ as determined with high-energy x-ray diffraction by Islam *et al.* [94]. The anomaly around 220 K is claimed to indicate the strong correlation of the diffuse scattering features with charge fluctuations in the CuO_2 planes within the pseudogap phase.

be consistent with the observed spectrum.

Independent investigations of underdoped $\text{YBa}_2\text{Cu}_3\text{O}_{6.63}$ with high-energy synchrotron x-ray diffraction reported diffuse scattering reflections due to lattice modulations with wave-vectors $(\sim \frac{2}{5}\ 0\ 0)$, the intensity of which is significantly enhanced upon entry into the pseudogap phase [94]. These diffuse scattering features were interpreted as manifestations of charge stripes in the CuO_2 planes, that use the underlying oxygen-ordered structure as a spatial template. Whether this is indeed so or not, is nevertheless difficult to tell. Both relevant phenomena – fluctuating electronic stripes in the CuO_2 planes and short-range oxygen order in the CuO chains (Section 5.1) – are associated with lattice distortions and are expected to be intimately coupled. Determining the origin of the observed superstructures and concluding on the possible presence of stripes in $\text{YBa}_2\text{Cu}_3\text{O}_{6+x}$ requires thorough and combined investigations. The x-ray studies presented in Section 5.5 provide new information on this issue.

5.3 Isotope substitution: ^{16}O - vs. ^{18}O -rich compounds

Large oxygen isotope effects have been reported for the almost optimally doped high-temperature superconductors $\text{HoBa}_2\text{Cu}_3\text{O}_{6.9}$ and $\text{YBa}_2\text{Cu}_3\text{O}_{6.9}$. Inelastic neutron scattering investigations revealed that substitution of ^{16}O for its heavy isotope ^{18}O in $\text{HoBa}_2\text{Cu}_3\text{O}_{6.9}$ results in a significant increase of the pseudogap temperature T^*

from 170 K to around 220 K [107]. The large isotope shift in T^* is absent in NMR and NQR experiments. This was interpreted as an indication that the time scale of the mechanism giving rise to the isotope effect is beyond the time scales that can be detected by these techniques, namely lies in the range: $10^{-8} \gg \tau > 10^{-13}$ s.

Moreover, ellipsometry investigations reported a large and anomalous oxygen isotope effect on the a -axis component of the far-infrared electronic response of detwinned $\text{YBa}_2\text{Cu}_3\text{O}_{6.9}$ [108]. A pronounced low-energy electronic mode occurs in the ^{18}O - compound around 240 cm^{-1} , which exhibits a significant aging effect. This mode is completely absent in the ^{16}O - compound, at least above 120 cm^{-1} . The data were interpreted in terms of a collective electronic mode which becomes pinned by isotopic defects arising from residual traces of ^{16}O in the ^{18}O -substituted sample. The pronounced anisotropy of the mode could indicate either the existence of a charge density wave, or the formation of stripes, without being able to distinguish between the two.

5.4 Experimental

The x-ray diffuse intensity in underdoped and optimally doped $\text{YBa}_2\text{Cu}_3\text{O}_{6+x}$ and overdoped $\text{Y}_{1-y}\text{Ca}_y\text{Ba}_2\text{Cu}_3\text{O}_{6+x}$ single crystals was investigated with high-energy x-ray diffraction at photon energies of 100 keV and 115 keV [102]. X-rays couple directly to the charge and are a suitable probe of charge order superstructures, including electronic stripes. The high photon energy ensures that both static charge order and excitations of dynamic nature (fluctuating stripes) can be detected¹. The advantages of high-energy diffraction for investigating short-range correlations were explained in Section 2.3.2. The probing of the whole sample volume, due to the weak x-ray absorption, and the accessibility of a large part of the reciprocal space, are the most important of them. Difficulties related to the absorption of x-rays by air or by components of the experimental setup, which were of crucial importance in the resonant studies of ruthenates (Chapters 3 and 4), are not relevant here.

5.4.1 Samples

Good quality single crystals of various oxygen contents and charge carrier concentrations were used in our x-ray investigations. These included:

- an optimally doped $\text{YBa}_2\text{Cu}_3\text{O}_{6+x}$ crystal with $x \sim 0.92$ and superconducting transition temperature (midpoint) $T_c = 92.7 \text{ K}$ (transition width: 1 K),

¹The detection of excitations is restricted by the energy resolution of the experiments. This was in our investigations of the order of 200-300 eV.

- an underdoped $\text{YBa}_2\text{Cu}_3\text{O}_{6+x}$ crystal with $x \sim 0.75$ and $T_c = 67$ K (width: 4 K),
- an underdoped $\text{YBa}_2\text{Cu}_3\text{O}_{6+x}$ crystal with $x \sim 0.62$ and $T_c = 59.5$ K (width: 2 K),
- a highly overdoped $\text{Y}_{0.8}\text{Ca}_{0.2}\text{Ba}_2\text{Cu}_3\text{O}_{6.95}$ crystal with $T_c = 73$ K (width: 6 K),
- a naturally underdoped $\text{YBa}_2\text{Cu}_4\text{O}_8$ crystal with $T_c = 80.5$ K (width: 1 K),
- an optimally doped $\text{YBa}_2\text{Cu}_3\text{O}_{6.92}$ crystal, in which ^{16}O was completely replaced by its heavy isotope ^{18}O .

All $\text{YBa}_2\text{Cu}_3\text{O}_{6+x}$ crystals, including the Ca-doped one, were grown by the floating-zone method in the crystal-growth group of the Max-Planck-Institute for Solid State Research, by C.T. Lin *et al.*. A detailed description of the growing procedure can be found, for example, in Ref. [109]. The $\text{YBa}_2\text{Cu}_4\text{O}_8$ sample was grown with the self-flux method by B. Dabrowski *et al.* at the Department of Physics, Northern Illinois University (USA) [97].

For the characterization of the samples and the determination of the superconducting transition temperature, dc-SQUID magnetometry was used in all cases. The doping level of the Ca-doped crystal was confirmed by comparing its Raman and infrared spectra to data in the literature. The crystal volumes of the $\text{YBa}_2\text{Cu}_3\text{O}_{6+x}$ samples were of the order of $2 \times 2 \times 0.4 \text{ mm}^3$, while that of the $\text{YBa}_2\text{Cu}_4\text{O}_8$ crystal approximately $0.5 \times 0.8 \times 0.1 \text{ mm}^3$. The optimally and overdoped crystals were fully detwinned. The thermomechanical detwinning technique described in Ref. [105] was used for this purpose. The underdoped crystals were on the contrary investigated in their as-grown twinned state. The $\text{YBa}_2\text{Cu}_4\text{O}_8$ compound is naturally twin-free.

The wave-vector components ($h \ k \ l$) are indexed in the following in the orthorhombic space-groups: $Pmmm$ for $\text{YBa}_2\text{Cu}_3\text{O}_{6+x}$ and $\text{Y}_{1-y}\text{Ca}_y\text{Ba}_2\text{Cu}_3\text{O}_{6+x}$, and $Ammm$ for $\text{YBa}_2\text{Cu}_4\text{O}_8$.

5.4.2 Experimental Setup

The high-energy x-ray diffraction investigations described in this chapter were carried out, partly at beamline BW5 of the Hamburger Synchrotronstrahlungslabor (HASYLAB) at the Deutsches Elektronen-Synchrotron (DESY) in Hamburg (Germany), and partly at beamline 11ID-C of the Advanced Photon Source (APS) at Argonne National Laboratory, in Argonne (USA), at x-ray energies of 100 keV and 115 keV, respectively. Both beamlines use multipole wigglers as insertion devices and are optimized for investigations at high x-ray energies.

The setup at BW5

The BW5 beamline is located at storage ring DORIS III ($E=4.5$ GeV) of HASY-LAB. A wiggler of critical energy 26.5 keV and minimum gap 20 mm, located at a distance of approximately 30 meters from the entrance of the experimental station (experimental hutch), is used as x-ray source. The low-energy part of the produced spectrum is absorbed by a 1.5 mm thick water-cooled copper filter, located before the hutch, which reduces the heat load of the optical elements that follow. The x-ray energy range which can be used for measurements is thus between 60 keV and 200 keV. The BW5 experiments described in the following were carried out at a photon energy of 100 keV.

A triple-axis diffractometer, designed and built at HASYLAB, is installed in horizontal scattering geometry at BW5 (Figure 5.6). At the sample position a HUBER Eulerian cradle supports the sample environment. The x-ray beam enters the hutch through a beamsize-defining slit system, which is kept under vacuum, for suppressing the production of ozone and minimizing the background radiation in the hutch. The beam is then monochromatized at a SiGe gradient crystal, mounted inside a helium-flushed tank. The lattice parameter variation across the crystal's volume allows the diffraction of a relatively broad energy spectrum. In this way, a large beam intensity is achieved, as needed for the investigation of weak diffuse features. The intensity of the monochromatic beam is monitored with the use of a silicon diode.

A SiGe gradient crystal, identical to the monochromator, can be also used as analyzer after the sample position, for the suppression of the background. A germanium solid-state detector, cooled with liquid nitrogen, is used for the detection of the scattered beam. Calibrated iron absorbers, mounted on a wheel between the sample and the analyzer, reduce the beam intensity when strong reflections are investigated. This is necessary due to the limited dynamic range of the detector.

For measurements at low temperatures, a closed-cycle (Displex) cryostat capable of reaching temperatures between 6 K and 350 K is mounted on the Eulerian cradle. In one case, a high-temperature Displex cryostat capable of reaching temperatures up to 850 K was used instead. The cryostat is mounted on the χ -circle of the diffractometer. The sample position is covered by an aluminum cap, inside which high vacuum is achieved with the use of a turbo pump.

All mechanical and electronic components at BW5 are controlled by the HASY-LAB standard software SPECTRA ON LINE.

The setup at 11ID-C

The 11ID-C beamline is located at the 7 GeV storage ring of APS. An elliptical multipole wiggler with critical energy 32 keV is used as x-ray source, providing x-

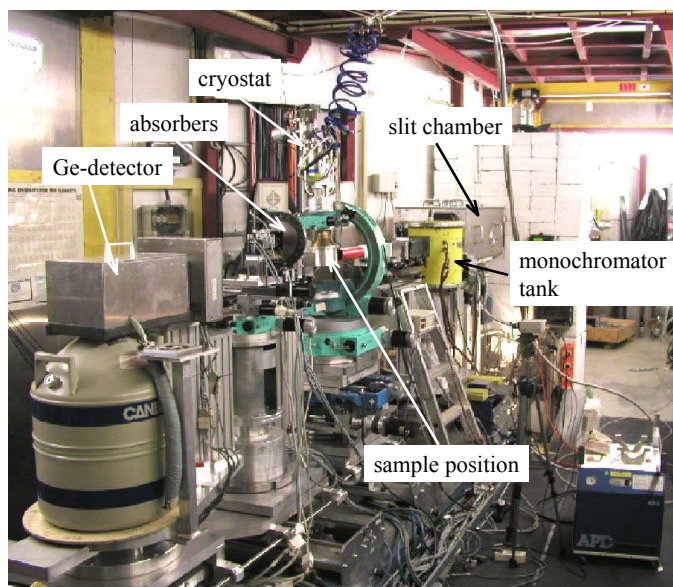


Figure 5.6: The experimental setup inside the BW5 experimental station. The x-ray beam enters the hutch on the right side of the photograph, through a beamsize-defining slit system. A SiGe gradient monochromator crystal ensures high monochromatic beam intensities. The sample is mounted on a closed-cycle cryostat on the χ -circle of a 4-circle diffractometer. A Ge solid-state detector is used for the detection of the scattered intensity.

rays in the energy range between 60 keV and 200 keV. The 11ID-C experiments described in the following were carried out at a photon energy of 115 keV.

A high-energy triple-axis x-ray diffractometer with three crystals (monochromator, sample, analyzer) and vertical scattering plane is available at the experimental station for single-crystal diffraction experiments. A schematic view of the diffractometer and a photograph of part of the setup are shown in Figures 5.7 and 5.8, respectively.

An annealed Si(311) crystal is used as first, horizontal monochromator. No second, vertical monochromator was used in our experiments. Brass collimators and slit systems reduce the detected background radiation. A germanium solid-state detector, cooled with liquid nitrogen, is used for the detection of the scattered beam. The intensity of the monochromatic beam before the sample is monitored by a Si diode. For measurements at low temperatures, a closed-cycle (Displex) cryostat is mounted on the sample tower of the diffractometer. In one case, a He-flow cryostat was used instead. The beamline is operated through a user interface implemented in the program package Igor run on Macintosh workstations. All motors are controlled by VME-based electronics via EPICS.

More information and technical specifications of the experimental setup at beam-

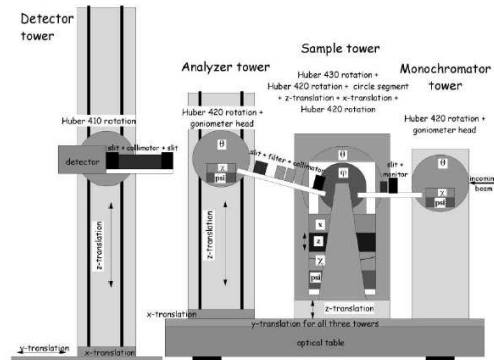


Figure 5.7: Schematic view of the high-energy triple-axis diffractometer at 11ID-C [110]. The x-ray beam enters the setup on the right side of the picture. The second monochromator, the sample, the analyzer and the detector are mounted on four different towers. The scattering plane is vertical.

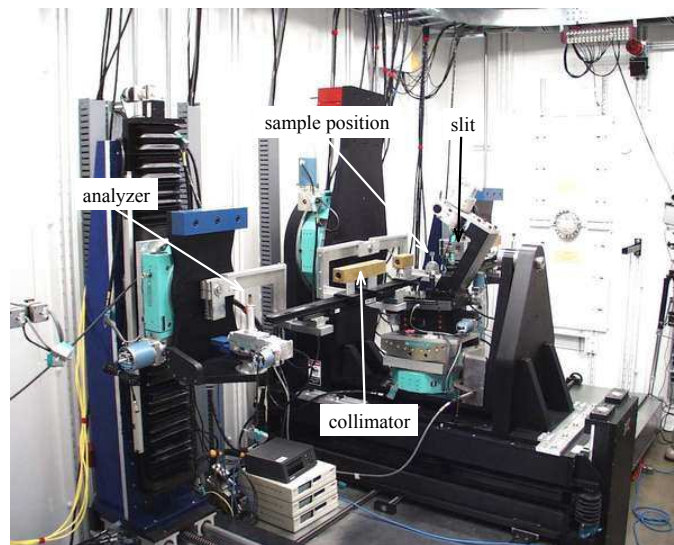


Figure 5.8: Part of the experimental setup inside the 11ID-C station. A Si(311) crystal is used as monochromator. The x-ray beam enters the hutch on the right side of the picture. After being diffracted by the sample and the analyzer, the x-rays are collected by a Ge-detector (not shown). Slits and collimators are used for suppressing the background.

line 11ID-C can be obtained in Ref. [110].

5.5 X-ray Diffraction Investigations

In order to resolve the origin of the diffuse scattering features in $\text{YBa}_2\text{Cu}_3\text{O}_{6+x}$, a systematic investigation of their dependence on temperature, oxygen content and charge carrier concentration was carried out. By comparing the diffuse patterns of three compounds with different oxygen contents – $\text{YBa}_2\text{Cu}_3\text{O}_{6.62}$, $\text{YBa}_2\text{Cu}_3\text{O}_{6.75}$ and $\text{YBa}_2\text{Cu}_3\text{O}_{6.92}$ – the variation of the periodicity, the intensity and the correlation length of the superstructures with changing oxygen concentration was studied. Surprisingly, a superstructure with periodicity equal to four elementary unit cells was observed in the optimally doped system. By then comparing two materials with almost the same oxygen content, but quite different charge carrier concentrations – $\text{YBa}_2\text{Cu}_3\text{O}_{6.92}$ and $\text{Y}_{0.8}\text{Ca}_{0.2}\text{Ba}_2\text{Cu}_3\text{O}_{6.95}$ – the effect of the hole doping was independently investigated. Electronic stripes in the CuO_2 planes are expected to be sensitively dependent on hole doping, while oxygen ion ordering in the CuO chains depends only on the amount of oxygen in the system. The diffuse features were found to be changing only with oxygen content and not with doping via Ca^{+2} substitution. The temperature dependence of the observed diffuse features was furthermore studied within a broad temperature range. Electronic stripes are expected to be sensitive to the pseudogap phenomena and the persistence of the diffuse features up to well above room temperature is a strong indication against a stripe-related origin of them. Finally, additional information is provided by the investigation of a stoichiometric, naturally defect-free compound – $\text{YBa}_2\text{Cu}_4\text{O}_8$. Electronic stripes should be much more easily observable in the absence of diffuse scattering from oxygen vacancy ordering. No diffuse superstructure reflections were nevertheless found in the scattering pattern of $\text{YBa}_2\text{Cu}_4\text{O}_8$.

5.5.1 Investigations of underdoped $\text{YBa}_2\text{Cu}_3\text{O}_{6+x}$ compounds

Scans along the $(h\ 0\ 2.5)$ direction in reciprocal space were carried out on underdoped $\text{YBa}_2\text{Cu}_3\text{O}_{6.75}$ and $\text{YBa}_2\text{Cu}_3\text{O}_{6.62}$ compounds at various temperatures. The resulting scattering intensity plots at a sample temperature of 30 K are shown in Figures 5.9 and 5.10, respectively. For the determination of the orientation (UB) matrix of the samples, the $(2\ 0\ 0)$ and $(2\ 0\ 6)$ main Bragg reflections were used.

In $\text{YBa}_2\text{Cu}_3\text{O}_{6.75}$ (Fig. 5.9) the intensity is peaked at positions $h = 4.33$ and $h = 4.66$, i.e. at wave-vectors $Q \pm 0.33$, with Q being the wave-vector of a main Bragg peak. This diffraction pattern reveals the existence of a superstructure in the material with a periodicity equal to three elementary unit cells, in accordance with Ref. [98]. The reflection at wave-vector $Q + 0.33$ is a factor of two stronger

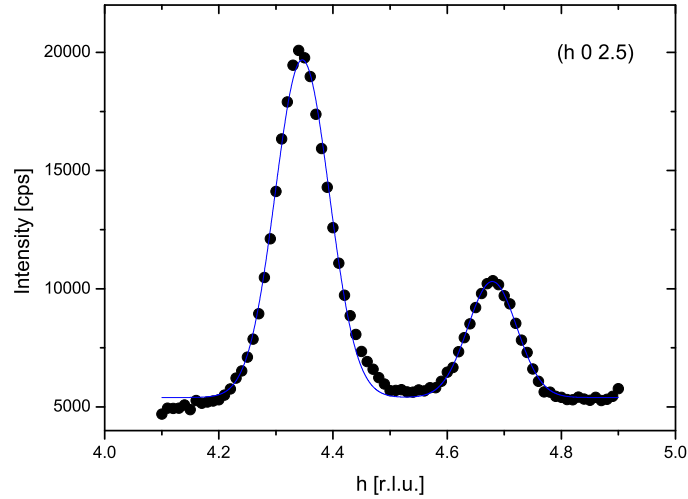


Figure 5.9: Scan along the $(h\ 0\ 2.5)$ reciprocal space direction in underdoped $\text{YBa}_2\text{Cu}_3\text{O}_{6.75}$ at temperature $T = 30$ K. The diffuse scattering pattern is characterized by a three-unit-cell periodicity (ortho-III phase), with reflections at $h = 4.33$ and $h = 4.66$. The solid line is a fit of Gaussian profiles to the data.

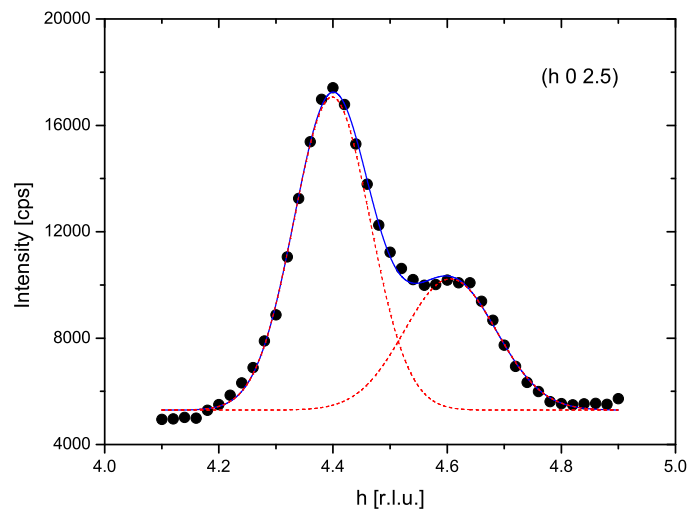


Figure 5.10: Scan along the $(h\ 0\ 2.5)$ reciprocal space direction in underdoped $\text{YBa}_2\text{Cu}_3\text{O}_{6.62}$ at temperature $T = 30$ K. The diffuse scattering pattern is characterized by a five-unit-cell periodicity (ortho-V phase), with reflections at $h = 4.4$ and $h = 4.6$. The solid line is a fit of Gaussian profiles to the data.

than the reflection at $Q - 0.33$. Both diffuse features are approximately 5 orders of magnitude weaker than the closest main Bragg reflections (e.g. $(4\ 0\ 3)$). The half-width at half-maximum of the superstructure peaks is of the order of 0.06 reciprocal lattice units (r.l.u.), which corresponds to a correlation length of the order of 20 Å along h . The correlations are thus only of short range.

A similar superstructure is observed in $\text{YBa}_2\text{Cu}_3\text{O}_{6.62}$ (Fig. 5.10), but the scattering intensity is in this case peaked at positions $h = 4.4$ and $h = 4.6$, i.e. at wave-vectors $Q \pm 0.4$. This diffraction pattern arises from a superstructure with periodicity equal to five elementary unit cells. The peak at $Q + 0.4$ is a factor of two stronger than at $Q - 0.4$. The half-width at half-maximum of the peaks is of the order of 0.08 r.l.u., which is translated into a correlation length of the order of 15 Å along h .

The temperature dependence of the integrated scattering intensity of the $(4.33\ 0\ 2.5)$ superstructure reflection in $\text{YBa}_2\text{Cu}_3\text{O}_{6.75}$, as determined from h -scans, is shown in Figure 5.11(a). For the calculation of the intensities the data were fitted with Gaussian profiles. The intensity follows a smooth decrease with increasing temperature, without showing any anomalies up to room temperature. The variation with temperature of the half-width at half-maximum of the reflection is shown in panel (b) of the same figure. The data indicate a small, smooth decrease of the width with increasing temperature, though the decrease is comparable in size with the experimental error bars. It is noted that the $(4.33\ 0\ 2.5)/(4.66\ 0\ 2.5)$ superstructures are clearly present up to a temperature of at least 500 K. Nevertheless, no reliable fitting of the peaks is possible above room temperature. This is because of the strong contribution of the 'tail' of the $(5\ 0\ 3)$ main Bragg reflection, which becomes broader with increasing temperature, due to the thermal diffuse scattering effect, and gradually covers part of the superstructure peaks. For this reason, only data up to 300 K are shown in Figure 5.11.

The temperature dependence of the integrated intensity of the $(4.4\ 0\ 2.5)$ diffuse reflection in $\text{YBa}_2\text{Cu}_3\text{O}_{6.62}$, as determined from h -scans, is shown in Figure 5.12(a). Again Gaussian profiles were used for the fitting of the peaks. The scattering intensity decreases smoothly with increasing temperature and has still a significant non-zero value at 400 K, the highest temperature investigated. The half-width at half-maximum of the peak is shown in panel (b) of the same figure. Like in $\text{YBa}_2\text{Cu}_3\text{O}_{6.75}$, the width remains almost constant up to high temperatures, indicating only a very small narrowing of the reflection upon warming.

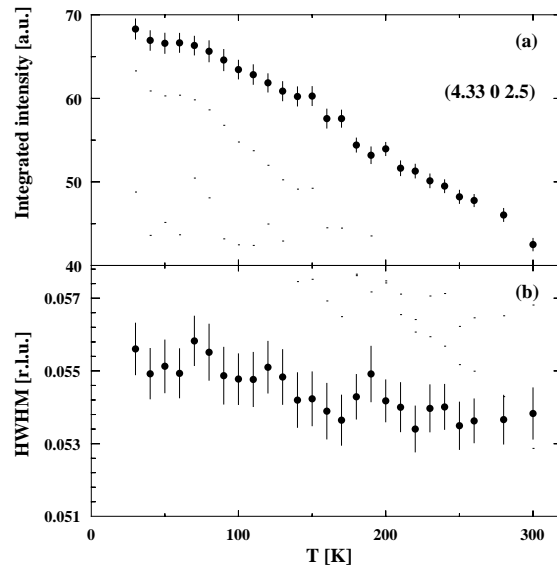


Figure 5.11: Temperature dependence of the integrated diffuse scattering intensity (a) and of the half-width at half-maximum (b) of the $(4.33\ 0\ 2.5)$ reflection in $\text{YBa}_2\text{Cu}_3\text{O}_{6.75}$, as determined from h -scans by fitting with Gaussian profiles.

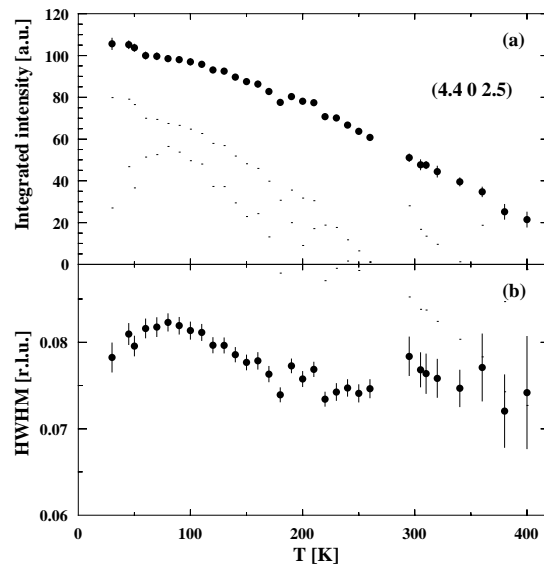


Figure 5.12: Temperature dependence of the integrated diffuse scattering intensity (a) and of the half-width at half-maximum (b) of the $(4.4\ 0\ 2.5)$ reflection in $\text{YBa}_2\text{Cu}_3\text{O}_{6.62}$, as determined from h -scans by fitting with Gaussian profiles.

5.5.2 Investigations of optimally doped and overdoped $\text{Y}_{1-y}\text{Ca}_y\text{Ba}_2\text{Cu}_3\text{O}_{6+x}$ compounds

For the investigation of optimally doped $\text{YBa}_2\text{Cu}_3\text{O}_{6.92}$ and overdoped $\text{Y}_{0.8}\text{Ca}_{0.2}\text{Ba}_2\text{Cu}_3\text{O}_{6.95}$ compounds, reciprocal space scans both in the hk - and in the hl - scattering planes were carried out at various temperatures. Figure 5.13 shows the variation of the scattering intensity along the $(h\ 0\ 5.6)$ direction in $\text{YBa}_2\text{Cu}_3\text{O}_{6.92}$ (full bullets) and $\text{Y}_{0.8}\text{Ca}_{0.2}\text{Ba}_2\text{Cu}_3\text{O}_{6.95}$ (empty bullets) at temperature 30 K.

The diffuse patterns of the two compounds are practically identical to each other. They are characterized by reflections at positions $Q \pm 0.25$ (Q : wave-vector of a main Bragg reflection), for example at $h = 4.25$ and $h = 4.75$. A superstructure with periodicity equal to four elementary unit cells is thus present in both materials. Such a superstructure had not been reported for optimally doped and overdoped $\text{YBa}_2\text{Cu}_3\text{O}_{6+x}$ compounds so far. Not only the periodicities, but also the relative intensities and the correlation lengths are the same in the two systems. The half-width at half-maximum of the superstructure reflections is in both cases of the order of 0.17 r.l.u., which corresponds to a correlation length of the order of 4 Å along h . Small deviations in intensity observed close to the $(4\ 0\ 5.6)$ position should be disregarded, because the contribution (tail) of the main Bragg reflection $(4\ 0\ 6)$ obstructs the diffuse intensity at this position. The diffuse peak at position $Q + 0.25$ is in all cases significantly stronger (factor of two) than the one at $Q - 0.25$.

In order to determine the temperature dependence of the integrated intensity in $\text{YBa}_2\text{Cu}_3\text{O}_{6.92}$, scans along the l direction were carried out. These were preferred to h scans, used for the same purpose in the ortho-III and ortho-V underdoped compounds, because they allow in this case the easier subtraction of the background. The modulation of the scattering intensity along l at $h = 4.25$ and $k = 0$ at low temperatures (30 K) is shown in Figure 5.14. The intensity is peaked at positions $l = 0, \pm 2.75, \pm 5.5$ etc. By fitting Gaussian profiles to the superstructure peaks, their integrated intensity was determined at various temperatures. The variation with temperature of the integrated intensity of the $(5.25\ 0\ 5.5)$ reflection is shown in Figure 5.15(a). The intensity decreases smoothly with increasing temperature, without any anomalies up to 500 K, the highest temperature investigated. No indication of an anomalous temperature dependence near the onset of the electronic pseudogap is found, as claimed for the ortho-V compound by Islam *et al.* [94]. The intensity variation observed in Ref. [94] is clearly larger than the statistical variation of the data presented in Figure 5.15(a).

The widths of the superstructure peaks are also determined by fitting. The variation with temperature of the half-width at half-maximum at the $(5.25\ 0\ 5.5)$ position is shown in Figure 5.15(b). The data clearly show a slight smooth increase with increasing temperature of the correlation length characterizing the ordering which gives rise to the diffuse features. At all temperatures the superstructure

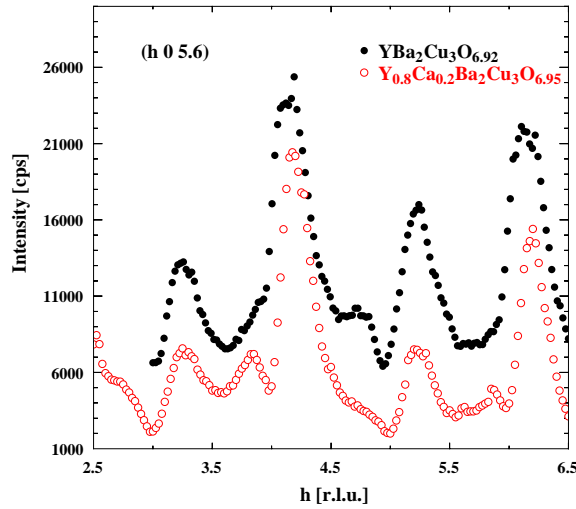


Figure 5.13: Scans along the $(h\ 0\ 5.6)$ reciprocal space direction in optimally doped $\text{YBa}_2\text{Cu}_3\text{O}_{6.92}$ (full bullets) and overdoped $\text{Y}_{1-y}\text{Ca}_y\text{Ba}_2\text{Cu}_3\text{O}_{6+x}$ (empty bullets) at temperature $T = 30$ K. The diffuse scattering patterns of the two compounds are practically identical, despite the different charge carrier concentrations, characterized by a four-unit-cell periodicity (new ortho-IV phase) with reflections at wave-vectors $q = 0.25$ and $q = 0.75$ off the main Bragg peaks.

peaks are very broad and dilute (up to almost 0.9 r.l.u. along l), indicating a very short-range order. The correlation length along l is of the order of 4 Å, i.e. smaller than one unit cell. This means that the correlations are only between neighboring CuO chain layers, BaO planes and CuO_2 planes.

A nice way of obtaining an overview of the diffuse pattern of a material is to create two-dimensional maps of specific areas in reciprocal space. This is done by performing a large number of scans along a certain direction, changing every time by a small amount the position on one of the axes perpendicular to the scattering direction. For example, by performing a large number of l -scans for various h values, an intensity map of the hl plane can be made. To do so, all l -scans are put together one next to the other using a proper imaging programme (in our case: Igor) and a color scale is applied for denoting the intensity at every point of the map, resulting in a three-dimensional contour plot, which allows the easy comparison of the patterns of different compounds.

Such a contour plot of the hl scattering plane of optimally doped $\text{YBa}_2\text{Cu}_3\text{O}_{6.92}$ at low temperatures (30 K) is shown in Figure 5.16(b). The diffuse superstructure reflections at $(4.25\ 0 \pm 2.75)$ are easily seen as light-red broad spots. More difficult to distinguish are the weaker $(4.75\ 0 \pm 2.75)$ diffuse reflections. It is interesting to compare this intensity map with the one of overdoped

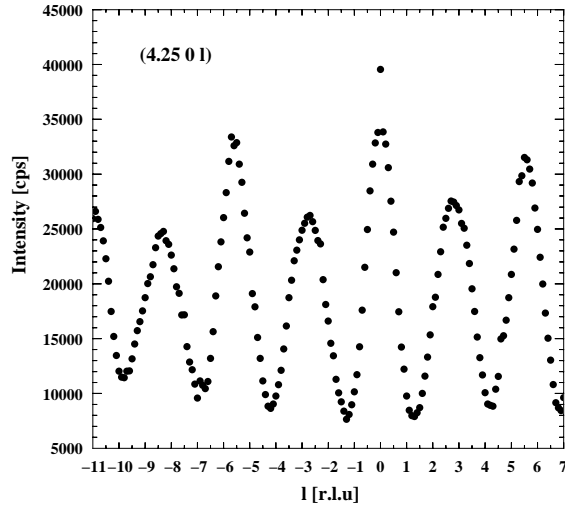


Figure 5.14: Scan along the $(4.25 \ 0 \ l)$ reciprocal space direction in optimally doped $\text{YBa}_2\text{Cu}_3\text{O}_{6.92}$ at temperature 30 K. Reflections are observed at positions $l = 0, \pm 2.75, \pm 5.5, \dots$. The periodicity of the diffuse intensity perpendicular to the CuO_2 planes is characteristic of interatomic distances within the unit cell.

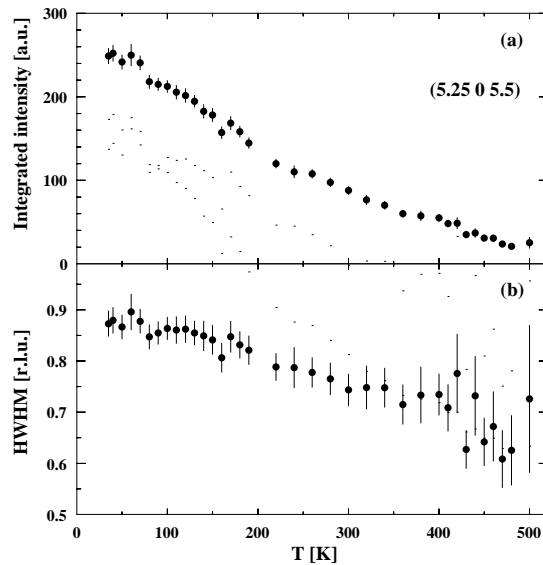


Figure 5.15: Temperature dependence of the integrated intensity (a) and of the half-width at half-maximum (b) of the $(5.25 \ 0 \ 5.5)$ reflection in $\text{YBa}_2\text{Cu}_3\text{O}_{6.92}$, as determined from l -scans by fitting with Gaussian profiles.

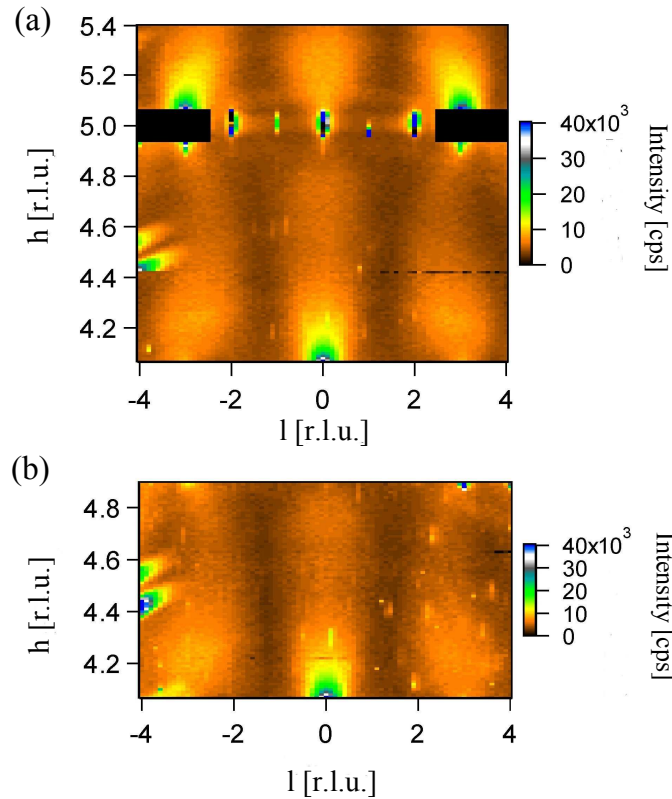


Figure 5.16: Contour plots of the diffuse intensity in the $(h\ 0\ l)$ plane of (a) ^{18}O - and (b) ^{16}O -rich optimally doped $\text{YBa}_2\text{Cu}_3\text{O}_{6.92}$ at low temperatures (30 K). In (a) the strong main Bragg reflections are masked. The diffuse patterns are virtually identical in the two materials, showing that any isotope effects in $\text{YBa}_2\text{Cu}_3\text{O}_{6+x}$ cannot originate from variations in the short-range oxygen order.

$\text{Y}_{0.8}\text{Ca}_{0.2}\text{Ba}_2\text{Cu}_3\text{O}_{6.95}$, shown in Figure 5.17(b). It is evident that the diffuse patterns of the two compounds are virtually identical to each other, exhibiting the same four-cell periodicity. The diffuse peaks which are far enough from main Bragg reflections, e.g. at positions $(4.25/4.75\ 0\ 2.75)$, $(5.25/5.75\ 0\ 5.5)$ and $(5.25\ 0\ 0)$, are all clearly observed. The conclusion drawn by the comparison of the h -scans in Figure 5.13 is thus confirmed and extended for the whole reciprocal space: $\text{YBa}_2\text{Cu}_3\text{O}_{6.92}$ and $\text{Y}_{0.8}\text{Ca}_{0.2}\text{Ba}_2\text{Cu}_3\text{O}_{6.95}$ are characterized by identical superstructures.

In the upper (a) panel of Figure 5.17 an intensity map of the $(h\ k\ 5.5)$ plane of $\text{Y}_{0.8}\text{Ca}_{0.2}\text{Ba}_2\text{Cu}_3\text{O}_{6.95}$ is shown. The diffuse peaks with the characteristic four-cell periodicity are clearly observed at all integer k -positions, e.g. at $(2.25/2.75\ 1\ 5.5)$, $(3.25/3.75\ 2\ 5.5)$ and $(2.25/2.75\ 3\ 5.5)$. No superstructures are observed along the k direction, i.e. parallel to the CuO chains.

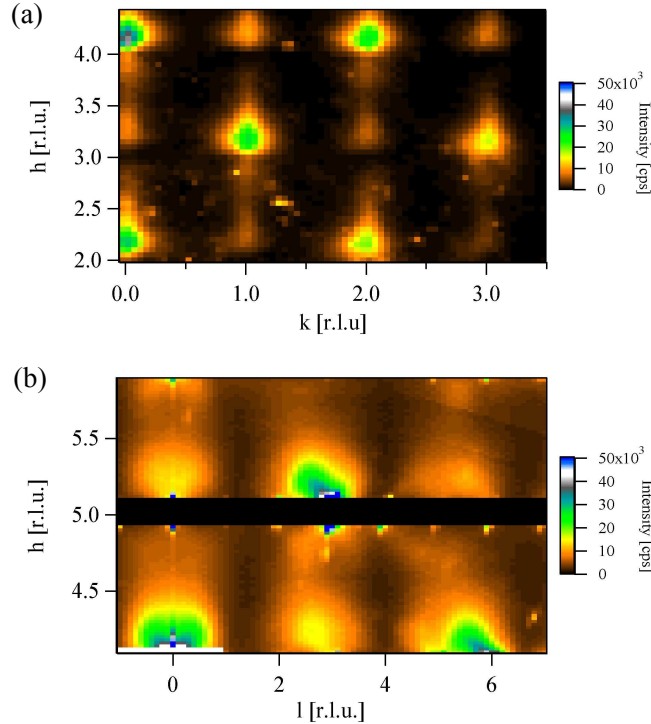


Figure 5.17: Contour plots of the diffuse intensity in the (a) $(h k 5.5)$ and (b) $(h 0 l)$ planes of overdoped $\text{Y}_{0.8}\text{Ca}_{0.2}\text{Ba}_2\text{Cu}_3\text{O}_{6.95}$. In (b) the main Bragg reflections are masked. The periodicity of the diffuse pattern is the same as in the optimally doped $\text{YBa}_2\text{Cu}_3\text{O}_{6.92}$ compound.

Motivated by the isotope effect observations in nearly optimally doped high-temperature superconductors (Section 5.3), we investigated an optimally doped $\text{YBa}_2\text{Cu}_3\text{O}_{6.92}$ sample, in which ^{16}O was fully substituted by ^{18}O . A contour plot of its diffuse intensity in the $(h 0 l)$ scattering plane is shown in Figure 5.16a. The direct comparison of this plot with the one corresponding to the material containing ^{16}O (panel (b) of the same figure) immediately leads to the conclusion that the oxygen isotope substitution has no influence on the diffuse pattern of $\text{YBa}_2\text{Cu}_3\text{O}_{6.92}$. The intensity maps of the materials containing different oxygen isotopes are identical.

5.5.3 Investigations of the stoichiometric $\text{YBa}_2\text{Cu}_4\text{O}_8$ compound

Reciprocal space scans along the l direction were carried out in $\text{YBa}_2\text{Cu}_4\text{O}_8$ at $k = 0$ for various h values. The resulting contour plot at low temperatures (30 K) is shown

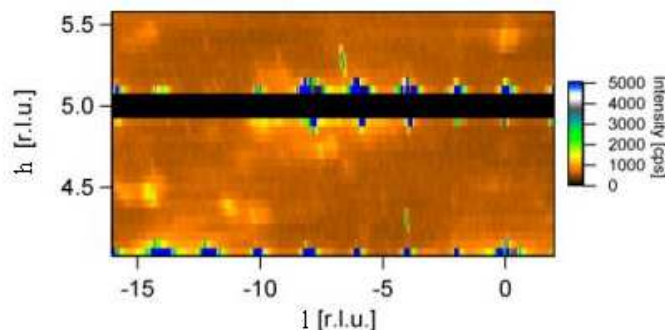


Figure 5.18: Contour plot of the diffuse intensity in the $(h\ 0\ l)$ plane of stoichiometric $\text{YBa}_2\text{Cu}_4\text{O}_8$. No diffuse intensity is observed within the experimental sensitivity.

in Figure 5.18. Interestingly, no diffuse features are observed in the intensity map throughout the whole reciprocal space area that was investigated. At least down to the intensity level of the diffuse peaks in optimally doped $\text{YBa}_2\text{Cu}_3\text{O}_{6.92}$, no superstructure reflections can be seen among the main Bragg peaks.

The $\text{YBa}_2\text{Cu}_4\text{O}_8$ sample was investigated extensively in three different experiments, carried out at two different beamlines (BW5 and 11ID-C), and along all three crystallographic directions. No signatures of diffuse scattering were found in any of these attempts. If superstructures of any kind are present in this system, the diffuse intensity originating from them must be at least one order of magnitude weaker than the features observed in the optimally doped $\text{YBa}_2\text{Cu}_3\text{O}_{6+x}$ compound. Such weak features, if existent, would lie below the sensitivity level of our experimental technique.

5.6 Discussion

The superstructures with periodicities equal to three and five unit cells in underdoped $\text{YBa}_2\text{Cu}_3\text{O}_{6+x}$ compounds with oxygen contents $x = 0.75$ and $x = 0.62$, respectively, are known as the 'ortho-III' and 'ortho-V' phases. As explained in Section 5.1, they originate from lattice distortions induced by short-range ordering of oxygen vacancies in the interleaved layers of the unit cell in a pattern defined by certain sequences of full and empty CuO chains. The properties of these ordered phases have been thoroughly investigated in a large number of neutron and high-energy x-ray diffraction experiments. The studies carried out so far have indicated that the superstructures related to the oxygen order are present only up to a certain oxygen content. Close to and above optimal doping ($x = 0.92$) no diffuse features were reported. The scattering pattern of $\text{YBa}_2\text{Cu}_3\text{O}_{6+x}$ compounds with $x > 0.87$

was assumed to exhibit the simple 'ortho-I' periodicity, with no superstructure reflections between the main Bragg peaks (Figure 5.2).

It is therefore particularly interesting that the high-energy x-ray diffraction experiments we carried out on optimally doped $\text{YBa}_2\text{Cu}_3\text{O}_{6.92}$ and strongly overdoped $\text{Y}_{0.8}\text{Ca}_{0.2}\text{Ba}_2\text{Cu}_3\text{O}_{6.95}$ compounds revealed the existence of a weak superstructure with four-cell periodicity in these systems. The observation was independently reported also in Ref. [103]. For the origin of the observed superstructure there are basically two possibilities:

1. it arises from a short-range ordering of the oxygen vacancies in the interleaved layers of the lattice and the associated lattice distortions, analogous to the ortho-III and ortho-V phases of the underdoped materials. This new 'ortho-IV' oxygen-ordered phase would correspond to a sequence of three full CuO chains followed by one empty.
2. it arises from spontaneous electronic stripe formation in the CuO_2 layers. Such a stripe order could use the oxygen vacancy ordering as a template, consistent with what suggested by Islam *et al.* for the underdoped system [94].

In the following we attempt a distinction between these possibilities, based on a combined evaluation of our experimental observations.

The similarity of the diffuse scattering patterns of the $\text{YBa}_2\text{Cu}_3\text{O}_{6.92}$ and $\text{Y}_{0.8}\text{Ca}_{0.2}\text{Ba}_2\text{Cu}_3\text{O}_{6.95}$ compounds (Figures 5.13, 5.16, 5.17) is a strong indication against the stripe-related scenario. Stripe correlations are expected to be characterized by a wave-vector which is strongly dependent on the charge carrier concentration, and by an amplitude which is strongly reduced in heavily overdoped samples. On the other hand, diffuse features due to lattice distortions induced by oxygen vacancy ordering are expected to depend exclusively on the oxygen content, which determines the density of vacancies in the interleaved layers. The investigated Ca-doped compound has almost the same oxygen content as the optimally doped material. Any superlattice reflections related to oxygen vacancy order should be therefore identical in the two samples. The hole doping in the two systems is, on the contrary, very different. The 20% substitution of trivalent Y^{+3} by divalent Ca^{+2} results in strong hole doping in the CuO_2 bilayers. If the diffuse features observed in $\text{YBa}_2\text{Cu}_3\text{O}_{6.92}$ were due to stripe correlations, they should appear much weaker and at different wave-vectors in overdoped $\text{Y}_{0.8}\text{Ca}_{0.2}\text{Ba}_2\text{Cu}_3\text{O}_{6.95}$. The experimental data show however the opposite: the diffuse features in $\text{Y}_{0.8}\text{Ca}_{0.2}\text{Ba}_2\text{Cu}_3\text{O}_{6.95}$ are characterized by the same periodicities, intensities and correlation lengths as in $\text{YBa}_2\text{Cu}_3\text{O}_{6.92}$. This observation is thus inconsistent with the assumption that electronic stripe correlations are the origin of the superstructure reflections. Instead it rather indicates that the diffuse features are due to oxygen vacancy ordering in an ortho-IV sequence of full and empty CuO chains. The absence of superstructures

along the k direction, i.e. parallel to the CuO chains (Figure 5.17a), is consistent with this picture. The large width of the superstructure reflections, indicative of small correlation lengths, is furthermore well explained by the small density of oxygen vacancies (high oxygen contents) in the investigated compounds. The correlation length in $\text{YBa}_2\text{Cu}_3\text{O}_{6.92}$ and $\text{Y}_{0.8}\text{Ca}_{0.2}\text{Ba}_2\text{Cu}_3\text{O}_{6.95}$ (approximately 4 Å along h) is a factor of 4 smaller than in the underdoped $\text{YBa}_2\text{Cu}_3\text{O}_{6.62}$ and $\text{YBa}_2\text{Cu}_3\text{O}_{6.75}$ systems (15-20 Å), which contain more oxygen vacancies.

Another property of the observed diffuse features which can provide information about their origin is their variation with temperature. Electronic stripes are generally expected to be quite sensitive to thermal vibrations and thus not likely to survive up to high temperatures. This is clearly seen in Nd-doped $\text{La}_{2-x}\text{Sr}_x\text{CuO}_4$, for instance, where the stripe-induced superstructures vanish already at temperatures well below room temperature (≈ 60 K) [18]. Superstructures induced by oxygen vacancy ordering, on the contrary, are stabilized by strong Coulomb interactions and are less sensitive to high temperatures than electronic correlations. Although oxygen diffusion kinetics become faster at higher temperatures leading to an increased disorder, oxygen vacancies can remain aligned in chains, at least of short length, up to temperatures significantly exceeding room temperature, as shown e.g. in Ref. [98].

What is more, it is reasonable to expect that stripe-induced diffuse features should exhibit certain anomalies in their temperature dependence at the superconducting transition temperature or at other temperatures associated with the onset of electronic instabilities, such as the electronic pseudogap. Superstructures related to oxygen vacancy ordering, on the other hand, are not influenced by electronic correlations in the bilayers and are rather expected to be characterized by a smooth temperature dependence determined by the evolution of oxygen diffusion kinetics with temperature. The persistence of the ortho-IV diffuse features in $\text{YBa}_2\text{Cu}_3\text{O}_{6.92}$ and $\text{Y}_{0.8}\text{Ca}_{0.2}\text{Ba}_2\text{Cu}_3\text{O}_{6.95}$ compounds up to temperatures as high as 500 K, as well as the absence of any kind of anomalies in their temperature dependences in the whole temperature range investigated (Figure 5.15), strongly favor the oxygen-order scenario for the origin of the superstructures against the stripe-involving theory.

There is one more experimental piece of evidence which supports our belief that the diffuse features in $\text{YBa}_2\text{Cu}_3\text{O}_{6+x}$ compounds, including the four-cell superstructure in optimally doped and overdoped samples, are due to oxygen ordering. This is the total absence of diffuse reflections in stoichiometric $\text{YBa}_2\text{Cu}_4\text{O}_8$ (Figure 5.18). This naturally underdoped compound does not sustain oxygen defects. All oxygen sites are occupied, and thus the system is ideal for testing the role of oxygen vacancies in $\text{YBa}_2\text{Cu}_3\text{O}_{6+x}$. If the diffuse features observed in $\text{YBa}_2\text{Cu}_3\text{O}_{6+x}$ are merely induced by the ordering of the oxygen vacancies, then these features should be absent in $\text{YBa}_2\text{Cu}_4\text{O}_8$, where no vacancies are present. If, on the contrary, the superstructures in $\text{YBa}_2\text{Cu}_3\text{O}_{6+x}$ originate from electronic stripe formation, then

they should be not only present, but also much easier to see in $\text{YBa}_2\text{Cu}_4\text{O}_8$. Indeed, the relatively low hole concentration in $\text{YBa}_2\text{Cu}_4\text{O}_8$ favors stripe formation. At the same time, the absence of superstructures related to oxygen vacancy ordering should make it easier to observe any stripe-induced or charge-density-wave-induced diffuse scattering which may be 'hidden' under the strong oxygen-order features in $\text{YBa}_2\text{Cu}_3\text{O}_{6+x}$. The fact that no such superstructures are observed in $\text{YBa}_2\text{Cu}_4\text{O}_8$, strongly indicates that the diffuse features in $\text{YBa}_2\text{Cu}_3\text{O}_{6+x}$ are due to vacancy ordering.

Our experimental observations thus clearly demonstrate that the diffuse features with four-cell periodicity observed in optimally doped and overdoped $\text{YBa}_2\text{Cu}_3\text{O}_{6+x}$ are not associated with electronic stripe correlations. This does not mean that the existence of such correlations is excluded. It just means that if such electronic instabilities, either of static or of dynamic nature, are present, they have certainly an intensity which is lower than the background of the above described measurements. The sensitivity of our technique thus sets an upper limit for the intensity of possibly existent stripe-induced diffuse scattering.

In all investigated systems – ortho-V, ortho-III, ortho-IV – a remarkable intensity asymmetry was found between the observed superstructure reflections. In particular, the reflection at wave-vector $Q+q$ was in all cases significantly stronger than the one at $Q-q$, with Q being a reciprocal lattice vector (position of main Bragg reflection) and q the wave-vector of the superstructure (0.4, 0.33, 0.25, respectively). The reason for this asymmetry is not quite clear, but is most probably associated to the atomic displacements caused by the oxygen vacancy superstructures [111]. A destructive interference between diffuse scattering due to disorder, on one hand, and displacive modulations caused by this disorder, on the other, could lead to such an asymmetry. A model based on this effect was suggested for $\text{YBa}_2\text{Cu}_3\text{O}_{6.92}$ in Ref. [103]. A similar effect was previously observed also in the diffraction patterns of quasi-one-dimensional charge density wave systems [112].

Our studies provided information concerning the isotope effects reported in neutron scattering and ellipsometry investigations in $\text{YBa}_2\text{Cu}_3\text{O}_{6+x}$ (Section 5.3). Based on the fact that the diffuse scattering patterns of optimally doped $\text{YBa}_2\text{Cu}_3\text{O}_{6.92}$ compounds containing different oxygen isotopes (^{16}O vs. ^{18}O) are identical (Figure 5.16), we draw the conclusion that isotope substitution does not affect the short-range oxygen order in this system. Hence any differences in the electronic properties between the two compounds do not originate from variations in the oxygen order or the associated atomic displacements. The driving force of the electronic isotope effects should rather be searched for in the interactions within the CuO_2 bilayers.

The results presented in this chapter are significant for the interpretation of phonon anomalies previously reported for $\text{YBa}_2\text{Cu}_3\text{O}_{6+x}$ [90, 91]. The substantial lattice deformations induced by the oxygen superstructures, which encompass the whole unit cell, are expected to influence charge and spin fluctuations con-

siderably. The results should be taken into account in the investigation of other high-temperature superconductors as well. Because of the layered crystal structure, almost all high-temperature superconductors contain oxygen acceptor vacancies or interstitials. These have been often assumed to be randomly incorporated into the crystal structure. Our studies clearly demonstrated that this is not the case in at least one copper oxide compound. Recent x-ray diffuse scattering studies on $\text{Bi}_2\text{Sr}_2\text{CaCu}_2\text{O}_{8+\delta}$ reported the existence of diffuse features in this system too, induced by two-dimensional short-range charge modulations (displacements) with correlation lengths of the order of a unit cell dimension [113, 114]. These results further indicate that charge inhomogeneities are a rather common feature of different families of cuprate superconductors.

Chapter 6

Summary

The strongly correlated electron systems in $\text{Ca}_{2-x}\text{Sr}_x\text{RuO}_4$, $\text{RuSr}_2\text{GdCu}_2\text{O}_8$ and $\text{YBa}_2\text{Cu}_3\text{O}_{6+x}$ transition metal oxides were investigated with resonant and high-energy x-ray scattering techniques. The main results and conclusions of the work are briefly summarized in the following.

Single crystals of Ca_2RuO_4 and $\text{Ca}_{1.9}\text{Sr}_{0.1}\text{RuO}_4$ were investigated with resonant x-ray diffraction at the Ru L_{II} and L_{III} absorption edges, i.e. at photon energies $E=2.968$ keV and $E=2.838$ keV, respectively. At the magnetically allowed $(1\ 0\ 0)$ and $(0\ 1\ 1)$ reciprocal space positions a new ordered phase was discovered above the magnetic phase transition at $T_N = 110$ K. The scattering from this phase has a strongly resonant character, with non-zero intensity only at energies very close to the absorption edges. It is observed exclusively in the $\sigma \rightarrow \pi'$ polarization channel, hence is characterized by a polarization which is parallel to the scattering plane. The temperature dependence of the scattering intensity from the new phase decreases smoothly with increasing temperature, without showing any anomalies, and vanishes at a phase transition at approximately 260 K. Based on the polarization and temperature dependences, as well as on complementary muon spin rotation (μSR) measurements, which indicate no ordered magnetic moment above the Néel temperature, we can draw the conclusion that the resonant scattering in the new phase originates from the ordering of the Ru $4d$ orbitals. The orbital ordering phase transition is also observed in the strontium-doped $\text{Ca}_{1.9}\text{Sr}_{0.1}\text{RuO}_4$ system, but at a lower temperature of approximately 130 K. The propagation vector of the orbital order remains unchanged in the doped compound, despite the change of the magnetic structure. Furthermore, an additional resonant signal was observed in both investigated $\text{Ca}_{2-x}\text{Sr}_x\text{RuO}_4$ systems at the $(1\ 1\ 0)$ position, which is forbidden both magnetically and by the space-group. The intensity of this signal decreases smoothly with increasing temperature with no anomalies up to the metal-insulator transition. Based on the temperature and polarization dependences of the scattering intensity at $(1\ 1\ 0)$, this can be attributed to the tilt order of the RuO_6 octahedra.

Micrometer-sized single crystals of $\text{RuSr}_2\text{GdCu}_2\text{O}_8$ were investigated with resonant x-ray diffraction at the Ru L_{II} absorption edge. Based on the azimuthal dependence of the scattering intensity at the $(\frac{1}{2} \frac{1}{2} \frac{1}{2})$ magnetic position, the exact direction of the magnetic moment in the material could be determined. The magnetic moment was found to be aligned not along the crystallographic c direction, as initially suggested by neutron scattering investigations, but instead along a direction which forms an angle of approximately 53 degrees with the c axis. In addition, the magnetic order parameter of the Ru spin-system was determined. The experimental data indicate a possible influence of the onset of superconductivity on the magnetic order parameter, but this is still to be confirmed.

Single crystals of underdoped, optimally doped and overdoped $\text{YBa}_2\text{Cu}_3\text{O}_{6+x}$, as well as stoichiometric $\text{YBa}_2\text{Cu}_4\text{O}_8$, were investigated with high-energy non-resonant x-ray diffraction at photon energies of 100 keV and 115 keV. A new superstructure with periodicity equal to four unit cells was discovered in optimally doped $\text{YBa}_2\text{Cu}_3\text{O}_{6.92}$ and overdoped $\text{Y}_{0.8}\text{Ca}_{0.2}\text{Ba}_2\text{Cu}_3\text{O}_{6.95}$. The superstructures are practically identical in the two compounds, which have almost the same oxygen content, but very different charge carrier concentrations. This indicates that the superstructures do not originate from electronic stripes in the CuO_2 planes, but rather from oxygen vacancy ordering in the Cu-O chains. This conclusion is supported by two more independent observations: the persistence of the superstructures up to temperatures well above room temperature; and the absence of diffuse scattering features in the stoichiometric $\text{YBa}_2\text{Cu}_4\text{O}_8$ compound, which contains no oxygen vacancies and should therefore make the observation of stripes easier. If such stripes do exist in $\text{YBa}_2\text{Cu}_3\text{O}_{6+x}$, then the intensity of the associated diffuse features must be at least one order of magnitude smaller than that of the aboved described signatures of oxygen order. The comparison of the diffuse scattering patterns of $\text{YBa}_2\text{Cu}_3\text{O}_{6.92}$ samples containing different oxygen isotopes (^{16}O vs. ^{18}O) revealed that these are identical. This means that variations in the oxygen order in the Cu-O chains cannot be responsible for isotope effects reported in previous work on this material.

Parts of this work were published in the following articles:

- J. Stempfer, I. Zegkinoglou, U. Rütt, M. v. Zimmermann, C. Bernhard, C.T. Lin, Th. Wolf, and B. Keimer, *Oxygen Superstructures Throughout the Phase Diagram of $(Y, Ca)\text{Ba}_2\text{Cu}_3\text{O}_{6+x}$* , Phys. Rev. Lett. **93**, 157007 (2004)
- I. Zegkinoglou, J. Stempfer, C.S. Nelson, J.P. Hill, J. Chakhalian, C. Bernhard, J.C. Lang, G. Srajer, H. Fukazawa, S. Nakatsuji, Y. Maeno, and B. Keimer, *Orbital Ordering Transition in Ca_2RuO_4 Observed with Resonant X-Ray Diffraction*, Phys. Rev. Lett. **95**, 136401 (2005).

Appendix A

Calculation of the absorption coefficient μ from fluorescence measurements

In the vicinity of an absorption edge of a material, the absorption coefficient μ can be expressed as the sum of two terms: a strongly energy-dependent edge contribution $\mu^{edge}(E)$, and a more weakly energy-dependent underlying contribution $\mu^{und}(E) \sim E^{-3}$, which is independent of the edge:

$$\mu(E) = \mu^{edge}(E) + \mu^{und}(E) \quad (\text{A.1})$$

Taking into consideration the scattering geometry of the experiment, the following expression can be extracted for μ , as calculated in Ref. [115]:

$$\mu(E) = \mu_1 f(E) + \frac{[I^F(E)(\mu_1 f(E) + \mu_F s) - I_1^F f(E)(\mu_1 + \mu_F s)] \cdot [\mu_2 - \mu_1 f_2]}{I_2^F(\mu_2 + \mu_F s) - I_1^F(\mu_1 + \mu_F s) f_2 - I^F(E)(\mu_2 - \mu_1 f_2)} \quad (\text{A.2})$$

Here, $\mu(E)$ is the absorption coefficient at energy E ; μ_F , μ_1 , μ_2 are the values of the absorption coefficient at energies E_F , E_1 , E_2 , respectively, where E_F is the energy of an x-ray emission line, E_1 lies *below* the relevant absorption edge ($\mu^{edge}(E_1) = 0$), and E_2 *above* it; $I^F(E)$ is the fluorescence intensity at energy E , and I_1^F , I_2^F its values at energy positions E_1 , E_2 , respectively; $f(E) = E_1^3/E^3$, $f_2 = f(E_2) = E_1^3/E_2^3$; and s is a geometrical factor given by $s = \frac{\sin\alpha}{\sin\beta}$, with α being the angle between the wave-vector \mathbf{k} of the incoming beam and the absorbing surface, and β the angle between the wave-vector \mathbf{k}' of the emitted (fluorescence) beam and the scattering surface.

The values μ_F , μ_1 , μ_2 can be obtained, for example, from the web site of the Lawrence Berkeley National Laboratory:

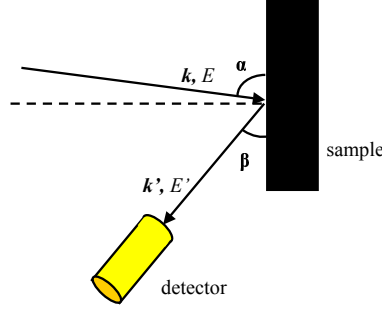


Figure A.1: Schematic view of the geometry for measuring the fluorescence yield from a sample. Incoming radiation with wave-vector \mathbf{k} and energy E tuned at the Ru L_{II} edge is absorbed by the sample. Fluorescence radiation with energy E' corresponding to the Ru $L_{\alpha 2}$ emission line is then emitted in all possible directions (4π solid angle). The angle between \mathbf{k} and the absorbing sample surface is α , that between the scattering vector \mathbf{k}' of the detected beam and the surface is β .

http://www-cxro.lbl.gov/optical_constants/

The density of the material is needed for these calculations. For Ca_2RuO_4 , this has the value: $\rho = 4.582 \text{ g/cm}^3$ (4 chemical formulae per unit cell).

The $L_{\alpha 2}$ emission line of Ru, which is excited when the incoming energy is tuned at the Ru L_{II} absorption edge, has an energy of $E_F = 2554 \text{ eV}$. The x-ray attenuation length at this energy is: $l_F = 4.6280 \mu\text{m}$, and the absorption coefficient: $\mu_F = 1/l_F = 0.2161 \mu\text{m}^{-1}$.

For incoming photon energy tuned at the Ru L_{II} edge ($E(L_{II})=2968 \text{ eV}$), we choose $E_1 = 2940 \text{ eV}$ and $E_2 = 3000 \text{ eV}$. The corresponding μ values are: $\mu_1 = 0.3465 \mu\text{m}^{-1}$ and $\mu_2 = 0.4272 \mu\text{m}^{-1}$.

The geometry factor s was of course different in every experiment. As an example, for the measurements on Ca_2RuO_4 at reciprocal space position (1 0 0) presented in Section 3.6, the incoming beam was perpendicular to the sample's surface, i.e. $\alpha = 90^\circ$, so the value of s was approximately: $s = \frac{\sin\alpha}{\sin\beta} = \frac{\sin 90^\circ}{\sin 66^\circ} = 1.0946$.

By substituting the above values in Equation A.2, the variation with energy of the absorption coefficient μ around the L_{II} absorption edge, shown e.g. for Ca_2RuO_4 in Figure 3.21, is determined.

Appendix B

Trigonometric calculations for determining the magnetic moment direction in $\text{RuSr}_2\text{GdCu}_2\text{O}_8$

For the calculation of the angle between the Ru magnetic moment $\boldsymbol{\mu}$ and the \mathbf{c} crystallographic direction in $\text{RuSr}_2\text{GdCu}_2\text{O}_8$, the vector representation of Figure 4.7, shown again in Figure B.1, was used. As seen in Section 4.4, from the azimuthal dependence of the $(\frac{1}{2} \frac{1}{2} \frac{1}{2})$ integrated intensity we obtain: $\alpha = 49^\circ$ and $B\hat{A}E = 53^\circ$. In addition, the following expressions hold:

$$C\hat{A}B = 90^\circ - \alpha = 90^\circ - 49^\circ = 41^\circ \quad (\text{B.1})$$

$$\begin{aligned} \cos(D\hat{A}F) &= \cos[(111), \hat{(001)}] = \cos \frac{\frac{1}{c^2}}{\sqrt{\frac{1}{a^2} + \frac{1}{b^2} + \frac{1}{c^2}} \cdot \sqrt{\frac{1}{c^2}}} = 0.2284 \\ \Rightarrow D\hat{A}F &= \cos^{-1} 0.2284 = 77^\circ \Rightarrow D\hat{A}E = 90^\circ - 77^\circ = 13^\circ \end{aligned} \quad (\text{B.2})$$

For simplicity, we consider the vectors $\boldsymbol{\mu}$ and \mathbf{c} to be unit vectors, thus: $|AC| = |AD| = 1$. Hence:

$$|AB| = |AC| \cos 41^\circ = 0.755, \text{ and } |AE| = |AD| \cos 13^\circ = 0.974 \quad (\text{B.3})$$

In triangle ABE :

$$B\hat{A}E = 53^\circ$$

$$|AO| = |AB| \cos 53^\circ = 0.755 \cos 53^\circ = 0.454$$

and:

Finally, in triangle ACD :

$$\sin(K\hat{A}D) = \frac{|KD|}{|AD|} = \frac{|CD|}{2|AD|} = 0.4525 \Rightarrow K\hat{A}D = 26.9^\circ$$

Thus:

$$C\hat{A}D = 2 \cdot K\hat{A}D = 53.8^\circ \tag{B.6}$$

The angle between $\boldsymbol{\mu}$ and \boldsymbol{c} is therefore equal to 53.8° .

Appendix C

Maple code for calculating the azimuthal dependence due to tilt order in Ca_2RuO_4

The following code was used for the calculation of the azimuthal dependence of the resonant intensity due to the tilt order of the RuO_6 octahedra in Ca_2RuO_4 . For the calculations the computer algebra programme MapleTM was used. The code was initially developed by J.P. Hill at BNL for the investigation of tilt order in YTiO_3 and appropriately modified in this work for Ca_2RuO_4 .

```
> restart;  
> with(linalg); with(plots);
```

Estimate the constants of the form factor ellipse:

```
> fa:=1;  
> fb:=1;  
> fc:=0.97;
```

Estimate the occupancies of the d_{xy} , d_{zx}/d_{yz} orbitals in the total wave-function: $\Psi = c_1|zx\rangle + c_2|xy\rangle$. We assume, in a first approximation, a fully occupied d_{xy} and half-occupied d_{zx}/d_{yz} orbitals:

```
> c1:=1/sqrt(5);  
> c2:=2/sqrt(5);
```

Rotate the form factor f1 for site 1 of the basis into the coordinate frame of the crystal. The angle α (alpha) describes the rotation about axis z , β (beta) the rotation about axis y , and γ (gamma) the rotation about axis x . Rz, Ry, Rx are the corresponding rotation matrices:

```

> gam:=arctan(c2/c1);
> beta:=45*Pi/180;
> alpha:=-45*Pi/180;
> f1:=Matrix([[fa,0,0],[0,fb,0],[0,0,fc]]);
> Rz:=Matrix([[cos(alpha),-sin(alpha),0],[sin(alpha),cos(alpha),0],[0,0,1]]);
> Rx:=Matrix([[1,0,0],[0,cos(gam),-sin(gam)],[0,sin(gam),cos(gam)]]);
> Ry:=Matrix([[cos(beta),0,sin(beta)],[0,1,0],[-sin(beta),0,cos(beta)]]);
> RIy:=Matrix(inverse(Ry));
> RIx:=Matrix(inverse(Rx));
> RIz:=Matrix(inverse(Rz));
> F:=Matrix(multiply(Rz,Rx,Ry,f1,RIy,RIx,RIz));

```

Consider the tilting angles of the octahedra:

```

> alpha:=11.8*Pi/180;
> beta:=12.7*Pi/180;
> gam:=0;

```

The corresponding rotation matrices are:

```

> Rz:=Matrix([[cos(alpha),-sin(alpha),0],[sin(alpha),cos(alpha),0],[0,0,1]]);
> Rx:=Matrix([[1,0,0],[0,cos(gam),-sin(gam)],[0,sin(gam),cos(gam)]]);
> Ry:=Matrix([[cos(beta),0,sin(beta)],[0,1,0],[-sin(beta),0,cos(beta)]]);

```

The form factor for site 1 becomes after the rotations:

```

> F1:=Matrix(multiply(Rz,Rx,Ry,F,Matrix(inverse(Ry)),Matrix(inverse(Rx)),
Matrix(inverse(Rz))));

```

Generate from F1 the form factors for the rest of the sites of the basis by applying the symmetry operations of the space group:

```

> symm1:=Matrix([[1,0,0],[0,1,0],[0,0,-1]]);symm2:=Matrix([[1,0,0],
[0,-1,0],[0,0,1]]);symm3:=Matrix([[-1,0,0],[0,1,0],[0,0,1]]);
> F2:=Matrix(multiply(symm1,F1,symm1));
> F3:=Matrix(multiply(symm2,F1,symm2));
> F4:=Matrix(multiply(symm3,F1,symm3));

```

Calculate the structure factors for positions (100), (110), (011). The angle ω (omega) is in all cases the scattering (Bragg) angle, e_i the polarization vector of the incoming beam, and sp , ss the polarization vectors of the scattered beam in $\sigma \rightarrow \pi'$, $\sigma \rightarrow \sigma'$ polarization geometries, respectively.

```

> F100:=F1-F4-F2+F3;
> F110:=F1+F4-F2-F3;
> F011:=F1-F2+F3-F4;

```

At (100):

```
> omega:=22.85*Pi/180;
> ei:=Vector[row]([0,1,0]);
> sp:=Vector[row]([-sin(omega),0,cos(omega)]);
> ss:=Vector[row]([0,1,0]);
```

Rotate the form factor into the lab frame:

```
> alpha:=0*Pi/180;
> beta:=90*Pi/180;
> gam:=-90*Pi/180;
> Rz:=Matrix([[cos(alpha),-sin(alpha),0],[sin(alpha),cos(alpha),0],
[0,0,1]]);
> Ry:=Matrix([[cos(beta),0,sin(beta)],[0,1,0],[-sin(beta),0,cos(beta)]]);
> Flab:=Matrix(multiply(Ry,Rz,F100,Matrix(inverse(Rz)),
Matrix(inverse(Ry))));
```

Perform the azimuthal rotations and calculate the scalar products of the resulting structure factor with the polarization vectors:

```
> Razi:=Matrix([[cos(psi),-sin(psi),0],[sin(psi),cos(psi),0],[0,0,1]]);
> Razii:=Matrix(inverse(Razi));
> Fazi:=Matrix(multiply(Razi,Flab,Razii));
> SF100_sp:=innerprod(sp,Fazi,ei)^2;
> SF100_ss:=innerprod(ss,Fazi,ei)^2;
```

The scattering intensities at (100) in the $\sigma \rightarrow \pi'$ and $\sigma \rightarrow \sigma'$ polarization channels:

```
> Int100_sp:=unapply(SF100_sp,psi);
> Int100_ss:=unapply(SF100_ss,psi);
```

Plot making and data storage commands:

```
> plot({Int100_sp(psi*3.1415926/180,18*Pi/180),Int100_ss(psi*3.1415926/180,
18*Pi/180)},psi=-180..360);
> pstr:=plot({Int100_sp(psi*3.1415926/180,18*Pi/180)},psi=-360..360);
> curves:=op(1,pstr);
> points:=op(1,curves);
> fd:=fopen("100_sipi.txt",WRITE);
> map(u->fprintf(fd,"%20.16f,%20.16f\n",op(1,u),op(2,u)),points);
> fclose(fd);
```

Repeat the same procedure for the (110) position:

```

> omega:=32.47*Pi/180;
> ei:=Vector[row]([0,1,0]);
> sp:=Vector[row]([-sin(omega),0,cos(omega)]);
> ss:=Vector[row]([0,1,0]);
> alpha:=0*Pi/180;
> beta:=134.6*Pi/180;
> gam:=90*Pi/180;
> Rz:=Matrix([[cos(alpha),-sin(alpha),0],[sin(alpha),cos(alpha),0],
[0,0,1]]);
> Ry:=Matrix([[cos(beta),0,sin(beta)],[0,1,0],[-sin(beta),0,cos(beta)]]);
> Rx:=Matrix([[1,0,0],[0,cos(gam),-sin(gam)],[0,sin(gam),cos(gam)]]);
> Flab:=Matrix(multiply(Ry,Rx,Rz,F110,Matrix(inverse(Rz)),
Matrix(inverse(Rx)),
Matrix(inverse(Ry))));
> Razi:=Matrix([[cos(psi),-sin(psi),0],[sin(psi),cos(psi),0],[0,0,1]]);
> Razii:=Matrix(inverse(Razi));
> Fazi:=Matrix(multiply(Razi,Flab,Razii));
> SF110_sp:=innerprod(sp,Fazi,ei)^2;
> SF110_ss:=innerprod(ss,Fazi,ei)^2;
> Int110_sp:=unapply(SF110_sp,psi);
> Int110_ss:=unapply(SF110_ss,psi);
> plot({Int110_sp(psi*3.1415926/180,18*Pi/180),Int110_ss(psi*3.1415926/180,
18*Pi/180)},psi=-360..360);
> plot({Int110_sp(psi*3.1415926/180,18*Pi/180)},psi=-360..360);
> pstr:=plot({Int110_sp(psi*3.1415926/180,18*Pi/180)},psi=-360..360);
> curves:=op(1,pstr);
> points:=op(1,curves);
> fd:=fopen("110_sipi.txt",WRITE);
> map(u->fprintf(fd,"%20.16f,%20.16f\n",op(1,u),op(2,u)),points);
> fclose(fd);
> pstr:=plot({Int110_ss(psi*3.1415926/180,18*Pi/180)},psi=-360..360);
> curves:=op(1,pstr);
> points:=op(1,curves);
> fd:=fopen("110_sisi.txt",WRITE);
> map(u->fprintf(fd,"%20.16f,%20.16f\n",op(1,u),op(2,u)),points);
> fclose(fd);

```

Repeat the same procedure for the (011) position:

```

> omega:=24.73*Pi/180;
> ei:=Vector[row]([0,1,0]);
> sp:=Vector[row]([-sin(omega),0,cos(omega)]);

```

```

> ss:=Vector[row]([0,1,0]);
> alpha:=90*Pi/180;
> beta:=65.3*Pi/180;
> gam:=0*Pi/180;
> Rz:=Matrix([[cos(alpha),-sin(alpha),0],[sin(alpha),cos(alpha),0],
[0,0,1]]);
> Ry:=Matrix([[cos(beta),0,sin(beta)],[0,1,0],[-sin(beta),0,cos(beta)]]);
> Rx:=Matrix([[1,0,0],[0,cos(gam),-sin(gam)],[0,sin(gam),cos(gam)]]);
> Flab:=Matrix(multiply(Ry,Rx,Rz,F011,Matrix(inverse(Rz)),
Matrix(inverse(Rx)),
Matrix(inverse(Ry))));
> Razi:=Matrix([[cos(psi),-sin(psi),0],[sin(psi),cos(psi),0],[0,0,1]]);
> Razii:=Matrix(inverse(Razi));
> Fazi:=Matrix(multiply(Razi,Flab,Razii));
> SF011_sp:=innerprod(sp,Fazi,ei)^2;
> SF011_ss:=innerprod(ss,Fazi,ei)^2;
> Int011_sp:=unapply(SF011_sp,psi);
> Int011_ss:=unapply(SF011_ss,psi);
> plot({Int011_sp(psi*3.1415926/180,18*Pi/180),Int011_ss(psi*3.1415926/180,
18*Pi/180)},psi=-360..360);
> plot({Int011_sp(psi*3.1415926/180,18*Pi/180)},psi=-360..360);
> pstr:=plot({Int011_sp(psi*3.1415926/180,18*Pi/180)},psi=-360..360);
> curves:=op(1,pstr);
> points:=op(1,curves);
> fd:=fopen("011_sipi.txt",WRITE);
> map(u->fprintf(fd,"%20.16f,%20.16f\n",op(1,u),op(2,u)),points);
> fclose(fd);
> pstr:=plot({Int011_ss(psi*3.1415926/180,18*Pi/180)},psi=-360..360);
> curves:=op(1,pstr);
> points:=op(1,curves);
> fd:=fopen("011_sisi.txt",WRITE);
> map(u->fprintf(fd,"%20.16f,%20.16f\n",op(1,u),op(2,u)),points);
> fclose(fd);

```

It is noted that both the form factor ellipse constants and the orbital occupancies, estimated in the beginning of the code, influence only the absolute values of the simulated scattering intensities and not the periodicities or the $\sigma \rightarrow \pi'$ to $\sigma \rightarrow \sigma'$ intensity ratios in the azimuthal dependences.

Bibliography

- [1] S. Maekawa, T. Tohyama, S.E. Barnes, S. Ishihara, W. Koshibae, and G. Khaliullin, *Physics of Transition Metal Oxides* (Springer-Verlag, 2004).
- [2] P.A. Cox, *Transition Metal Oxides. An Introduction to their Electronic Structure and Properties* (Oxford University Press, New York, 1992).
- [3] Y. Tokura and N. Nagaosa, *Science* **288**, 462 (2000).
- [4] S. Sugano, Y. Tanabe, and H. Kamimura, *Multiplets of Transition Metal Ions in Crystals* (Academic Press, New York and London, 1970).
- [5] H. Jahn and E. Teller, *Phys. Rev.* **49**, 874 (1936).
- [6] J. Hubbard, *Proc. Roy. Soc.* **A276**, 238 (1963).
- [7] P. Fazekas, *Lecture Notes on Electron Correlation and Magnetism* (World Scientific Publishing Co. Pte. Ltd., 1999).
- [8] P.W. Anderson, *Phys. Rev.* **115**, 2 (1959).
- [9] J.B. Goodenough, *Magnetism and the Chemical Bond* (Robert E. Krieger Publishing Company, Huntington, New York, 1976).
- [10] C.P. Poole, H.A. Farach, and R.J. Creswick, *Superconductivity* (Academic Press, 1995).
- [11] M. Tinkham, *Introduction to Superconductivity* (McGraw-Hill, Inc., 1996).
- [12] J.G. Bednorz and K.A. Müller, *Z. Phys. B* **64**, 189 (1986).
- [13] G.F. Sun, K.W. Wong, B.R. Xu, Y. Xin, and D.F. Lu, *Phys. Lett. A* **192**, 122 (1994).
- [14] J. Bardeen, L.N. Cooper, and J.R. Schrieffer, *Phys. Rev.* **108**, 1175 (1957).
- [15] J. Orenstein and A.J. Millis, *Science* **288**, 468 (2000).

-
- [16] D.A. Bonn, *Nature Physics* **2**, 159 (2006).
- [17] P.W. Anderson, *Science* **235**, 1196 (1987).
- [18] J.M. Tranquada, B.J. Sternlieb, J.D. Axe, Y. Nakamura, and S. Uchida, *Nature* **375**, 561 (1995).
- [19] D.J. Scalapino and S.R. White, *Phys. Rev. B* **58**, 8222 (1998).
- [20] D.J. Scalapino, *Science* **284**, 1282 (1999).
- [21] V.J. Emery, S.A. Kivelson, and J.M. Tranquada, *Proc. Natl. Acad. Sci. USA* **96**, 8814 (1999).
- [22] S.A. Kivelson, E. Fradkin, and V.J. Emery, *Nature* **393**, 550 (1998).
- [23] S.-W. Cheong, G. Aeppli, T.E. Mason, H. Mook, S.M. Hayden, P.C. Canfield, Z. Fisk, K.N. Clausen, and J.L. Martinez, *Phys. Rev. Lett.* **67**, 1791 (1991).
- [24] T.E. Mason, G. Aeppli, and H.A. Mook, *Phys. Rev. Lett.* **68**, 1414 (1992).
- [25] S.A. Kivelson, I.P. Bindloss, E. Fradkin, V. Oganessian, J.M. Tranquada, A. Kapitulnik, and C. Howald, *Rev. Mod. Phys.* **75**, 1201 (2003).
- [26] T. Senthil and M.P.A. Fisher, *Phys. Rev. B* **62**, 7850 (2000).
- [27] V.J. Emery and S.A. Kivelson, *Nature* **374**, 434 (1995).
- [28] P.J. Duke, *Synchrotron Radiation. Production and Properties* (Oxford Science Publications, 2000).
- [29] B.E. Warren, *X-ray Diffraction* (Addison-Wesley, 1969).
- [30] J. Als-Nielsen, *Elements of Modern X-ray Physics* (John Wiley & Sons Ltd, 2001).
- [31] S.W. Lovesey and S.P. Collins, *X-Ray Scattering and Absorption by Magnetic Materials* (Oxford University Press Inc., New York, 1996).
- [32] N.W. Ashcroft and N.D. Mermin, *Solid State Physics* (Saunders College Publishing, 1976).
- [33] F. de Bergevin and M. Brunel, *Acta Cryst.* **A37**, 314 (1981).
- [34] K. Namikawa, M. Ando, T. Nakajima, and H. Kawata, *J. Phys. Soc. Jpn* **54**, 4099 (1985).

- [35] D. Gibbs, D.R. Harshman, E.D. Isaacs, D.B. McWhan, D. Mills, and C. Vettier, *Phys. Rev. Lett.* **61**, 1241 (1988).
- [36] E.D. Isaacs, D.B. McWhan, C. Peters, G.E. Ice, D.P. Siddons, J.B. Hastings, C. Vettier, and O. Vogt, *Phys. Rev. Lett.* **62**, 1671 (1989).
- [37] Y. Murakami, J.P. Hill, D. Gibbs, M. Blume, I. Koyama, M. Tanaka, H. Kawata, T. Arima, Y. Tokura, K. Hirota, and Y. Endoh, *Phys. Rev. Lett.* **81**, 582 (1998).
- [38] H. Nakao, Y. Wakabayashi, T. Kiyama, Y. Murakami, M. v. Zimmermann, J.P. Hill, D. Gibbs, S. Ishihara, Y. Taguchi, and Y. Tokura, *Phys. Rev. B* **66**, 184419 (2002).
- [39] S. Grenier, J.P. Hill, D. Gibbs, K.J. Thomas, M. v. Zimmermann, C.S. Nelson, V. Kiryukhin, Y. Tokura, Y. Tomioka, D. Casa, T. Gog, and C. Venkataraman, *Phys. Rev. B* **69**, 134419 (2004).
- [40] A. Stunault, F. de Bergevin, D. Wermeille, C. Vettier, Th. Brückel, N. Bernhoeft, G. J. McIntyre, and J. Y. Henry, *Phys. Rev. B* **60**, 10170 (1999).
- [41] S.B. Wilkins, P.D. Hatton, M.D. Roper, D. Prabhakaran, and A.T. Boothroyd, *Phys. Rev. Lett.* **90**, 187201 (2003).
- [42] S.S. Dhesi, A. Mirone, C. De Nadaï, P. Ohresser, P. Bencok, N.B. Brookes, P. Reutler, A. Revkolevski, A. Tagliaferri, O. Toulemonde, and G. van der Laan, *Phys. Rev. Lett.* **92**, 056403 (2004).
- [43] K.J. Thomas, J.P. Hill, Y.-J. Kim, P. Abbamonte, L. Venema, A. Rusydi, Y. Tomioka, Y. Tokura, D.F. McMorrow, and M. van Veenendaal, *Phys. Rev. Lett.* **92**, 237204 (2004).
- [44] D.F. McMorrow, S.E. Nagler, K.A. McEwen, and S.D. Brown, *J. Phys.: Condens. Matter* **15**, L59 (2003).
- [45] I. Zegkinoglou, J. Strempler, C.S. Nelson, J.P. Hill, J. Chakhalian, C. Bernhard, J.C. Lang, G. Srajer, H. Fukazawa, S. Nakatsuji, Y. Maeno, and B. Keimer, *Phys. Rev. Lett.* **95**, 136401 (2005).
- [46] J.P. Hannon, G.T. Trammel, M. Blume, and D. Gibbs, *Phys. Rev. Lett.* **61**, 1245 (1988).
- [47] J.P. Hill and D.F. McMorrow, *Acta Cryst.* **A52**, 236 (1996).
- [48] W.R. Busing and H.A. Levy, *Acta Cryst.* **22**, 457 (1967).

- [49] Y. Maeno, H. Hashimoto, K. Yoshida, S. Nishizaki, T. Fujita, J.G. Bednorz, and F. Lichtenberg, *Nature (London)* **372**, 532 (1994).
- [50] K. Ishida, H. Mukuda, Y. Kitaoka, K. Asayama, Z.Q. Mao, Y. Mori, and Y. Maeno, *Nature (London)* **396**, 658 (1998).
- [51] M. Braden, G. André, S. Nakatsuji, and Y. Maeno, *Phys. Rev. B* **58**, 847 (1998).
- [52] V.I. Anisimov, I.A. Nekrasov, D.E. Kondakov, T.M. Rice, and M. Sigrist, *Eur. Phys. J. B* **25**, 191 (2002).
- [53] T. Hotta and E. Dagotto, *Phys. Rev. Lett.* **88**, 017201 (2002).
- [54] J.S. Lee, Y.S. Lee, T.W. Noh, S.-J. Oh, Jaejun Yu, S. Nakatsuji, H. Fukazawa, and Y. Maeno, *Phys. Rev. Lett.* **89**, 257402 (2002).
- [55] J.H. Jung, Z. Fang, J.P. He, Y. Kaneko, Y. Okimoto, and Y. Tokura, *Phys. Rev. Lett.* **91**, 056403 (2003).
- [56] O. Friedt, M. Braden, G. André, P. Adelman, S. Nakatsuji, and Y. Maeno, *Phys. Rev. B* **63**, 174432 (2001).
- [57] V.M. Goldschmidt, *Naturwissenschaften* **14**, 477 (1926).
- [58] J.B. Goodenough, *Phys. Rev.* **100**, 555 (1955).
- [59] Z. Fang, N. Nagaosa, and K. Terakura, *Phys. Rev. B* **69**, 045116 (2004).
- [60] T. Mizokawa, L.H. Tjeng, G.A. Sawatzky, G. Ghiringhelli, O. Tjernberg, N.B. Brookes, H. Fukazawa, S. Nakatsuji, and Y. Maeno, *Phys. Rev. Lett.* **87**, 077202 (2001).
- [61] M. Kubota, Y. Murakami, M. Mizumaki, H. Oshumi, N. Ikeda, S. Nakatsuji, H. Fukazawa, and Y. Maeno, *Phys. Rev. Lett.* **95**, 026401 (2005).
- [62] H. Fukazawa, S. Nakatsuji, and Y. Maeno, *Physica B* **281-282**, 613 (2000).
- [63] H. Fukazawa and Y. Maeno, *J. Phys. Soc. Jpn.* **70**, 460 (2001).
- [64] S. Nakatsuji, S. Ikeda, and Y. Maeno, *J. Phys. Soc. Jpn.* **66**, 1868 (1997).
- [65] G. Cao, S. McCall, M. Shepard, J.E. Crow, and R.P. Guertin, *Phys. Rev. B* **56**, R2916 (1997).
- [66] C.S. Alexander, G. Cao, V. Dobrosavljevic, S. McCall, J.E. Crow, E. Lochner, and R.P. Guertin, *Phys. Rev. B* **60**, R8422 (1999).

- [67] Th. Brückel, D. Hupfeld, J. Strempler, W. Caliebe, K. Mattenberger, A. Stunault, N. Bernhoeft, and G.J. McIntyre, *Eur. Phys. J. B* **19**, 475 (2001).
- [68] N. Bernhoeft, A. Hiess, S. Langridge, A. Stunault, D. Wermeille, C. Vettier, G. H. Lander, M. Huth, M. Jourdan, and H. Adrian, *Phys. Rev. Lett.* **81**, 3419 (1998).
- [69] N. Bernhoeft, *Acta Cryst. A* **55**, 274 (1999).
- [70] M. v. Zimmermann, C.S. Nelson, Y.-J. Kim, J.P. Hill, D. Gibbs, H. Nakao, Y. Wakabayashi, Y. Murakami, Y. Tokura, Y. Tomioka, T. Arima, C.-C. Kao, D. Casa, C. Venkatamaran, and Th. Gog, *Phys. Rev. B* **64**, 064411 (2001).
- [71] P. Steffens, O. Friedt, P. Alireza, W.G. Marshall, W. Schmidt, F. Nakamura, S. Nakatsuji, Y. Maeno, R. Lengsdorf, M.M. Abd-Elmeguid, and M. Braden, *Phys. Rev. B* **72**, 094104 (2005).
- [72] L. Bauernfeind, W. Widder, and H.F. Braun, *Physica C* **254**, 151 (1995).
- [73] J.W. Lynn, B. Keimer, C. Ulrich, C. Bernhard, and J.L. Tallon, *Phys. Rev. B* **61**, R14964 (2000).
- [74] C. Bernhard, J.L. Tallon, Ch. Niedermayer, Th. Blasius, A. Golnik, E. Brücher, R.K. Kremer, D.R. Noakes, C.E. Stronach, and E.J. Ansaldo, *Phys. Rev. B* **59**, 14099 (1999).
- [75] J.L. Tallon, J.W. Loram, G.V.M. Williams, and C. Bernhard, *Phys. Rev. B* **61**, R6471 (2000).
- [76] E. Abel, *Raman Scattering in Superconducting $RuSr_2GdCu_2O_8$ Single Crystal and Thin Films*, Master's thesis, Max-Planck-Institute for Solid State Research / University of Stuttgart, 2001.
- [77] O. Chmaissem, J.D. Jorgensen, H. Shaked, P. Dollar, and J.L. Tallon, *Phys. Rev. B* **61**, 6401 (2000).
- [78] A.C. McLaughlin, W. Zhou, J.P. Attfield, A.N. Fitch, and J.L. Tallon, *Phys. Rev. B* **60**, 7512 (1999).
- [79] R.S. Liu, L.-Y. Jang, H.-H. Hung, and J.L. Tallon, *Phys. Rev. B* **63**, 212507 (2001).
- [80] G.V.M. Williams and S. Krämer, *Phys. Rev. B* **62**, 4132 (2000).
- [81] A. Butera, A. Fainstein, E. Winkler, and J. Tallon, *Phys. Rev. B* **63**, 054442 (2001).

- [82] Z.H. Han, J.I. Budnick, W.A. Hines, P.W. Klamut, M. Maxwell, and B. Dabrowski, *J. Mag. Mag. Mat.* **299**, 338 (2006).
- [83] T. Nachtrab, *c-Achsen-Transporteigenschaften des intrinsischen Supraleiter-Ferromagnet-Hybrids $RuSr_2GdCu_2O_8$* , Ph.D. thesis, Eberhard-Karls-Universität zu Tübingen, 2004.
- [84] T. Nachtrab, C. Bernhard, C.T. Lin, D. Koelle, and R. Kleiner, *C.R.Physique* **7**, 68 (2006).
- [85] C.T. Lin, B. Liang, C. Ulrich, and C. Bernhard, *Physica C* **364-365**, 373 (2001).
- [86] G.E. Bacon, *Neutron Diffraction* (Clarendon, Oxford, 1975).
- [87] P.J. Brown, in *International Tables for Crystallography, Vol. C* (Ed. 2004).
- [88] V.L. Ginzburg, *Sov. Phys. JETP* **4**, 153 (1957).
- [89] M.K. Wu, J.R. Ashburn, C.J. Torng, P.H. Hor, R.L. Meng, L. Gao, Z.J. Huang, Y.Q. Wang, and C.W. Chu, *Phys. Rev. Lett.* **58**, 908 (1987).
- [90] H.A. Mook, P. Dai, S.M. Hayden, G. Aeppli, T.G. Perring, and F. Doğan, *Nature* **395**, 580 (1998).
- [91] H.A. Mook and F. Doğan, *Nature* **401**, 145 (1999).
- [92] M. v. Zimmermann, A. Vigliante, T. Niemöller, N. Ichikawa, T. Frello, J. Madsen, P. Wochner, S. Uchida, N.H. Andersen, J.M. Tranquada, D. Gibbs, and J.R. Schneider, *Europhys. Lett.* **41**, 629 (1998).
- [93] V. Hinkov, S. Pailhès, P. Bourges, Y. Sidis, A. Ivanov, D.P. Chen, C. Bernhard, and B. Keimer, *Nature* **430**, 650 (2004).
- [94] Z. Islam, S.K. Sinha, D. Haskel, J.C. Lang, G. Srajer, B.W. Veal, D.R. Haffner, and H.A. Mook, *Phys. Rev. B* **66**, 092501 (2002).
- [95] J.D. Jorgensen, B.W. Veal, A.P. Paulikas, L.J. Nowicki, G.W. Crabtree, H. Claus, and W.K. Kwok, *Phys. Rev. B* **41**, 1863 (1990).
- [96] H. Shaked, J.D. Jorgensen, D.G. Hinks, R.L. Hitterman, and B. Dabrowski, *Physica C* **205**, 225 (1993).
- [97] B. Dabrowski, K. Rogacki, Ch. Zheng, and D.G. Hinks, *Physica C* **291**, 287 (1997).

- [98] N.H. Andersen, M. v. Zimmermann, T. Frello, M. Käll, D. Mønster, P.-A. Lindgård, J. Madsen, T. Niemöller, H.F. Poulsen, O. Schmidt, J.R. Schneider, Th. Wolf, P. Dosanjh, R. Liang, and W.N. Hardy, *Physica C* **317**, 259 (1999).
- [99] D. de Fontaine, G. Ceder, and M. Asta, *Nature* **343**, 544 (1990).
- [100] V. Plakhty, B. Kviatkovsky, A. Stratilatov, Yu. Chernenkov, P. Burlet, J.Y. Henry, C. Marin, E. Ressouche, J. Schweizer, F. Yakou, E. Elkaim, and J.P. Lauriat, *Physica C* **235-240**, 867 (1994).
- [101] P. Schleger, H. Casalta, R. Hadfield, H.F. Poulsen, M. v. Zimmermann, N.H. Andersen, J.R. Schneider, R. Liang, P. Dosanjh, and W.N. Hardy, *Physica C* **241**, 103 (1995).
- [102] J. Stremper, I. Zegkinoglou, U. Rütt, M. v. Zimmermann, C. Bernhard, C.T. Lin, Th. Wolf, and B. Keimer, *Phys. Rev. Lett.* **93**, 157007 (2004).
- [103] Z. Islam, X. Liu, S.K. Sinha, J.C. Lang, S.C. Moss, D. Haskel, G. Srajer, P. Wochner, D.R. Lee, D.R. Haeffner, and U. Welp, *Phys. Rev. Lett.* **93**, 157008 (2004).
- [104] J. Chrosch and E.K.H Salje, *Physica C* **225**, 111 (1994).
- [105] V.I. Voronkova and Th. Wolf, *Physica C* **218**, 175 (1993).
- [106] P. Dai, H.A. Mook, and F. Doğan, *Phys. Rev. Lett.* **80**, 1738 (1998).
- [107] D. Rubio Temprano, J. Mesot, S. Janssen, K. Conder, A. Furrer, H. Mutka, and K.A. Müller, *Phys. Rev. Lett.* **84**, 1990 (2000).
- [108] C. Bernhard, T. Holden, A.V. Boris, N.N. Kovaleva, A.V. Pimenov, J. Humlicek, C. Ulrich, C.T. Lin, and J.L. Tallon, *Phys. Rev. B* **69**, 052502 (2004).
- [109] C.T. Lin, W. Zhou, W.Y. Liang, E. Schönherr, and H. Bender, *Physica C* **195**, 291 (1992).
- [110] U. Rütt, M.A. Beno, J. Stremper, G. Jennings, C. Kurtz, and P.A. Montano, *Nucl. Inst. Meth. Phys. Res. A* **467-468**, 1026 (2001).
- [111] V. Plakhty, P. Burlet, and J.Y. Henry, *Phys. Lett. A* **198**, 256 (1995).
- [112] S. Rouzière, S. Ravy, J.-P. Pouget, and S. Brazovskii, *Phys. Rev. B* **62**, R16231 (2000).
- [113] J.P. Castellan, B.D. Gaulin, H.A. Dabkowska, A. Nabialek, G. Gu, X. Liu, and Z. Islam, *Phys. Rev. B* **73**, 174505 (2006).

- [114] M. Izquierdo, S. Megtert, J.P. Albouy, J. Avila, M.A. Valbuena, G. Gu, J.S. Abell, G. Yang, M.C. Asensio, and R. Comes, Phys. Rev. B **74**, 054512 (2006).
- [115] D. Hupfeld, *Untersuchung der magnetischen Eigenschaften von Gadolinium-Europium-Sulfid-Mischkristallen mit resonanter Austauschstreuung*, Ph.D. thesis, DESY / University of Hamburg, 1999.

Deutsche Zusammenfassung

In der vorliegenden Arbeit werden die Ergebnisse von Untersuchungen stark korrelierter Elektronensystemen in Übergangsmetalloxiden präsentiert, die mit Hilfe von resonanter beziehungsweise hochenergetischer Röntgenbeugung durchgeführt worden sind. Dabei wurden drei verschiedene Systeme untersucht: 1) das $4d$ Elektronensystem in $\text{Ca}_{2-x}\text{Sr}_x\text{RuO}_4$, 2) das Hybrid-Elektronensystem in $\text{RuSr}_2\text{GdCu}_2\text{O}_8$, und 3) das $3d$ Elektronensystem im hochtemperatursupraleitenden $\text{YBa}_2\text{Cu}_3\text{O}_{6+x}$.

Die elektronischen und magnetischen Eigenschaften des Systems $\text{Ca}_{2-x}\text{Sr}_x\text{RuO}_4$ sind durch eine starke Wechselwirkung zwischen dem magnetischen, dem orbitalen und dem Gitterfreiheitsgrad gekennzeichnet. Diese Wechselwirkung muss berücksichtigt werden, um einen Einblick in das Phasendiagramm des Materials zu erhalten. Bemerkenswert ist dabei, dass die Ersetzung von Kalzium durch Strontium zu einer markanten Variation der Eigenschaften führt, obwohl beide Ionen isovalent sind. Einkristalle der Verbindungen Ca_2RuO_4 und $\text{Ca}_{1.9}\text{Sr}_{0.1}\text{RuO}_4$ wurden in dieser Arbeit mittels resonanter Röntgenbeugung an den Ru L_{II} und L_{III} Absorptionskanten ($E=2.968$ keV beziehungsweise 2.838 keV) untersucht. Die Messungen wurden an der 4ID-D Beamline der Advanced Photon Source Synchrotronstrahlungsquelle in Argonne, USA, durchgeführt. An den magnetisch erlaubten Positionen $(1\ 0\ 0)$ und $(0\ 1\ 1)$ im reziproken Raum wurde oberhalb des magnetischen Phasenübergangs bei $T_N = 110$ K eine neue Phase entdeckt. Diese wird durch die resonante Streuung an den Absorptionskanten beobachtet. Die gestreute Intensität ist nur im sogenannten $\sigma \rightarrow \pi'$ Polarisationskanal zu finden, wird also durch eine gedrehte Strahlungspolarisation gekennzeichnet, die parallel zur Streuebene ist, senkrecht zum Polarisationsvektor der einfallenden Strahlung. Die Temperaturabhängigkeit der Streuintensität in der neuen Phase weist keine Anomalien auf, sondern zeigt bei steigender Temperatur einen langsamen Abfall bis zu einem Phasenübergang bei ungefähr 260 K. Anhand der Polarisations- und Temperaturabhängigkeiten, sowie ergänzender Muonspinrotationsmessungen (μSR), die kein geordnetes magnetisches Moment oberhalb der Néel-Temperatur angedeutet haben, kann der Schluss gezogen werden, dass die Orbitalordnung der Ursprung der Streuintensität in der neuen Phase ist. Der Orbitalordnungsphasenübergang ist auch im strontiumdotierten

$\text{Ca}_{1.9}\text{Sr}_{0.1}\text{RuO}_4$ System zu beobachten, allerdings bei einer niedrigeren Temperatur von ungefähr 130 K. Trotz der Änderung der magnetischen Struktur bleibt der Ausbreitungsvektor der Ordnung in der dotierten Verbindung unverändert. Des Weiteren wurde in beiden untersuchten $\text{Ca}_{2-x}\text{Sr}_x\text{RuO}_4$ Systemen ein zusätzliches Resonanzsignal an der $(1\ 1\ 0)$ Position beobachtet, die sowohl magnetisch als auch kristallographisch verboten ist. Die Intensität dieses Signals sinkt bei steigender Temperatur ohne Anomalien bis zum Metall-Isolator-Übergang. Anhand der Temperatur- und Azimutwinkelabhängigkeiten ist diese Streuintensität auf die Tiltordnung der RuO_6 Oktaeder zurückzuführen.

Das Hybridsystem $\text{RuSr}_2\text{GdCu}_2\text{O}_8$ wird durch die seltene Koexistenz langreichweitiger magnetischer Ordnung und Supraleitung in seiner Einheitszelle charakterisiert. Während sich die Ru Spins in den Ru-O Ebenen unterhalb von 136 K antiferromagnetisch anordnen, etabliert sich in den Cu-O Ebenen unterhalb einer niedrigeren kritischen Temperatur T_c Supraleitung. Die T_c Werte liegen zwischen 15 K und 46 K und sind von den Synthesebedingungen abhängig. Kleine Einkristalle des Materials mit Größe um die $50\ \mu\text{m}$ wurden mittels resonanter Röntgenbeugung an der Ru L_{II} Absorptionskante untersucht. Die Messungen wurden am gleichen Instrument und unter den gleichen experimentellen Bedingungen wie die am $\text{Ca}_{2-x}\text{Sr}_x\text{RuO}_4$ System durchgeführt. Anhand der Azimutwinkelabhängigkeit der Resonanzintensität an der magnetischen $(\frac{1}{2}\ \frac{1}{2}\ \frac{1}{2})$ Position konnte die Richtung des magnetischen Moments im Material genau bestimmt werden. Es wurde insbesondere gefunden, dass das magnetische Moment nicht entlang der kristallographischen c -Richtung orientiert ist, wie ursprünglich anhand von Neutronenbeugungsuntersuchungen vorgeschlagen, sondern entlang einer Richtung, die ungefähr 53 Grad von der c -Achse entfernt ist. Des Weiteren wurde der magnetische Ordnungsparameter des Ru Spinsystems temperaturabhängig verfolgt. Dabei hat sich gezeigt, dass der Einbruch der Supraleitung möglicherweise einen Einfluss auf die magnetische Ordnung hat, was allerdings noch zu bestätigen ist.

Der Hochtemperatursupraleiter $\text{YBa}_2\text{Cu}_3\text{O}_{6+x}$ wurde oft in Hinblick auf die langanhaltende Diskussion über die mögliche Entstehung von sogenannten Streifenphasen (stripes) in Kupraten und ihre Rolle bei der Etablierung von Supraleitung untersucht. Spin- und Ladungsanregungen, die bei Neutronen- und Röntgenstreuungsmessungen beobachtet wurden, wurden als Zeichen von eindimensionalen Streifen interpretiert. Andere Untersuchungen bezweifeln allerdings den eindimensionalen Charakter dieser Ordnung. Eine definitive Antwort auf diese Frage wird durch die Existenz von eindimensionalen, teilweise gefüllten Cu-O Ketten im Gitter erschwert. Zur Klärung der Frage, ob die zu beobachtenden Überstruktureffekte aus elektronischen Streifen in den CuO_2 -Ebenen oder eher aus Sauerstofffehlstellenordnung in den Cu-O Ketten entstammen, wurden sowohl unterdotierte, optimal dotierte und überdotierte, teilweise mit Kalzium substituierte $\text{YBa}_2\text{Cu}_3\text{O}_{6+x}$ Einkristalle, als auch stoichiometrische $\text{YBa}_2\text{Cu}_4\text{O}_8$ Kristalle, mittels hochenergetis-

cher nicht-resonanter Röntgenbeugung untersucht. Die Messungen wurden an den Beamlines BW5 am Hamburger Synchrotronstrahlungslabor und 11ID-C an der Advanced Photon Source in Argonne, USA bei Photonenenergien von 100 keV beziehungsweise 115 keV durchgeführt. Eine neue Überstrukturphase mit einer Periodizität von vier Elementarzellen wurde im optimal dotierten $\text{YBa}_2\text{Cu}_3\text{O}_{6.92}$ und im überdotierten $\text{Y}_{0.8}\text{Ca}_{0.2}\text{Ba}_2\text{Cu}_3\text{O}_{6.95}$ entdeckt. Die Überstrukturreflexe sehen in beiden Verbindungen, die praktisch den gleichen Sauerstoffgehalt aber sehr unterschiedliche Ladungsträgerkonzentrationen haben, fast identisch aus. Dies weist darauf hin, dass die Überstrukturen nicht auf Streifen, sondern auf die Sauerstoffordnung zurückzuführen sind. Dieser Schluss wird von zwei zusätzlichen Beobachtungen unterstützt: das Weiterbestehen der Überstrukturen bis zu Temperaturen deutlich höher als Raumtemperatur; und die Abwesenheit der Überstrukturen im stoichiometrischen $\text{YBa}_2\text{Cu}_4\text{O}_8$ Material, das keine Sauerstofflücken enthält und deshalb die Beobachtung von Streifen erleichtern sollte. Sollten solche Stripes elektronischer Natur in $\text{YBa}_2\text{Cu}_3\text{O}_{6+x}$ existieren, müsste die Intensität der entsprechenden Reflexe um mindestens eine Größenordnung kleiner sein als die der oben beschriebenen Überstrukturreflexe der Sauerstoffordnung. Durch den Vergleich der Streuintensitäten der Überstrukturreflexe von $\text{YBa}_2\text{Cu}_3\text{O}_{6.92}$ Proben, die unterschiedliche Sauerstoffisotope enthalten (^{16}O vs. ^{18}O), wurde des Weiteren festgestellt, dass diese identisch sind. Dies bedeutet, dass Änderungen in der Sauerstoffordnung in den Cu-O Ketten nicht für Isotopeffekte in diesem Material verantwortlich sein können.

Teile der Arbeit wurden in den folgenden Publikationen veröffentlicht:

- J. Stempfer, I. Zegkinoglou, U. Rütt, M. v. Zimmermann, C. Bernhard, C.T. Lin, Th. Wolf, and B. Keimer, *Oxygen Superstructures Throughout the Phase Diagram of $(\text{Y,Ca})\text{Ba}_2\text{Cu}_3\text{O}_{6+x}$* , Phys. Rev. Lett. **93**, 157007 (2004)
- I. Zegkinoglou, J. Stempfer, C.S. Nelson, J.P. Hill, J. Chakhalian, C. Bernhard, J.C. Lang, G. Srajer, H. Fukazawa, S. Nakatsuji, Y. Maeno, and B. Keimer, *Orbital Ordering Transition in Ca_2RuO_4 Observed with Resonant X-Ray Diffraction*, Phys. Rev. Lett. **95**, 136401 (2005).

Acknowledgements

This work would not have been possible without the important contributions of numerous people. I would like at this point to express my deepest gratefulness to all of them, apologizing in advance to those I might unintentionally forget.

I am very grateful to...

...Prof. Dr. Keimer, for giving me the opportunity to carry out this work in the scientifically exciting environment of his group and for his constant support during all of its stages, for allowing me to learn from his excellent knowledge of physics, for being always accessible and willing to help despite his restricted time, for giving me the chance to participate in numerous scientific conferences and workshops, which contributed to my knowledge and experience, and for the careful reading, correcting and commenting on the final version of the thesis.

...Dr. Jörg Stempfer, for accepting to supervise the accomplishment of my thesis and for doing so in an excellent way, for the innumerable things he taught me from his rich knowledge and experience, for his patient and continuous guidance over the four years of the thesis and especially during the difficult adapting period in the beginning, for his help and support, which he always generously provided in any issue that came up, and of course for carefully reading and correcting the thesis manuscript.

...Prof. Dr. Helmut Dosch for kindly accepting the task of reading and reviewing the thesis.

...Britta Bohnenbuck for her help and support during the last one and a half years of the thesis, for being a great colleague and collaborator, with whom it is always a pleasure to work, and for her stimulating ideas and nice company during the synchrotron experiments.

...Heinrich Klann for his valuable help in any kind of technical, mechanical or

software-related issues that came up in the x-ray laboratory at MPI. Without his knowledge and experience, his exceptional skills, and his hard work, the operation of the laboratory would not have been possible. I also thank him for designing and constructing the sample holders used in the synchrotron experiments.

...Manfred Ohl for his help in technical issues in the x-ray laboratory, as well as issues related to radiation safety and ordering of equipment.

...all the people I had the pleasure to collaborate with in numerous synchrotron experiments. Special thanks to Dr. Christie S. Nelson and Dr. John P. Hill for our excellent and fruitful collaboration in the investigation of ruthenates, for the plenty of stimulating discussions, for providing the $\text{Ca}_{1.9}\text{Sr}_{0.1}\text{RuO}_4$ sample, and for giving access to the code used as a basis in this work for the calculation of the tilt-order structure factors in Ca_2RuO_4 . Special thanks also to: Dr. George Srajer, Dr. Jonathan C. Lang and the rest of the scientific and technical staff of Sector 4 at APS for the outstanding support they provided us during the beamtimes at 4ID-D¹; Dr. Martin von Zimmermann and the rest of the BW5 staff for their help during the experiments at HASYLAB; and Dr. Mark Beno and the staff of Sector 11 at APS for their support during the beamtimes at 11ID-C¹.

...all the people, whose work I benefited from, for the completion of this thesis. Especially I would like to thank: Prof. Dr. Christian Bernhard for providing the $\text{YBa}_2\text{Cu}_3\text{O}_{6+x}$ and $\text{RuSr}_2\text{GdCu}_2\text{O}_8$ samples, for his help in the thermal treatment of the $\text{YBa}_2\text{Cu}_3\text{O}_{6+x}$ crystals, for performing, together with Dr. Jacques Chakhalian, the μSR measurements on Ca_2RuO_4 , and for the plenty of fruitful discussions I had the chance to profit from; Dr. Chengtian Lin and his collaborators for growing the $\text{YBa}_2\text{Cu}_3\text{O}_{6+x}$ and $\text{RuSr}_2\text{GdCu}_2\text{O}_8$ samples; Prof. Dr. Yoshiteru Maeno and his collaborators for growing and providing the Ca_2RuO_4 single crystals; Dr. Jacques Chakhalian for his contribution to the μSR measurements, as well as to one of the synchrotron experiments; Dr. Giniyat Khaliullin for his useful theoretical suggestions concerning the orbitally ordered state in Ca_2RuO_4 , for the numerous, particularly interesting discussions I had the opportunity to have with him, and for the help he always willingly offered in any kind of issues related to solid state physics; Eva Brücher for performing SQUID measurements on part of the $\text{YBa}_2\text{Cu}_3\text{O}_{6+x}$ and Ca_2RuO_4 samples; and Helmut Wendel for the treatment of part of the $\text{YBa}_2\text{Cu}_3\text{O}_{6+x}$ samples and for allowing access to the Laue camera of his group.

¹Use of the Advanced Photon Source is supported by the US Department of Energy, Office of Basic Energy Sciences, under Contract No. W-31-109-Eng-38.

...Britta Bohnenbuck and Björn Hornbostel, for correcting the german summary of the thesis.

...Dr. Sabine Andergassen, Roland Gersch, Björn Hornbostel, Dr. Jorge Serrano Gutiérrez, Dr. Jörg Strempler, Anton Suchanek, and Dr. Michael Wanitschek, for their help in working with L^AT_EX.

...my office-mates Vladimir Damljanović, Vladimir Hinkov and Markus Raichle, for all the nice moments I experienced next to them in the last four years, for creating a really pleasant and stimulating working environment, for all the interesting discussions I had the pleasure to have with them, and for the help and advice they offered whenever needed.

...Claudia Hagemann, for her efficient help in any kind of administrative issues, and for her assistance in every-day problems, especially during the first months of my stay in Germany.

...all my colleagues, present and past, in Prof. Keimer's group, for contributing to a pleasant working environment, for their friendliness and help, and for plenty of stimulating discussions. Many thanks to: Dr. Peter Adler, Ali Al-Sawalmih, Ibrahim Al-Suraihy, Pegor Aynajian, Mohammed Bakr, Dr. Sibel Bayrakci, Prof. Dr. Christian Bernhard, Dietrich Böhme, Britta Bohnenbuck, Dr. Alexander Boris, Markus Bröll, Benjamin Bruha, Kathrin Buchner, Dr. Lucia Capogna, Dr. Jacques Chakhalian, Vladimir Damljanović, Mael Guennou, Vladimir Hinkov, Dr. Thomas Keller, Dr. Giniyat Khaliullin, Dr. Heon-Jung Kim, Dr. Myung-Whun Kim, Taryl Leaton Kirk, Heinrich Klann, Dr. Natalia Kovaleva, Dr. Alexandre Lebon, Prof. Dr. Peter Lemmens, Dr. Bing Liang, Dr. Lina Machtoub, Dr. Maxim Mostovoy, Dr. Timur Mukhamedjanov, Bernard Nansseu, Manfred Ohl, Dr. Alexei Pimenov, Dr. Pavlo Popovich, Markus Raichle, Dr. Uta Rütt, Dr. Jorge Serrano Gutiérrez, Dr. Jörg Strempler, Anton Suchanek, Heiko Uhlig, Dr. Clemens Ulrich, Petar Yordanov and Li Yu.

...all members of the scientific, technical and administrative staff of the Max-Planck-Institutes in Stuttgart, for creating a unique international research environment with excellent infrastructure, which provided ideal conditions for carrying out this work.

...Longinus Raschke for his help in so many daily-life issues and for doing his best to make my settling down in Stuttgart and my stay there as easy and pleasant as possible.

...all my wonderful friends I had the luck to meet during my stay in Germany, whose company and support helped me overcome the difficulties and problems I found on my way, both in relation to the thesis and in general, and contributed to the last four years being for me a great experience. Special thanks to Björn Hornbostel, as well as Anastasia Adamidou, Dr. Erik Ahlswede, Dr. Kannan Balasubramanian, Dr. Esther Barrena, Britta Bohnenbuck, Dr. Lucia Capogna, Franck Dahlem, Vladimir Damljanović, Dr. Jean-René Duclère, Rubén Esteban, Dr. Alicia Forment, Dimas García de Oteyza, Dr. Martin Geisler, Mael Guennou, Javier Herrero Martín, Vladimir Hinkov, Dr. Georgios Katsaros, Eduardo Lee, Dr. Bing Liang, Magalí Lingenfelder, Dr. Carlos Manzano, Dr. Alicia Maroto, Ajo Mula, Alicia Nieto, Dr. Hiroki Okudera, Alena Palanevich, Sotiria Papantoniou, Dr. David Quirion, Christian Reich, Thomas Reindl, Julius Reiß, Dr. Diego Repetto, Torsten Rudolf, Martina Sauter, Dr. Jorge Serrano Gutiérrez, Olga Shakuro, Marina and Milan Struhar, Anton Suchaneck, Miloš Vračar, Dr. Rodney Wiersma, Petar Yordanov, Monika Zoelde, and Dr. Eva Zurek.

...last but not least, my beloved parents and my sister Teresa, without the love, support and constant encouragement of whom the completion of this work, like many other things in my life, would not have been possible.

Curriculum Vitae

Name: Ioannis Zegkinoglou
Date of birth: March 20, 1979
Place of birth: Athens, Greece
Nationality: Greek

Academic education

10/2002 - 10/2006: Ph.D. studies at the Max-Planck-Institut für Festkörperforschung, Stuttgart. Supervisor: Prof. Dr. Bernhard Keimer
Oral defense: 01/2007

11/2002: Diploma in Physics: 8/10, *'very good'*
Department of Physics, National and Kapodistrian University of Athens, Greece

04/2001 - 06/2002: Diploma Thesis: 10/10
Broadband AC Dielectric Relaxation Spectroscopy and Hydration Properties of Segmented Polyurethanes
Supervisor: Prof. Dr. Aglaia Vassilikou-Ntova

10/1997 - 11/2002: Studies of Physics
Department of Physics, National and Kapodistrian University of Athens, Greece

06/1997: University entrance examinations

06/1996: School leaving diploma: 19.3/20

09/1993 - 06/1996: 22nd Lyceum of Athens, Greece
09/1990 - 06/1993: 68th Gymnasium of Athens, Greece
09/1984 - 06/1990: 139th Primary School of Athens, Greece